Department of Materials Science and Engineering

Densification of Na-ion compounds by conventional and cold sintering.

Ademola Joseph Adetona

A thesis submitted in partial fulfilment of the requirements for the degree of Doctor of Philosophy

Supervisors

Prof. Ian Reaney[1]

Dr Brant Walkley[2]

[1]Department of Materials Science and Engineering

[2]Department of Chemical and Biological Engineering

March 2024.

Declaration

This thesis, “Densification of Na-ion compounds by conventional and cold-sintering”, results from work in the Functional Materials and Device Laboratory in the Department of Materials Science and Engineering at the University of Sheffield between September 2019 and January 2024.

The candidate acknowledges the assistance of Professor Nicola Morley of the Department of Materials Science and Engineering, University of Sheffield, for Superconducting Quantum Interference Device (SQUID) measurements and Igor Levin of the National Institute of Standards and Technology, Gaithersburg, U.S.A. for Transmission Electron Microscopy (TEM) measurements.

Except where otherwise stated, either directly or by reference, the work is the author's original creation, and the author understands the use of unfair means in the University Guidelines (Unfair means cheating and plagiarism | Support for new students | The University of Sheffield). This work has not been partially or fully submitted for any degree or award at any other university.

The manuscripts below have been published or are in preparation for publication and are included as result chapters in this thesis.

- A.J. Adetona, G. Wang, B. Walkley, D.C. Sinclair & I.M. Reaney, (2023). Effect of ZrO_2 stoichiometry on the structural and electrical properties of $Na_3Zr_{2-x}Si_2PO_{12-2x}$ solid electrolyte. https://doi.org/10.1016/j.jeurceramsoc.2023.12.071 (*Journal of the European Ceramic Society*).
- Aqueous cold sintering of $Na_{0.7}CoO_2$: A benign, facile method for the densification of cathodes for Na-ion solid-state battery applications. (*submitted for peer-review*).

Ademola Joseph Adetona

Sheffield, United Kingdom.

March 2024.

Don't give up. Keep trying, even when things get tough. Success may surprise you if you push through setbacks.

- *Thomas A. Edison.*

Acknowledgement

My deepest and sincerest appreciation goes to my supervisor and mentor, Prof. Ian Reaney, for his unwavering support, patience, advice, and guidance. I am incredibly grateful for the wealth of knowledge he impacted in our numerous meetings. Also, my appreciation goes to my co-supervisor, Dr. Brant Walkley, for his advice and guidance.

In addition, I would like to express my heartfelt gratitude and appreciation to Prof. Derek Sinclair for his unwavering support and guidance throughout the doctoral journey with Impedance Spectroscopy.

I want to thank the following people from the Functional Materials and Devices Group:

- Dr Ge Wang (The University of Manchester), my good friend, whom I always bother. Thank you for being patient and taking the time to help me in and out of the lab.
- The Post-doc: Dr Jessica Andrews and Dr Daniel Button.
- My Lab-mate: Dr Meshari Alotaibi, Fawaz Almutairi, Step Mudd, James Al-Watt, Mr Babatunde, Yongbo and James Killen.
- The Lab technician Kerry McLaughlin for always being willing to help and support in and out of the lab.

From the Basic Characterisation Lab to the Sorby Centre, I thank Robert Moorhead, Oday Hussein, Cheryl Shaw, and Lee Ma for guiding and supporting me around the XRD, the basic characterisation equipment and SEM equipment.

In addition, I appreciate the PGR Tutors, Dr Rebecca Boston (former) and Dr Nik Reeves-McLaren (current), for giving me space and time to express myself when challenged. Also, I want to thank Andy Keating (for ensuring I secured a place in the department) and Ann Newbould (she is always willing to help) for their support and assistance in all the administrative tasks that need completion.

My sincere appreciation goes to my examiners, Prof. Robert Freer (external) and Dr Rebecca Boston (internal), for their meticulous review of my thesis, insightful feedback, and valuable discussion and contributions during my viva.

My family (My lovely wife, Theresa, who is my pillar, fighter and confidant and my beautiful girls, Oluwadamilola and Oluwadarasimi), for the love, care, and patience they

had and for condoling my excesses, anger, and frustration during the writing period. My parents and siblings are not forgotten for the support and prayers to complete this project.

My profound gratitude goes to the entire staff of the University of Lagos, Nigeria and my grassroot department, the Department of Chemistry, University of Lagos, Nigeria.

I sincerely appreciate the Tertiary Education Trust Fund (TETFUND) for the support and Funds to complete my program.

I dedicate this project to God almighty, who made me start and finish the program brilliantly.

Abstract

NZSP (NASICON) solid electrolyte has good conductivity for Na-ion solid-state batteries (SSSBs), enabling efficient ion transport at room temperature. NZSP crystal symmetry and stability contribute to its high ionic conductivity (10^{-3} – 10^{-4} Scm^{-1}) at room temperature, promoting durability and enhanced battery performance. $Na_3Zr_2Si_2PO_{12}$ (NZSP) have been widely studied; to date, $Na_{1+x}Zr_2Si_xP_{3-x}O_{12}$ compositions invariably contain *m*-ZrO_2 as a secondary phase. Here, the solid-state method is used to prepare single-phase NZSP by modifying the mole fraction of the ZrO_2 reactant, thereby creating Zr and O vacancies. In addition, the effect of *m*-ZrO_2 reactant in suppressing the impurity phase and promoting the ionic conductivity of NZSP was investigated and compared with the literature. X-ray diffraction, scanning electron microscopy, Raman and FTIR spectroscopy, dilatometry studies, and Electrochemical impedance spectroscopy are used to characterise the structural, morphology and electrical properties of NZSP and results compared with 'stoichiometric' $Na_3Zr_2Si_2PO_{12}$ and literature.

In addition, NZSP was densified by the cold sintering method. The density, phase assemblage, morphology and conductivity of cold sintered samples were investigated using a combination of Archimedes/geometric density measurement, XRD, SEM and impedance spectroscopy. Furthermore, the impact of post-annealing on the morphology and conductivity of the cold-sintered NZSP ceramics was studied and compared with conventional sintered NZSP.

Overall, cold sintering had only a limited effect on NZSP densification, with post-annealing required at temperatures > 400 °C to obtain a reasonable relative density (89%) with conductivity lower by 10-fold compared to the conventionally sintered NZSP.

The NASICON-type $Na_{1.3}Ti_2P_3O_{12}$ (NTP) has been widely investigated for various applications. In this context, $Na_{1.3}Ti_{1.7}Al_{0.3}P_3O_{12}$ (NATP) was studied as a potential solid electrolyte for Na-ion solid-state batteries. Sintering studies by the conventional method resulted in a ceramic with a relative density of ~ 92.0%. Phase identification study by XRD revealed a rhombohedral structure with an *R-3c* space group. Morphology and shrinkage studies were analysed by scanning electron microscopy and dilatometer, respectively. Impedance spectroscopy plots resulted in the RT conductivity value of 10^{-7} S/cm.

The densification of NATP by cold sintering method was studied, and the effect of different transient solvents (aqueous and organic solvents) on NATP ceramic was investigated. The density, structure, morphology, and impedance response were studied as a function of the transient solvents, post-annealing and pressing pressure. The densification results were compared with the NATP ceramic sintered conventionally and the literature.

Sodium cobaltate ($Na_{0.7}CoO_2$, NCO) is a well-known cathode material in Na-ion batteries. This study explored its properties as a possible solid electrolyte by densifying the NCO ceramic using the conventional sintering method. The relative density studies achieved only ~ 92.0%, and the resulting phase, morphology, magnetic and electrical properties were investigated using XRD, SEM, SQUID magnetometer and Impedance spectroscopy. The conventionally sintered NCO ceramics exhibited a hexagonal structure with a $P6_3/mmc$ space group. The magnetic studies resulted in a classic paramagnetic behaviour down to 6K with a change in magnetic behaviour to spin-glass. The impedance spectroscopy studies exhibited an ionic conductivity of ~ 10^{-2} Scm^{-1} at room temperature with a low E_a of 0.027 ± 0.015 eV.

Densification of NCO by cold sintering technique was investigated, and the effect of different transient solvents on the phase, morphology, magnetic and electrical properties were studied, and the results were compared with conventionally sintered NCO ceramic. The density of the aqueous cold sintered ceramic achieved a ρ_r of ~ 98.0%, which exceeded that of the conventional sintered (ρ_r ~ 92.0%) NCO ceramics whilst maintaining high values of conductivity (between ~10^{-1} to 10^{-2} Scm^{-1}), with subtle differences observed with conventionally sintered NCO samples. The magnetic studies resulted in a classic paramagnetic behaviour with no significant changes in the susceptibility as a function of temperature. The impedance spectroscopy studies of the aqueous cold sintered NCO exhibited an ionic conductivity of ~ 10^{-2} Scm^{-1} at room temperature with an E_a of 0.037 ± 0.017 eV, similar to the conventional sintered NCO. Overall, the transient solvents for the densification of NCO ceramic produce different but complimentary responses.

Abbreviations

NCO	Sodium cobalt oxide ($Na_{0.7}CoO_2$)
IPA	Isopropanol
CS	Cold sintered
ρ_r	Relative density
IS	Impedance spectroscopy.
NZSP	Sodium Zirconium Silicate Phosphate
NATP	Sodium Aluminium Titanate Phosphate
ICDD	International Centre for Diffraction Data
In-Ga	Indium Gallium
SEM	Scanning electron microscopy
SQUID	Superconducting Quantum Interference Device

Contents

Chapter 1

1.0 Introduction

1.1 Energy Storage and Sustainability.

Global warming is forcing the world to rethink how it satisfies its energy demands. In addition, the current global production and distribution crisis has demonstrated that fossil fuels cannot be depended on as the mainstay of energy production [1]. The shortage and restriction of fossil fuels due to the war and sanctions have increased the price worldwide, making world leaders focus on sustainable and decarbonised energy sources. For example, the European Union has increased its total expenditure on sustainable energy generation to hundreds of billions of euros [2]. Also, the European and some African countries have adjusted their budget to accommodate energy from sources other than fossil fuels. The United Kingdom announced that by the year 2040, gasoline vehicles will be banned [3] to meet the 2050 net-zero carbon emission target and reduce our dependence on fossil fuels [4].

One recent effect of CO_2 emission on climate change was the heatwave that swept across several European countries in July 2022 [5]. A temperature > 40 °C was recorded in the UK, and wildfires destroyed properties and farms, causing chaos and panic across Europe. BP's statistical review of world energy consumption before the pandemic in the year 2020 reported that over 84% of the world's energy consumption is from fossil fuels. Coal, 27.0 %; crude oil, 33.0 %; and over 24.0 % comes from natural gas, as shown in Figure 1.1. Regrettably, these fuels are non-renewable, and ¾ of human CO_2 emissions arise from these sources. Driving research on renewable and low-carbon energy technologies [6, 7].

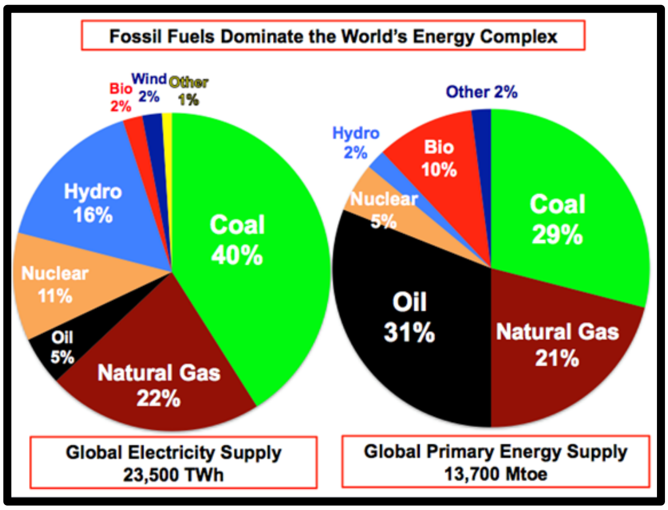

Figure 1.1. Global energy generation and distribution from fossil fuels [6].

1.2 Battery and Energy Storage Technologies

Battery technologies are essential for energy storage and are integral to electric vehicles, mobile devices, and the widespread use of intermittent renewable energy sources (e.g. wind and solar) [8]. Over the years, scientists have investigated various energy storage devices, including flywheels [9, 10], redox-flow batteries [11, 12], large-scale compressed gas [13] and rechargeable batteries [14-16]. Among these energy storage devices, Rechargeable batteries are attractive because they suit different specific applications; they are helpful for stable energy over sustainable periods and are scalable for grid storage and mobile applications [17, 18]. Rechargeable batteries allow consumers to power their devices, such as cars, phones, and home appliances, using the stored energy from the batteries. Also, batteries have the benefit of being non-polluting when handled professionally and are fabricated from environmentally friendly materials [19, 20]. Many portable battery technologies exhibit moderate capacities and cycle life; therefore, high energy density batteries with long cycle life are essential to reduce the dependence on fossil fuels [21].

1.2.1 Li-ion Batteries

SONY Corporation commercialised the first Li-ion batteries (LIBs) in 1991 [22, 23]. Since then, Li-ion batteries have been the most widely researched rechargeable energy storage technology, Figure 1.2.1. The advantages of Li-ion batteries to earlier technologies are the superior energy and power densities [24], high columbic efficiencies [24], low self-discharge properties [25], fast charging [25], and low maintenance [24]. LIBs contribute over 65% of global sales [26], and the demand for portable electronic devices has seen an increase in the production of LIBs. However, with the high demand for portable electronic devices, LIBs have the challenges of low retention and operational difficulties [27], dendrite formation [24], leakage [28], explosions/fires during charging, and high manufacturing costs [27]. The organic electrolyte used in LIB poses a significant threat to battery fabrication as it may cause battery leakage, which can eventually lead to battery explosion [28]. The demand for Li-ion batteries has hiked the price of Li_2CO_3, a precursor of Li-ion. Adopting Li-ion batteries for large-scale energy storage systems will further increase the cost of lithium precursors and batteries [29].

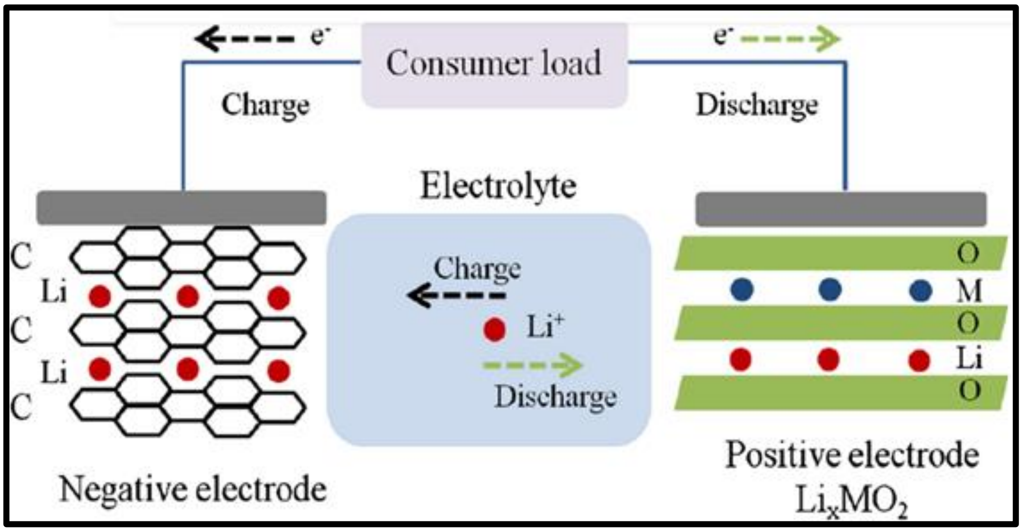

Figure 1.2.1. Li-ion battery Schematic [24].

1.2.2 Na-ion Batteries

Na-ion batteries (NIBs) are becoming increasingly popular for large-scale energy storage due to the abundance, affordability, and low toxicity of sodium compounds. They are promising alternatives to Li-ion technology, and lately, research on NIBs has increased due to the similarity in the chemistry of LIBs and NIBs. Many researchers estimate NIBs to surpass LIB in terms of usage in the long term [30]. However, NIB's volumetric and gravimetric energy density is lower than that of LIBs due to the larger ionic radius of Na. The abundance of Na-ion precursors in the ocean and earth's crust lowers the cost of Na-ion precursors and has propelled NIBs as the likely contenders for future large-scale energy storage devices [31]. Organic electrolytes used in NIB can cause safety issues such as leakage, high flammability, and low energy density, which restrict their extensive usage [32-36]. Therefore, Na-ion solid-state batteries (SSSIB) that use solid electrolytes and solid electrodes may overcome the shortcomings of SIBs, Figure 1.2.2.

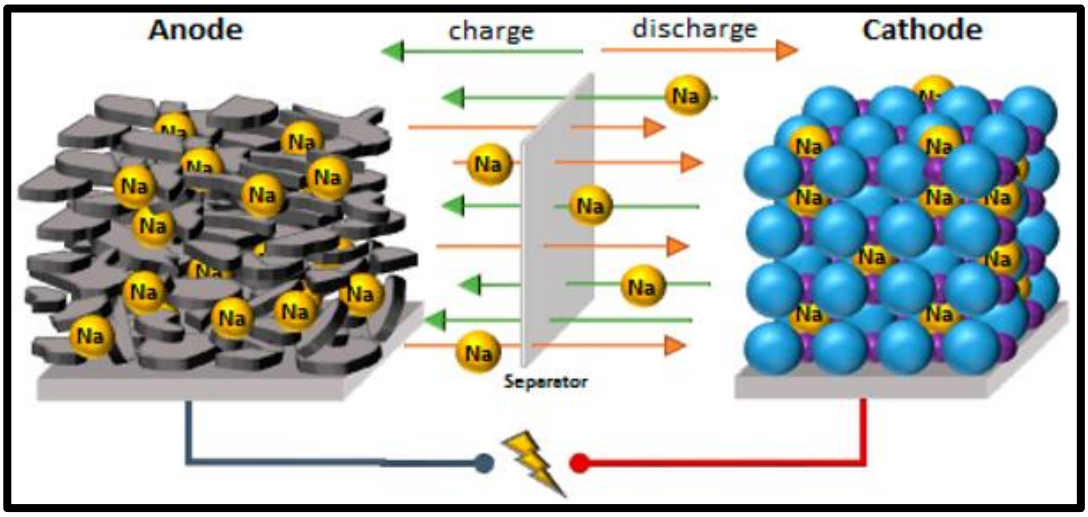

Figure 1.2.2 Na-ion solid-state battery schematic [31].

1.2.3 Solid Electrolytes

Solid-state batteries (SSBs) utilise a solid electrolyte instead of a liquid organic or gel-like electrolyte found in Li-ion and Na-ion batteries [37]. One of the advantages of exploring Na SSBs (SSSBs) is the abundance and affordability of sodium precursors [38]. Lithium resources are limited and concentrated in a few regions, making LIBs expensive. On the other hand, sodium precursors are widely available, and their production costs are cheaper [39, 40]. Therefore, SSSBs may offer a cost-effective, improved safety and more sustainable energy storage solution, especially in large-scale applications [41]. Solid electrolytes (SEs) eliminate the risk of leakage, degradation and thermal runaway associated with liquid electrolytes [42-44]. The enhanced safety of the electrolyte makes SSBs highly desirable for various applications, including consumer electronics and electric vehicles [45-52].

Various solid electrolytes (SEs), such as ceramics, glasses, and polymer materials, have been explored to improve battery performance and reduce the interfacial resistance between solid electrodes and electrolytes [53-57]. Among these solid electrolytes, oxide-based solid electrolytes have been extensively studied for their ease of preparation, stability [55], fast-ion conduction [55], non-flammability [57], ion mobility and potential applications in batteries and advanced energy storage devices [55-58]. The conductivity of oxide-based Na-ion solid electrolytes depends on factors such as the Na-ion concentration, Na^+ mobility/diffusion, crystal symmetry and preparation routes [65-69].

1.3 Cold Sintering of Na-ion Compounds

There are several methods of preparing and densifying Na-ion compounds; among these methods, conventional sintering is the most widely accepted technique, which requires a temperature ≥ 1000 °C and several hours to achieve densification [33-36]. Cold sintering can potentially densify Na-ion compounds at a lower temperature (≤ 300 °C) and shorter time (< 30 minutes) using a transient solvent and externally applied pressure [66]. Randall [67, 68], the leading researcher in cold sintering technology, has extensively investigated and demonstrated the feasibility of the process. However, the technique is new, and there are questions about the mechanism and properties of materials prepared by this low-temperature technique [69].

1.4 Aims of the Project

This research investigates the properties of Na-ion compounds prepared by the solid-state reaction methods and the densification of the Na-ion compounds by conventional and cold sintering techniques. To this end, three different Na-ion compounds, sodium cobaltate ($Na_{0.7}CoO_2$), sodium aluminium titanate phosphate ($Na_{1.3}Ti_{1.7}Al_{0.3}P_3O_{12}$) and sodium zirconium silicate phosphate ($Na_3Zr_{2-x}Si_2PO_{12-2x}$) were densified using conventional and cold sintering technique. Their suitability for low-temperature densification is assessed, and their structure, phase, microstructure, and electrical properties are compared.

1.5 References

[1] P. G. Smil and V. Smil, Energy at the Crossroads: Global Perspectives and Uncertainties. MIT Press, 2003.

[2] A. Patt, N. Komedatova, A. Battaglini, and J. Lilliestam, “Regional integration to support full renewable power deployment for Europe by 2050,” Environmental Politics, vol. 20, no. 5, pp. 727–742, Sep. 2011, https://doi.org/10.1080/09644016.2011.608537.

[3] M. Shammut, M. Cao, Y. Zhang, C. Papaix, Y. Liu, and X. Gao, “Banning Diesel Vehicles in London: Is 2040 Too Late?,” Energies, vol. 12, no. 18, p. 3495, Sep. 2019, https://doi.org/10.3390/en12183495.

[4] J. Dixon, K. Bell, and S. Brush, “Which way to net zero? A comparative analysis of seven UK 2050 decarbonisation pathways,” Renewable and Sustainable Energy Transition, vol. 2, p. 100016, Aug. 2022, https://doi.org/10.1016/j.rset.2021.100016.

[5] E. J. L. Chappin and G. P. J. Dijkema, “On the impact of CO_2 emission-trading on power generation emissions,” Technological Forecasting and Social Change, vol. 76, no. 3, pp. 358–370, Mar. 2009, doi.org/10.1016/j.techfore.2008.08.004.

[6] B. Dudley, “BP Statistical Review of World Energy 2016.

[7] M. H. Abbasi, B. Abdullah, M. Ahmad, A. Rostami, and J. Cullen, “Heat transition in the European building sector: Overview of the heat decarbonisation practices through heat pump technology,” Sustainable Energy Technologies and Assessments, vol. 48, p. 101630, Dec. 2021, doi.org/10.1016/j.seta.2021.101630.

[8] H. Zsiborács, N.H. Baranyai, A. Vincze, L. Zentkó, Z. Birkner, K. Máté, G. Pintér, Intermittent Renewable Energy Sources: The Role of Energy Storage in the European Power System of 2040, Electronics. 8 (2019) 729. https://doi.org/10.3390/electronics8070729.

[9] M. A. Awadallah and B. Venkatesh, Energy Storage in Flywheels: An Overview, Canadian Journal of Electrical and Computer Engineering, vol. 38, no. 2, pp. 183–193, 2015, https://doi.org/10.1109/cjece.2015.2420995.

[10] D. Bender, “Flywheels,” Energy Storage, pp. 249–289, Jun. 2017, https://doi.org/10.1142/9789813208964_0007.

[11] S. Gentil, D. Reynard, and H. H. Girault, “Aqueous organic and redox-mediated redox flow batteries: a review,” Current Opinion in Electrochemistry, vol. 21, pp. 7–13, Jun. 2020, https://doi.org/10.1016/j.coelec.2019.12.006.

[12] F. Pan and Q. Wang, “Redox Species of Redox Flow Batteries: A Review,” Molecules, vol. 20, no. 11, Nov. 2015, https://doi.org/10.3390/molecules201119711.

[13] A. M. Elberry, J. Thakur, A. Santasalo-Aarnio, & M. Larmi, “Large-scale compressed hydrogen storage as part of renewable electricity storage systems” International Journal of Hydrogen Energy, Mar. 2021, doi.org/10.1016/j.ijhydene.2021.02.080.

[14] J. B. Goodenough, “Rechargeable batteries: challenges old and new,” Journal of Solid-State Electrochemistry, vol. 16, no. 6, pp. 2019–2029, May 2012, https://doi.org/10.1007/s10008-012-1751-2.

[15] P. V. Braun, J. Cho, J. H. Pikul, W. P. King, and H. Zhang, “High power rechargeable batteries,” Current Opinion in Solid State and Materials Science, vol. 16, no. 4, pp. 186–198, Aug. 2012, https://doi.org/10.1016/j.cossms.2012.05.002.

[16] J. Liu, C. Xu, Z. Chen, S. Ni and Z.X. Shen, Progress in aqueous rechargeable batteries, Green Energy and Environment. 3 (2018) 20–41. https://doi.org/10.1016/j.gee.2017.10.001.

[17] X. Lin, M. Salari, L. Arava, P. Ajayan, and M. Grinstaff, “High-temperature electrical energy storage: advances, challenges, and frontiers,” Chemical Society Reviews, vol. 45, no. 21, pp. 5848–5887, Oct. 2016, https://doi.org/10.1039/C6CS00012F.

[18] B. Pinnangudi, M. Kuykendal & S. Bhadra, “Smart Grid Energy Storage”, Sci. Direct Jan 2017 https://www.sciencedirect.com/B9780128053218000045

[19] H. Zhao, Y. Nie, Y. Li, T. Wu, E. Zhao, J. Song, S. Komarneni, Low-cost and eco-friendly synthesis of octahedral $LiMn_2O_4$ cathode material with excellent electrochemical performance, Ceramics International. 45 (2019) 17183–17191. https://doi.org/10.1016/j.ceramint.2019.05.273.

[20] Z. Liu, B. Xue, Z. Xie, and G. Zhao, “Grid-Grade Rechargeable Batteries and Predication in Future,” Highlights in Science, Engineering and Technology, vol. 3, pp. 63–72, Jul. 2022, https://doi.org/10.54097/hset.v3i.694.

[21] D. Larcher and J-M. Tarascon, “Towards greener and more sustainable batteries for electrical energy storage,” Nature Chemistry, vol. 7, no. 1, pp. 19–29, Nov. 2014, https://doi.org/10.1038/nchem.2085.

[22] J. Rohan, M. Hasan, S. Patil, D. P., and T. Clancy, “Energy Storage: Battery Materials and Architectures at the Nanoscale,” ICT - Energy - Concepts Towards Zero – Power Information and Communication Technology, Feb. 2014, doi.org/10.5772/57139.

[23] E. E. Ferg, F. Schuldt, and J. Schmidt, “The challenges of a Li-ion starter lighting and ignition battery: A review from the cradle to the grave,” Journal of Power Sources, vol. 423, pp. 380–403, May 2019, doi.org/10.1016/j.jpowsour.2019.03.063.

[24] C. Sun, X. Zhang, C. Li, K. Wang, X. Sun, and Y. Ma, “High-efficiency sacrificial pre-lithiation of Li-ion capacitors with superior energy-storage performance,” Energy Storage Materials, pp. 160–166, Jan. 2020, doi.org/10.1016/j.ensm.2019.08.023

[25] A. K. M. Ahasan Habib, S. M. A. Motakabber, and M. I. Ibrahimy, “A Comparative Study of Electrochemical Battery for Electric Vehicles Applications,” IEEE Xplore, Nov.2019. https://ieeexplore.ieee.org/abstract/document/9071955/?casa_token=PgjSAibw3MAAAAA:JpvTzd6L2uSKCx2dp82F6hJ47oKTJZIOx5awS8KaYp5AA5P_S95qLoJ8e7jqJf2yt6eUboYbrrRt.

[26] I. Tsiropoulos, D. Tarvydas and N. Lebedeva, Lithium-ion batteries for mobility and stationary storage applications scenarios for costs and market growth global supply and demand of lithium-ion batteries today and in the future, (2018). https://doi.org/10.2760/87175.

[27] J. Duan, X. Tang, H. Dai, Y. Yang, W. Wu, X. Wei, Y. Huang, Building Safe Lithium-Ion Batteries for Electric Vehicles: A Review, Electrochemical Energy Reviews. 3 (2019) 1–42. https://doi.org/10.1007/s41918-019-00060-4.

[28] D. Ouyang, M. Chen, Q. Huang, J. Weng, Z. Wang, and J. Wang, “A review on the thermal hazards of the Li-ion battery & the Corresponding Countermeasures” Applied Sciences, vol. 9, p. 2483, no. 12, Jun. 2019, https://doi.org/10.3390/app9122483.

[29] L. Gaines, K. Richa, and J. Spangenberger, “Key issues for Li-ion battery recycling.” MRS Energy & Sustainability, vol. 5, 2018, https://doi.org/10.1557/mre.2018.13.

[30] M. I. Jamesh and A. S. Prakash, “Advancement of technology towards developing Na-ion batteries,” Journal of Power Sources, vol. 378, pp. 268–300, Feb. 2018, https://doi.org/10.1016/j.jpowsour.2017.12.053.

[31] J.F. Peters, A. Peña Cruz, M. Weil, Exploring the Economic Potential of Sodium-Ion Batteries, Batteries. 5 (2019) 10. https://doi.org/10.3390/batteries5010010.

[32] Y. B. Rao, K. K. Bharathi, and L. N. Patro, “Review on the synthesis and doping strategies in enhancing the Na-ion conductivity of $Na_3Zr_2Si_2PO_{12}$ solid electrolytes,” Solid State Ionics, vol. 366–367, Aug. 2021, https://doi.org/10.1016/j.ssi.2021.115671.

[33] Q. Huang, G. Chen, P. Zheng, W. Li, and T. Wu, “NASICON-structured Na-ion conductor for next-generation energy storage,” Functional Materials Letters, vol. 14, no. 03, p. 2130005, Apr. 2021, https://doi.org/10.1142/s179360472130005x.

[34] S. S. Das, P. K. Srivastava, and N. B. Singh, “Fast-ion conducting phosphate glasses and glass ceramic composites: Promising materials for solid-state batteries,” Journal of Non-Crystalline Solids, vol. 358, no. 21, pp. 2841–2846, Oct. 2012, https://doi.org/10.1016/j.jnoncrysol.2012.05.031.

[35] Z. Yu, S.-L. Shang, D. Wang, Y.C. Li, H.P. Yennawar, G. Li, H.-T. Huang, Y. Gao, T.E. Mallouk, Z.-K. Liu, D. Wang, Synthesis and understanding of $Na_{11}Sn_2PSe_{12}$ with enhanced ionic conductivity for all-solid-state Na-ion battery, Energy Storage Materials. 17 (2019) 70–77. https://doi.org/10.1016/j.ensm.2018.11.027.

[36] T. Takahashi, K. Kuwabara, & M. Shibata, “Solid-state ionics - conductivities of Na-ion conductors based on NASICON,” Solid State Ionics, vol. 1, no. 3, pp. 163–175, Aug. 1980, https://doi.org/10.1016/0167-2738(80)90001-6.

[37] A. Mauger, C. Julien, A. Paolella, M. Armand, K. Zaghib, Building Better Batteries in the Solid State: A Rev., Materials. 12 (2019) 3892. doi.org/10.3390/ma12233892.

[38] P. Jiang, G. Du, Y. Shi, F. She, P. Guo, G. Qian, X. Lu, F. Xie, X. Lu, Ultrafast sintering of $Na_3Zr_2Si_2PO_{12}$ solid electrolyte for long lifespan solid-state Na-ion batteries, Chemical Engineering Journal. 451 (2023) 138771– 138771. https://doi.org/10.1016/j.cej.2022.138771.

[39] J.F. Peters, A. Peña Cruz, M. Weil, Exploring the Economic Potential of Sodium-Ion Batteries, Batteries. 5 (2019) 10. https://doi.org/10.3390/batteries5010010.

[40] A. Rudola, A.J.R. Rennie, R. Heap, S.S. Meysami, A. Lowbridge, F. Mazzali, R. Sayers, C.J. Wright, J. Barker, Commercialization of high energy density sodium-ion batteries: Faradion’s journey and outlook, Journal of Materials Chemistry A. (2021). https://doi.org/10.1039/D1TA00376C.

[41] A.M. Bates, Y. Preger, L. Torres-Castro, K.L. Harrison, S.J. Harris, J. Hewson, Are solid-state batteries safer than lithium-ion batteries, Joule. 6 (2022) 742–755. https://doi.org/10.1016/j.joule.2022.02.007.

[42] B. Xu, J. Lee, D. Kwon, L. Kong, M. Pecht, Mitigation strategies for Li-ion battery thermal runaway: A review, Renewable and Sustainable Energy Reviews. 150 (2021) 111437. https://doi.org/10.1016/j.rser.2021.111437.

[43] Y. Chen, Y. Kang, Y. Zhao, L. Wang, J. Liu, Y. Li, Z. Liang, X. He, X. Li, N. Tavajohi, B. Li, a review of lithium-ion battery safety concerns: The issues, strategies, and testing standards, Journal of Energy Chemistry. 59 (2021) 83–99. https://doi.org/10.1016/j.jechem.2020.10.017.

[44] D. Ouyang, M. Chen, Q. Huang, J. Weng, Z. Wang, J. Wang, A Review on the Thermal Hazards of the Lithium-ion Battery and the Corresponding Countermeasures, Applied Sciences. 9 (2019) 2483. https://doi.org/10.3390/app9122483.

[45] D.H.S. Tan, A. Banerjee, Z. Chen, Y.S. Meng, From nanoscale interface characterisation to sustainable energy storage using all-solid-state batteries, Nature Nanotechnology. 15 (2020) 170–180. https://doi.org/10.1038/s41565-020-0657-x.

[46] Y. Tian, G. Zeng, A. Rutt, T. Shi, H. Kim, J. Wang, J. Koettgen, Y. Sun, B. Ouyang, T. Chen, Z. Lun, Z. Rong, K. Persson, G. Ceder, Promises and Challenges of Next-Generation "Beyond Li-ion" Batteries for Electric Vehicles and Grid Decarbonization, Chemical Reviews. 121 (2020) 1623–1669. https://doi.org/10.1021/acs.chemrev.0c00767.

[47] M. Semadeni, Energy storage as an essential part of sustainable energy systems, RePEc: Research Papers in Economics. 24 (2003). https://doi.org/10.3929/ethz-a-004532521.

[48] S.Y. Hong, Y. Kim, Y. Park, A. Choi, N.-S. Choi, K.T. Lee, Charge carriers in rechargeable batteries: Na-ions vs Li-ions, Energy & Environmental Science. 6 (2013) 2067. https://doi.org/10.1039/c3ee40811f.

[49] Y. Yu, H. Xu, Z. Wang, G. Shao, Transport of Sodium Ions in Solids: Progress in First-Principle Theoretical Formulation of Potential Solid Sodium-Ion Electrolytes, Batteries & Supercaps. 4 (2021) 1096–1107. doi.org/10.1002/batt.202000320.

[50] F. Wu, K. Zhang, Y. Liu, H. Gao, Y. Bai, X. Wang, C. Wu, Polymer electrolytes and interfaces toward solid-state batteries: Recent advances and prospects, Energy Storage Materials. 33 (2020) 26–54. doi.org/10.1016/j.ensm.2020.08.002.

[51] W. Zhang, C. Zhao, X. Wu, Research Progresses on Interfaces in Solid-State Sodium Batteries: A Topic Review, Advanced Materials Interfaces. 7 (2020).

https://doi.org/10.1002/admi.202001444.

[52] Y. Huang, B. Shao, F. Han, Interfacial challenges in all-solid-state lithium batteries, Current Opinion in Electrochemistry. 33 (2022) 100933. doi.org/10.1016/j.coelec.2021.100933.

[53] S. Gandi, V.S. Chidambara Swamy Vaddadi, S.S. Sripada Panda, N.K. Goona, S.R. Parne, M. Lakavat, A. Bhaumik, Recent progress in the development of glass and glass-ceramic cathode/solid electrolyte materials for next-generation high capacity all-solid-state sodium-ion batteries: A review, Journal of Power Sources. 521 (2022) 230930. https://doi.org/10.1016/j.jpowsour.2021.230930.

[54] C. Zhou, S. Bag, Venkataraman Thangadurai, Engineering Materials for Progressive All-Solid-State Na Batteries, ACS Energy Letters. 3 (2018) 2181–2198. https://doi.org/10.1021/acsenergylett.8b00948.

[55] J.A.S. Oh, L. He, B. Chua, K. Zeng, L. Lu, Inorganic sodium solid-state electrolyte and interface with sodium metal for room-temperature metal solid-state batteries, Energy Storage Materials. 34 (2021) 28–44. doi.org/10.1016/j.ensm.2020.08.037.

[56] E. Matios, H. Wang, W. Li, Interface Engineering on Solid-State Ceramic Electrolyte by Graphene-like Coating for Electrochemically Stable Sodium Metal Batteries, ECS Meeting Abstracts. MA2019-01 (2019) 152–152. https://doi.org/10.1149/ma2019-01/2/152.

[57] Y. Lu, L. Li, Q. Zhang, Z. Niu, J. Chen, Electrolyte and Interface Engineering for Solid-State Sodium Batteries, Joule. 2 (2018) 1747–1770. https://doi.org/10.1016/j.joule.2018.07.028.

[58] M.V. Reddy, C.M. Julien, A. Mauger, K. Zaghib, Sulfide and Oxide Inorganic Solid Electrolytes for All-Solid-State Li Batteries: A Review, Nanomaterials. 10 (2020) 1606. https://doi.org/10.3390/nano10081606.

[59] S. Teng, J. Tan, A. Tiwari, Recent developments in garnet-based solid-state electrolytes for thin film batteries, Current Opinion in Solid State and Materials Science. 18 (2014) 29–38. https://doi.org/10.1016/j.cossms.2013.10.002.

[60] J.B. Bates, J. Wang, N.J. Dudney, Solid electrolytes-the beta aluminas, Physics Today. 35 (1982) 46–53. https://doi.org/10.1063/1.2915170.

[61] Y. Wang, Y. Wu, Z. Wang, L. Chen, H. Li, F. Wu, Doping strategy and mechanism for oxide and sulfide solid electrolytes with high ionic conductivity, Journal of Materials Chemistry A. 10 (2022) 4517–4532. doi.org/10.1039/D1TA10966A.

[62] Y. Chen, K. Wen, T. Chen, X.-J. Zhang, M. Armand, S. Chen, Recent progress in all-solid-state lithium batteries: The emerging strategies for advanced electrolytes and their interfaces, 31 (2020) 401–433. doi.org/10.1016/j.ensm.2020.05.019.

[63] H.-L. Yang, B.-W. Zhang, K. Konstantinov, Y.-X. Wang, H.-K. Liu, S.-X. Dou, Progress and Challenges for All-Solid-State Sodium Batteries, Advanced Energy and Sustainability Research. 2 (2021) 2000057. doi.org/10.1002/aesr.202000057.

[64] S. Jian, Y. Cao, W. Feng, G. Yin, Y. Zhao, Y. Lai, T. Zhang, X. Li, H. Wu, H. Bi, Y. Dong, Recent progress in solid polymer electrolytes with various dimensional fillers: a review, Materials Today Sustainability. 20 (2022) 100224–100224. https://doi.org/10.1016/j.mtsust.2022.100224.

[65] M. Avdeev, Crystal Chemistry of NASICONs: Ideal Framework, Distortion, and Connection to Properties, Chemistry of Materials. 33 (2021) 7620–7632. https://doi.org/10.1021/acs.chemmater.1c02695.

[66] Z. Grady, A. Ndayishimiye, and C. Randall, "A dramatic reduction in the sintering temperature of the refractory Na β′′-Al_2O_3 solid electrolyte via cold sintering Journal of Materials Chemistry A, volume 9, number. 38, pp. 22002–22014, Oct. 2021, https://doi.org/10.1039/D1TA05933E.

[67] J. Guo, R. Floyd, S. Lowum, J.-P. Maria, T. Herisson de Beauvoir, J.-H. Seo, C.A. Randall, Cold Sintering: Progress, Challenges, and Future Opportunities, Annual Review of Materials Research. 49 (2019) 275–295. https://doi.org/10.1146/annurev-matsci-070218-010041.

[68] J.-P. Maria, X. Kang, R.D. Floyd, E.C. Dickey, H. Guo, J. Guo, A. Baker, S. Funihashi, C.A. Randall, Cold sintering: Current status and prospects, Journal of Materials Research. 32 (2017) 3205–3218. https://doi.org/10.1557/jmr.2017.262.

[69] S. Grasso, M. Biesuz, L. Zoli, G. Taveri, A.I. Duff, D. Ke, A. Jiang, M.J. Reece, A review of cold sintering processes, Advances in Applied Ceramics. 119 (2020) 115–143. https://doi.org/10.1080/17436753.2019.1706825.

Chapter 2

2.0 Literature Review

2.1 Battery Science and Technology

The technology behind batteries is constantly improving to increase their energy density [1-3], cycle life [4], and reduce cost [4, 5]. A battery is an energy storage system consisting of one or more electrochemical devices that convert stored chemical energy into electrical energy [6]. Energy generation in a battery is through a redox reaction, and electrons flow to and from the electrodes via an externally connected circuit to provide an electric current [7]. To balance the electron flow in a battery, ions flow through the electrolytic solution in contact with the electrodes. There are two main types of batteries: primary batteries and rechargeable batteries.

2.2 Primary batteries

A primary battery consists of electrochemical cells whose redox cannot be reversed. They are non-rechargeable once the stored energy is depleted. They possess high energy density and low self-discharge and are relatively cheap and readily available. However, they have a low C-rate (the speed at which a battery is fully charged or discharged) and constitute a massive waste problem due to the difficulties of recycling [3, 14]. They are used in many compact electronics, such as toys, remote controls, animal trackers and radios [15]. Examples of these batteries include galvanic cells [8], zinc-air [9], zinc-carbon [10], zinc-chloride [11], and alkaline and silver oxide-based devices [12-13].

2.2.1 Galvanic cell

The first energy generation cell (primary cell), known as the Galvanic cell, was invented by Luigi Galvani in 1780. One of the most notable examples of a Galvanic cell is the Daniel cell, which consists of a Zn rod (oxidation, anode) inserted in a concentrated zinc sulphate ($ZnSO_4$) solution with a Cu rod (reduction, cathode) immersed in a copper sulphate ($CuSO_4$) solution. Oxidation and reduction occur at the electrodes within an acid/salt medium to produce electrical energy. Electrons flow from the Zn to the Cu electrode through the external circuit to create power [16]. At the same time, ions move through the salt bridge, as illustrated in Figure 2.1. Other examples of Galvanic cells include Leclanchè cells, dry cells, and Volta cells [16-17]. The reactions occurring at the electrodes are shown in equations 1-3.

At the anode, an oxidation half-cell reaction occurs:

$$Zn \rightarrow Zn^{2+} + 2e^{-} \qquad (1)$$

Whereas at the cathode, the reduction half-cell reaction:

$$Cu^{2+} + 2e^{-} \rightarrow Cu \qquad (2)$$

With the overall response of the system:

$$Zn + CuSO_{4\,(aq)} \rightarrow ZnSO_{4\,(aq)} + Cu \qquad (3)$$

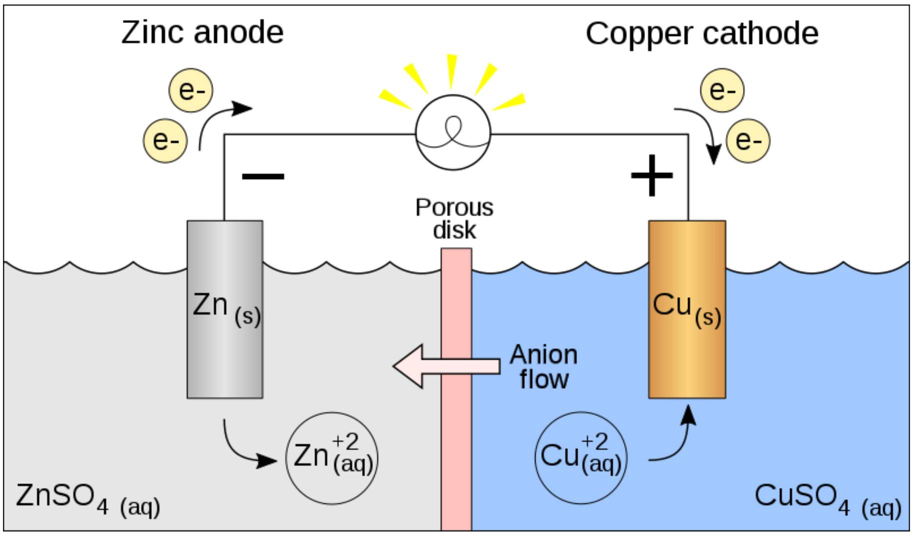

Figure 2.1. Schematic of a zinc-copper Galvanic cell [18].

2.3 Rechargeable batteries

Rechargeable batteries comprise electrochemical cells whose redox can be reversed. They are more cost-efficient over the long term, compatible with all climates, have reliable starting power and are attractive among energy storage technologies [19]. They are used for stable energy over sustainable periods and are ideal for mobile applications [20]. Figure 2.2 shows the energy densities of different rechargeable batteries. Examples of rechargeable batteries include Pb-acid [21], Ni-Cd [22], Ni-Metal Hydride [23], and Li-ion and Na-ion batteries [24-25].

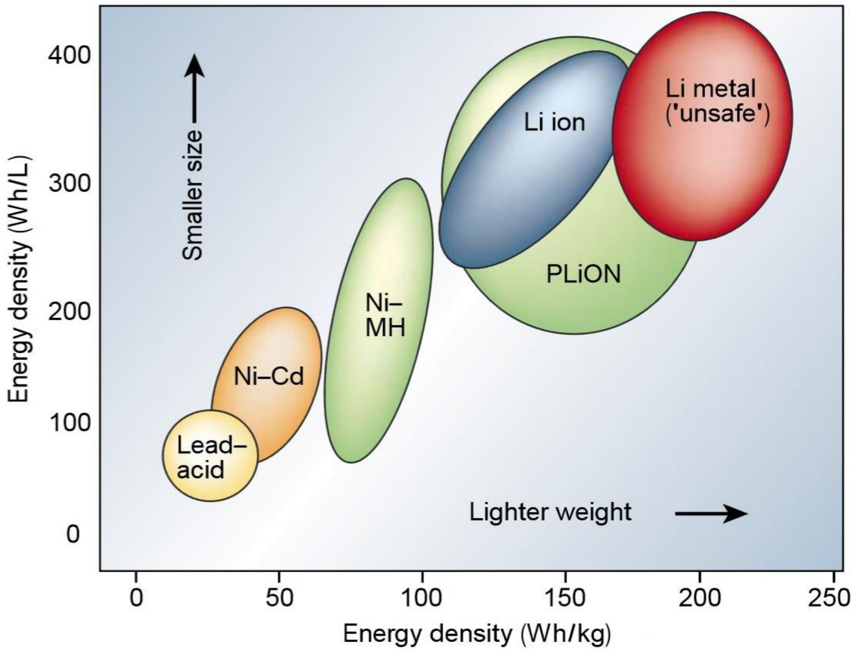

Figure 2.2 Energy densities of different rechargeable batteries [79].

2.3.1 Pb-acid batteries

The lead-acid battery industry is one of the largest and oldest rechargeable energy storage industries in the world. Gaston Plantè, a French physicist, invented the Pb-acid battery in 1859, making it the first and oldest form of its kind [26]. Pb-acid batteries are typically used in non-portable, heavy-duty applications such as power generation and distribution, energy storage, power backups, and the automotive industry. These batteries are appealing due to their low cost, large power-to-weight ratio, and ability to supply high currents when necessary [27]. However, they have a low energy-to-volume ratio and energy-to-weight ratio. The Pb-acid battery consists of a lead-oxide (PbO) anode, lead (Pb) cathode, and concentrated sulphuric acid solution (H_2SO_4) as the electrolyte. Pb is a hazardous material, and the acidic sulphuric acidic electrolytes pose environmental concerns for future applications. Figure 2.3 illustrates the schematic of the charging and discharging process of the Pb-acid battery. These batteries come in various configurations, such as sealed cells with a capacity of 12000Ah, primarily used for starting and ignition in vehicles and are the least expensive option for any energy storage applications, providing excellent performance. Lead-acid batteries have an electrical efficiency between 75-80% and are suitable for energy storage and electric vehicles [28-32]. The reactions occurring at the electrodes are shown in the equations 4-7.

During the discharge, the reactions are:

Negative:

$Pb_{(s)} + HSO_4^-{}_{(aq)} + H_2O_{(l)} \rightarrow PbSO_{4(s)} + H_3O^+{}_{(aq)} + 2e^-$ (oxidation) (4)

Positive

$PbO_2 + HSO_4^-{}_{(aq)} + 3H_3O^+{}_{(aq)} + 2e^- \rightarrow PbSO_{4(s)} + 5H_2O_{(l)}$ (reduction) (5)

Whereas during the charging, the reactions are:

Negative:

$PbSO_{4(s)} + H_3O^+{}_{(aq)} + 2e^- \rightarrow Pb_{(s)} + HSO_4^-{}_{(aq)} + H_2O_{(l)}$ (reduction) (6)

Positive:

$PbSO_{4(s)} + 5H_2O_{(l)} \rightarrow PbO_{2(s)} + HSO_4^-{}_{(aq)} + 3H_3O^+{}_{(aq)} + 2e^-$ (oxidation) (7)

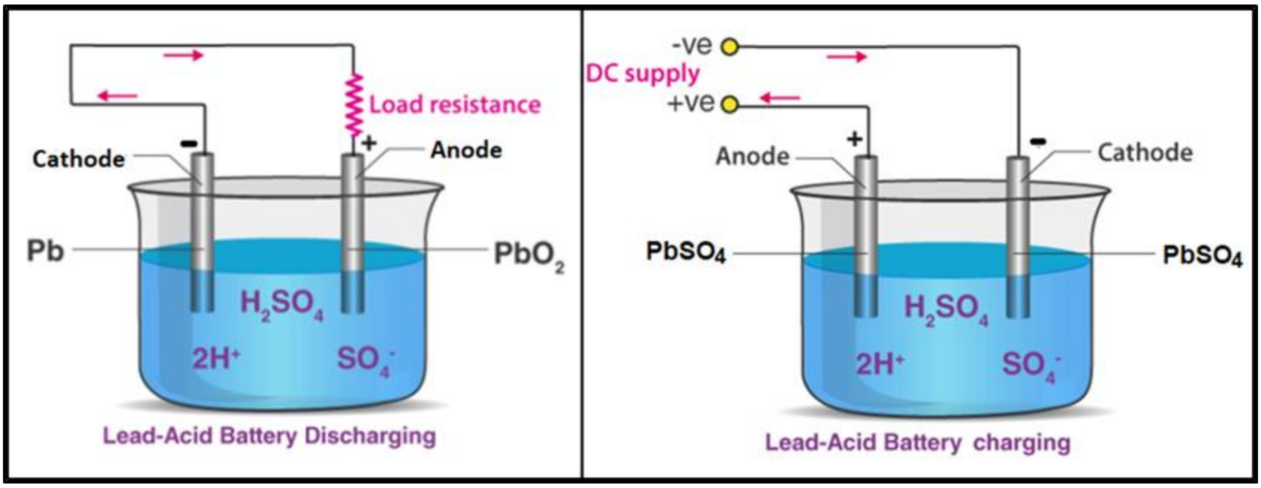

Figure 2.3. Schematic of a Pb-acid battery with the discharging and charging process [32].

2.3.2 Li-ion batteries

LIBs are employed in many applications due to their high coulombic efficiency, low self-discharge, fast charging, and low maintenance [32-35, 79]. Currently, LIBs contribute over 65% of global sales [36]. Li-ion batteries (LIBs) have superior energy and power densities [24, 33]. In all LIBs, lithium-ions travel from the negative electrode to the positive electrode via the electrolyte during discharging, and the lithium electron travels to the negative electrode when charging via the external circuit. The demand for portable electronic devices has increased in price compared to other types of batteries. LIBs have high energy density [35], minimal memory effect, and low self-discharge [37]. These batteries use an intercalated Li compound as electrode material [38]. Typically, LIBs in mobile devices are based on the cathode $LiCoO_2$, which offers high energy density and low safety risks, Figure 2.4 [39-41]. Properties of LIBs include good cycle durability (400:1200 cycles), high nominal cell voltage (NMC 3.6/3.85V), reasonable charge-discharge rate (80:90%), high specific power (250:340 W/kg) and high energy density (250: 693 Wh/L) [42-44]. There are various LIBs; the most popular ones are Lithium nickel cobalt aluminium (NCA) [45], Lithium Nickel Manganese Cobalt (NMC) [46], Lithium Manganese spinel (LMO) [47], Lithium titanate (LTO) [48] and Lithium Iron Phosphate (LFP) [49]. The atomic number of Li is 3, with two electrons in the nucleus and one in the valence shell; Li can readily participate in a redox reaction due to its electronic configuration ($1s^22s^1$). The valence electron ($2s^1$) is easily removed, leaving behind two inner electrons and creating a Li^+-ion. The reactions occurring at the electrodes are shown in the equations 8-10.

At the cathode, the reaction is typically:

$$CoO_2 + Li^+ + e^- \rightarrow LiCoO_2 \tag{8}$$

And at the anode (graphite):

$$LiC_6 \rightarrow C_6 + Li^+ + e^- \tag{9}$$

With an overall reaction:

$$LiC_6 + CoO_2 \rightarrow C_6 + LiCoO_2 \tag{10}$$

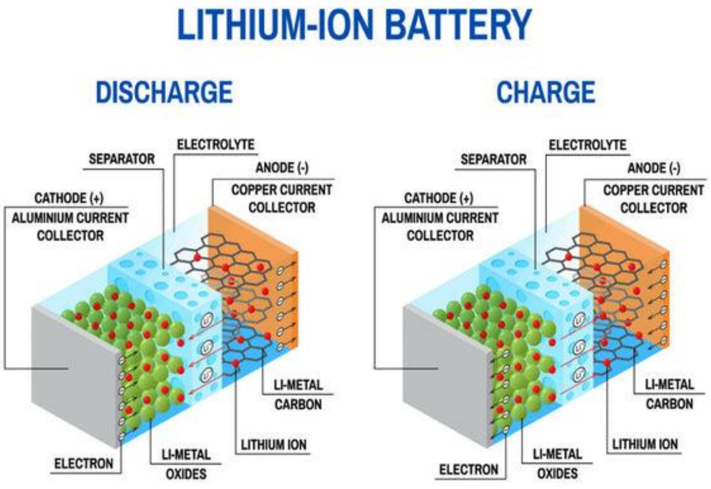

Figure 2.4. Schematic of a Li-ion battery [50].

2.3.2.1 Challenges with Li-ion batteries

Li-ion batteries have gained popularity in various applications due to their numerous benefits, including high energy density, long cycle life, and low self-discharge rate. However, these batteries have some challenges that need to be addressed. Safety remains a significant concern, as Li-ion batteries can cause fires or explosions if overheated, resulting in a short circuit, overcharging, or physically destroying the battery [51]. In addition, LIBs have a limited lifespan despite a long cycle life, and their performance gradually declines over time, leading to a reduction in capacity and increased internal resistance [52]. Finally, recycling is a significant environmental challenge in battery technology [53-56].

2.3.3 Na-ion batteries

Na-ion batteries (NIBs) are considered viable alternatives to LIBs due to their similarity in working patterns and the abundance of sodium precursors [57]. NIBs are attractive due to the low toxicity, cost, and abundance of Na compounds, Figure 2.5. NIBs are an attractive option for replacing Li-ion technology in the long run [58-59]. However, the volumetric and gravimetric energy density of NIBs is lower than that of LIB due to the large ionic radius of Na [60-61]. Despite these limitations, researchers have increased focus on NIBs due to their similarity in chemistry with LIBs and the abundance of Na-ion precursors [62-63].

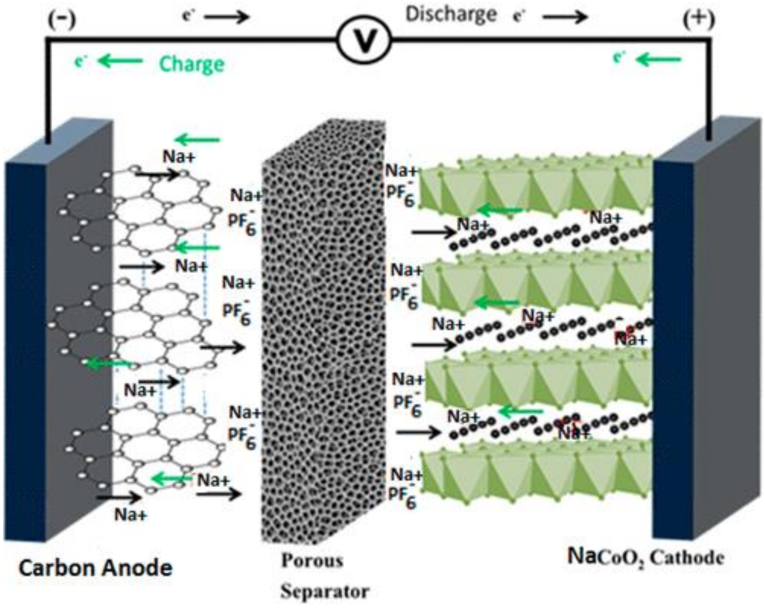

Figure 2.5. Schematic of a Na-ion battery [64].

2.4 Solid-state batteries

Solid-state batteries (SSBs) use solid electrolytes and electrodes instead of a liquid or gel electrolyte, providing numerous benefits over traditional LIBs and NIBs. These benefits include higher energy density, improved safety, and longer cycle life [65-66]. The solid electrolyte in SSBs is typically made from different materials, such as metal oxides and sulfides. SSBs function similarly to traditional LIBs and NIBs, with ions hopping through the solid electrolyte during charging and discharging. A solid electrolyte can also use high-capacity anode materials, such as lithium/sodium metal, which are typically unsafe for liquid electrolyte batteries due to dendrite formation [67]. The development of SSBs comes with some challenges, including synthesising and processing the solid electrolyte to ensure high ionic conductivity, mechanical stability, and electrode compatibility [68]. In addition, the interface between the solid electrolyte and electrodes must be optimised to improve the battery performance and stability, as shown in Figure 2.6. Despite these challenges, SSBs are promising for handheld electronics, electric vehicles, and grid energy storage. Currently, research is focused on optimising solid electrolyte materials, the electrolyte-electrode interface, and improving the performance and durability of SSBs [69-71].

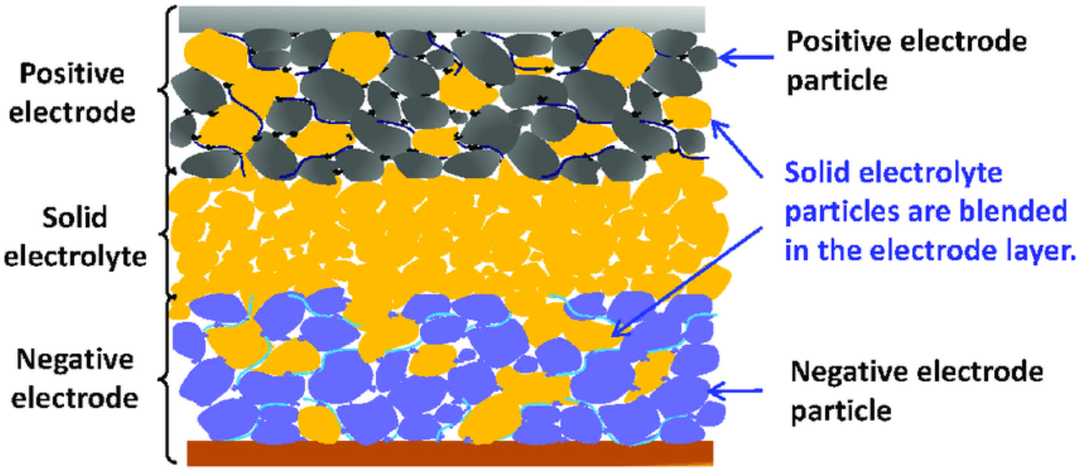

Figure 2.6. Schematic of a solid-state battery [71].

2.4.1 Na-ion SSBs

Sodium-ion solid-state batteries (SSSBs) are a new type of battery that uses solid electrodes and electrolytes, Figure 2.7. With advancements in solid electrolytes, electrode materials, interface engineering, and manufacturing techniques, SSSBs garner significant attention as a viable alternative to Li-ion batteries. Exploiting the abundance of Na-ion precursors, cost benefits and technological advancements, SSSBs are safer and more efficient [72-73]. One major improvement area has been using solid electrolytes (sulfides, oxides, and polymer-based materials). The solid electrolyte in SSSBs is typically a ceramic (e.g. $Na_3Zr_2Si_2PO_{12}$) or glass material that allows for the conduction of Na^+-ions. The electrodes in SSSBs are also solid, usually made of Na metal, $NaTi_2PO_{12}$, and $Na_3V_2PO_{12}$ (anode) or Na-ion intercalation materials such as $NaCoO_2$, $NaFePO_4$, or $NaMnO_4$ (cathode) [74]. Furthermore, advancement has been made in improving ion transportation within the structure and enhanced interfacial engineering between the solid electrolyte and electrodes [75]. The conduction mechanism in SSSBs is similar to that in conventional Na-ion batteries [76-78]. Despite the advantages of SSSBs, there are several challenges to overcome in their development. The synthesis and preparation of the solid electrolyte is a significant challenge, as it must possess high ionic conductivity, be mechanically stable, and be chemically compatible with the electrodes. The interface between the electrolyte and the electrodes also affects the performance and stability of the battery [77-78].

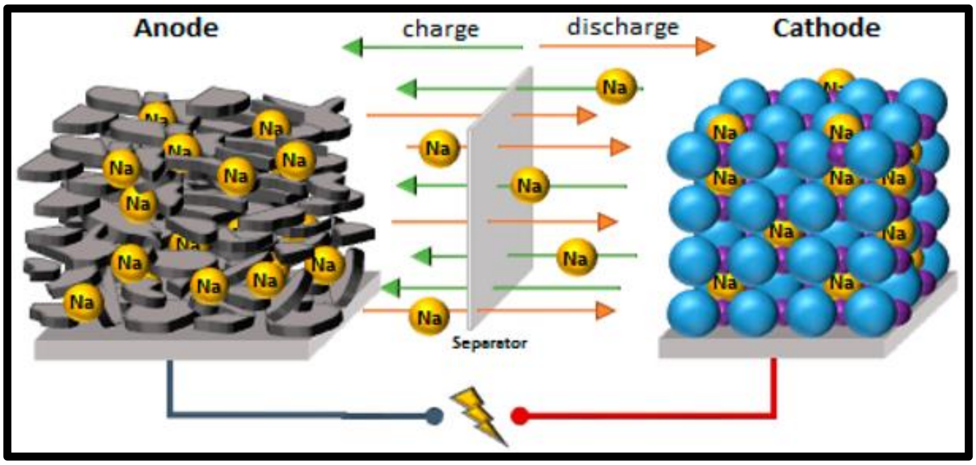

Figure 2.7. Schematic of a Na-ion solid-state battery [76].

2.5 Chemistry and crystal chemistry of Na-ion conductors

The ideal crystal structure for ionic conduction needs an open, flexible framework that enables charged species to move without impacting the lattice [80, 88]. Typically, ionic conductors have a high degree of disorder, such as an amorphous, glassy structure or a crystal structure with a high degree of structural complexity with open sites for ions to move through [81-83]. Small ions with a high charge density, such as Li^+ (Figure 2.8), can move more easily through the lattice than larger ions with a lower charge density, such as Na, K and Ca [84]. This is because small ions can fit easily into the open sites in the crystal lattice and are more strongly attracted to the surrounding anions [85]. Examples of Na-ion compounds used commercially or studied for SSSBs include $NaCoO_2$ (cathode), $Na_3Zr_2Si_2PO_{12}$ (a solid electrolyte) and $Na_3Ti_2P_3O_{12}$ (anode). In a Na-ion solid compound, Na-ions move through open sites in the crystal lattice, allowing them to insert and extract. The rate of ion movement depends on the ion size, lattice connectivity, defects, and imperfections in the crystal structure [84]. In Na-ion anodes, the conduction mechanism involves Na-ion intercalation into the lattice during battery charging. The intercalation is facilitated by the open sites in the crystal structure, allowing the Na^+ to insert between the lattice layers [86].

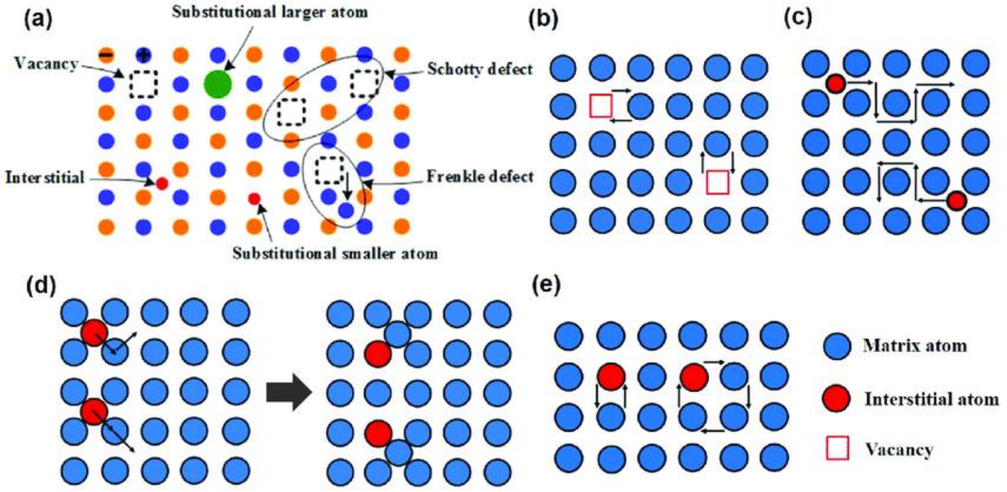

Figure 2.8. Schematics of ionic conduction showing the vacancy, interstitial sites, Schottky effect, substitutional smaller atom and Frenkle defect mechanisms [87].

2.6 Methods of preparing Na-ion compounds

The preparation of Na-ion compounds involves a series of intricate processes to achieve the desired properties for ionic compounds. Na-ion conductors are compounds that can transport ions within their solid lattice [88]. These materials are of great interest in various fields due to their improved performance, safety, and durability. Preparing these compounds involves selecting suitable precursors based on the target ions and desired properties. Methods for preparing inorganic solid ion compounds include solid-state reaction [89], hydrothermal synthesis [90], co-precipitation [91], and sol-gel method [92]. These techniques allow for control over the composition, crystal structure, and morphology of the resulting material, ultimately influencing the properties of the ionic compounds. Irrespective of the type of solid ionic compounds (e.g. Na-ion or Li-ion) being prepared, it is crucial to carefully control factors such as mechanical stability, thermal stability, and electrochemical stability during the preparation process.

2.7 Solid-state reaction

The solid-state reaction method is a widely used technique for preparing various ceramic materials. Different solid compounds with varying compositions and properties have been synthesised using this method, making it a valuable technique in solid-state ionic and ceramics [88-89]. The process involves the reaction of two or more solid reactants with the help of an organic solvent (e.g. ethanol) and milling media (zirconia media) to trigger a chemical reaction. The controlled reaction between the reactants/precursors forms the desired solid compounds.

The steps involved in the solid-state reaction method include:

i. Selection of reactants: The first step is selecting appropriate reactants with the desired ionic components. These reactants should be compatible and reactive with each other.
ii. Grinding or milling: The solid reactants are thoroughly mixed by grinding or milling in an organic solvent. This ensures a homogenous mixture and promotes the interaction between the ionic components.
iii. Heat treatment: The mixed reactants are then subjected to a heat treatment, usually called the calcination stage. This is carried out in a furnace at a specific temperature and time. The temperature and duration of heat treatment depend on the specific reactants and the desired final product.
iv. Reaction and formation of the solid ionic conductor: This stage is crucial in forming ceramic compounds. It involves a heat treatment process that causes the intermediates to undergo a chemical reaction, creating a new solid phase.

2.8 Sintering

Sintering technology has existed since the Paleolithic period, and humans have used it to produce ceramic and various materials [93]. Sintering involves heating materials (usually in powder or granular form) below their melting point to form a solid mass without complete fusion. The process improves material properties such as strength, density, and porosity. Sintering of ionic conductors involves heating powder materials to a high temperature, allowing them to densify and form a solid mass, Figure 2.9. There are various sintering processes, which include conventional, cold-sintering, spark plasma and many more.

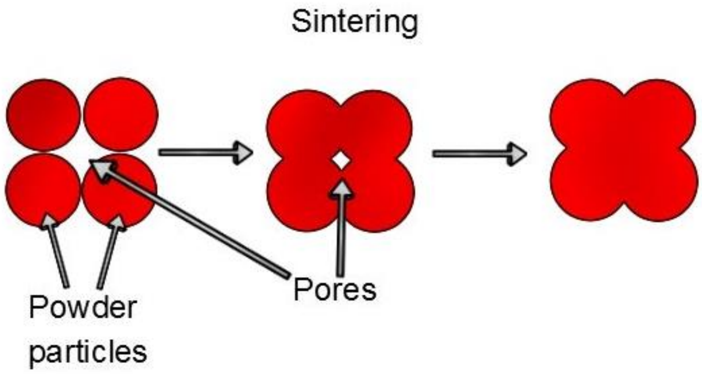

Figure 2.9. Sintering of ceramic [94].

2.8.1 Conventional sintering

Conventional sintering has been the primary route for densifying ceramic materials and ionic conductors [95-95]. During conventional sintering, powdered compounds are heated to a temperature below their melting point, causing them to undergo plastic deformation and necking, leading to the consolidation of particles into a solid mass, as shown in Figure 2.10. The overall sintering process involves several stages, including heating to an intermediate temperature to remove volatile impurities whilst the material has open porosity, a densification temperature to promote particle diffusion and consolidation, and a cooling stage to reduce thermal stresses and prevent cracking [96]. Conventional sintering can consolidate various materials, including ceramics, metals, and composites, by creating materials with excellent properties, such as increased strength and toughness [97-98].

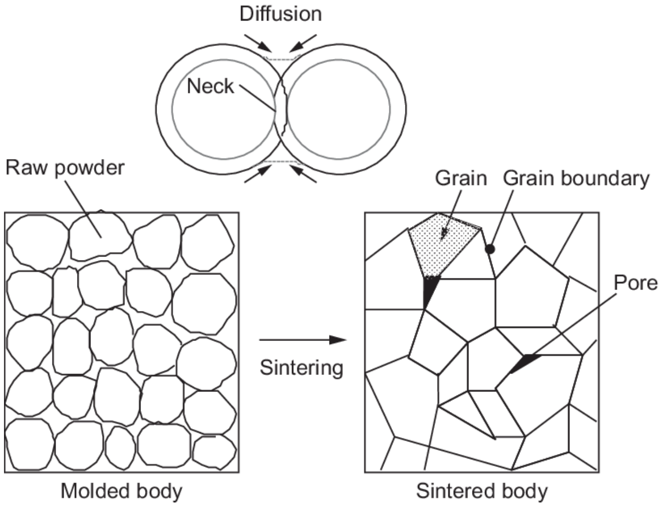

Figure 2.10. Conventional sintering process of ceramic [101].

2.8.1.1 Challenges of the conventional sintering process

The traditional process of sintering has several advantages over other types of sintering. However, it has challenges to overcome.

i. High energy consumption: Conventional sintering processes typically require high temperatures and long dwell times, resulting in high energy consumption and increased production costs [99-101].
ii. Inhomogeneous particle distribution and grain growth: Conventional sintering can lead to uneven distribution of particles and excessive grain growth within the ceramic, causing variations in mechanical properties and structural integrity [99].
iii. Porosity and densification: Achieving a high density and low porosity in the final sintered ceramic can be challenging. Uneven shrinkage during sintering can result in the formation of open pores and reduced density [100].

2.8.2 Cold Sintering Process and the Mechanism

The cold sintering process (CSP) is a novel technique for fabricating ceramic materials at low temperatures. Cold sintering allows the densification of ceramics at significantly low temperatures, typically below 300 °C. The process involves applying pressure to compact ceramic powder in the presence of a transient solvent and heat [102-105]. The solvent acts as a catalyst to promote particle rearrangement, and the heat promotes densification. CSP involve several stages, which include material dissolution, particle rearrangement, hydrothermal crystal growth or glass/intermediate phase formation, and grain growth or recrystallization of glass. The thermodynamics and kinetic processes of the stages involved in the CSP are explained in Figure. 2.11(a) and introducing a liquid phase into the particle-particle contacts allows for particle rearrangement. Moisturising the particle ensembles with an appropriate amount of aqueous solution (H_2O or volatile solvents) lubricates the particle surface and allows the liquid phase to dissolve the sharp edges of the particles partially. This creates more interstitial space for the particles to slide, thus facilitating the particle rearrangement [102]. Applying pressure aids in redistributing the liquid phase and filling the particles' interstitials, resulting in the initial particle compaction. Heating the material eliminates the porosity and promotes the growth of crystalline structures. Aqueous solutions play a crucial role in CSP by creating the right conditions for precipitation and recrystallization through hydrothermal reactions. The Gibbs free energy change for crystallisation from an aqueous solution to a solid material is much lower in CSP than in conventional sintering, Figure 2.11(b). Aqueous solutions ensure low-temperature transport for sintering, minimising the need for Gibbs-free energy alteration [106-109].

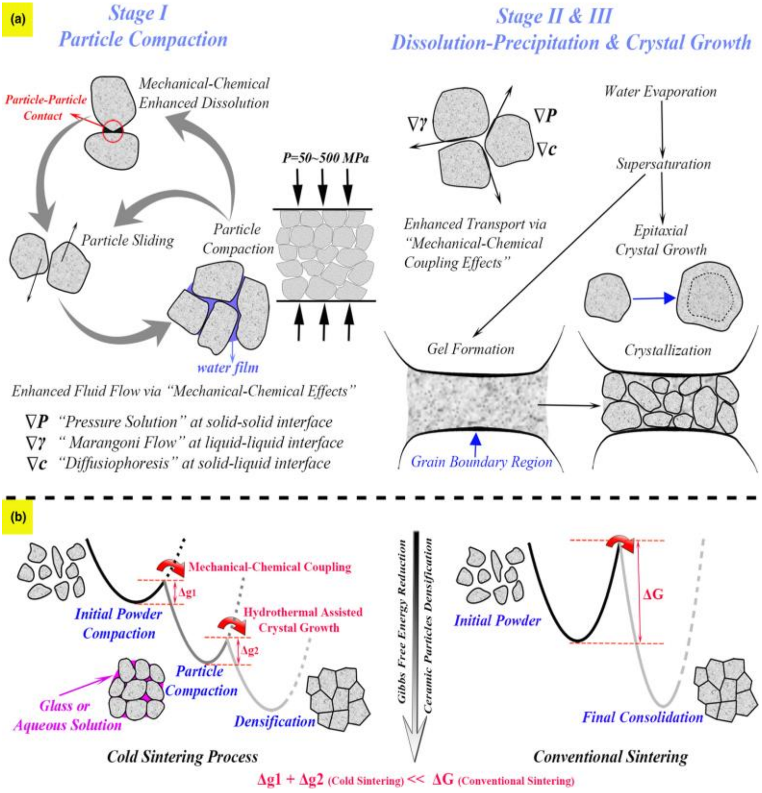

Figure 2.11. Schematic of the cold sintering process (a) microstructure and mechanisms of the cold sintering process, (b) Gibbs free-energy evolution of the cold sintering process compared to conventional sintering [102].

Many researchers have adopted the cold sintering method across the globe for ceramic materials densification. Kähäri and co-workers [110] were the first to introduce the cold sintering method with the technique further developed at Pennsylvania State University, USA, by Randall and associates [111-112]. The Randall group used this method to densify ferroelectric and dielectric materials, achieving dense ceramics at ≤ 200 °C. Over eighty ceramic materials have been densified using the cold sintering technique with over 85% relative density [113-114]. Reaney and co-workers at the University of Sheffield have also worked extensively on developing novel microwave (MW) materials using this new method to densify ceramic at low temperatures [115-118].

Factors affecting the crystallisation and particle densification processes, along with the basic steps and practical strategies employed for different material systems based on their dissolution nature, were discussed by Guo *et al*., [111]. The internal properties of the material (composition, crystal structure, particle size, and solubility) are the factors that determine the success of crystallisation and densification. In addition, external influences (establishing a suitable aqueous solution system and adjusting pH value and concentration) are critical for creating a favourable hydrothermal environment for chemical reactions, Figure 2.12. Post-heat treatment is sometimes necessary to fully densify the ceramic or convert intermediate compounds to the correct crystal structures.

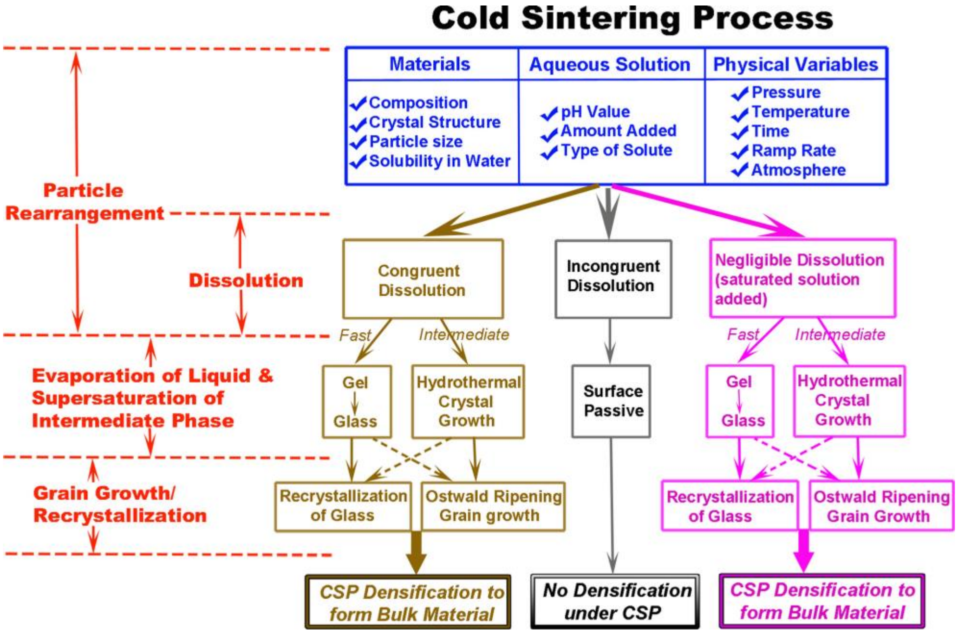

Figure 2.12. A comprehensive summary of the cold sintering process outlining the fundamental mechanisms and potential routes for diverse types of material [111].

Andrews *et al.*, [116] reviewed the cold sintering technique for various ceramic materials. The study examined the effects of cold sintering on congruent and non-congruent materials, highlighting the advantages and limitations of the technique. It was found that materials that dissolve incongruently in solvents can be challenging to cold sintered, but the study suggests a hydrothermal-assisted CSP that uses reactive intermediate phases. On the other hand, congruent materials, such as sodium molybdate, lithium molybdate, and ZnO, can be easily densified using CSP with the aid of transient solvents like H_2O or acetic acid. Furthermore, the study recommends a solution of eutectic reaction precursor for incongruent materials such as $BaTiO_3$ and $SrTiO_3$. The review provides valuable insights into optimising and applying the cold sintering technique for different ceramic materials, which can benefit future research and development. Guo *et al.*, [111] conducted a comprehensive study on the densification of various ferroelectric oxide materials (KH_2PO_4, $NaNO_2$, and $BaTiO_3$) using the CSP. The study provided insightful information on the thermodynamic properties and fundamental mechanisms of CSP. Three different ferroelectric oxide materials were successfully densified using aqueous solvents, achieving high relative densities (ρ_r) of 98% for KH_2PO_4, 85% for $NaNO_2$, and 90% for $BaTiO_3$. The study also revealed that the Gibbs free energy of CSP is significantly lower than that of the conventional sintering method, making CSP more energy efficient. Furthermore, the electrochemical properties of the ferroelectric materials densified using CSP were comparable to those achieved using the traditional sintering method. The group concluded that the CSP presents a promising, cost-effective, and energy-saving method for ceramic processing.

Boston and co-workers [114] conducted a study on the reactive intermediate phase of strontium titanate using the cold sintering process, and the results of their study were quite promising. The team was able to densify strontium titanate at a significantly lower temperature of 180 °C by reacting an aqueous solution of SrO_2 with TiO_2 to form $SrTiO_3$. Additionally, the post-annealing temperature of 950 °C was introduced to completely densify the material, resulting in a 96% dense ceramic for the $SrTiO_3$ after post-annealing. This was a significant achievement since traditional methods of densifying $SrTiO_3$ require temperatures of at least 1400 °C. The team's findings suggest that CSP could be used to densify various ceramics and other materials that require high-temperature processing.

Wang and co-worker [115] employed an innovative approach to densified multilayer ceramic capacitors (MLCC) using the CSP. $Bi_{0.95}Li_{0.05}$-$V_{0.9}Mo_{0.1}O_4$-$Na_2Mo_2O_7$ with a high permittivity value and relative density of over 95% was prepared. The microstructural properties of the MLCC were evaluated against the MLCC prepared by the conventional method. Their study found that the MLCC prototypes produced by CSP were comparable to those prepared by conventional methods. The study demonstrates the potential of CSP as a viable alternative for densifying MLCCs.

2.8.2.1 Challenges of the cold sintering process

Cold sintering has several potential advantages over conventional sintering, including reduced energy consumption, lower processing temperatures, and the ability to create materials with unique properties. It has been used in processing ceramics, metals, and composites and has potential applications in energy storage, electronics, and biomedical engineering. However, before it can become a viable industrial-scale process, various challenges must be overcome [119 -120]:

i. Scalability: The main challenge of cold sintering is scaling up the process from laboratory to industrial scale. Currently, the process is typically carried out using small lab-based samples. Concerns about its scale-up to produce large and uniform material with consistent properties are debated [108].
ii. Material compatibility: Materials compatibility with the cold sintering process is a significant challenge. While the technique has been successfully applied to a range of ceramic materials [106-109], there are limitations to the types of materials that can be densified by cold sintering, e.g. NATP and NZSP, which are difficult at this juncture.
iii. Process optimisation: The cold sintering process involves several steps that need optimisation to improve the ceramic properties. However, a comprehensive grasp of the material mechanisms and the ability to control each step in the process is required.
iv. Equipment requirements: To commercialise the technique, the process requires specialised equipment, such as high-pressure presses or special furnaces. This could require a significant initial investment in capital equipment to lessen its accessibility for smaller companies.
v. Standards and regulations: As with any new materials processing technique, there may be a need for new standards and rules to ensure the materials meet the regulated safety and quality standards.

2.9 Other low-energy ceramic sintering techniques

There are various methods for densifying ceramics. Some of the densification/sintering processes are explained below [121].

2.9.1 Flash sintering

Flash sintering is a rapid consolidation process that involves applying an electric field to a ceramic or powder, causing fast heating and sintering. This process can produce dense materials in minutes and has potential applications in energy storage and catalysis [122]. Flash sintering is based on electric field-assisted diffusion, which involves the migration of charged species through a material under the influence of an electric field. When a powder compact is subjected to an electric field, ions migrate within the material structure, leading to localised heating and sintering. The process is characterised by a rapid increase in temperature and a sharp drop in electrical resistance, indicating the onset of sintering. One of the advantages of flash sintering is the fast processing time, which can produce dense materials in a matter of seconds. This can reduce the energy required for processing and minimise the time required for manufacturing. Flash sintering can produce materials with unique properties and microstructures, including improved mechanical and electrical properties [123]. However, flash sintering also has some limitations, such as the need for high electric fields and the potential for uneven heating and cracking. Additionally, the process requires careful control of the sintering parameters, such as the voltage, the particle size, and the sintering temperature, to ensure the reproducibility of the process and the quality of the resulting materials [124].

2.9.2 Spark plasma sintering

Spark plasma sintering (SPS) is a rapid consolidation process that involves the application of a high electric field to a powder ceramic, causing fast heating and sintering [125]. The process is also known as pulsed electric current sintering, field-assisted sintering, or electric current activated/assisted sintering. SPS combines the advantages of conventional sintering and hot pressing, allowing for the consolidation of powders into dense materials with fine microstructures and improved mechanical properties [126]. During the process, a powder compact is placed between two electrodes and subjected to a high electric current (typically in the range of 10-1000 A), which generates localised heating and causes sintering to occur. One of the advantages of SPS is its ability to produce materials with fine-grained microstructures due to the rapid heating and cooling rates involved [127]. Compared to materials produced using conventional sintering methods, this can lead to improved mechanical properties, such as increased strength and toughness. SPS can consolidate various materials, including ceramics, metals, and composites, and can be carried out at relatively low temperatures and pressures. However, SPS also has some limitations, such as the high equipment cost and the need to carefully control the sintering parameters, such as the applied electric field, the temperature, and the pressure. Additionally, there may be limitations regarding the size and shape of the samples that can be processed using SPS [128].

2.10 Preparation of Na-ion compounds by solid-state reaction method.

The solid-state reaction method has been the primary route for preparing ceramics materials of cation (Li, Na, K, Ca, and Mg) compounds [129-135] with the fabrication of $Na_3Zr_2Si_2PO_{12}$, Na_xCoO_2 and $Na_{1.3}Al_{0.3}Ti_{1.7}P_3O_{12}$ reported by various researchers.

2.10.1 NASICON and NASICON-type compounds.

The development of NASICON solid electrolytes for SSSBs was pioneered by Hong and Goodenough in 1976. NASICON is an acronym for Sodium Super Ionic Conductors, an oxide-based inorganic solid electrolyte with the general formula $A_xM_2(PO_4)_3$ [129-136]. The "A-site" is usually represented by monovalent ions such as Na^+ or Li^+, the "x" represents the number of monovalent ions present in the system and the "M-site" can be occupied by trivalent (Sc^{3+}, Fe^{3+} and La^{3+}), tetravalent (Zr^{4+}, Ti^{4+} and Ge^{4+}) and or pentavalent (Ta^{5+} and V^{5+}) elements, the P-site can be co-shared by silicon and/or phosphorus. NASICON is often used in the literature to refer to $Na_3Zr_2Si_2PO_{12}$ (NZSP) more specifically [138 - 140]. However, based on the general formula of NASICON, several modifications have been made to accommodate dopants/elements, which are generally called NASICON-type compounds. Examples include $Na_{1.3}Ti_{1.7}Al_{0.3}PO_{12}$, $NaTi_2PO_{12}$, $Na_3V_2P_3O_{12}$, and $Na_3Sc_2P_3O_{12}$. NASICON and NASICON-type conductors have similar crystal chemistry and conduction mechanisms. These compounds have good conductivity (10^{-6} – 10^{-1} S/cm) at room temperature, negligible electronic conductivity ($\geq 10^{-12}$ S/cm), good thermal stability, enhanced safety, reliable device integration, high densification, and cost-effective preparation route for large-scale production [130 - 140]. These compounds consist of mobile ions arranged in a skeleton structure, allowing ions to move within the system. The conductivity of these compounds depends on the number of vacancies, mobile ions, and the activation energy for hopping. Ion movement is determined by the ions' size and charge, lattice connectivity, defects, and imperfections in the crystal structure.

2.11 $Na_3Zr_2Si_2PO_{12}$ (NZSP) and its conduction mechanism

NZSP with the formula $Na_{1+x}Zr_2Si_xP_{3-x}O_{12}$ ($0.0 \leq x \leq 3.0$) has been extensively studied as a favourable choice of solid electrolyte for SSSBs and solid ionic devices [141-148]. The ionic conductivity of NZSP depends on factors such as the Na-ion concentration, Na^+ mobility/diffusion and crystal symmetry [139]. NZSP is a remarkable solid electrolyte material with high Na-ion conductivity (10^{-4} – 10^{-3} S/cm). The Na^+ ions move through channels in the ZrO_6 octahedra and SiO_4/PO_4 tetrahedra structure. Figure 2.13 (a and b) shows the crystal symmetries of NZSP, monoclinic (*C12/c*) and rhombohedral (*R-3c*), respectively. The *C12/c* phase occurred between $1.8 \leq x \leq 2.2$, and the *R-3c* phase at $x \geq 2.2$. The mechanism that drives the conduction of Na-ion through the crystal lattice of NZSP is the movement of Na-ion from one lattice site to another via interstitial vacancies in the crystal structure. The interconnected framework of zirconium, silicon, phosphorus, and oxygen atoms forms these channels of a three-dimensional network of interstitial sites. At elevated temperatures, the Na-ion become thermally activated and can move through these interstitial vacancies, facilitated by oxygen vacancies that act as charge carriers in the conduction process. The Na-ion can hop along these channels from one lattice site to another, contributing to the solid electrolyte's overall conductivity. The high conductivity of NZSP can be attributed to its unique crystal structure and the presence of oxygen vacancies that provide accessible diffusion pathways for Na^+ [140-148].

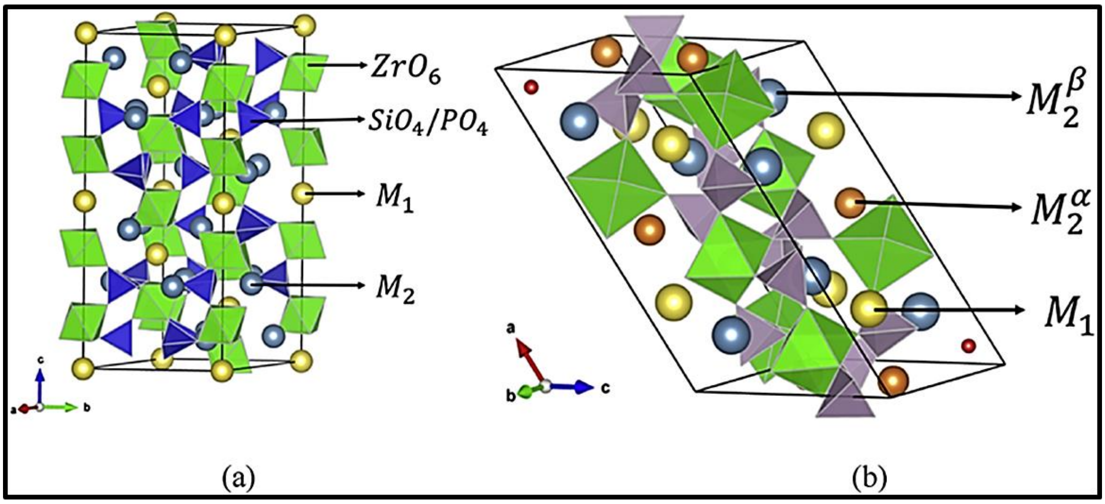

Figure 2.13. Unit cells of $Na_{1+x}Zr_2Si_xP_{3-x}O_{12}$ solid electrolyte: (a) rhombohedral structure with two Na^+ sites (M_1 and M_2), and (b) monoclinic structure with three Na^+ sites, the M_2 sites split into M_2^α and M_2^β [144].

2.11.1 Preparation of NZSP

Various methods have been employed to prepare NZSP to improve the conductivity and suppress/minimise the formation of the *m*-ZrO_2 and Na_3PO_4 impurity phases. The formation of the *m*-ZrO_2 secondary phase has been reported by all researchers involved in the preparation of NZSP. Table 2.1 summarises the different methods of preparing NZSP (solid-state, sol-gel, solution-assisted solid-state reaction, tape casting, co-precipitation, spark plasma and cold-sintering), conditions (the sintering temperature and time, crystal structure and the RT ionic conductivity) doping techniques, and reactants modification adopted to suppress and/or minimise the formation of *m*-ZrO_2 and Na_3PO_4 secondary phases and enhance the ionic conductivity. A study on the crystal symmetry of ZrO_2 revealed that *cubic* ZrO_2 promotes higher conductivity and suppresses the formation of the *m*-ZrO_2 impurity phase [140]. In the study, cubic ZrO_2 was used as one of the reactants in the preparation of NZSP, as it is known that c-ZrO_2 is more reactive than other forms of ZrO_2 (monoclinic and tetragonal). However, *c*-ZrO_2 didn't suppress the formation of the *m*-ZrO_2 impurity phase, and the conductivity of the NZSP was only 10^{-4} S/cm. Jalalian-Khakshour [141] studied the impact of nanoparticle reactants on the structural and electrical properties of $Na_3Zr_2Si_2PO_{12}$ (NZSP) using the solid-state method. The sintering temperature and time variation studied were examined on the structural and electrical properties of NZSP. The study confirmed that nanoparticle precursors sintered at 1230 °C for 40 hrs resulted in a relative density of 96.3% with monoclinic crystal symmetry of NZSP and secondary impurity phase of *m*-ZrO_2. The RT ionic conductivity of the nano-NZSP reported was 1.16 x 10^{-3} S/cm, suggesting that Nano-precursors increased the ionic conductivity by 10-fold. However, the *m*-ZrO_2 secondary phase was not suppressed. Narayanan [142] studied the effects of excess precursors (Na and P) on the morphology and electrical properties of NZSP using the solid-state method. The precursors used were silicon (IV) oxide, zirconium (IV) oxide, and trisodium tetra-phosphate with the addition of 10% sodium trioxonitrate (V) to regulate the NZSP pH. Various sintering temperatures between 1100 – 1280 °C were investigated to achieve the optimum sintering temperature for forming NZSP and suppressing the *m*-ZrO_2 impurity phase. The highest RT ionic conductivity of 1.13 mS/cm was obtained at 1230 °C for 5 hrs without suppressing the *m*-ZrO_2 impurity phase. In addition, the effect of dopants (F^-, Sc^{3+}, Mg^{2+}, Ce^{4+}, Gd^{3+} and Yb^{3+}) has been investigated on the morphology and conductivity of NZSP. However, some of the dopants improved the conductivity of NZSP by 10-fold, but none suppressed the formation of *m*-ZrO_2. The ubiquitous presence of *m*-ZrO_2 has been reported with no breakthrough on ways to suppress/minimise its formation.

Table 2.1.

Preparation methods, sintering temperature, time, crystal structure and RT conductivity of NZSP.

NASICON	Preparation methods	Sintering Temp. (°C)	Time (Hours)	Crystal structure	Ionic conductivity (S/cm)	Ref.
$Na_{3.05}Zr_2Si_{2.05}P_{0.95}O_{12}$	Sol-gel	1000	3	Rhombohedral	2.01×10^{-4}	143
$Na_{2.8}Zr_2Si_{1.8}P_{1.2}O_{12}$	Co-precipitation method	1175	5	Rhombohedral	-	144
$Na_3Zr_2Si_2PO_{12}$	Solid-state	1230	40	Monoclinic	1.16×10^{-3}	141
$Na_3Zr_2Si_2PO_{13}$	Solid-state	1250	5	Monoclinic	6.1×10^{-4}	142
$Na_3Zr_2Si_2PO_{12}$	Spark Plasma	1250	5	Monoclinic	1.8×10^{-3}	145
$Na_3Zr_2Si_2PO_{12}$	Tape casting	1100	4	Monoclinic	4.4×10^{-4}	146
$Na_3Zr_2(SiO_4)_2(PO_4)$	SA-SSR	1250	5	Monoclinic	1.03×10^{-3}	147
$Na_{3.256}Mg_{0.128}Zr_{1.872}Si_2PO_{12}$	Cold sintering (780 MPa)	140	2	Rhombohedral	5.0×10^{-4}	108
$Na_{3.256}Mg_{0.128}Zr_{1.872}Si_2PO_{12}$	Solid-state	1300	24	Monoclinic & Rhombohedral	2.7×10^{-3}	148

2.12 NASICON-type compounds

NASICON-type compounds have found widespread application in numerous fields. For example, $NaTi_2PO_{12}$ (NTP) has intriguing properties used as an ion exchange material [157], gas sensors [158], thermal barrier coatings [159], luminescence [160], nuclear waste management [161] and electrolyte material in SSSBs [149-156]. The large energy band gap and low electronic conductivity of NTP have limited its performance in energy applications [162]. Several approaches to enhance its electrochemical properties have been investigated, including particle size reduction, surface modifications, and the use of dopants (e.g. Al). $Na_{1.3}Ti_{1.7}Al_{0.3}PO_{12}$ (NATP) is a doped form of NTP with improved properties as a solid ionic conductor [158]. The Al dopant in NTP improves the properties of NATP as a solid ionic conductor. NATP, like its parent NTP, has a NASICON-type framework with MO_6 octahedra and PO_4 and TiO_4 occupying the tetrahedra site, as shown in Figure 2.14. NATP has a rhombohedral structure (*R-3c*) with Na-ions located at two sites in the *R-3c* structure, Figure 2.14a. The Na1 (Wyckoff position 18e) site is almost empty, and Na2 (Wyckoff position 6b) is fully occupied. Within the 3D structure, Na^+-ions migrate by hopping mechanism from the occupied site (Wyckoff position 6b) to the empty lattice (Wyckoff position 18e) [163]. Figure 2.14b shows the Ragone plot of the energy density of the different types of Na-ion storage applications.

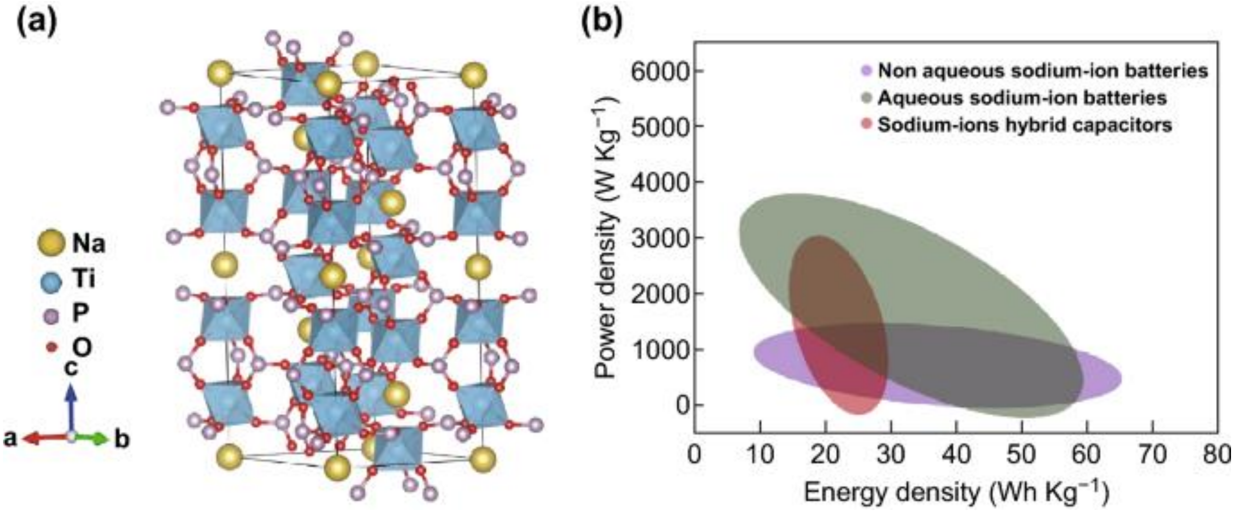

Figure 2.14. Structure of NaTi$_2$(PO$_4$)$_3$ and b) Ragone plot of NaTi$_2$(PO$_4$)$_3$-based materials for energy application [164].

2.12.1 Preparation and properties of NASICON-type compounds

In a study by Sun *et al.*, [165], sodium titanium phosphate (NTP) was prepared using an ultra-low temperature method. The study examined the ultraviolet properties of NTP, morphology, and particle size using various characterisation techniques, SEM, XRD, FT-IR, UV-Vis, TGA, and DSC. SEM image confirmed agglomeration of the grains with a size range between 50-80nm, and the crystal structure revealed a rhombohedral symmetry. The study concluded that NTP could be an excellent ultraviolet shielding material, providing a protective coating against radiation. Hung [166] used the hydrothermal method to prepare NTP nanoparticles as a potential anode material for SSSB. The crystalline structure, phase and morphologies were investigated by SEM, TGA, XRD, and TEM. The study concluded that nano-sized NTP synthesised at 250 °C for 5 hours has a rhombohedral structure with good crystallinity and high phase purity and that NTP nanoparticles could be used as an efficient anode material for energy storage in SIBs. Tolganbek *et al.,* [167] studied NASICON-structured ($Li_{1.3}Al_{0.3}Ti_{1.7}P_3O_{12}$) solid electrolytes using the solid-state and sol-gel methods. The research aimed to investigate the cause of impurities in the solid electrolyte by changing the aluminium and phosphate reactant sources. The density, morphology, and electrical properties were examined, and the results showed that both methods exhibited improved density and electrical properties with increasing sintering temperatures. The activation energy for LATP using the solid state and sol-gel method was in the 0.25 - 0.4 eV range. The ionic conductivity values of the two methods were in the range of 1.2 x 10^{-5} to 2.8 x 10^{-5} S cm^{-1}. Liu *et al.*, [168] studied the microstructure and ionic conductivity of $Li_{1.3}Al_{0.3}Ti_{1.7}P_3O_{12}$ using the cold sintering method. After post-annealing at 650 °C for 2 hours, LATP resulted in a relative density of ~ 92.0% using different transient solvents. The ionic conductivity was 8.04 x 10^{-5} S/cm. The grain boundary contribution was responsible for the increase in ionic conductivity. The group confirmed that increasing pressure increases relative density and ionic conductivity. Rohde *et al.*, [158] investigated the thermal conductivity and diffusivity of $Na_{1.3}Al_{0.3}Ti_{1.7}PO_{12}$ (NATP), which was purchased from NEI corporation. They achieved over 95 % relative density but with an $AlPO_4$ impurity phase. The conductivity of NZSP, however, was two orders of magnitude higher than that of NATP. The study also claimed that NATP has higher thermal conductivity and diffusivity than NZSP at room temperature. The impact of heat treatment on the grain size and ionic conductivity of NATP and $Na_{1.8}Al_{0.8}Ge_{1.2}(PO_4)_3$ (NAGP) was studied by Nieto-Munoz *et al.*, [169].

Solid state reaction method was used to prepare these Na-ion compounds, and the effect of single and double heat treatment on the microstructure and ionic conductivity was investigated. The results revealed that a single heat treatment with a longer crystallisation time promotes grain growth and decreases the activation energy. The ionic conductivity at 100 °C for NATP is ~ 10^{-5} S/cm, while the conductivity of NAGP is ~ 10^{-7} S/cm. The effect of Nb^{5+} dopant on NTP was investigated by Voronina [170]. Structural and electrochemical properties were investigated using ex-situ operando XRD techniques and cyclic measurements. The results confirmed that the Nb^{5+} dopant reduced the energy band gap of the Na-ion compound based on the density functional theory (DFT) calculation. $Na_{2.9}Nb_{0.05}Ti_{1.95}(PO_4)_3$ also has an improved electrical conductivity, capacity, and rate capability, making it a suitable anode material. The group concluded that 5.0% Nb dopant on NTP increases the cyclability and electrode performance, and the fabrication of a cell resulted in a capacity of over 105 $mAhg^{-1}$ after 100 cycles at 0.2 C, with a capacity retention of over 82.0 %.

2.13 Na_xCoO_2 and its crystal chemistry

The research and development of layered transition metal oxides with the general formula A_xMO_2 (M= Co, Ni, Cr, Mn, and Fe) is increasing among researchers. The A_xMO_2 has a hexagonal structure comprising MO_6 octahedrons sharing edges to form a 2D network, with the amount of alkali-ion between the MO_6 sites varying. Delmas *et al.*, [171] established the notation for the non-stoichiometric of A_xMO_2, where "A" represents the alkali metals (Li or Na) and "M" represents transition metals (Co, Ni, Mn). The layered structure of A_xMO_2 was characterised based on the number of alkali-ions present in the structure using the letters (P or O) and numbers (2 or 3). The letter (P or O) refers to the alkali-ion site as prismatic or octahedral. In contrast, the number (2 or 3) refers to the number of alkali-ion layers in the unit cell perpendicular to the layers.

Jansen and Hoppe [172] discovered the hexagonal structure of Na_xCoO_2 in 1974, Figure 2.15. The crystal structure of Na_xCoO_2 has a Na-ion layer intercalated between CoO_2 layers, in accordance with the structural descriptions of Delmas *et al.,* [171]. The CoO_2 layer has a rhombohedral distortion with CoO_6 octahedral stacked edge-sharing, and the Co-ion forms a 2D triangular lattice in its crystal structure. The electrostatic repulsion of the Na-ion movement leads to Na_xCoO_2 with distinct phases. Na_xCoO_2 exhibits five different phases according to the phase diagram by [173], depending on the Na:Co ratio and temperature: O3 ($x = 1.0$, R-3m, $a = 2.8880$ and $c = 15.6019$); O′3 ($x = 0.83$, C2/m, $a = 4.8912$, $b = 2.8681$ and $c = 5.7937$, $\beta = 111.84°$); P'3 ($x = 0.67$, C2/m, $a = 4.9126$, $b = 2.8270$ and $c = 5.7087$, $\beta = 106.06°$); P2 ($0.68 \leq x \leq 0.76$, $P6_3/mmc$, $a = 2.8320$ and $c = 10.8971$) and P3 ($x = 0.56$, R3m, $a = 2.8192$ and $c = 16.5880$). There are several potential phase transition sequences in NCO on heating depending on the Na-Co ratio [174].

$$(O3 + O'3) \xrightarrow{773\ K} O'3 \xrightarrow{808\ K} P'3 \xrightarrow{823\ K} (P'3 + P2) \xrightarrow{993\ K} P2$$

The transition temperatures are approximate and extracted from the phase diagram of Na_xCoO_2. Also, a small temperature window of ~ 10 °C in which P'3 and O'3 coexist was reported by [173]. Na_xCoO_2 has several properties, making it a promising material for energy applications. Its thermoelectric properties, cycling and reversible capacity, high metallic conductivity, magnetically ordered states and superconductivity properties make it a suitable candidate for many energy applications [175 - 186].

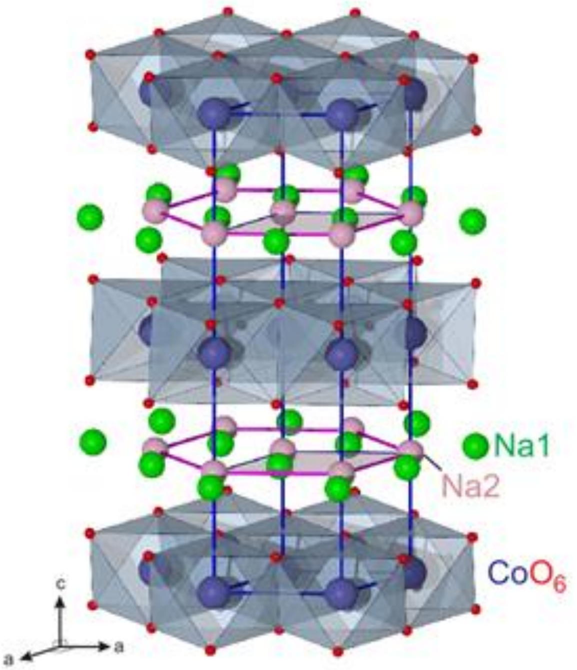

Figure 2.15. The crystal structure of $Na_{0.7}CoO_2$. The image displays the layered structure of Na and CoO_6, with the magnetic cobalt atoms arranged in a frustrated triangular setting. [175].

2.13.1 Conduction mechanism in Na_xCoO_2 (NCO)

The conduction mechanism in Na_xCoO_2 is predominantly governed by the migration of Na^+ within the crystal lattice. In $NaCoO_2$, Co^{3+} ions form an octahedral arrangement, while the Na^+ ions occupy the interlayer spaces between the octahedral layers. The octahedral cobalt sites allow redox reactions, where cobalt ions can interchange between oxidation states of Co^{3+} and Co^{4+}. When a voltage is applied across the electrodes of a sodium cobaltate-based solid-state battery, the Na^+ ions migrate within the crystal lattice [187-188]. This migration occurs due to the electrochemical potential difference created by the applied voltage. Na^+ move from the anode (a sodium-storing material) toward the cathode (typically a sodium cobaltate-based material). The migration of Na^+ ions in the sodium cobaltate follows a vacancy-mediated mechanism. The movement of Na^+ ions from one lattice site to another involves the diffusion of these vacancies, allowing the Na^+ ions to hop from one octahedral interlayer to the neighbouring interlayer sites [189-190].

2.13.2 Preparation methods and properties of Na_xCoO_2

Several studies have prepared A_xMO_2 compounds of Li and Na compounds using various methods. Lei and co-workers [173] prepared different compositions of layered Na_xCoO_2 by the solid-state method. Phase identification of the Na_xCO_2 was performed by XRD, and studies show that the O3, O'3 and P'3 exist at a fixed stoichiometry while the P2 phase is formed at a range of compositions (0.67 ≤ x ≤ 0.76). The four phases have different electrochemical properties. Due to the stoichiometry of the phases, phase purity and exposure to the atmosphere are problems encountered during the preparation of Na_xCoO_2. Roy (191) used the sol-gel method, with polyvinyl alcohol and carbon sources as gelating agents, to synthesise $NaCoO_2$ with a smooth morphology and micron-sized particles. The characterisation of the $NaCoO_2$ was investigated by TGA; attenuated total reflectance Fourier transforms Infra-red microscopy, XRD, and FESEM to examine the composition and morphology.

The electrochemical performance of $NaCoO_2$ was investigated in a Na-ion battery. It was suggested that particle agglomeration adversely affected Na-ion battery performance. Popescu [192] conducted a study to examine the impact of external pressure and Mn doping on the properties of Na_xCoO_2. Their findings indicate that both Mn doping and external pressure have a similar effect on the structural properties of Na_xCoO_2. Ding *et al.*, [193] studied the electrochemical properties of $Na_{0.74}CoO_2$ as a potential cathode material for SSSBs. The $Na_{0.74}CoO_2$ was prepared by the solid-state method and it exhibited good cycling performance for SSSBs. At a 2.0 - 3.8 V voltage range, a specific discharge capacity of 107 $mAhg^{-1}$ was achieved at 0.1 C. The columbic efficiency was 89.0% for each cycle, and the voltage polarisation was between 150 – 250 mV at a 0.1 C charge/discharged rate. A capacity fading of about 0.1% per cycle up to 40 cycles in $NaPF_6$ electrolyte was observed. The study showed that $Na_{0.74}CoO_2$ had better electrochemical performance in $NaPF_6$ than $NaClO_4$. The electrochemical performance of $Na_{0.67}CoO_2$ was studied by Shacklette *et al.*, [194]**.** All the possible phases (O2, O3, P2 and P3) were examined, and it was discovered that the P2 phase (0.6 ≤ x ≤ 0.75) offers better cycle life and energy efficiency advantages. Phase transitions as a function of temperature were observed for P2 Na_xCoO_2. The P3 phase $Na_{0.7}CoO_2$ is challenging to synthesise, and dopants affect the structure and properties.

Superconducting materials are suitable thermoelectric materials (materials that allow heat flow, thereby inducing the flow of electricity). Ishida [195], Yang [196] and Lynn [197] all reported the superconducting behaviour in Na_xCoO_2 (0.3 ≤ x ≤ 0.4). The group intercalated H_2O via oxidation into Na_xCoO_2 (0.3 ≤ x ≤ 0.4). Superconductivity was determined from the changes observed in the structure. The water forms two additional layers between the Na and CoO_2, increasing the c-axis lattice parameter of the hexagonal $P6_3/mmc$ space group from 11.16 Å to 19.5 Å. The arrangement of Na ions differs from that of the parent compound, while the water adopts a structure reminiscent of ice. The magnetic measurement confirmed the superconducting behaviour of the hydrated $Na_{0.35}CoO_2$. The ultrafast oxygen evolution reaction in P2 phase $Na_{0.67}CoO_2$ was studied by Wang *et al.*, [198]. The high activity is attributed to the shorter O-O separation, which facilitates the formation of peroxide ions through O–O interactions that lead to the O_2 evolution. $Na_{0.67}CoO_2$ shows a high activity for oxygen evolution reaction (OER) at room temperature in an alkaline solution. The onset of the OER varies with the pH of the alkaline solution, which is influenced by the loss of H^+ ions from the surface oxygen. Also, the strong hybridisation of the O–2p and low-spin Co^{III}/Co^{IV} π-bonding d-states also plays a vital role in the OER process. $Na_{0.67}CoO_2$ demonstrates excellent OER activity due to its short O–O separation, which increases the rate of a reaction.

2.14.1 Cold sintering of Li-ion and Na-ion compounds

Cold sintering has been used extensively to densify various Na and Li-containing materials such $LiMgPO_4$ [201], LCO-LLZAO [199], $Li_{6.25}La_3Zr_2Al_{0.25}O_{12}$ (LLZAO) [199], LLZO, Li_2MoO_4 based microwave dielectric ceramic capacitors, Bioglass® and Bioglass® polymer composites (here the dissolution of the glass was aided by a high concentration of Na) [200] and NASICON electrolytes $Na_{3.256}Mg_{0.128}Zr_{1.872}Si_2PO_{12}$ [108].

The densification of the Li-based compound of $Li_{6.25}La_3Zr_2Al_{0.25}O_{12}$ (LLZAO) solid electrolyte and $LiCoO_2$ (LCO) cathode material was studied by Li *et al.*, [199]. The LLZAO achieved a relative density of 87% using deionised water, while the composite of LCO-LLZAO achieved a relative density of 95% using 5M LiCl as a binder. The total conductivity of 20% LLZAO-LCO composite increased by 1000-fold. Investigation on LCO-LLZAO composites revealed that SEM and computer topography confirmed a continuous LCO matrix with the LLZAO phase evenly distributed but isolated throughout the ceramics. The electronic conductivity of the cold-sintered LCO-LLZAO ceramics at room temperature was comparable to the conventional sintered sample. The results provided valuable insights into the aqueous cold sintering of lithium-based compounds.

Studies on the densification of various ferroelectric, microwave, and dielectric materials were conducted by Guo *et al.*, [191-192]. Bulk monolithic and multilayer substrates, as well as ceramic-polymer composite materials, were investigated. Dielectric materials such as Li_2MoO_4, $(LiBi)_{0.5}MoO_4$, $(1-x)Li_2MoO_{4-x}PTFE$, $(1-x)(LiBi)_{0.5}MoO_{4-x}PTFE$ and

$Na_2Mo_2O_7$ composites were studied. The material resulted in a relative density of over 90%, with good microwave dielectric properties, which were comparable to those obtained by the conventional method. Table 2.2 summarises some Li and Na-ion compounds densified by the cold sintering technique.

Table 2.2

Densification of Li and Na-ion compounds by the CSP. The amount of transient solvents used, processing conditions and the relative densities of the cold sintered ceramic. BNT = $Bi(NO_3)_3$-NaOH-TiO_2.

Li and Na-ion compounds	Amount of solvents used	Processing condition			ρ_r (%)	Ref
		Temp. (°C)	Pressure (MPa)	Time (Minutes)		
$LiFePO_4$	0.95 wt% 2M LiOH	240	30 - 750	30	85	202
Li_2MoO_4	4 - 25 wt% H_2O	120	350	15	96	203
$Li_{1.5}Al_{0.5}Ge_{1.5}(PO_4)_3$	10 wt% H_2O	120	400	30	79	204
$Li_2Mg_3TiO_6$	20 wt% 4M LiOH	180	300	60	90	205
Li_2MoO_4 - $BaFe_{12}O_{19}$	10 - 20 wt% H_2O	120	55 - 70	40 - 10	94 - 97	206
$Na_{0.5}Bi_{0.5}MoO_4$ - Li_2MoO_4	5 - 10 wt% H_20	150	200	30	93 - 96	207
$Na_{0.5}Bi_{0.5}TiO_3$	5 - 20 wt% BNT	180	200 - 550	15 - 75	74	208
NaCl	4 wt% H_2O	25	50 - 300	10	95	209
$Na_{3.256}Mg_{0.128}Zr_{1.872}Si_2PO_{12}$	30 wt% H_2O	180	300 - 780	120	83	108
$Na_2Mo_2O_7$	5 - 10 wt% H_2O	150	200	30	95	210
$NaNO_2$	7 wt% H_2O	120	350	180	98	211
$NaNO_3$ - $Ca(OH)_2$	10 wt% H_2O	120	500	10	-	212
$Na_{3.4}Sc_{0.4}Zr_{1.6}Si_2PO_{12}$	10 wt% H_2O	250	300	10	77	213
$Na_{3.4}Sc_{0.4}Zr_{1.6}Si_2PO_{12}$	10 wt% 1M acetic acid	250	300	10	77	213
$Na_{3.4}Sc_{0.4}Zr_{1.6}Si_2PO_{12}$	10 wt% 1M NaOH	250	300	10	82	213
$Na_{3.4}Sc_{0.4}Zr_{1.6}Si_2PO_{12}$	10 wt% 1M KOH	250	300	10	86	213
$Na_{3.4}Sc_{0.4}Zr_{1.6}Si_2PO_{12}$	10 wt% 1M HNO_3	250	300	10	81	213

2.15 Extended objectives

The following composition of Na-ion compounds ($Na_3Zr_2Si_2PO_{12}$, $Na_{1.3}Al_{0.3}Ti_{1.7}P_3O_{12}$ and $Na_{0.7}CoO_2$) were selected according to our literature survey.

i. The solid-state reaction method has been one of the major routes of preparing NZSP, but the *m*-ZrO_2 impurity phase is ubiquitous in all reported literature. Single-phase NZSP is prepared here, however, by modifying the mole fraction of the ZrO_2 reactant to suppress/minimise the impact of the *m*-ZrO_2 impurity phase on the structural and electrical properties of NZSP. A new formula, "$Na_3Zr_{2-x}Si_2PO_{12-2x}$", is derived and modified to accommodate the reduction in mole fraction of ZrO_2. The densification of NZSP by the cold-sintering method is studied with a view to reducing the high energy demand of conventional sintering of NZSP. The structure and properties of cold vs. conventionally sintered NZSP are investigated.

ii. $Na_{0.7}CoO_2$ (NCO) is a well-studied cathode material for SSSBs due to its intriguing properties. NCO ($Na_{0.7}CoO_2$) is a P2 type, and a literature survey concluded that this composition has potential properties for battery applications. NCO powder from NEI Corporations was purchased, and its properties were investigated as a potential solid electrolyte/cathode for SSSBs. Densification of NCO by conventional and cold-sintering is performed, and the resulting samples are compared.

iii. NTP is an anode material. The introduction of Aluminium as a dopant to form $Na_{1.3}Al_{0.3}Ti_{1.7}P_3O_{12}$ (NATP) results in a potential solid electrolyte. NATP powder from NEI Corporation is densified using conventional and cold sintering, and the microstructure and properties of samples are compared in order to determine optimum processing conditions/methods for this compound.

2.16 References

[1] Y. Sun, Promising All-Solid-State Batteries for Future Electric Vehicles, *ACS Energy Letters*, vol. 5, no. 10, pp. 3221–3223, Oct. 2020, doi.org/10.1021/acsenergylett.0c01977.

[2] H. Zsiborács, N.H. Baranyai, A. Vincze, L. Zentkó, Z. Birkner, K. Máté, G. Pintér, Intermittent Renewable Energy Sources: The Role of Energy Storage in the European Power System of 2040, Electronics. 8 (2019) 729. doi.org/10.3390/electronics8070729.

[3] A. M. Bernardes, D. C. R. Espinosa, and J. A. S. Tenório, Recycling of batteries: a review of current processes and technologies, *Journal of Power Sources*, vol. 130, no. 1–2, pp. 291–298, May 2004, doi.org/10.1016/j.jpowsour.2003.12.026.

[4] H. Ge, X. Feng, D. Liu, and Y. Zhang, Recent advances and perspectives for Zn-based batteries: Zn anode & electrolyte, *Nano Research Energy*, Nov. 2022, doi.org/10.26599/nre.2023.9120039.

[5] Y. Liang and Y. Yao, “Designing modern aqueous batteries,” vol. 8, no. 2, pp. 109–122, Nov. 2022, doi.org/10.1038/s41578-022-00511-3.

[6] O. Dumont, G. F. Frate, A. Pillai, S. Lecompte, M. De paepe, and V. Lemort, “Carnot battery technology: A state-of-the-art review,” *Journal of Energy Storage*, vol. 32, p. 101756, Dec. 2020, doi.org/10.1016/j.est.2020.101756.

[7] S. T. Revankar, “Chemical Energy Storage,” *Storage and Hybridization of Nuclear Energy*, pp. 177–227, 2019, doi.org/10.1016/b978-0-12-813975-2.00006-5.

[8] B. Jeong, J. D. Ocon, and J. Lee, “Electrode Architecture in Galvanic and Electrolytic Energy Cells,” *Angewandte Chemie International Edition*, vol. 55, no. 16, pp. 4870–4880, Mar. 2016, doi.org/10.1002/anie.201507780.

[9] J. Zhang, Q. Zhou, Y. Tang, L. Zhang, and Y. Li, “Zinc-air batteries: Are they ready for prime time,” *Chemical Science*, vol. 10, no—39, pp. 8924–8929, Oct. 2019, https://doi.org/10.1039/C9SC04221K.

[10] E. Sayilgan, T. Kukrer, G. Civelekoglu, F. Ferella, A. Akcil, F. Veglio, M. Kitis, A review of technologies for the recovery of metals from spent alkaline and zinc–carbon batteries, Hydrometallurgy. 97 (2009) 158–166. doi.org/10.1016/j.hydromet.2009.02.008.

[11] X. Lu, G. Li, J. Y. Kim, J. P. Lemmon, V. L. Sprenkle, and Z. Yang, “A novel low-cost sodium–zinc chloride battery,” *Energy & Environmental Science*, vol. 6, no. 6, p. 1837, 2013, doi.org/10.1039/c3ee24244g.

[12] U. Köhler, C. Antonius, and P. Bäuerlein, “Advances in alkaline batteries,” *Journal of Power Sources*, vol. 127, no. 1–2, pp. 45–52, Mar. 2004, doi.org/10.1016/j.jpowsour.2003.09.006.

[13] Z. Wang, C. Peng, K. Yliniemi, and M. Lundström, “Recovery of High-Purity Silver from Spent Silver Oxide Batteries by Sulfuric Acid Leaching and Electrowinning,” *ACS Sustainable Chemistry & Engineering*, vol. 8, no. 41, pp. 15573–15583, Sep. 2020, doi.org/10.1021/acssuschemeng.0c04701.

[14] J. Li, D. Wang, and M. Pecht, “An electrochemical model for high C-rate conditions in lithium-ion batteries,” *Journal of Power Sources*, vol. 436, p. 226885, Oct. 2019, doi.org/10.1016/j.jpowsour.2019.226885.

[15] R. M. Dell, D. A. J. Rand, P. Connor, and R. (Bob) D. Bailey, *Understanding Batteries*. Cambridge: Royal Society of Chemistry, 2007.

[16] M. Hatch and Y. L. Cooper, “Henderson byte: Galvani and Volta,” *Preview*, vol. 2019, no. 203, pp. 12–12, Nov. 2019, doi.org/10.1080/14432471.2019.1673282.

[17] K. L. Caneva, M. Pera, and J. Mandelbaum, “The Ambiguous Frog: The Galvani-Volta Controversy on Animal Electricity,” *Journal of Interdisciplinary History*, vol. 23, no. 4, p. 796, 1993, doi.org/10.2307/206308.

[18] S. J. Moura and H. E. Perez, “Better Batteries Through Electrochemistry”, *Mechanical Engineering*, vol. 136, no. 06, pp. S15–S21, Jun. 2014, doi.org/10.1115/1.2014-jun-6.

[19] X. Lin, M. Salari, L. M. R. Arava, P. M. Ajayan, and M. W. Grinstaff, High temperature electrical energy storage: advances, challenges, & frontiers, *Chemical Society Reviews,* vol. 45, no. 21, pp. 5848, Oct. 2016, doi.org/10.1039/C6CS00012F.

[20] H. Zhao, Y. Nie, Y. Li, T. Wu, E. Zhao, J. Song, S. Komarneni, Low-cost and eco-friendly synthesis of octahedral LiMn2O4 cathode material with excellent electrochemical performance, Ceramics International. 45 (2019) 17183–17191. doi.org/10.1016/j.ceramint.2019.05.273.

[21] D. Pletcher and R. Wills, “A novel flow battery - A lead acid battery based on an electrolyte with soluble lead (II),” *Journal of Power Sources*, vol. 149, pp. 96-102, Sep. 2005, doi.org/10.1016/j.jpowsour.2005.01.048.

[22] E. Blumbergs, V. Serga, E. Platacis, M. Maiorov, and A. Shishkin, “Cadmium Recovery from Spent Ni-Cd Batteries: A Brief Review,” *Metals*, vol. 11, no. 11, p. 1714, Oct. 2021, doi.org/10.3390/met11111714.

[23] S. K. Dhar, S. R. Ovshínsky, P. R. Gifford, D. A. Corrigan, M. A. Fetcenko, and S. Venkatesan, “Nickel/metal hydride technology for consumer and electric vehicle batteries-a review and update,” *Journal of Power Sources*, vol. 65, no. 1–2, pp. 1–7, Mar. 1997, doi.org/10.1016/s0378-7753(96)02599-2.

[24] N. Nitta, F. Wu, J. T. Lee, and G. Yushin, “Li-ion battery materials: present and future,” *Materials Today*, vol. 18, no. 5, pp. 252–264, Jun. 2015, doi.org/10.1016/j.mattod.2014.10.040.

[25] M. H. Han, E. Gonzalo, G. Singh, and T. Rojo, “A comprehensive review of sodium layered oxides: powerful cathodes for Na-ion batteries,” *Energy & Environmental Science*, vol. 8, no. 1, pp. 81–102, 2015, doi.org/10.1039/c4ee03192j.

[26] M. El Haj Assad, A. Khosravi, M. Malekan, M.A. Rosen, and M.A. Nazari, Energy storage, Design and Performance Optimization of Renewable Energy Systems. (2021) 205–219. doi.org/10.1016/B978-0-12-821602-6.00016-X.

[27] R.D. Prengaman, A.H. Mirza, Recycling concepts for lead–acid batteries, Lead-Acid Batteries for Future Automobiles. (2017) 575–598. doi.org/10.1016/b978-0-444-63700-0.00020-9.

[28] N. Maleschitz, Cell design for high-rate operation, (2017). doi.org/10.1016/b978-0-444-63700-0.00011-8.

[29] H. Jafari and M. R. Rahimpour, “Pb-acid Batteries,” *Rechargeable Batteries*, pp. 17–39, Apr. 2020, https://doi.org/10.1002/9781119714774.ch2.

[30] V. Mahajan, R. S. Bharj, and J. Bharj, “Role of nano-carbon additives in lead-acid batteries: A review,” *Bulletin of Materials Science*, vol. 42, no. 1, Jan. 2019, doi.org/10.1007/s12034-018-1692-1.

[31] B. Hong, L. Jiang, H. Xue, F. Liu, M. Jia, J. Li, Y. Liu, Characterization of nano-lead-doped active carbon and its application in lead-acid battery, Journal of Power Sources. 270 (2014) 332–341. doi.org/10.1016/j.jpowsour.2014.07.145.

[32] S. R. Salkuti, “Electrochemical batteries for smart grid applications,” *International Journal of Electrical and Computer Engineering (IJECE)*, vol. 11, no. 3, p. 1849, Jun. 2021, doi.org/10.11591/ijece.v11i3.pp1849-1856.

[33] V. Etacheri, R. Marom, R. Elazari, G. Salitra, and D. Aurbach, "Challenges in the development of advanced Li-ion batteries: a review," *Energy & Environmental Science*, vol. 4, no. 9, p. 3243, 2011, https://doi.org/10.1039/c1ee01598b.

[34] R. Moshtev and B. Johnson, "State of the art of commercial Li-ion batteries," *Journal of Power Sources*, vol. 91, no. 2, pp. 86–91, Dec. 2000, doi.org/10.1016/s0378-7753(00)00458-4.

[35] D. Deng, "Li-ion batteries: basics, progress, and challenges," *Energy Science & Engineering*, vol. 3, no. 5, pp. 385–418, Sep. 2015, doi.org/10.1002/ese3.95.

[36] X. Hu, C. Wang, X. Zhu, C. Yao, and P. Ghadimi, "Trade structure and risk transmission in the international automotive Li-ion batteries trade," *Resources, Conservation and Recycling*, vol. 170, p. 105591, Jul. 2021, doi.org/10.1016/j.resconrec.2021.105591.

[37] B. Diouf and R. Pode, "Potential of Li-ion batteries in renewable energy" *Renewable Energy*, vol. 76, pp. 375–380, Apr. 2015, doi.org/10.1016/j.renene.2014.11.058.

[38] J. Cabana, L. Monconduit, D. Larcher, and M. R. Palacín, "Beyond Intercalation-Based Li-ion Batteries: The state of the art and challenges of electrode materials reacting through conversion reactions," *Advanced Materials*, vol. 22, no. 35, pp. E170–E192, Aug. 2010, doi.org/10.1002/adma.201000717.

[39] D. C. Bock, A. C. Marschilok, K. J. Takeuchi, and E. S. Takeuchi, "Batteries used to power implantable biomedical devices," *Electrochimica Acta*, vol. 84, pp. 155–164, Dec. 2012, doi.org/10.1016/j.electacta.2012.03.057.

[40] M. Nawaz, J. Ahmed, and M.S. Khan, "Cell balancing techniques for Li-ion batteries in healthcare devices," Feb. 2022, doi.org/10.1109/gcwot53057.2022.9772908.

[41] D.M. Spillman, E.S. Takeuchi, Lithium-ion batteries for medical devices, IEEE Xplore. (1999) 203–208. https://doi.org/10.1109/BCAA.1999.795991.

[42] L. Liao, P. Zuo, Y. Ma, X. Chen, Y. An, Y. Gao, G. Yin, Effects of temperature on charge/discharge behaviours of $LiFePO_4$ cathode for Li-ion batteries, Electrochimica Acta. 60 (2012) 269-273. doi.org/10.1016/j.electacta.2011.11.041

[43] Z. Favors, W. Wang, H.H. Bay, Z. Mutlu, K. Ahmed, C. Liu, M. Ozkan, C.S. Ozkan, Scalable Synthesis of Nano-Silicon from Beach Sand for Long Cycle Life Li-ion Batteries, Scientific Reports. 4 (2014) 1–7. https://doi.org/10.1038/srep05623.

[44] H. Li, Z. Wang, L. Chen, and X. Huang, “Research on Advanced Materials for Li-ion Batteries,” *Advanced Materials*, vol. 21, no. 45, pp. 4593–4607, Dec. 2009, https://doi.org/10.1002/adma.200901710.

[45] A. Zülke, Y. Li, P. Keil, R. Burrell, S. Belaisch, M. Nagarathinam, M.P. Mercer, H.E. Hoster, High-Energy Nickel-Cobalt-Aluminium Oxide (NCA) Cells on Idle: Anode- versus Cathode-Driven Side Reactions, Batteries & Supercaps. 4 (2021) 934–947. https://doi.org/10.1002/batt.202100046.

[46] T. Wang, K. Ren, M. He, W. Dong, W. Xiao, H. Pan, J. Yang, Y. Yang, P. Liu, Z. Cao, X. Ma, H. Wang, Synthesis and Manipulation of Single-Crystalline Lithium Nickel Manganese Cobalt Oxide Cathodes: A Review of Growth Mechanism, Frontiers in Chemistry. 8 (2020). https://doi.org/10.3389/fchem.2020.00747.

[47] K. Amine, J. Liu, S. Kang, I. Belharouak, Y. Hyung, D. Vissers, G. Henriksen, Improved lithium manganese oxide spinel/graphite Li-ion cells for high-power applications, Journal of Power Sources. 129 (2004) 14–19. doi.org/10.1016/j.jpowsour.2003.11.007.

[48] J. Qiu, C.-S. Lai, E. MacA. Gray, S. Li, S. Qiu, Ekaterina Strounina, C. Sun, C. Chen, Q. Zhang, Blue hydrogenated lithium titanate as a high-rate anode material for lithium-ion batteries, 2 (2014) 6353–6353. doi.org/10.1039/c4ta00556b.

[49] X.-G. Yang, T. Liu, and C.-Y. Wang, “Thermally modulated lithium iron phosphate batteries for mass-market electric vehicles,” *Nature Energy*, vol. 6, no. 2, pp. 176–185, Jan. 2021, doi.org/10.1038/s41560-020-00757-7.

[50] G.E. Blomgren, The Development and Future of Li-on Batteries, Journal of Electrochemical Society. 164 (2016) A5019–A5025. doi.org/10.1149/2.0251701jes.

[51] D. Deng, “Li-ion batteries: basics, progress, and challenges,” *Energy Science & Engineering*, vol. 3, no. 5, pp. 385–418, Sep. 2015, doi.org/10.1002/ese3.95.

[52] J. F. Peters and M. Weil, “Providing a common base for life cycle assessments of Li-Ion batteries,” *Journal of Cleaner Production*, vol. 171, pp. 704–713, Jan. 2018, doi.org/10.1016/j.jclepro.2017.10.016.

[53] V. Etacheri, R. Marom, R. Elazari, G. Salitra, and D. Aurbach, “Challenges in the development of advanced Li-ion batteries: a review,” *Energy & Environmental Science* vol. 4, no. 9, p. 3243, 2011, doi.org/10.1039/c1ee01598b.

[54] Y. Tian, G. Zeng, A. Rutt, T. Shi, H. Kim, J. Wang, J. Koettgen, Y. Sun, B. Ouyang, T. Chen, Z. Lun, Z. Rong, K. Persson, G. Ceder, Promises and Challenges of Next-Generation Batteries for Electric Vehicles and Grid Decarbonization, Chemical Reviews. 121 (2020) 1623–1669. doi.org/10.1021/acs.chemrev.0c00767.

[55] G. Assat and J.-M. Tarascon, "Fundamental understanding and practical challenges of anionic redox activity in Li-ion batteries," *Nature Energy*, vol. 3, no. 5, pp. 373–386, Apr. 2018, doi.org/10.1038/s41560-018-0097-0.

[56] R. Kumar, J. Liu, J.-Y. Hwang, and Y.-K. Sun, "Recent research trends in Li–S batteries," *Journal of Materials Chemistry A*, vol. 6, no. 25, pp 11582–11605, Jun. 2018. doi.org/10.1039/C8TA01483C.

[57] K. Chayambuka, G. Mulder, D.L. Danilov, P.H.L. Notten, From Li-ion Batteries toward Na-Ion Chemistries: Challenges and Opportunities, Advanced Energy Materials. 10 (2020) 2001310. https://doi.org/10.1002/aenm.202001310.

[58] K. Kubota, M. Dahbi, T. Hosaka, S. Kumakura, and S. Komaba, "Towards K-ion and Na-ion Batteries as 'Beyond Li-ion,'" *The Chemical Record*, vol. 18, no. 4, pp. 459–479, Feb. 2018, https://doi.org/10.1002/tcr.201700057.

[59] E. Goikolea, V. Palomares, S. Wang, I.R. Larramendi, X. Guo, G. Wang, T. Rojo, Na-Ion Batteries—Approaching Old and New Challenges, Advanced Energy Materials. 10 (2020) 2002055. https://doi.org/10.1002/aenm.202002055.

[60] K. Chayambuka, G. Mulder, D. L. Danilov, and P. H. L. Notten, "From Li-Ion Batteries toward Na-Ion Chemistries: Challenges and Opportunities," *Advanced Energy Materials*, vol. 10, no. 38, Aug. 2020, https://doi.org/10.1002/aenm.202001310.

[61] M. H. Han, E. Gonzalo, G. Singh, and T. Rojo, "A comprehensive review of sodium layered oxides: powerful cathodes for Na-ion batteries," *Energy & Environmental Science*, vol. 8, no. 1, pp. 81–102, 2015, https://doi.org/10.1039/c4ee03192j.

[62] J. F. Peters, A. Peña Cruz, and M. Weil, "Exploring the Economic Potential of Na-ion Batteries, *Batteries*, vol. 5, no. 1, Mar. 2019, doi.org/10.3390/batteries5010010.

[63] M. Á. Muñoz-Márquez, M. Zarrabeitia, S. Passerini, and T. Rojo, "Structure, Composition, Transport Properties, and Electrochemical Performance of the Electrode-Electrolyte Interphase in Non-Aqueous Na-ion Batteries," *Advanced Materials Interfaces*, vol. 9, no. 8, Jan. 2022, doi.org/10.1002/admi.202101773.

[64] K. Abraham, "How Comparable are Na-ion Batteries to Li-ion counterparts," *ACS Energy Lett.*, vol. 5, no. 11, Oct. 2020, doi.org/10.1021/acsenergylett.0c02181.

[65] Y. Xiao, Y. Wang, S.-H. Bo, J. C. Kim, L. J. Miara, and G. Ceder, "Publisher Correction: Understanding interface stability in solid-state batteries," *Nature Reviews Materials*, Mar. 2020, https://doi.org/10.1038/s41578-020-0191-3.

[66] M. B. Dixit, J.-K. Park, P. Kenesei, J. Almer, and K. B. Hatzell, "Status and the prospect of *in situ* and *operando* characterisation of solid-state batteries," vol. 14, no. 9, pp. 4672–4711, Sep. 2021, https://doi.org/10.1039/d1ee00638j.

[67] A. M. Bates, Y. Preger, L. Torres-Castro, K. L. Harrison, S. J. Harris, and J. Hewson, "Are solid-state batteries safer than lithium-ion batteries?," *Joule*, vol. 6, no. 4, pp. 742–755, Apr. 2022, https://doi.org/10.1016/j.joule.2022.02.007.

[68] M. Balaish, J. C. Gonzalez-Rosillo, K. J. Kim, Y. Zhu, Z. D. Hood, and J. L. M. Rupp, "Processing thin but robust electrolytes for solid-state batteries," *Nature Energy*, vol. 6, no. 3, pp. 227–239, Feb. 2021, doi.org/10.1038/s41560-020-00759-5.

[69] L. Wang, J. Li, G. Lu, W. Li, Q. Tao, C. Shi, H. Jin, G. Chen, S. Wang, Fundamentals of Electrolytes for Solid-State Batteries: Challenges and Perspectives, Frontiers in Materials. 7 (2020). https://doi.org/10.3389/fmats.2020.00111.

[70] M. B. Dixit, N. Muralidharan, Anand Parejiya, R. Amin, Rachid Essehli, and Ilias Belharouak, "Current Status and Prospects of Solid-State Batteries as the Future of Energy Storage," Jul. 2021, https://doi.org/10.5772/intechopen.98701.

[71] A. Sakuda, "Favorable composite electrodes for all-solid-state batteries," *Journal of the Ceramic Society of Japan*, vol. 126, no. 9, pp. 675–683, Sep. 2018, https://doi.org/10.2109/jcersj2.18114.

[72] A. Bates, S. Mukherjee, N. Schuppert, B. Son, J. G. Kim, and S. Park, "Modeling and simulation of 2D lithium-ion solid-state battery," *International Journal of Energy Research*, vol. 39, no. 11, pp. 1505–1518, May 2015, doi.org/10.1002/er.3344.

[73] C. Zhao, L. Liu, X. Qi, Y. Lu, F. Wu, J. Zhao, Y. Yu, Y.-S. Hu, L. Chen, Solid-State Sodium Batteries, Advanced Energy Materials. 8 (2018) 1703012. doi.org/10.1002/aenm.201703012.

[74] V. Thangadurai and B. Chen, "Solid Li- and Na-Ion Electrolytes for Next Generation Rechargeable Batteries," *Chemistry of Materials*, vol. 34, no. 15, pp. 6637–6658, Jul. 2022, doi.org/10.1021/acs.chemmater.2c01475.

[75] P. Jiang, G. Du, J. Cao, X. Zhang, C. Zou, Y. Liu, X. Lu, Solid-State Li-ion Batteries with Oxide Solid Electrolytes: Progress and Perspective, Energy Technology. 11 (2023) 2201288. https://doi.org/10.1002/ente.202201288.

[76] M. P. Fertig, K. Skadell, M. Schulz, C. Dirksen, P. Adelhelm, and M. Stelter, "From High to Low-Temp: The Revival of Na-Beta Alumina for Na Solid-State Batteries" *Batteries & Supercaps*, vol. 5, no. 1, Sep. 2021, doi.org/10.1002/batt.202100131.

[77] W.-R. Hou, X. Guo, X. Shen, K. Amine, H. Yu, and J. Lu, "Solid electrolytes and interfaces in all-solid-state sodium batteries: Progress and perspective," *Nano Energy*, vol. 52, pp. 279–291, Oct. 2018, doi.org/10.1016/j.nanoen.2018.07.036.

[78] J. F. Peters, A. Peña Cruz, and M. Weil, "Exploring the Economic Potential of Na-ion Batteries," *Batteries*, vol. 5, p. 10, Mar. 2019, doi.org/10.3390/batteries5010010.

[79] D. Deng, "Li-ion batteries: basics, progress, and challenges," *Energy Science & Engineering*, vol. 3, no. 5, pp. 385–418, Sep. 2015, doi.org/10.1002/ese3.95.

[80] A. Manthiram, J.-H. Kim, Y. N. Kim, and K.-T. Lee, "Crystal chemistry and properties of mixed ionic-electronic conductors," *Journal of Electroceramics*, vol. 27, no. 2, pp. 93–107, Feb. 2011, https://doi.org/10.1007/s10832-011-9635-x.

[81] T. Oku, "Crystal structures of perovskite halide compounds used for solar cells," *Reviews on advanced materials science*, vol. 59, no. 1, pp. 264–305, Jul. 2020, https://doi.org/10.1515/rams-2020-0015.

[82] H. D. Megaw, "Crystal structure of double oxides of the perovskite-type," *Proceedings of the Physical Society*, vol. 58, no. 2, Mar. 1946, https://doi.org/10.1088/0959-5309/58/2/301.

[83] D. O. Semykina, O. A. Podgornova, S. B. Moodakare, R. Vedarajan, and N. V. Kosova, "Crystal Chemistry and Ionic Conductivity of the NASICON-Related Phases in the $Li_{3-x}Na_xV_2(PO_4)_3$ System," *Inorganic Chemistry*, vol. 62, no. 15, pp. 5939–5950, Mar. 2023, https://doi.org/10.1021/acs.inorgchem.2c04351.

[84] L. Chen, Z.-M. Li, J. Ma, H. Ling, F. Kang, and Y.-B. He, "Progress and Perspective of All-Solid-State Lithium Batteries with High Performance at Room Temperature," vol. 34, no. 11, Oct. 2020, https://doi.org/10.1021/acs.energyfuels.0c02915.

[85] F. Cherkaoui, "Crystal chemistry and ionic conductivity of a new NASICON-related solid solution $Na_{1+x}Zr_{2-x/2}Mg_{x/2}(PO_4)_3$," *Solid State Ionics*, vol. 21, no. 4, pp. 333–337, Nov. 1986, https://doi.org/10.1016/0167-2738(86)90195-5.

[86] Y. Lu, K. H. Shin, Y. Yu, Y. Hu, J. Liang, K. Chen, H. Yuan, Ho Seok Park, D. Wang, Multiple Active Sites Carbonaceous Anodes for Na + Storage: Synthesis, Electrochemical Properties and Reaction Mechanism Analysis, Advanced Functional Materials. 31 (2020). https://doi.org/10.1002/adfm.202007247.

[87] Y. Zheng, Y. Yao, J. Ou, M. Li, D. Luo, H. Dou, Z. Li, K. Amine, A. Yu, Z. Chen, A review of composite solid-state electrolytes for lithium batteries: fundamentals, key materials and advanced structures, Chemical Society Reviews. 49 (2020) 8790–8839. https://doi.org/10.1039/d0cs00305k.

[88] L. Pietronero, A. Avogadro, Mechanisms of ionic conduction in glassy solid electrolytes, Solid State Ionics. 3-4 (1981) 7–11. https://doi.org/10.1016/0167-2738(81)90045-x.

[89] R.B. Schwarz, Formation of amorphous alloys by solid-state reactions, Materials Science and Engineering. 97 (1988) 71–78. https://doi.org/10.1016/0025-5416(88)90014-6.

[90] N. Kumada, Preparation and crystal structure of new inorganic compounds by hydrothermal reaction, Journal of the Ceramic Society of Japan. 121 (2013) 135–141. https://doi.org/10.2109/jcersj2.121.135.

[91] L. Liu, N. Zhang, K. Sun, T. Yang, High rate performance of Li[$Ni_{1/3}Co_{1/3}Mn_{1/3}$]O_2 synthesized via co-precipitation method by different precipitators, Journal of Physics and Chemistry of Solids. 70 (2009) 727–731. https://doi.org/10.1016/j.jpcs.2009.02.013.

[92] J. Zhao, J. He, X. Ding, J. Zhou, Y. Ma, S. Wu, R. Huang, A novel sol–gel synthesis route to $NaVPO_4F$ as cathode material for hybrid Li-ion batteries, Journal of Power Sources. 195 (2010) 6854–6859. doi.org/10.1016/j.jpowsour.2010.04.003.

[93] P. Vandiver, O. Soffer, B. Klima, and J. Svoboda, The origins of ceramic technology. *Science.org*, 1989. https://doi.org/10.1126/science.246.4933.1002

[94] A. Aytimur, S. Koçyiğit, İ. Uslu, Calcia Stabilized Ceria Doped Zirconia Nanocrystalline Ceramic, Journal of Inorganic and Organometallic Polymers and Materials. 24 (2014) 927–932. https://doi.org/10.1007/s10904-014-0064-6.

[95] R. Chaim, M. Levin, Amit Shlayer, C. Estournès, Sintering and densification of nanocrystalline ceramic oxide powders: a review, 107 (2008) 159–169. https://doi.org/10.1179/174367508x297812.

[96] K. Uchino, "Manufacturing Methods for Piezoelectric Ceramic Materials" Advanced Piezoelectric Materials, pp. 385–421, 2017, https://doi.org/10.1016/b978-0-08-102135-4.00010-2.

[97] K. Biswas, "Solid State Sintering of Si-C Ceramics," *Materials Science Forum*, vol. 624, pp. 71–89, Jun. 2009, doi.org/10.4028/www.scientific.net/msf.624.71.

[98] Z. Zhang, L. Zhang, Y. Liu, C. Yu, X. Yan, B. Xu, L. Wang, Synthesis and characterisation of Argyrodites solid electrolytes for solid-state Li-ion batteries, Journal of Alloys and Compounds. 747 (2018) 227–235. doi.org/10.1016/j.jallcom.2018.03.027.

[99] V. Tikare, M. V. Braginsky, and E. A. Olevsky, "Numerical Simulation of Solid-State Sintering: I, Sintering of Three Particles," vol. 86, no. 1, pp. 49–53, Jan. 2003, https://doi.org/10.1111/j.1151-2916.2003.tb03276.x.

[100] J. Svoboda and H. Riedel, "New solutions describing the formation of inter-particle necks in solid-state sintering," vol. 43, no. 1, pp. 1–10, Jan. 1995, https://doi.org/10.1016/0956-7151(95)90255-4.

[101] K. Uchino, "Manufacturing Methods for Piezoelectric Ceramic Materials" Advanced Piezoelectric Materials, pp. 385–421, 2017, https://doi.org/10.1016/b978-0-08-102135-4.00010-2.

[102] H. Guo, A. Baker, J. Guo, C.A. Randall, Cold Sintering Process: A Novel Technique for Low-Temperature Ceramic Processing of Ferroelectrics, Journal of the American Ceramic Society. 99 (2016) 3489–3507. doi.org/10.1111/jace.14554.

[103] D. Wang, H. Guo, C. S. Morandi, C. A. Randall, and S. Trolier-McKinstry, "Cold sintering and electrical characterisation of lead zirconate titanate piezoelectric ceramics," *APL Materials*, vol. 6, no. 1, Jan. 2018, doi.org/10.1063/1.5004420.

[104] D. Wang, L. Li, J. Jiang, Z. Lu, G. Wang, K. Song, D. Zhou, I.M. Reaney, Cold sintering of microwave dielectric ceramics and devices, Journal of Materials Research. 36 (2021) 333–349. https://doi.org/10.1557/s43578-020-00029-w.

[105] L. Li, J. Andrews, R. Mitchell, D. Button, D. C. Sinclair, and I. M. Reaney, "Aqueous Cold Sintering of Li-Based Compounds," *ACS Applied Materials & Interfaces*, vol. 15, no. 16, pp. 20228–20239, Apr. 2023, https://doi.org/10.1021/acsami.3c00392.

[106] J. Hao, J. Guo, C. Ma, F.-Z. Yao, B. Yao, M. Si, E. Zhao, H. Wang, Cold Sintering of Na_2WO_4 Ceramics using a Na_2WO_4-$2H_2O$ Chemistry, Journal of the European Ceramic Society. 41, 2021, doi.org/10.1016/j.jeurceramsoc.2021.05.019.

[107] J.G. Pereira da Silva, M. Bram, A.M. Laptev, J. Gonzalez-Julian, Q. Ma, F. Tietz, O. Guillon, sintering of a sodium-based NASICON electrolyte: A comparative study between cold, field-assisted and conventional sintering methods, Journal of the European Ceramic Society. 39 (2019) 2697–2702. doi.org/10.1016/j.jeurceramsoc.2019.03.023.

[108] H. Leng, J. Huang, J. Nie, and J. Luo, “Cold sintering and ionic conductivities of $Na_{3.256}Mg_{0.128}Zr_{1.872}Si_2PO_{12}$ solid electrolytes,” *Journal of Power Sources*, vol. 391, pp. 170–179, Jul. 2018, https://doi.org/10.1016/j.jpowsour.2018.04.067.

[109] L. Cong, W. Huajing, M. Jianzhang, D. Baoyu, W. Xiao, L. Tengfei, Z. Xinghua, Y. Xing, Effect of dwell time on cold sintering assisted sintering based highly transparent $0.9K_{0.5}Na_{0.5}NbO_{3-0.1}LiBiO_3$ ceramics, Journal of Alloys and Compounds. 826 (2020) 154249. https://doi.org/10.1016/j.jallcom.2020.154249.

[110] H. Kähäri, M. Teirikangas, J. Juuti, and H. Jantunen, “Dielectric Properties of Lithium Molybdate Ceramic Fabricated at Room Temperature,” *Journal of the American Ceramic Society*, vol. 97, no. 11, Oct. 2014, doi.org/10.1111/jace.13277.

[111] H. Guo, A. Baker, J. Guo, and C. A. Randall, “Cold Sintering Process: A Novel Technique for Low-Temperature Ceramic Processing of Ferroelectrics,” *Journal of the American Ceramic Society*, vol. 99, no. 11, pp. 3489–3507, Oct. 2016, https://doi.org/10.1111/jace.14554.

[112] J. Guo, S. S. Berbano, H. Guo, A. L. Baker, M. T. Lanagan, and C. A. Randall, “Cold Sintering Process of Composites: Bridging the Processing Temperature Gap of Ceramic and Polymer Materials,” *Advanced Functional Materials*, vol. 26, no. 39, pp. 7115–7121, Aug. 2016, https://doi.org/10.1002/adfm.201602489.

[113] Y. Liu, J. Liu, Q. Sun, D. Wang, K.R. Adair, J. Liang, C. Zhang, L. Zhang, S. Lu, H. Huang, X. Song, X. Sun, Insight into the Microstructure and Ionic Conductivity of Cold Sintered NASICON Solid Electrolyte for Solid-State Batteries, ACS Applied Materials and Interfaces. 11 (2019) 27890–27896. doi.org/10.1021/acsami.9b08132

[114] R. Boston, J. Guo, S. Funahashi, A. L. Baker, I. M. Reaney, and C. A. Randall, “Reactive intermediate phase cold sintering in strontium titanate,” *RSC Advances*, vol. 8, no. 36, pp. 20372–20378, May 2018, https://doi.org/10.1039/C8RA03072C.

[115] D. Wang, S. Zhang, D. Zhou, K. Song, A. Feteira, Y. Vardaxoglou, W. Whittow, D. Cadman, I.M. Reaney, Temperature Stable Cold Sintered $(Bi_{0.95}Li_{0.05})(V_{0.9}Mo_{0.1})O_4$-$Na_2Mo_2O_7$ Microwave Dielectric Composites, Materials. 12 (2019) 1370. https://doi.org/10.3390/ma12091370.

[116] J. Andrews, D. Button, and I. M. Reaney, “Advances in cold sintering: Improving energy consumption and unlocking new potential in component manufacturing,”

Johnson Matthey Technology Review, vol. 64, no. 2, pp. 219–232, Apr. 2020, Available online: https://eprints.whiterose.ac.uk/159803/

[117] D. Wang, H. Guo, C. S. Morandi, C. A. Randall, and S. Trolier-McKinstry, "Cold sintering and electrical characterisation of lead zirconate titanate piezoelectric ceramics," *APL Materials*, vol. 6, no. 1, Jan. 2018, doi.org/10.1063/1.5004420.

[118] D. Wang, L. Li, J. Jiang, Z. Lu, G. Wang, K. Song, D. Zhou, I.M. Reaney, Cold sintering of microwave dielectric ceramics and devices, Journal of Materials Research. 36 (2021) 333–349. https://doi.org/10.1557/s43578-020-00029-w.

[119] A. Galotta and V. M. Sglavo, The cold sintering process: A review on processing features, densification mechanisms and perspectives, *Journal of the European Ceramic Society*, vol. 41, no. 16, Dec. 2021, doi.org/10.1016/j.jeurceramsoc.2021.09.024

[120] J. Guo, R. Floyd, S. Lowum, J.-P. Maria, T. Herisson de Beauvoir, J.-H. Seo, C.A. Randall, Cold Sintering: Progress, Challenges, and Future Opportunities, Annual Review of Materials Research. 49 (2019) 275–295. doi.org/10.1146/annurev-matsci-070218-010041.

[121] K. Ishizaki, Sridhar Komarneni, and Makoto Nanko, "Sintering mechanisms and advanced sintering methods for porous materials," Jan. 1998, https://doi.org/10.1007/978-1-4615-5811-8_3.

[122] C. E. Dancer, Flash sintering of ceramic materials, *Materials Research Express*, vol. 3, no. 10, p. 102001, Oct. 2016, doi.org/10.1088/2053-1591/3/10/102001.

[123] M. Biesuz and V. M. Sglavo, "Flash sintering of ceramics", *Journal of the European Ceramic Society*, vol. 39, no. 2, pp. 115–143, Feb. 2019, https://doi.org/10.1016/j.jeurceramsoc.2018.08.048.

[124] B. Yoon, V. Avila, I. R. Lavagnini, J. V. Campos, and L. M. Jesus, "Reactive Flash Sintering of Ceramics: A Review," *Advanced Engineering Materials*, vol. 25, no. 5, p. 2200731, Sep. 2022, https://doi.org/10.1002/adem.202200731.

[125] V. Mamedov, "Spark plasma sintering as advanced PM sintering method," *Powder Metallurgy*, vol. 45, no. 4, pp. 322–328, Dec. 2002, doi.org/10.1179/003258902225007041.

[126] S. D. Oguntuyi, O. T. Johnson, and M. B. Shongwe, "Spark plasma sintering of ceramic matrix composite of TiC: microstructure, densification, and mechanical properties: a review," *The International Journal of Advanced Manufacturing*

Technology, vol. 116, no. 1–2, pp. 69–82, Jun. 2021, doi.org/10.1007/s00170-021-07471-y.

[127] J.-S. Lee, C.-M. Chang, Y. I. Lee, J.-H. Lee, and S.-H. Hong, "Spark Plasma Sintering (SPS) of NASICON Ceramics," *Journal of the American Ceramic Society*, vol. 87, no. 2, pp. 305–307, Feb. 2004, https://doi.org/10.1111/j.1551-2916.2004.00305.x.

[128] M. Kotobuki and S. Yanagiya, "Li-ion conductivity of $Li_{1+2x}Zr_{2-x}Ca_x(PO_4)_3$ solid electrolyte prepared by spark plasma sintering," *Journal of Alloys and Compounds*, vol. 862, p. 158641, May 2021, https://doi.org/10.1016/j.jallcom.2021.158641.

[129] M. Avdeev, Crystal Chemistry of NASICONs: Ideal Framework, Distortion, and Connection to Properties, Chemistry of Materials. 33 (2021) 7620–7632. https://doi.org/10.1021/acs.chemmater.1c02695.

[130] R. Rajagopalan, Z. Zhang, Y. Tang, C. Jia, X. Ji, H. Wang, Understanding crystal structures, ion diffusion mechanisms and sodium storage behaviour of NASICON materials, Energy Storage Materials. 34 (2021) 171–193. httpdoi.org/10.1016/j.ensm.2020.09.007.

[131] Development of solid-state electrolytes for Na-ion battery–A short review, *Nano Materials Science*, vol. 1, Jun. 2019, doi.org/10.1016/j.nanoms.2019.02.007.

[132] B. C. Saha, A. K. Bera, & S. M. Yusuf, "Mechanism of Na-ion Conduction in the Highly Efficient Layered Battery Material $Na_2Mn_3O_7$," *ACS Applied Energy Materials*, vol. 4, no. 6, pp. 6040–6054, Jun. 2021, doi.org/10.1021/acsaem.1c00825.

[133] R. Jalem, A. Hayashi, F. Tsuji, A. Sakuda, and Y. Tateyama, "First-Principles Calculation Study of Na^+ Superionic Conduction Mechanism in W- and Mo-Doped Na_3SbS_4 Solid Electrolytes," *Chemistry of Materials*, vol. 32, no. 19, pp. 8373–8381, Sep. 2020, https://doi.org/10.1021/acs.chemmater.0c02318.

[134] B.J. Morgan, Understanding fast-ion conduction in solid electrolytes, Philosophical Transactions of the Royal Society A: Mathematical, Physical and Engineering Sciences. 379 (2021). https://doi.org/10.1098/rsta.2019.0451.

[135] A. K. Bera and S. M. Yusuf, "Temperature-Dependent Na-ion Conduction and Its Pathways in the Crystal Structure of the Layered Battery Material $Na_2Ni_2TeO_6$," *The Journal of Physical Chemistry C*, vol. 124, no. 8, pp. 4421–4429, Jan. 2020, https://doi.org/10.1021/acs.jpcc.9b11191.

[136] F. Meutzner, W. Münchgesang, N.A. Kabanova, M. Zschornak, T. Leisegang, V.A. Blatov, D.C. Meyer, On the Way to New Possible Na-Ion Conductors: The Voronoi–

Dirichlet Approach, Data Mining and Symmetry Considerations in Ternary Na Oxides, Chemistry – a European Journal. 21 (2015) 16601–16608. https://doi.org/10.1002/chem.201501975.

[137] Y. Xiao, Y. Wang, S.-H. Bo, J. C. Kim, L. J. Miara, and G. Ceder, "Understanding interface stability in solid-state batteries," *Nature Reviews Materials*, vol. 5, no. 2, pp. 105–126, Dec. 2019, https://doi.org/10.1038/s41578-019-0157-5.

[138] M. Samiee, B. Radhakrishnan, Z. Rice, Z. Deng, Y.S. Meng, S.P. Ong, J. Luo, Divalent-doped $Na_3Zr_2Si_2PO_{12}$ natrium superionic conductor: Improving the ionic conductivity via simultaneously optimising the phase and chemistry of the primary and secondary phases, Journal of Power Sources. 347 (2017) 229–237. https://doi.org/10.1016/j.jpowsour.2017.02.042.

[139] L. Shen, J. Yang, G. Liu, M. Avdeev, and X. Yao, "High ionic conductivity and dendrite-resistant NASICON solid electrolyte for all-solid-state sodium batteries," *Materials Today Energy*, vol. 20, p. 100691, Jun. 2021, https://doi.org/10.1016/j.mtener.2021.100691.

[140] S.K. Pal, R. Saha, G.V. Kumar, S. Omar, Designing High Ionic Conducting NASICON-type $Na_3Zr_2Si_2PO_{12}$ Solid-Electrolytes for Na-Ion Batteries, The Journal of Physical Chemistry C. 124 (2020) 9161–9169. https://doi.org/10.1021/acs.jpcc.0c00543.

[141] A. Jalalian-Khakshour, C.O. Phillips, L. Jackson, T.O. Dunlop, S. Margadonna, D. Deganello, Solid-state synthesis of NASICON ($Na_3Zr_2Si_2PO_{12}$) using nanoparticle precursors for optimisation of ionic conductivity, Journal of Materials Science. 55 (2019) 2291–2302. https://doi.org/10.1007/s10853-019-04162-8.

[142] S. Narayanan, S. Reid, S. Butler, and V. Thangadurai, "Sintering temperature, excess sodium, and phosphorous dependencies on morphology and ionic conductivity of NASICON $Na_3Zr_2Si_2PO_{12}$," *Solid State Ionics*, vol. 331, pp. 22–29, Mar. 2019, doi: 10.1016/j.ssi.2018.12.003.

[143] P. Yadav, M.C. Bhatnagar, Structural studies of NASICON material of different compositions by sol–gel method, Ceramics International. 38 (2012) 1731–1735. https://doi.org/10.1016/j.ceramint.2011.09.022.

[144] A. Ignaszak, P. Pasierb, R. Gajerski, S. Komornicki, Synthesis and properties of Nasicon-type materials, Thermochimica Acta. 426 (2005) doi.org/10.1016/j.tca.2004.07.002.

[145] J.-S. Lee, C.-M. Chang, Y.I. Lee, J.-H. Lee, S.-H. Hong, Spark Plasma Sintering (SPS) of NASICON Ceramics, Journal of the American Ceramic Society. 87 (2004) 305–307. https://doi.org/10.1111/j.1551-2916.2004.00305.x.

[146] K. Okubo, H. Wang, K. Hayashi, M. Inada, N. Enomoto, G. Hasegawa, T. Osawa, H. Takamura. A dense NASICON sheet prepared by tape-casting and low-temp. sintering, Electrochimica Acta. 278 (2018) 176–181. doi.org/10.1016/j.electacta.2018.05.020.

[147] S. Naqash, Q. Ma, F. Tietz, O. Guillon, $Na_3Zr_2(SiO_4)_2(PO_4)$ prepared by a solution-assisted solid-state reaction, Solid State Ionics. 302 (2017) 83–91. https://doi.org/10.1016/j.ssi.2016.11.004.

[148] A. Chakraborty, Raghunayakula Thirupathi, S. Bhattacharyya, K. Singh, S. Omar, Mg-doped NASICON-type electrolyte for rechargeable solid-state sodium-ion batteries, 572 (2023) 233092, doi.org/10.1016/j.jpowsour.2023.233092.

[149] N. Voronina, J. H. Jo, J. U. Choi, A. Konarov, J. Kim, and S.-T. Myung, "Revealing sodium storage mechanism in lithium titanium phosphate: A combined experimental and theoretical study," *Journal of Power Sources*, vol. 455, p. 227976, Apr. 2020, https://doi.org/10.1016/j.jpowsour.2020.227976.

[150] N. O. Bonsu, "Towards a circular and low-carbon economy: Insights from the transitioning to electric vehicles and net zero economies.," *Journal of Cleaner Production*, vol. 256, Feb. 2020, https://doi.org/10.1016/j.jclepro.2020.120659.

[151] Y. Sun, Q. Wu, X. Liang, and H. Xiang, "Recent developments in carbon-based materials as high-rate anode for sodium-ion batteries," *Materials Chemistry Frontiers*, vol. 5, no. 11, pp. 4089–4106, Jun. 2021, doi.org/10.1039/D0QM01124J.

[152] S. Guo, J. Yi, Y. Sun, and H. Zhou, "Recent advances in titanium-based electrode materials for stationary sodium-ion batteries," *Energy & Environmental Science*, vol. 9, no. 10, pp. 2978–3006, 2016, https://doi.org/10.1039/c6ee01807f.

[153] A. Balasankar, S.E. Arthiya, S. Ramasundaram, P. Sumathi, S. Arokiyaraj, T. Oh, K. Aruchamy, G. Sriram, M.D. Kurkuri, Recent Advances in the Preparation and Performance of Porous Titanium-Based Anode Materials for Sodium-Ion Batteries, Energies. 15 (2022) 9495. https://doi.org/10.3390/en15249495.

[154] X. Chen and Y. Zhang, "The main problems and solutions in the practical application of anode materials for sodium ion batteries and the latest research progress," *International Journal of Energy Research*, vol. 45, no. 7, pp. 9753–9779,

Feb. 2021, https://doi.org/10.1002/er.6500.

[155] S. Dong, N. Lu, Y. Wu, Y. Zhang, & G. Zhu, Titanate for Na-ion storage, *Nano Today*, vol. 42, p. 101349, Feb. 2022, https://doi.org/10.1016/j.nantod.2021.101349.

[156] X. Jiang, Z. Zeng, L. Xiao, X. Ai, H. Yang, and Y. Cao, "An All-Phosphate and Zero-Strain Na-ion Battery Based on $Na_3V_2(PO_4)_3$ Cathode, $NaTi_2(PO_4)_3$ Anode, and Tri-methyl Phosphate Electrolyte with Intrinsic Safety and Long Lifespan," vol. 9, no. 50, pp. 43733–43738, Dec. 2017, https://doi.org/10.1021/acsami.7b14946.

[157] Y. Li, Z. Ding, K. Wang, L. Wan, T. Lu, G. Zhu, Z. Gong, L. Pan, Suppressing the oxygen-related parasitic reactions in $NaTi_2(PO_4)_3$-based hybrid capacitive deionization with cation exchange membrane, Journal of Colloid and Interface Science. 591 (2021) 139–147. https://doi.org/10.1016/j.jcis.2021.02.013.

[158] M. Rohde, I. U. I. Mohsin, C. Ziebert, and H. J. Seifert, "Ionic and Thermal Transport in Na-ion-Conducting Ceramic Electrolytes," *International Journal of Thermophysics*, vol. 42, no. 10, Jul. 2021, doi.org/10.1007/s10765-021-02886-x.

[159] M. Cretin, P. Fabry, & L. Abello, "Study of $Li_{1+x}Al_xTi_{2-x}(PO_4)_3$ for Li potentiometric sensors," *Journal of The European Ceramic Society*, vol. 15, no. 11, pp. 1149–1156, Jan. 1995, https://doi.org/10.1016/0955-2219(95)00079-a.

[160] M. Liu, J. Cai, H. Ao, Z. Hou, Y. Zhu, & Y. Qian, "$NaTi_2(PO_4)_3$ Solid-State Electrolyte Protection Layer on Zn Metal Anode for Superior Long-Life Aqueous Zinc-ion Batteries," vol. 30, no. 50, Dec. 2020, https://doi.org/10.1002/adfm.202004885.

[161] R. S. Boyko, O. V. Chukova, O. V. Gomenyuk, P. G. Nagornyi, and S. G. Nedilko, "Origin of red luminescence of sodium titanium phosphate crystals," *physica status solidi (c)*, vol. 2, no. 1, Jan. 2005, https://doi.org/10.1002/pssc.200460272.

[162] R. Raja Madhavan, A. S. Gandhi, and K. V. Govindan Kutty, "Sodium titanium phosphate $NaTi_2(PO_4)_3$ waste forms for immobilisation of simulated high-level waste from fast reactors," *Ceramics International*, vol. 43, no. 12, pp. 9522–9530, Aug. 2017, https://doi.org/10.1016/j.ceramint.2017.04.138.

[163] H. Dai, W. Xu, Z. Hu, Y. Chen, J. Gu, F. Xie, W. Wei, R. Guo, G. Zhang, Novel Solid-State Sodium-on Battery with Wide Band Gap $NaTi_2(PO_4)_3$ Nanocrystal Electrolyte, ACS Omega. 6 (2021) 11537–11544. doi.org/10.1021/acsomega.1c00664.

[164] M. Wu, W. Ni, J. Hu, J. Ma, NASICON-Structured $NaTi_2(PO_4)_3$ for Sustainable Energy Storage, Nano-Micro Letters. 11 (2019). doi.org/10.1007/s40820-019-0273-1.

[165] F. Sun, R. Wang, H. Jiang, W. Zhou, Synthesis of sodium titanium phosphate at ultra-

low temperature, Research on Chemical Intermediates. 39 (2012) 1857–1864. https://doi.org/10.1007/s11164-012-0720-9.

[166] T.-F. Hung, W.-H. Lan, Y.-W. Yeh, W.-S. Chang, C.-C. Yang, J.-C. Lin, Hydrothermal Synthesis of Sodium Titanium Phosphate Nanoparticles as Efficient Anode Materials for Aqueous Sodium-Ion Batteries, ACS Sustainable Chemistry & Engineering. 4 (2016) 7074–7079. doi.org/10.1021/acssuschemeng.6b01962.

[167] N. Tolganbek, Y. Yerkinbekova, A. Khairullin, Z. Bakenov, K. Kanamura, A. Mentbayeva, Enhancing purity and ionic conductivity of NASICON-typed $Li_{1.3}Al_{0.3}Ti_{1.7}(PO_4)_3$ solid electrolyte, Ceramics International. 47 (2021) 18188–18195. https://doi.org/10.1016/j.ceramint.2021.03.137.

[168] Y. Liu, J. Liu, Q. Sun, D. Wang, K.R. Adair, J. Liang, C. Zhang, L. Zhang, S. Lu, H. Huang, X. Song, X. Sun, Insight into the Microstructure and Ionic Conductivity of Cold Sintered NASICON Solid Electrolyte for Solid-State Batteries, ACS Applied Materials & Interfaces. (2019) 27890–27896. doi.org/10.1021/acsami.9b08132.

[169] A.M. Nieto-Muñoz, J.F. Ortiz-Mosquera, A.C.M. Rodrigues, The impact of the heat-treatment protocol on the grain size and ionic conductivity of NASICON glass-ceramics, Journal of the European Ceramic Society. 40 (2020) 5634–5645. https://doi.org/10.1016/j.jeurceramsoc.2020.05.026.

[170] N. Voronina, J.H. Jo, J.U. Choi, C.-H. Jo, J. Kim, S.-T. Myung, Nb-Doped titanium phosphate for sodium storage: electrochemical performance and structural insights, Journal of Materials Chemistry A. 7 (2019) 5748–5759. https://doi.org/10.1039/C8TA11517F.

[171] C. Delmas, C. Fouassier, P. Hagenmuller, Structural classification and properties of the layered oxides, Physica B+C. 99 (1980) 81–85. https://doi.org/10.1016/0378-4363(80)90214-4.

[172] M. Jansen, R. Hoppe, Notiz zur Kenntnis der Oxocobaltate des Natriums, Zeitschrift Für Anorganische Und Allgemeine Chemie. 408 (1974) 104–106. https://doi.org/10.1002/zaac.19744080203.

[173] Y. Lei, X. Li, L. Liu, G. Ceder, Synthesis and Stoichiometry of Different Layered Sodium Cobalt Oxides, Chemistry of Materials. 26 (2014) 5288–5296. https://doi.org/10.1021/cm5021788.

[174] L. Viciu, J.W.G. Bos, H.W. Zandbergen, Q. Huang, M.L. Foo, S. Ishiwata, A.P. Ramirez, M. Lee, N.P. Ong, R.J. Cava, Crystal structure and elementary properties of Na_xCoO_2

(x=0.32, 0.51, 0.6, 0.75, and 0.92) in the three-layer $NaCoO_2$ family, Physical Review B. 73 (2006). https://doi.org/10.1103/physrevb.73.174104.

[175] Y. Sassa, I. Umegaki, H. Nozaki, O. K. Forslund, C. Delmas, J. C. Orain, A. Amato, D. Andreica, M. Månsson, J. Sugiyama, Investigation of the Magnetic Properties of $Na_{0.7}CoO_2$ Prepared by Electrochemical Reaction, DORA PSI (Paul Scherrer Institute). (2018). https://doi.org/10.7566/jpscp.21.011019.

[176] B. Senthilkumar, C.S. Johnson, P. Senguttuvan, Layered Na-ion Transition-Metal Oxide Electrodes for Na-Ion Batteries, Transition Metal Oxides for Electrochemical Energy Storage. (2022) 101–119. https://doi.org/10.1002/9783527817252.ch5.

[177] X. Gao, J. Chen, H. Liu, S. Yin, Y. Tian, X. Cao, G. Zou, H. Hou, W. Wei, L. Chen, X. Ji, Copper-substituted Na_xMO_2 (M = Fe, Mn) cathodes for Na-ion batteries: Enhanced cycling stability through suppression of Mn (III) formation, Chemical Engineering Journal. 406 (2021) 126830. doi.org/10.1016/j.cej.2020.126830.

[178] A. Kanwade, S. Gupta, A. Kankane, M. Kumar Tiwari, A. Srivastava, J.A.K. Satrughna, S.C. Yadav, P. M. Shirage, Transition metal oxides as a cathode for indispensable Na-ion batteries, RSC Advances. 12 (2022) 23284–23310. https://doi.org/10.1039/D2RA03601K.

[179] A.J. Toumar, Shyue Ping Ong, W. Lance Richards, S. Dacek, G. Ceder, Vacancy Ordering in O3 -Type Layered Metal Oxide Sodium-Ion Battery Cathodes, Physical Review Applied. 4 (2015). https://doi.org/10.1103/physrevapplied.4.064002.

[180] Y. Biecher, Structure, electronic structure and dynamic in layered transition metal oxides for Na-ion batteries, Archives-Ouvertes.fr. (2019). theses.hal.science/tel-03475586.

[181] K. Kato, H. Kasai, A. Hori, M. Takata, H. Tanaka, S. Kitagawa, A. Kobayashi, N. Ozawa, M. Kubo, H. Arikawa, T. Takeguchi, M. Sadakiyo, M. Yamauchi, Superionic Conduction in Co-Vacant P2-Na_xCoO_2 Created by Hydrogen Reductive Elimination, Chemistry - an Asian Journal. 2016 1537–1541. doi.org/10.1002/asia.201600370.

[182] A. Patra, J. Davis, S. Pidaparthy, M.H. Karigerasi, B. Zahiri, A.A. Kulkarni, M.A. Caple, D.P. Shoemaker, J.M. Zuo, P.V. Braun, Electrodeposition of atmosphere-sensitive ternary sodium transition metal oxide films for sodium-based electrochemical energy storage, Proceedings of the National Academy of Sciences. 118 (2021) e2025044118. https://doi.org/10.1073/pnas.2025044118.

[183] Y. Miyazaki, N. Igawa, K. Yubuta, Incommensurately modulated crystal structure

of α′ (O′3)-type sodium cobalt oxide Na_xCoO_2 (x ∼ 0.78), Acta Crystallographica Section B: Structural Science, Crystal Engineering and Materials. 77 (2021) 371–377. https://doi.org/10.1107/S205252062100370X.

[184] D.J. Singh, D. Kasinathan, Thermoelectric Properties of Na_xCoO_2 and Prospects for Other Oxide Thermoelectrics, Journal of Electronic Materials. 36 (2007) 736–739. https://doi.org/10.1007/s11664-007-0154-0.

[185] T. Shibata, Y. Fukuzumi, W. Kobayashi, Y. Moritomo, Fast discharge process of layered cobalt oxides due to high Na^+ diffusion, Scientific Reports. 5 (2015) 9006. https://doi.org/10.1038/srep09006.

[186] M. Leng, J. Bi, Z. Xing, W. Wang, X. Gao, J. Wang, Z. Qian, A new perspective on the composition-structure-property relationships on Nb/Mo/Cr-doped O3-type layered oxide as cathode materials for sodium-ion batteries, Chemical Engineering Journal. 413 (2021) 127824. https://doi.org/10.1016/j.cej.2020.127824.

[187] A. K. Rai, L. T. Anh, J. Gim, V. Mathew, and J. Kim, "Electrochemical properties of Na_xCoO_2 (x~0.71) cathode for rechargeable sodium-ion batteries," *Ceramics International*, vol. 40, no. 1, pp. 2411–2417, Jan. 2014, https://doi.org/10.1016/j.ceramint.2013.08.013.

[188] P. Kehne, C. Guhl, Q. Ma, F. Tietz, L. Alff, René Hausbrand, Philipp Komissinskiy, Electrochemical Performance of All-Solid-State Sodium-Ion Model Cells with Crystalline Na_xCoO_2 Thin-Film Cathodes, 166 (2019) A5328–A5332. https://doi.org/10.1149/2.0491903jes.

[189] P. Mandal, Anomalous transport properties of Co-site impurity doped NaxCoO2, Journal of Applied Physics. 104 (2008). https://doi.org/10.1063/1.2978212.

[190] M. Ogata, A new triangular system: Na_xCoO_2, Journal of Physics: Condensed Matter. 19 (2007) 145282–145282.doi.org/10.1088/0953-8984/19/14/145282.

[191] P. Roy and S. K. Srivastava, *Nanomaterials for Electrochemical Energy Storage Devices*. John Wiley & Sons, 2019. Accessed: Sep. 12, 2022. [Online]. Available: https://books.google.com/books?hl=en&lr=&id=ubG2DwAAQBAJ&oi=fnd&pg=PA377&dq=Jan+et+al.

[192] C. Popescu, L. Pinsard-Gaudart, N. Dragoe, Pressure effect and Mn doping in Na_xCoO_2, Journ. of App. Physics. 112 (2012) 053503. doi.org/10.1063/1.4747908.

[193] J.J. Ding, Y.N. Zhou, Q. Sun, X.Q. Yu, X.Q. Yang, Z.W. Fu, Electrochemical properties of P2-phase $Na_{0.74}CoO_2$ compounds as cathode material for rechargeable sodium-

ion batteries, Electrochimica Acta. 87 (2013) 388–393. https://doi.org/10.1016/j.electacta.2012.09.058.

[194] L.W. Shacklette, T. Richard Jow, L.W. Townsend, Rechargeable Electrodes from Sodium Cobalt Bronzes, 135 (1988) 2669–2674. doi.org/10.1149/1.2095407.

[195] K. Ishida, Y. Ihara, Y. Maeno, C. Michioka, M. Kato, K. Yoshimura, K. Takada, T. Sasaki, H. Sakurai, E. Takayama-Muromachi, Unconventional Superconductivity and Nearly Ferromagnetic Spin Fluctuations in $Na_xCoO_2·yH_2O$, Journal of the Physical Society of Japan. 72 (2003) 3041–3044. doi.org/10.1143/jpsj.72.3041.

[196] H.D. Yang, J.-Y. Lin, C.P. Sun, Y.C. Kang, C.L. Huang, K. Takada, T. Sasaki, H. Sakurai, E. Takayama-Muromachi, Evidence of nodal superconductivity in $Na_{0.35}CoO_2·1.3H_2O$: A specific-heat study, Physical Review B. 71 (2005). https://doi.org/10.1103/physrevb.71.020504..

[197] J.W. Lynn, Q. Huang, C.M. Brown, V.L. Miller, M.L. Foo, R.E. Schaak, C.Y. Jones, E.A. Mackey, R.J. Cava, Structure and dynamics of superconducting Na_xCoO_2 hydrate and its unhydrated analogue, Physical Review B. 68 (2003). https://doi.org/10.1103/physrevb.68.214516.

[198] H. Wang, J. Wu, Andrei Dolocan, Y. Li, Xujie Lü, N. Wu, K. Park, S. Xin, M. Lei, W. Yang, J.B. Goodenough, Short O–O separation in layered oxide $Na_{0.67}CoO_2$ enables an ultrafast oxygen evolution reaction, Proceedings of the National Academy of Sciences of the United States of America. 116 (2019) 23473–23479. https://doi.org/10.1073/pnas.1901046116.

[199] L. Li, J. Andrews, R. Mitchell, D. Button, D. C. Sinclair, and I. M. Reaney, "Aqueous Cold Sintering of Li-Based Compounds," *ACS Applied Materials & Interfaces*, vol. 15, no. 16, pp. 20228–20239, Apr. 2023, https://doi.org/10.1021/acsami.3c00392.

[200] J. Andrews, G. Bullock, C.A. Miller, J. Booth, H. Ren, N.L. Kelly, J.V. Hanna, I.M. Reaney, Cold sintering of bioglass and bioglass/polymer composites, 106 (2023) 3396–3409. https://doi.org/10.1111/jace.19022.

[201] D. Wang, J. Chen, G. Wang, Z. Lu, S.-K. Sun, J. Li, J. Jiang, D. Zhou, K. Song, I.M. Reaney, Cold sintered $LiMgPO_4$ based composites for low temperature co-fired ceramic (LTCC) applications, 103 (2020) 6237–6244. doi.org/10.1111/jace.17320.

[202] J.-H. Seo, J. Guo, H. Guo, K. Verlinde, D.S.B. Heidary, R. Rajagopalan, C. A. Randall, Cold sintering of a Li-ion cathode: $LiFePO_4$-composite with high volumetric capacity, Ceram. Int. 43 (2017) 15370–15374,

https://doi.org/ 10.1016/j.ceramint.2017.08.077.

[203] J. Guo, H. Guo, A.L. Baker, M.T. Lanagan, E.R. Kupp, G.L. Messing, C.A. Randall, Cold sintering: a paradigm shifts for processing and integration of ceramics, Angew. Chemie Int. Ed. 55 (2016) 11457–11461, doi.org/10.1002/ ange.201605443.

[204] W. Lee, C.K. Lyon, J. Seo, R. Lopez-Hallman, Y. Leng, C. Wang, M.A. Hickner, C. A. Randall, E.D. Gomez, Ceramic–salt composite electrolytes from cold sintering, Adv. Funct. Mater. 29 (2019) 1807872, https://doi.org/10.1002/ adfm.201807872.

[205] Y. Liu, P. Liu, C. Hu, Low-temperature preparation, and microwave dielectric properties of cold sintered $Li_2Mg_3TiO_6$ nanocrystalline ceramics, Ceram. Int. 44 (2018) 21047–21052, https://doi.org/10.1016/j.ceramint.2018.08.141.

[206] S.S. Faouri, A. Mostaed, J. S.Dean, D. Wang, D. C.Sinclair, S. Zhang, W. G. Whittow, Y. Vardaxoglou, I.M. Reaney, High-quality factor cold sintered Li_2MoO_4 single bond $BaFe_{12}O_{19}$ composites for microwave applications, Acta Mater. 166 (2019) 202–207, https://doi.org/10.1016/j.actamat.2018.12.057.

[207] D. Wang, D. Zhou, S. Zhang, Y. Vardaxoglou, W.G. Whittow, D. Cadman, I. M. Reaney, Cold- sintered temperature stable $Na_{0.5}Bi_{0.5}MoO_4$–Li_2MoO_4 microwave composite ceramics, ACS Sustain. Chem. Eng. 6 (2018) 2438–2444, https://doi.org/10.1021/acssuschemeng.7b03889.

[208] H.Q. Huang, J. Tang, J. Liu, Preparation of $Na_{0.5}Bi_{0.5}TiO_3$ ceramics by hydrothermal-assisted cold sintering, Ceram. Int. 45 (2019) 6753–6758, https:// doi.org/10.1016/j.ceramint.2018.12.166.

[209] W.B. Hong, L. Li, M. Cao, X.M. Chen, Plastic deformation, and effects of water in room temperature cold sintering of NaCl microwave dielectric ceramics, J. Am. Ceram. Soc. 101 (2018) 4038–4043, https://doi.org/10.1111/jace.15572.

[210] D. Wang, S. Zhang, D. Zhou, K. Song, A. Feteira, Y. Vardaxoglou, W. Whittow, D. Cadman, I.M. Reaney, Temperature stable cold sintered $(Bi_{0.95}Li_{0.05})$ $(V_{0.9}Mo_{0.1})O_4$-$Na_2Mo_2O_7$ microwave dielectric composites, Materials 12 (2019) 1370, https://doi.org/10.3390/ma12091370.

[211] H. Guo, A. Baker, J. Guo, C.A. Randall, Cold sintering process: a novel technique for low- temperature ceramic processing of ferroelectrics, J. Am. Ceram. Soc. 99 (2016) 3489–3507, https://doi.org/10.1111/jace.14554.

[212] Q. Yu, L.C. Zhu Jianga, T. Lu, B. Suleiman, G. Leng, Z. Wu, Y. Ding, Y. Li, A novel low-temperature fabrication approach of composite phase change materials for high

temperature thermal energy storage, Appl. Energy 237 (2019) 367–377, https://doi.org/10.1016/j.apenergy.2018.12.072.

[213] J.G.P. da Silva, M. Bram, A.M. Laptev, J. Gonzalez-Julian, Q. Ma, F. Tietz, O. Guillon, sintering of a sodium-based NASICON electrolyte: a comparative study between cold, field-assisted and conventional sintering methods, J. Eur. Ceram. Soc. 39 (2019) 2697–2702, https://doi.org/10.1016/j. jeurceramsoc.2019.03.023.

Chapter 3

3.0 Experimental procedures

3.1 Sample preparation

Chemicals and reagents were purchased from NEI corporations, U.S.A. and Sigma Aldrich chemicals, with purity ranging from 98 – 99.5%. Prior to the solid-state and cold-sintering processes, some reagents were dried according to Table 3.1.

Table 3.1.

Reagents source, drying temperature and sample purity.

Reagents/chemicals	Drying Temperature (°C)	Purity (%)	Company
m-ZrO_2	1000	98	Sigma Aldrich
Na_3PO_4	180	99	Sigma Aldrich
SiO_2	-	99	Sigma Aldrich
$Na_{0.7}CoO_2$	-	98.5	NEI Corporations
$Na_{1.3}Al_{0.3}Ti_{1.7}P_3O_{12}$	-	99.2	NEI Corporations

3.1.1 Solid-state preparation of NZSP

To achieve the systematic reduction/elimination of the ZrO_2 impurity phase, m-ZrO_2, SiO_2 and Na_3PO_4 powders were chosen and weighed in accordance with the mole fractions shown in equation 3.1. The new formula, "$Na_3Zr_{2-x}Si_2PO_{12-2x}$", was derived from the existing NZSP formula $Na_{1+x}Zr_2Si_xP_{3-x}O_{12}$ but modified to accommodate the reduction in mole fractions of ZrO_2. The reactants, m-ZrO_2 and Na_3PO_4, were pre-heated according to Table 3.1 to remove gases and hydrates. Stoichiometric amounts of m-ZrO_2, Na_3PO_4 and SiO_2 were batched with a tolerance of ±0.0005 grams according to equation 3.1.

$$(2-x)ZrO_2 + Na_3PO_4 + 2SiO_2 \longrightarrow Na_3Zr_{2-x}Si_2PO_{12-2x} \qquad 3.1$$

Where x represents the mole fractions of the compositional series (0.0, 0.10, 0.20, 0.30, 0.40, 0.50 and 0.60) prepared.

Mixtures were ball milled at 300 rpm for 12 hours using zirconia milling media in isopropanol, then dried at 120 °C for 12 hours according to the preparation method reported by Naqash *et al.*, [2]. The dried mixtures were ground to form a fine powder and heated at 400 °C for 5 hours to remove residue. The powders were pelletised and calcined for 12 hours at 900 °C, forming an NZSP mixture. The NZSP mixture was further ball-milled at 300 rpm for 12 hours and dried, and the powders were pelletised. The NZSP pellets were buried in NZSP powder before being subjected to different sintering temperature studies (1100 - 1250 °C for 6 – 12 hours) with a heating and cooling rate of 5 °C/min. The optimum sintering temperature and time that favours the formation of NZSP and suppresses/minimises the formation of *m*-ZrO_2 and Na_3PO_4 were recorded. Figure 3.1 shows the schematic solid-state process of preparing NZSP.

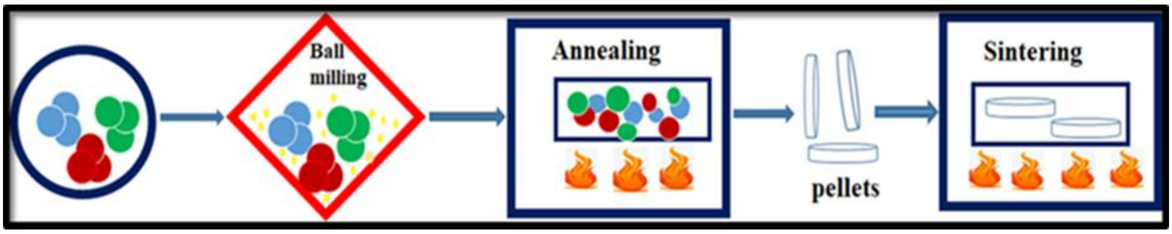

Figure 3.1. Solid-state reaction method of preparing NZSP ceramics.

3.1.2 Cold sintering of Na-ion compounds

0.3g ± 0.0005 of either NZSP, NATP or NCO were weighed and mixed with the suitable solvent in a mortar and pestle. The moist powder was transferred into a 10 mm die and placed in a Specac Uniaxial press fitted with heating platens, as shown in Figure 3.2, to aid densification, re-arrangement, and re-precipitation of the cold sintered Na-ion ceramics. The chemistry of each Na-ion compound determines the types of parameters for cold sintering [1]. Several trials were conducted by varying the transient solvents, temperature, time, pressure, and the amount of solvent (mL) required for an optimum cold sintering condition. Table 3.2 shows the processing condition used for the densification of the Na-ion compounds by cold sintering technique.

Table 3.2.

Cold sintering conditions for Na-ion compounds.

Na-ion compounds (0.3g)	Transient solvents	Solvent amount (wt.%)	Temp. (°C)	Time (Hours)	Pressure (MPa)	Post annealing
NZSP	Distilled H_2O	20 - 30	120	1	120 - 500	Yes
NATP	Distilled H_2O, IPA, 1M NaOH and CH_3COOH	5-10	200	1	375 - 500	Yes
NCO	Distilled H_2O, IPA and 1M NaOH	10-20	150 – 200	0.15 - 1.0	250 - 500	No
NCO	Co (II) acetate, citric acid, and Na acetate.	0.05g	200	1	500	No

3.1.2.1 Preparation strategy for densifying NZSP by cold sintering technique

To obtain the powder required to cold sinter NZSP, conventional pellets of NZSP (1250 °C, 6 hours) were manually crushed and ground to obtain a fine uniform powder. The NZSP powder was then cold sintered according to the strategy discussed in section 3.1.2. Although this solution may not be suitable for scale-up and commercialization, it was considered pragmatic to achieve the project objectives since calcined (900 °C) green NZSP powder cold sintered badly and was poorly crystalline. Typically, powders with the dominant NZSP crystal structure require >1100 °C with high crystalline quality only achieved close to the sintering temperature. Cold-sintered NZSP pellets were also subjected to a post-sintering anneal (400-1250 °C). No commercial NZSP powder could be sourced during the period these experiments were conducted.

3.1.2.2 Densification of NCO and NATP by cold sintering technique

To overcome the setbacks encountered for NZSP in section 3.1.2.1, NCO and NATP powder was sourced from NEI Corporations, U.S.A. The NCO and NATP green powder was further processed by solid-state reaction method to decrease the particle size and densify according to the strategy discussed in section 3.1.2.

Figure 3.2. Cold-sintering press for Na-ion Compounds.

3.1.3 Conventional Sintering

NZSP, NATP and NCO powder were pelletised with a 10 mm steel die using a Specac Uniaxial press. The pellets were placed in an alumina crucible on a platinum foil and heated to the sintering temperatures and time shown in Table 3.3 at a fixed heating and cooling rate of 5 °C/min.

Table 3.3.

Optimum conventional sintering temperatures and time of Na-ion compounds.

Na-ion Compounds	Temperature (°C)	Time (Hours)
NZSP	1250	6
NATP	900	12
NCO	800	12

3.2 Density measurement

The Na-ion compounds' theoretical (ρ_{th}) and experimental densities (ρ_{ex}) were calculated. The theoretical density of the Na-ion compounds was calculated according to equation 3.2a.

$$\rho_{th} = \frac{mZ}{VNA} \qquad 3.2a$$

ρ_{th} is the theoretical density (g/cm^3), *m* is the mass of the Na-ion compound (g/mol), *V* is the volume of the unit cell (cm^3), N_A is the Avogadro's number, and *Z* is the number of formula units per unit cell. The value of Z varies based on the crystal structure of the Na-ion compounds. For monoclinic $Na_3Zr_2Si_2PO_{12}$, *Z* = 4, for rhombohedral $Na_3Zr_2Si_2PO_{12}$ Z = 6, for hexagonal $Na_{0.7}CoO_2$, Z = 6 and orthorhombic $Na_{1.3}Al_{0.3}Ti_{1.7}P_3O_{12}$, Z = 4. The lattice parameter of Na-ion compounds is calculated from the X-ray diffraction pattern by applying Bragg's equation 3.2b.

$$2d\sin\theta = n\lambda \qquad 3.2b$$

λ is the wavelength of the incident radiation, θ is Bragg's angle, *n* is the reflection order (integer number), and *d* is the separating distance between two lattice points (d - spacing).

For monoclinic $Na_{1+x}Zr_2Si_xP_{3-x}O_{12}$, the d-spacings are calculated from the lattice parameter in equation 3.3.

$$d^2 = \frac{h^2}{a^2 sin^2\beta} + \frac{k^2}{b^2} + \frac{l^2}{c^2 sin^2\beta} - \frac{2hlcos\beta}{acsin^2\beta} \qquad 3.3$$

For hexagonal $Na_{0.7}CoO_2$, the d-spacings are calculated from the lattice parameter in equation 3.4.

$$d^2 = \frac{3a^2}{4(h^2 + hk + k^2)} + \frac{c^2}{l^2} \qquad 3.4$$

For orthorhombic $Na_{1.3}Al_{0.3}Ti_{1.7}P_3O_{12}$, the d-spacing can be calculated from the lattice parameter in equation 3.5.

$$d^2 = \frac{a^2}{h^2} + \frac{b^2}{k^2} + \frac{c^2}{l^2} \qquad 3.5$$

a, b, and c are the lattice parameters, and *hkl* are the Miller Indices of the Na-ion crystals. The ρ_{th} can also be obtained directly from the International Centre for Diffraction Data (ICDD) database, X-ray refinement data and literature.

i. The ρ_{th} of $Na_3Zr_2(SiO_4)_2(PO_4)$ = 3.24 g/cm^3 [2-4].
ii. The ρ_{th} of $Na_{1.3}Al_{0.3}Ti_{1.7}PO_{12}$ = 2.97 g/cm^3 [5].
iii. The ρ_{th} of $Na_{0.7}CoO_2$ = 4.74 g/cm^3 [6, 7].

The Na-ion compounds' experimental density (ρ_{ex}) was calculated using the Archimedes principle and geometric method.

- Archimedes’ method (suspending the sample in air and water and measuring the resulting displacement).
- Geometric method (weighing the mass and measuring the diameter and thickness of the pellets).

The Archimedes’ method is suitable for water-insoluble samples, while the geometric method is ideal for water-soluble samples (many cold-sintered samples are partially water-soluble).

3.2.1 Sample Preparation and Measurement

i. Archimedes' method of measurement

The ρ_{ex} of the Na-ion ceramic was measured using the equipment in Figure 3.3. The solvent (water) temperature was first calibrated, and the Na-ion ceramic pellets were calculated according to equation 3.6. The average of three measurements was recorded.

$$\rho_{ex} = \frac{\text{Weight of Na–ion ceramic (air)}}{\text{Weight of Na–ion ceramic (air)} - \text{Weight of Na–ion ceramic (water)}} \qquad 3.6$$

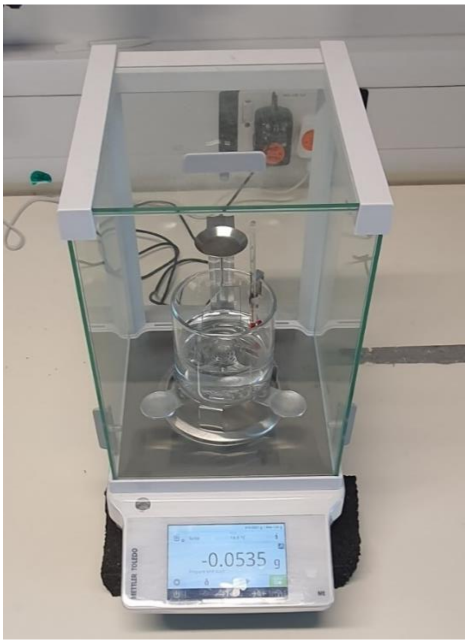

Figure 3.3. Archimedes density measurement.

ii. Geometric measurement

The mass of the Na-ion ceramic pellet was measured by a laboratory balance, and the pellets’ thickness and diameter were measured using a digital Vernier calliper (with a margin of error of ± 0.005 mm). The average of three measurements was recorded, and the ρ_{ex} of the Na-ion compound was calculated according to equation 3.7.

$$\rho_{ex} = \frac{m}{V} \qquad 3.7$$

The relative density (ρ_r) of the Na-ion compounds is calculated according to equation 3.8.

$$\rho_r = \frac{\rho_{ex}}{\rho_{th}} \text{ x } 100 \qquad 3.8$$

3.3 X-ray diffraction (XRD)

X-ray diffraction is a technique that uses the scattering of X-rays by a crystal lattice to determine a material's structure and phase composition. The incidence radiation interacts with the crystal lattice of a crystalline material according to Bragg's equation (3.4) [8]. Once Bragg's law is satisfied, reflections are detected with periodic intensities proportional to the crystal lattice spacing, Figure 3.4.

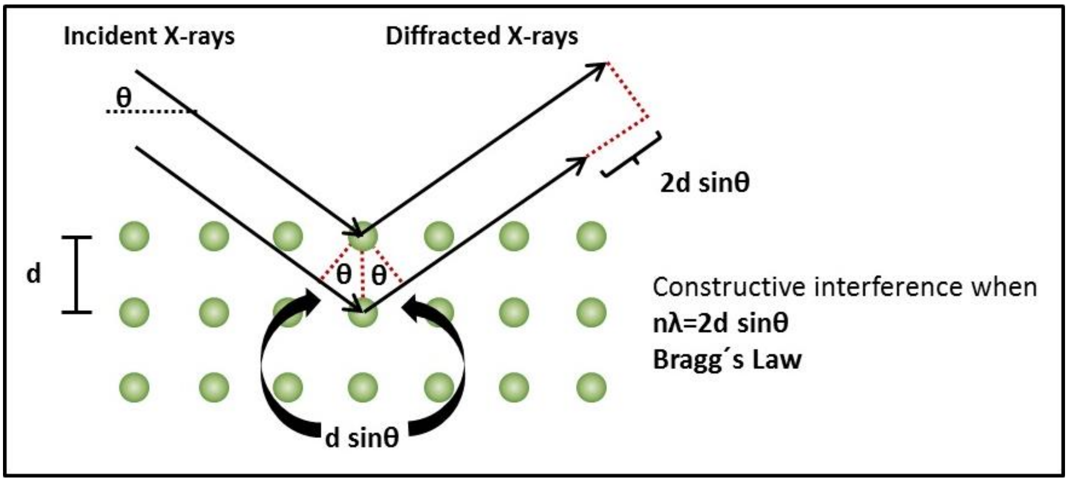

Figure 3.4. Schematic of the incident and diffracted X-ray radiation [9].

3.3.1 Sample Preparation and Measurement

The phase identification of the Na-ion compounds was carried out using a PANalytical Aeris X-ray diffractometer in the 2θ range of 10 – 100° with a step size of 0.02° and Cu Kα radiation of 1.5418Å. The PANalytical Aeris X-ray diffractometer uses an automated technique to gather information faster with high exactness and accuracy, and up to six samples can be prepared and queued simultaneously for measurement, reducing the waiting time, Figure 3.5.

The sample holders were first cleaned using isopropanol ($CH_3OHCHCH_3$), ensuring no residue was left from the previous users. The ceramic pellets were crushed and ground into a fine powder, and about 10 – 20 mg of the Na-ion compound powder was placed in a sample holder and pressed to obtain a smooth surface. The PANalytical Aeris x-ray diffractometer parameters are fixed (Cu Kα radiation = 1.5418 Å, step size = 0.02), making it easy to use. Data were collected on a flashcard and transferred to the ICDD PDF-4+ software for phase identification and analyses. Table 3.4 shows the diffraction data from the Na-ion compounds, precursors, and secondary phases.

Phase refinement was performed on the diffraction data of NZSP (x = 0.0 and 0.60) using Topas 5 software, which uses the principle of the Rietveld method. The Rietveld method uses the least squares refinement procedure to fit powdered X-ray diffraction data. Topas 5 refinement software allows for the determination of crystal structure, lattice parameters and phase quantification. It refined the structure of a material against the observed powder diffraction pattern by considering the instrumentation parameters and background correction.

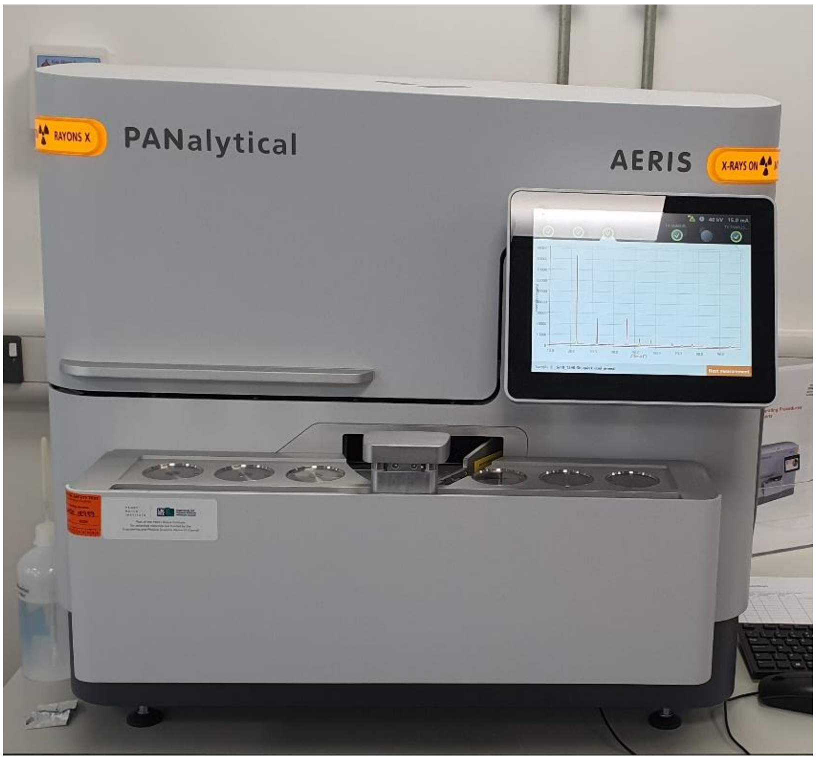

Figure 3.5. PANalytical Aeris X-ray diffractometer.

Table 3.4.

Diffraction patterns of the Na-ion compounds and precursors.

Diffraction Pattern	PDF card
M-$Na_3Zr_2Si_2PO_{12}$	00-035-0412
R-$Na_3Zr_2Si_2PO_{12}$	01-076-1449
m-ZrO_2	01-065-0728
$Na_{0.7}CoO_2$	00-078-2822
$Na_{1.3}Al_{0.3}Ti_{1.7}P_3O_{12}$	04-011-7800
$AlPO_4$	00-011-0500

3.3.2 Limitations of the X-ray technique

There are several limitations to using X-ray diffraction to characterise materials [10-12]:

i. The sample needs to be prepared in a finely powdered form, which can be time-consuming and may require additional grinding or milling, leading to potential grain alignment or orientation problems [11].
ii. XRD is primarily useful for analysing crystalline materials. Due to the lack of well-defined diffraction peaks, it may not provide accurate results for amorphous or poorly crystalline materials [10].
iii. XRD provides information about the near-surface structure of a material, typically up to a few micrometres. It cannot probe deeper into the bulk of the material [12].
iv. The interpretation of XRD patterns can be complex. Identifying and distinguishing between phases, crystal structures, and lattice parameters can be challenging, especially in overlapping diffraction peaks.
v. Certain materials may be reactive or incompatible with X-ray radiation, which limits their suitability for XRD analysis. Additionally, materials that exhibit strong X-ray absorption or fluorescence can generate background noise or spectral artefacts, which may interfere with the diffraction pattern.

3.4 Particle size measurement

The Malvern Mastersizer 3000 is a device that measures the particle size distribution of powdered material such as Na-ion compounds using laser technology, Figure 3.6. The Mastersizer uses a laser beam of light scattered through the powder suspension at various angles and intensities during the measurement. Samples can be measured using the hydro-dispersion or powder-dispersion methods. The latter requires a high quantity of powdered samples with good surface tension, while the hydro-dispersion method requires a few milligrams of the powdered sample [13].

3.4.1 Sample Preparation and Measurement

The process does not require an intensive sample preparation stage except for the Na-ion compounds to be a fine powder. Prior to the measurement, the Mastersizer was cleaned thoroughly with water (H_2O) to remove agglomerated particles left by previous users. The laser energy obscuration range was varied between 5 – 10 % to ensure accurate and reliable particle size analysis. The background and sample measurement duration were 30 and 10 seconds, respectively. The stirrer speed was 2000 rpm during the operation, and the background stability timeout was 5 minutes. About 5 -10 mg of the Na-ion compound powder was dispersed in water up to the obscuration range before measurements were taken. A higher quantity of Na-ion powder beyond the obscuration range could cause agglomeration, foaming, bubbles, and inaccurate results. A lower amount of Na-ion powder below the obscuration limit will not produce any reading. The particle size distribution was recorded on the monitor and the data analysis.

Figure 3.6. The Malvern Mastersizer 3000 particle analyser with a hydro system.

3.4.2 Limitations of the Particle Size Analyser

The Malvern Mastersizer particle analyser has the following limitations [13-14]:

i. The Mastersizer can measure particles between 0.01 and 3500 µm, making it unsuitable for nano-powders and larger particles.
ii. The accuracy and precision of the particle analyser can be impacted by the sample quantity and effectiveness of the dispersant. Too many powders above the obscuration limit may cause inaccurate size distribution results [13].
iii. High concentrations of fines or agglomerated powder may present analysis challenges with inaccurate measurement.
iv. The Mastersizer assumes spherical particles for size distribution measurement. Accuracy is compromised with non-spherical particles, such as fibres or irregular shapes [14].
v. The accuracy of particle size analysis depends on proper instrument calibration to ensure accurate results.

3.5 Scanning Electron Microscopy

Scanning Electron Microscopy (SEM) is useful in providing comprehensive information about a sample's morphology, topography, and elemental composition. The process involves scanning a focused beam of electrons across the sample surface, generating primarily secondary electrons, backscattered electrons and characteristic X-rays, which are collected by the appropriate detector and used to form an image or obtain compositional analysis [15].

3.5.1 Sample Preparation and Measurements.

The FEI Inspect F and F50 Scanning electron microscopy were used to examine $Na_{1.3}Al_{0.3}Ti_{1.7}P_3O_{12}$, $Na_3Zr_{2-x}Si_2PO_{12-2x}$ and $Na_{0.7}CoO_2$ morphology, topography, and elemental composition. Due to the reactivity and sensitivity of the Na-ion compounds with water, fractured surfaces of some sintered ceramics were investigated. The polished and/or fractured surface of the sintered pellets was mounted on an aluminium stub and sputtered with ~5 nm carbon to make the surface conduct and to avoid beam charging. The polished/fractured conducting pellets were placed in the SEM. The chamber pressure < 5.00×10^{-5} bar with an accelerating voltage between 10 - 15 kV, spot size 3.0 – 4.0. The spot size refers to the size of the electron beam that is used to scan the surface of a sample or the area over which the electron beam is focused on the sample. When the spot size is smaller, the beam is focused on smaller features on the sample surface, resulting in higher resolution. Conversely, a larger spot size produces a lower resolution but gives a better signal-to-noise ratio and benefits studies of surface topography and elemental mapping. A working distance of ≤ 10 mm was typically used. The images generated from the microscopy were further analysed by the line intercept method for grain size determination.

EDS enabled the identification and quantification of elemental composition in the NCO sample. EDS measurement was performed on cold-sintered NCO ceramic with an accelerating voltage of 15.0 to 20.0 kV to increase the penetration depth, improve signal-to-noise ratio, and enhance spectral resolution and sensitivity. Back-scattering mode with a spot size of 3.5 - 4.0 and the same working distance as SE imaging was used to quantify the density or weight-averaged atomic number contrast images to help identify secondary phases.

The Inspect F and F50 were equipped with an EDAX energy dispersive X-ray detector and GENESIS spectrum software, which detect the elemental composition and mapping in the ceramic, respectively. A schematic of a scanning electron microscope is shown in Figure 3.7, illustrating the location of the detectors (X-ray, BSE and SE), coils and the electron gun within the column.

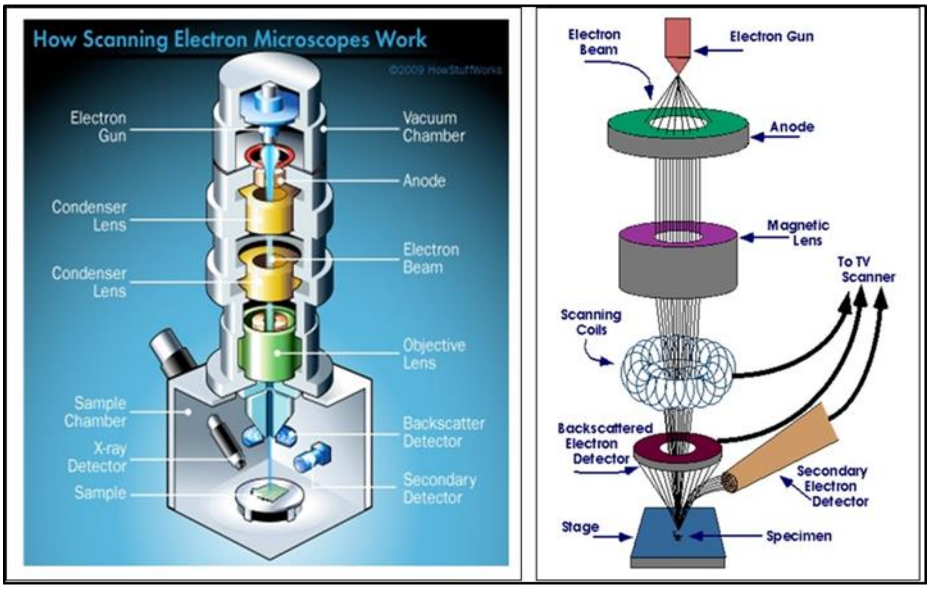

Figure 3.7. Schematic of a Scanning electron microscopy [15].

3.5.2 Limitations of the Scanning Electron Microscopy

Despite the high-resolution imaging and elemental analysis offered by SEM, there are several limitations associated with the use of the equipment [16-17]:

i. Sample preparation for SEM often involves meticulous cleaning, mounting, and coating with a conductive material. Sample damage can occur during the preparation, affecting the integrity of the sample or introducing artefacts.
ii. The high-energy electron beam used in SEM can cause sample damage for sensitive materials such as polymers or biological samples [16].
iii. Samples should have a flat surface, as the SEM images only show the specimen's topography. Samples that are irregular, highly rough, or have complex geometries may present poor imaging. SEM provides topographical information about the sample surface but cannot reveal internal structures like TEM.
iv. Charge build-up on non-conductive samples can lead to image distortions and artefacts. Conductive coatings like low-voltage imaging or charge neutralisation mitigate this effect [17].

3.6 Dilatometry

Dilatometry is a thermo-analytical technique used to determine the shrinkage or expansion of a material (ceramics, metals, composites, or polymers) caused by a chemical or physical process at a controlled temperature. The technique accurately predicts information about the thermal behaviour, glass transition temperature, phase transition, density change, additives influence, and sintering kinetics of a material [18].

3.6.1 Sample Preparation and Measurement

Green powder of the Na-ion compounds (NZSP and NATP) was pressed into a cylindrical shape of ~ 25 mm diameter and ≤ 12 mm high. Both ends of the sample were polished and carefully placed in an alumina crucible sample carrier. Alumina crucibles are used as the sample holder because it has a higher melting point and does not react with the ceramic material. During operation, the crucible is placed in the homogenous temperature zone of the furnace, and the furnace is heated according to the pre-selected temperature, Figure 3.8. The furnace temperature ranges from 25 to 1600 °C with a resolution between 0.1 – 1 nm. The sample temperature is controlled through a thermocouple, which measures the change in length of the (NZSP and NATP) samples.

The sample carrier and pushrod were calibrated to a change in the sample size, and the sum of the length changes was measured and recorded according to the sample pushrod and carrier. The pushrod then transmits the changes mechanically to the electro-optical displacement system, and the results are displayed on the monitor. The volume change behaviour of the ceramic was recorded at a fixed heating/cooling rate of 10 °C/min.

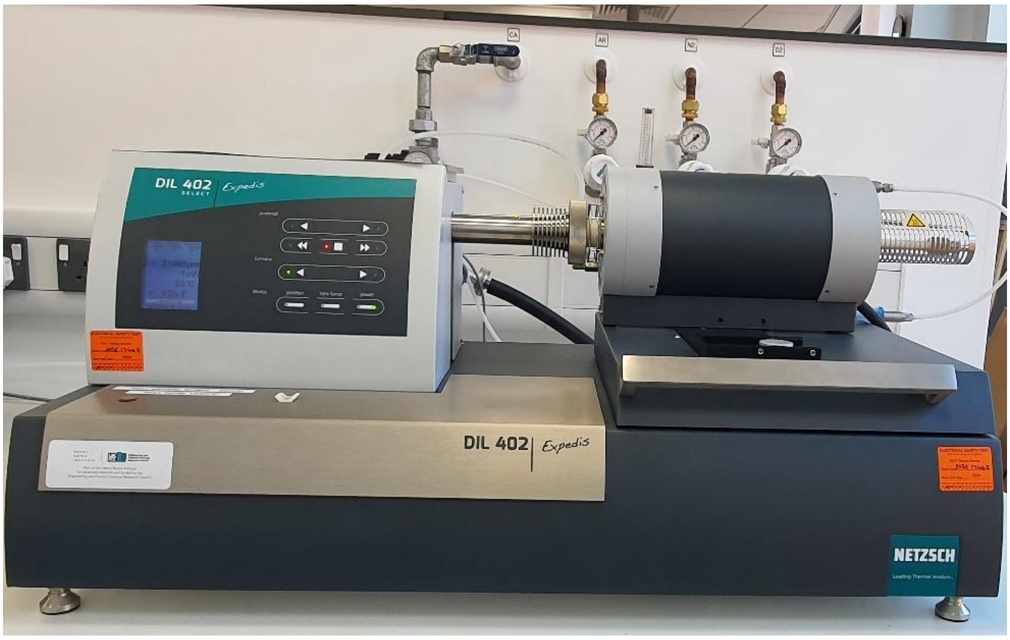

Figure 3.8. A dilatometer attached to the gas pipes.

3.6.2 Limitations of a dilatometry technique

Limitations of the dilatometer include:

i. Dilatometers often have a limited temperature range for accurately measuring the expansion or contraction of a material, which can restrict their applicability to materials with specific temperature characteristics.

ii. They are primarily designed to measure the expansion or contraction of solids. They are not suitable for measuring liquids or gases [19].

iii. The sample size and shape can affect the measurements' accuracy. Irregularly shaped or small samples may pose challenges in getting accurate results.

iv. Accurate measurements require proper thermal contact between the sample and the dilatometer to avoid errors caused by air gaps or insufficient thermal contact [20].

v. Dilatometers are specifically designed to measure the thermal expansion or contraction of materials. They may not be suitable for measuring dimensional changes such as those due to mechanical stress or phase transitions.

3.7 Raman Spectroscopy

Raman spectroscopy is an effective analytical method that examines the vibrational modes of a material. The technique offers valuable insights into a material's molecular structure, chemical composition, and physical characteristics by studying the inelastic scattering of light. [21]. The phenomenon was discovered in 1928 by Sir C. V. Raman. The sample preparation for Raman does not require detailed or rigorous preparation.

3.7.1 Sample preparation and data acquisition in Raman Spectroscopy

NZSP pellets were polished to have a smooth, levelled surface. The smooth surface pellet was mounted on the Apiezon putty, and a glass slide was gently pressed on top of the pellet to secure it firmly. For ZrO_2 powder, a small amount was placed between two glass slides, which were gently squeezed together to obtain a smooth powder. Data acquisition was obtained by placing the sample in the microscope objective lens, and the stage height was raised to 0.5mm for the 50x objective focus lens. The lens focus was adjusted between 5x, 20x and 50x objectives with varying stage heights for better imaging. Prior to the sample preparation stage, the Raman Renishaw inVia microscope was switched on from the laser box, and a 20-second wait time was required for the laser to come off the standby mode. The laser power was set to 20 mW on the remote interface unit, and a 5-minute wait time was essential for the green (514.5 nm) laser to warm up. The instrument calibration was run with the green laser, the WiRE software 3.4 data measurement was selected on the computer monitor, and the laser shutter was opened. On the monitor, the range tab was set between (low limit) 50 – 4000 cm^{-1} (high limit) and the acquisition tab was set to 100 % for ceramics (NZSP) and between 1-10 % for powder (ZrO_2). A minimum of 10-second laser exposure time was irradiated on the sample before the measurement was taken. Spectra acquisition was collected on the monitor, and results were copied on a flash drive for further image processing. Figure 3.9 shows a Renishaw inVia Raman spectroscopy.

Figure 3.9. A Renishaw inVia Raman spectroscopy.

3.7.2 Limitations of the Raman Spectroscopy

The following limitations are encountered for Raman spectroscopy [22-25]:

i. Raman spectroscopy requires samples to be in a solid or powdered state, which may require preparation techniques such as drying, grinding, or dilution. Sometimes, sample preparation can alter the sample's composition or structure, leading to inconsistent results [22-23].

ii. Raman spectroscopy is a technique that uses laser light to interact with a sample, which can result in local heating. However, this heating can sometimes create issues with heat-sensitive materials or biological samples, as it may cause changes in the sample that can affect the Raman spectrum [24].

iii. Raman spectroscopy typically requires higher concentrations and longer acquisition times than other spectroscopic techniques [22].

iv. Raman spectroscopy can be challenging due to fluorescence, a prevalent problem in spectroscopy. The intense fluorescence glow frequently overshadows the Raman signal, making it difficult to read the spectrum accurately. [25].

v. Raman spectroscopy can only probe a few μm into the sample due to its surface-sensitive nature. This limits the analysis of samples with complex structures or layered materials, as deeper layers cannot be probed.

3.8 Fourier Transform Infrared Spectroscopy

Fourier Transform Infrared Spectroscopy (FTIR) is used to analyse both qualitative and quantitative infra-red active regions of crystalline and non-crystalline compounds. The method is cheap and fast for analysing organic, inorganic, and liquid materials. An appropriate IR source and detection method are necessary to obtain a compound's best-infrared spectra and analyses are on a scale of microns [26–29].

3.8.1 Sample Preparation and Measurements

About 0.2 - 0.3g of potassium bromide (KBr) was added to about 0.005g NZSP powder, and the mixture was ground in a mortar to form a finely homogenous mixture. The KBr was stored in an oven due to its hygroscopic nature, and the powdered KBr was transferred quickly to reduce atmospheric reaction. Two stainless steel discs were placed in a pre-cut cardboard. On top of the first disc, the cut-out hole was filled with the finely ground powder mixture and the second steel disk was placed on it and pressed with a hydraulic press. The hydraulic press was pumped and left for a few seconds before the pressure was released, and the discs were pulled apart. The thin, homogenous, transparent NZSP - KBr disc film was gently removed and inserted into the IR sample holder, and the spectrum was run. The NZSP - KBr sample disc was positioned in a holder in the path of the IR source, and the IR beam passed through a partially silvered mirror, dividing it into two equal-intensity beams. A detector reads the signal and converts it into a spectrum, which is then analysed by a computer to identify the peaks. A schematic diagram of an FTIR spectroscopy is shown in Figure 3.10.

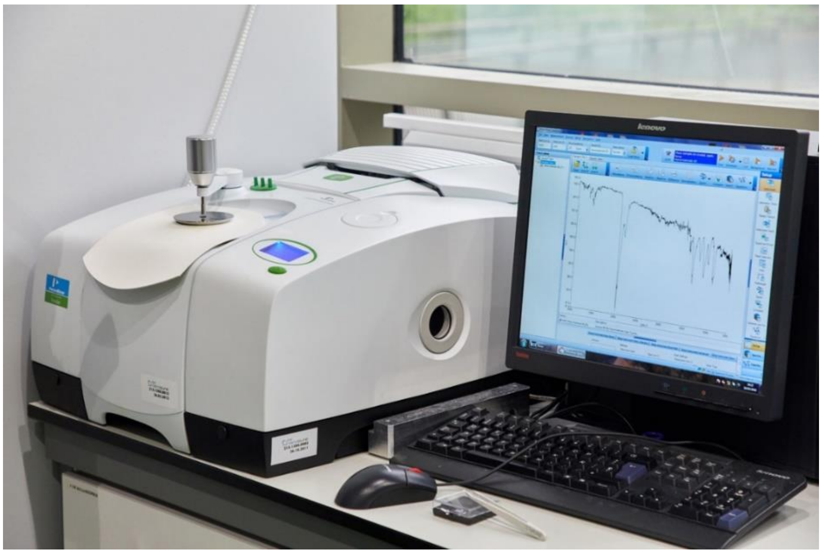

Figure 3.10. Fourier Transform Infra-Red Spectroscopy.

3.8.2 Limitations of the FTIR Spectroscopy

There are several limitations of Fourier Transform Infrared Spectroscopy, which include:

i. FTIR requires the sample to be transparent, such as a thin film or a liquid solution. This can be time-consuming and may require additional steps for sample preparation [31].
ii. FTIR is more suitable for analysing compounds with strong infrared absorbance while ineffective for those with low or no absorbance in the infra-red region.
iii. FTIR spectra can be complicated, particularly for mixtures or samples with multiple components, making it difficult to identify and quantify compounds [32].
iv. FTIR measurements can be sensitive to sample thickness. Non-uniform thickness can affect accuracy and reproducibility.

3.9 SQUID Magnetometer

Superconducting Quantum Interference Device (SQUID) is a sensitive magnetometer that detects magnetic fields using superconducting loops containing Josephson junctions. SQUID has an energy sensitivity value higher than other semiconductor devices like FET. The total magnetic moment of the material is measured by the extraction technique using a field produced by passing the sample through pick-up coils. As the sample moves in either direction, the SQUID picks up the signal, and the characteristic curve is recorded once the moment has been determined [38, 39].

3.9.1 Sample Preparation and Measurements.

NCO pellet was ground to a fine powder and loaded into a capsule-like sample holder. The weight of the empty sample holder and the NCO-loaded sample holder was measured on a weighing balance with a tolerance of ±0.005. The difference between the NCO-loaded and empty sample holder was recorded as the weight of the NCO. For the measurement, a blank sample holder was first placed in the SQUID magnetometer to record the background signal of the system. The NCO-loaded sample holder was covered with a wad of cotton and closed. The NCO-loaded sample holder was perforated with holes to allow airflow during the magnetic measurement. The sample was gently mounted on the sample stage in the magnetometer and was oriented with respect to the SQUID sensor to obtain an accurate magnetic reading. The sample was well shielded from external magnetic fields, reducing the external magnetic field’s influence on the measurement. The liquid helium coolant chamber in the magnetometer allows the magnetic signal readings to be taken below room temperature. The magnetic signal measurements were taken at various temperatures from 757 K to 2 K. The result was transferred to a flash drive and analysed. To obtain an accurate magnetic response, the background signal previously measured was subtracted from the NCO reading, the results were multiplied by the weight of the NCO earlier estimated, and the magnetic response of the NCO was plotted. Figure 3.11 shows the image of a SQUID magnetometer.

Figure 3.11. A SQUID Magnetometer.

3.9.2 Limitations of SQUID magnetometers

There are a few limitations of a SQUID magnetometer [40-42]:

i. SQUID magnetometers require cooling to extremely low temperatures (typically below 4 Kelvin) to function correctly. This makes them expensive to operate and limits their applicability in specific environments [41].
ii. SQUID magnetometers are large and bulky, making them less suitable for portable or field applications.
iii. SQUID magnetometers must be shielded from external magnetic fields, adding complexity and cost to the measurements [40].

iv. SQUID magnetometers require regular calibration for accurate measurements. Calibration involves applying known magnetic fields of known strengths and directions to the device [42].
v. SQUID magnetometers are expensive compared to other magnetometers due to the need for cryogenic cooling and specialised equipment.

3.10 Transmission Electron Microscopy

Transmission Electron Microscopy (TEM) is a technique used to probe the internal structure of a material. A beam of electrons is used to acquire detailed information and images at the atomic and molecular level regarding the composition and structure of materials. TEM can easily detect information about a material's crystal structure, atomic arrangement, phase compositions and defects. Detailed sample preparation is essential in TEM to achieve high-quality images [43].

3.10.1 Sample Preparation and Measurements

NCO samples were prepared by mechanically polishing the conventional sintered pellets followed by dimpling and ion-thinning until perforation or by dispersing powders on lacey-carbon coated support grids. Mechanical thinning of the conventional sintered NCO samples, which exhibited low densities and crumbled under pressure, proved challenging. Therefore, the conventional sintered NCO ceramics were embedded in brass for mechanical stability prior to sectioning and polishing, following the technique described in [44]. Ion thinning was accomplished using the Gatan Precision Ion Polishing System (PIPS) II, operated at 4.5 kV with the samples kept at 100 °C.

Electron diffraction and imaging experiments were performed in a Titan (S)TEM (Thermo Fischer) operated at 300 kV and equipped with a OneView (Gatan) camera.

Electron energy loss (EELS) and X-ray energy dispersive spectra were recorded in another Titan (S)TEM operated at 300 kV, featuring an aberration-corrected and monochromated probe. The spectra were collected in STEM mode. For EELS, the collection angle of the spectrometer was 13.5 mrad, and the convergence of the electron beam was 23 mrad, yielding a sub-nm probe; the spectra were recorded using the dispersion of 0.2 eV/channel. The same convergence angle was used for collecting EDS data. EDS and EELS spectra were processed and analysed in the HyperSpy and Digital Micrograph software.

The Cliff-Lorimer method was used to determine the elemental concentrations from EDS intensities. Background-subtracted core-loss EELS spectra were corrected for plural scattering according to the Fourier-ratio deconvolution method. The Co L_3/L_2 white-line intensity ratio was determined following the procedure outlined by [43-45] and implemented in a Digital Micrograph script. $CoNb_2O_6$, Co_3O_4, and $CoSi_2$ were used as references for Co^{2+}, Co^{2+}/Co^{3+} (1:2 ratio), and Co^{4+} oxidation states, respectively. A Schematic of a TEM is shown in Figure 3.12, which illustrates the basic components used in the formation of images and diffraction patterns (in the back focal plane). Modern instruments often contain aberration correction coils and spectrometers to record Electron Energy loss and Energy Dispersive X-ray spectra.

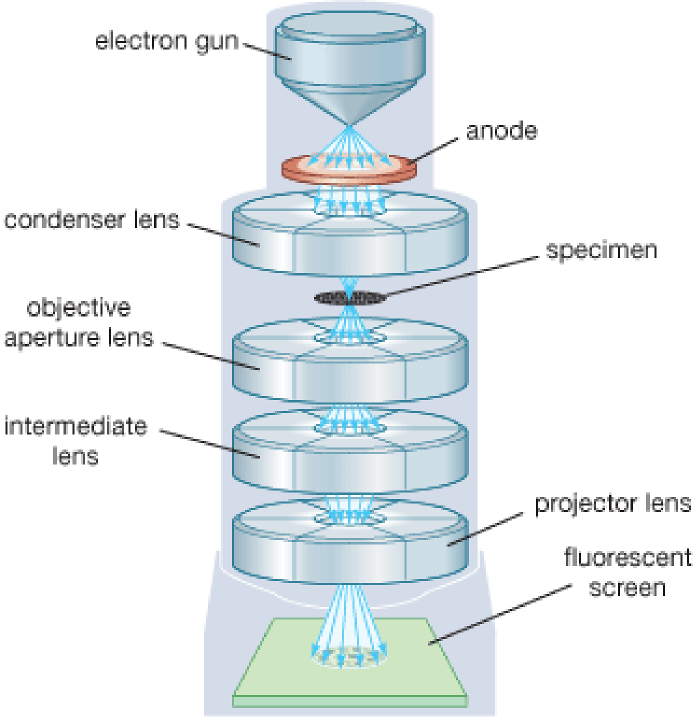

Figure 3.12. Schematics of transmission electron microscopy [44].

3.10.2 Limitations of the TEM

i. Preparing TEM samples requires meticulous skills and techniques, including cutting, thinning, and coating the specimens. The process can be time-consuming and may introduce artefacts or damage to the sample [46].

ii. The high-energy electron beam used in TEM can cause damage to the sample, such as radiation damage, electron beam-induced specimen decomposition, or charging effects. This can limit the time that the sample can be observed or affect the interpretation of the results.
iii. TEM is a sophisticated and expensive instrument requiring specialised training and maintenance. The equipment's cost and operation are limitations for many laboratories [47].
iv. TEM typically requires a vacuum to prevent electron scattering and provide a clear image. This limits the types of samples that can be analysed and may not be suitable for studying samples sensitive to vacuum conditions or in situ phenomena [48].
v. TEM is an excellent tool for studying the physical structure and shape of materials. However, it may not be the best choice for identifying particular elements in the sample or performing chemical analysis. For obtaining chemical information, one can use energy-dispersive X-ray spectroscopy (EDS) or electron energy loss spectroscopy (EELS), but these methods require specialised equipment and additional sample preparation [46].

3.11 Impedance Spectroscopy

Impedance spectroscopy is a versatile technique for studying various materials, phenomena, and devices. It is used to extract resistance and capacitance values as a function of temperature and other variables, e.g. pO_2, dc bias, and time. It is suitable for studying the interfacial properties of a conducting material. An Impedance spectroscope can simplify the total resistance (R_{dc}) into its components, i.e. it allows the separation and characterisation of different electroactive regions. Also, it is used to determine electrical properties such as resistivity, conductivity, permittivity, modulus, and capacitance depending on frequency and temperature range [33].

3.11.1 Electrode Materials

Electrodes need to be applied to the ceramic's surface to measure the resistivity of the solid electrolytes. The choice of alloy is vital to determine the type of conduction (ionic or electronic) present in a sample. Two commonly used alloy types are blocking and non-blocking, which undergo no chemical reaction with the ceramic.

3.11.2 Blocking Electrodes.

A blocking electrode is one in which Faradaic reactions are impossible, so it behaves like an ideal capacitor. The charge carrier in the sample is blocked at the electrode interface. It is helpful for impedance measurement because it simplifies the experiment. Using a blocking electrode means that the behaviour observed experimentally can be attributed to the capacitive behaviour of the double-layer electrodes without the confounding effects of electron-transfer reactions [33].

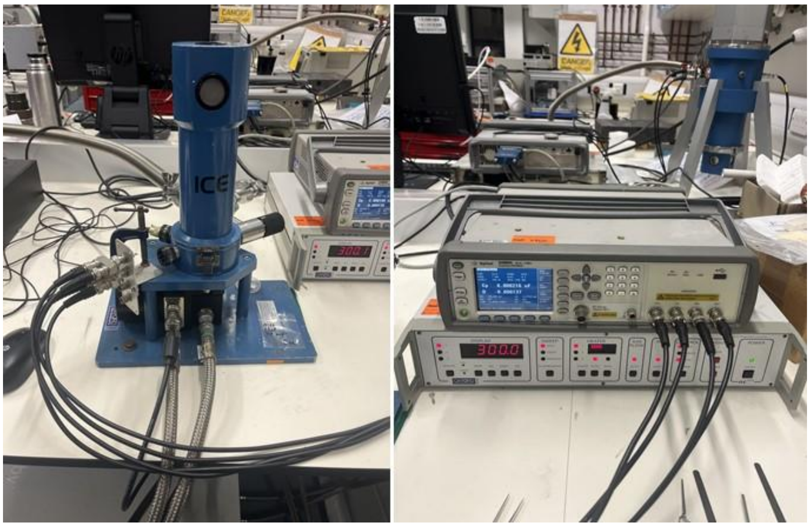

Figure 3.13. Electrochemical Cryocooler Impedance Spectroscopy.

3.11.3 Non-blocking electrodes.

Finding a non-blocking electrode with zero charge transfer resistance at the electrode-electrolyte interface can be challenging. Typically, inert-blocking electrodes like Au and Pt are used due to their capacitive response, which forms a double layer and can be easily identified from the AC response. These non-blocking electrodes can be deposited as thin films, requiring evaporation. Alternatively, they can be applied as an organo-paste on the ceramic, which must be dried and fired at 400-900 °C. However, this method is also time-consuming and may not be used on samples that cannot withstand high firing temperatures. Sometimes, Ag paste is used, which is dried and hardened at RT. However, this method may result in ion exchange between the Ag alloy and the ceramics at elevated temperatures, which could affect the accuracy of the measurements [34].

3.11.4 In-Ga alloy electrode.

In-Ga alloys in liquid form are frequently utilised on cold-sintered ceramic with an electronic conductivity mechanism. They serve as a means of transporting electrons across the interface between the sample and electrode without causing blockages [33]. These electrodes are considered a viable alternative to Pt and Au due to their ease of use, inertness, and efficient blocking response. Furthermore, the In-Ga electrode does not require high-temperature firing once applied to ceramics.

3.11.5 Sample Preparation and Measurements.

Two impedance spectrometers (Agilent 4294A Compression jig and Oxford instrument CCC1104 closed cycle cooler Cryostat) were used to record the electrical properties of the Na-ion compounds in this thesis. The sintered Na-ion pellets were polished gently to obtain a smooth surface, which is ideal for alloy coating. The smooth pellet surface of the Na-ion compounds was sputtered with gold on both sides and annealed at 850 °C for 2 hours, or liquid In-Ga alloy in the case of NCO ceramics without further annealing. The electroded pellets were placed in the conductivity jigs, and readings were taken from RT – 800 °C for the Agilent 4294A compression jig impedance spectroscopy. The jig characterisation consisting of the blank, open circuit capacitance and the closed-circuit resistance was taken to correct the jig's error. For low-temperature measurement, the Oxford instrument CCC1104 closed cycle cooler Cryostat were used to take readings from 140 – 320K, as shown in Figure 3.13. After the impedance measurement, a geometric factor involving the pellet thickness and sample-electrode contact area (surface area normalisation) was performed. Data analysis and circuit fitting were analysed using Zview Software version 2.4 Scribner Associates. Table 3.5 shows the frequency range and measurement accuracy of the impedance spectrometers.

Table 3.5.

Impedance Analyser

Impedance analyser	Frequency range (Hz)	Nominal ac voltage (mV)	Measurement accuracy (± %)
Agilent 4294A	0.04k - 1M	100	0.08
Cryocooler	10m - 1M	100	0.1

The impedance of the Na-ion ceramics was measured over a wide range of frequencies, typically 10^{-2} to 10^{-7} Hz. The in-and-out-phase voltage components across the sample were measured using an alternating voltage and a standard resistor in series. These components were divided by the current's magnitude, giving the impedance's resistive and reactive components. The measurements were repeated as a step-wise function of frequency. Table 3.6 shows the different electroactive regions of a ceramic sample, which are characterised by resistance and capacitance, usually placed in parallel. The product of resistance (R) and capacitance (C) gives the characteristic relaxation time or time constant (τ) for each parallel RC element in equation 3.9.

Table 3.6.

The magnitude of their capacitance identifies electroactive regions.

Origin of the RC Element	Normalised Capacitance (Fcm^{-1})
Electrochemical reaction	10^{-4}
Sample - Electrode interface	10^{-7} - 10^{-5}
Surface layer	10^{-9} - 10^{-7}
Bulk ferroelectric	10^{-10} - 10^{-9}
Grain boundary	10^{-11} - 10^{-8}
Minor second phase	10^{-11}
Bulk/grain boundary	10^{-12}

The electrical microstructure of Na-ion compounds can be analysed using the brickwork model, shown in Figure 3.14.

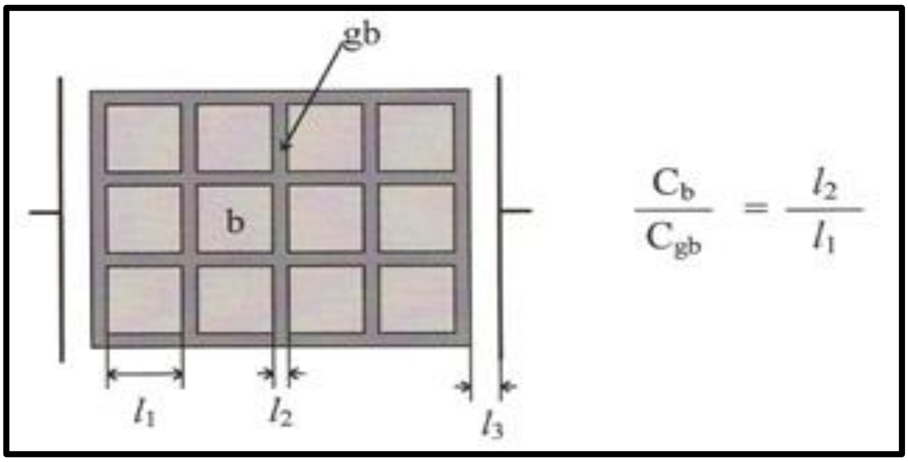

Figure 3.14. The Brickwork layer model shows the thickness of the grains, grain boundaries and sample-electrode interface [33].

$$\tau = RC = \varepsilon_0\varepsilon'/\sigma \qquad 3.9$$

$$C = \varepsilon'\varepsilon_0\frac{A}{l} \qquad 3.10$$

Where $\mathcal{E}_0$ is the permittivity of the free space, $\mathcal{E}'$ is the relative permittivity of the ionic conductor, A is the sample surface area, and l is the thickness of the pellets. τ is a geometry-independent parameter related to the conductivity (σ) and permittivity (ε') of the ceramic. To observe and access the whole spectra of the impedance data, different temperature measurements were performed at various frequencies to understand the electrical properties of the ceramics. Table 3.7 shows the relationship between the impedance data and the other spectroscopic plots.

Table 3.7.

Relation between the four basic Immittance functions

Formalism	Symbol	M	Z	Y	Ɛ
Electric Modulus	M^*	M^*	μZ^*	μY^{*-1}	$\mathcal{E}^{*-1}$
Complex Impedance	Z^*	$\mu^{-1}M^*$	Z^*	Y^{*-1}	$\mu^{-1}\mathcal{E}^*$
Admittance	Y^*	μM^{*-1}	Z^{*-1}	Y^{*-1}	$M^*\mathcal{E}^*$
Complex Capacitance	$\mathcal{E}^*$	M^{*-1}	$\mu^{-1}Z^{*-1}$	$\mu^{-1}Y^*$	$\mathcal{E}^*$

$$\mu = j\omega C_c \qquad 3.11$$

C_c is the capacitance of the empty cell.

Impedance, Z*

$$Z^* = Z' - jZ'' \qquad 3.12$$

Z* is the Impedance, and Z’ and Z” are the real and imaginary components of the complex impedance.

$$Z' = \frac{1}{\omega C_0}\cdot\frac{\varepsilon''}{(\varepsilon'^2+\varepsilon''^2)}; \qquad Z'' = -\frac{1}{\omega C_0}\cdot\frac{\varepsilon'}{(\varepsilon'^2+\varepsilon''^2)} \qquad 3.13$$

Admittance, Y*

$$Y^* = Y' + jY'' \qquad 3.14$$

$$Y^* = \frac{1}{Z^*} = \frac{1}{Z' - jZ''} = \frac{Z' + jZ''}{(Z')^2 + (Z'')^2} \tag{3.15}$$

$$Y' = \frac{Z'}{\left(Z'^2 + Z''^2\right)} \qquad Y'' = -\frac{Z''}{\left(Z'^2 + Z''^2\right)} \tag{3.16}$$

$$Y' = \omega\, C_0 \cdot \varepsilon'' \qquad Y'' = \omega\, C_0 \cdot \varepsilon' \tag{3.17}$$

Electric Modulus, M^*

$$M^* = M' + jM'' \tag{3.18}$$

$$M^* = jwC_0Z^* = j\omega C_0 (Z' - jZ'') = \omega C_0 Z'' + j\omega C_0 Z' \tag{3.19}$$

$$j = \sqrt{-1} \qquad j^2 = -1 \tag{3.20}$$

$$M' = \omega C_0 Z'' \qquad M'' = \omega C_0 Z' \tag{3.21}$$

$$M' = -\frac{\varepsilon'}{\left(\varepsilon'^2 + \varepsilon''^2\right)} \qquad M'' = \frac{\varepsilon''}{\left(\varepsilon'^2 + \varepsilon''^2\right)} \tag{3.22}$$

Permittivity, ε^*

$$\varepsilon^* = \varepsilon' - j\varepsilon'' \tag{3.23}$$

$$\varepsilon^* = [jwC_0Z^*]^{-1} \tag{3.24}$$

$$\varepsilon^* = \frac{1}{M^*} = \frac{1}{M' - jM''} = \frac{Z'' - jZ'}{(Z')^2 + (Z'')^2} \tag{3.25}$$

$$\varepsilon' = -\frac{1}{\omega\, C_0} \cdot \frac{Z''}{\left(Z'^2 + Z''^2\right)} \qquad \varepsilon'' = \frac{1}{\omega\, C_0} \cdot \frac{Z'}{\left(Z'^2 + Z''^2\right)} \tag{3.26}$$

$$\omega_{max} RC = \omega_{max} \tau = 1 \tag{3.27}$$

$$\omega_{max} = 2\pi f_{max} \tag{3.28}$$

$$\sigma = \frac{1}{R} \tag{3.29}$$

ω is the angular frequency, C_0 is the free space capacitance, f_{max} is the maximum frequency, σ is the conductivity, and Y is the Admittance.

3.11.6 Limitations of Impedance Spectroscopy

Some of the limitations of impedance spectroscopy include [34-36]:

1. Electrical contact is crucial for impedance spectroscopy, which can be challenging to achieve and maintain, especially on non-conductive or irregular surfaces [34].
2. Impedance spectroscopy data analysis involves fitting experimental data into mathematical models, making interpretation complex and subjective. The accuracy of the results depends on the choice and validity of the models used [34].
3. Impedance spectroscopy requires specialised equipment and techniques to measure the complex impedance at different frequencies, making it a more challenging technique than simpler measurement methods.
4. The impedance measurement can be affected by artefacts from the electrode and the sample [35].
5. Impedance spectroscopy assumes a uniform and homogeneous system surface, which may not be present in real-world samples, leading to errors in the measurements [36].

3.12 Activation energy (E_a) calculation from the Arrhenius plot

The activation energy E_a (eV) of the Na-ion compounds was calculated according to the Arrhenius equation below [37]. Extrapolation of the variables in equation 3.30 gave the constant (-0.19842), which is used as a multiplier with the gradient to calculate the activation energy of the Na-ion compounds in electron volts (eV). To calculate the gradients of the Arrhenius plot, the conductivity value (bulk, grain boundary and total) of the Na-ion compounds were recorded at different temperatures, and the extrapolation of these values by the standard least square method using Origin software was used to calculate the Activation energy of the Na-ion compounds.

$$\sigma = \sigma_{\circ}\, exp\left[-\frac{E_a}{kT}\right] \qquad 3.30$$

$\sigma: conductivity\ (S/cm)$

$\sigma_{\circ}: pre - exponential\ factor\ (S/cm)$

$E_a: activation\ energy\ (eV)$

$k: Boltzman\ constant\ (8.617343\ x\ 10^{-5}\ eV.K^{-1})$

$T: temperature\ (K)$

From equation (3.30): $\ln \sigma = \ln \sigma_o - \frac{E_a}{kT}$ 3.31

From equation (3.31): $\ln \sigma\ [-\frac{E_a}{1000k}]*[\frac{1000}{T}] + \ln \sigma_o$ 3.32

$$a = [-\frac{E_a}{1000k} * \log e] \quad 3.33$$

$$E_a = -1000k * \frac{1}{\log e} * a \quad 3.34$$

$$E_a(eV) = -0.19842 * a \quad 3.35$$

$a = Gradient\ of\ the\ Arrhenius\ plot.$

Note: The gradient of the Arrhenius plots was calculated by the standard least square method using Origin software. Therefore, the activation energies (E_a) in electron Volts (eV) of the Na-ion compounds are calculated according to equation 3.35.

3.13 Conclusion

A comprehensive study into the preparation methods, characterisation techniques and sintering studies of the Na-ion compound was reported. The solid-state reaction method was discussed for the preparation of NZSP, ensuring control over the chemical composition and homogeneity of the Na-ion compound. Both conventional and cold-sintering methods were investigated for the densification of the Na-ion compounds ($Na_3Zr_{2-x}Si_2PO_{12-2}$, $Na_{1.3}Al_{0.3}Ti_{1.7}P_3O_{12}$ and $Na_{0.7}CoO_2$). Many characterisation techniques such as X-ray diffraction, SEM, TEM, Dilatometry, Raman, FTIR, Archimedes density measurement, Particle size analyser, SQUID magnetometer and Impedance spectroscopy were employed to analyse the Na-ion compounds. Each characterisation technique used specific underlying principles, sample preparation techniques and instrumentation settings to extract meaningful information about the Na-ion compounds. Archimedes' method employed the principle of fluid displacement to quantify the density. SEM, TEM and X-ray utilised electron or X-ray beam interactions with the sample to generate structural and topographical details. Dilatometry involves monitoring dimensional changes as a function of temperature. FTIR and Raman spectroscopy examined light absorption and scattering to probe vibrational modes. SQUID measures the magnetic response as a function of temperature, and Impedance spectroscopy measures the response of electrical properties to frequency variations. Also, the limitations associated with each characterisation technique were discussed.

3.14 References

[1] J. Andrews, D. Button, and I. M. Reaney, "Advances in Cold Sintering: Improving energy consumption and unlocking new potential in component manufacturing," *Johnson Matthey Technology Review*, vol. 64, no. 2, pp. 219–232, Apr. 2020, https://doi.org/10.1595/205651320X15814150061554.

[2] S. Naqash, D. Sebold, F. Tietz, and O. Guillon, "Microstructure-conductivity relationship of $Na_3Zr_2(SiO_4)_2(PO_4)$ ceramics," *Journal of the American Ceramic Society*, vol. 102, no. 3, pp. 1057–1070, Aug. 2018, doi.org/10.1111/jace.15988.

[3] Q. Ma, M. Guin, S. Naqash, C.-L. Tsai, F. Tietz, and O. Guillon, "Scandium-Substituted $Na_3Zr_2(SiO_4)_2(PO_4)$ Prepared by a Solution-Assisted Solid-State Reaction Method as Sodium-Ion Conductors," *Chemistry of Materials*, vol. 28, no. 13, pp. 4821–4828, Jun. 2016, https://doi.org/10.1021/acs.chemmater.6b02059.

[4] M. K. Chong, Z. Zainuddin, F. S. Omar, and M. H. H. Jumali, "$Na_3Zr_2(SiO_4)_2(PO_4)$ solid electrolyte: Influence of milling duration on microstructure and ionic conductivity mechanism," *Ceramics International*, vol. 48, no. 15, pp. 22147–22154, Aug. 2022, https://doi.org/10.1016/j.ceramint.2022.04.202.

[5] M. Dahbi, N. Yabuuchi, K. Kubota, K. Tokiwa, and S. Komaba, "Negative electrodes for Na-ion batteries," *Physical Chemistry Chemical Physics*, vol. 16, no. 29, p. 15007, 2014, https://doi.org/10.1039/c4cp00826j.

[6] R. Richter, D. Shopova, W. Xie, A. Weidenkaff, and F. Lechermann, "Thermopower Enhancement from Engineering the $Na_{0.7}CoO_2$ Interacting Fermiology via Fe Doping," *Advances in Condensed Matter Physics*, vol. 2018, pp. 1–7, 2018, https://doi.org/10.1155/2018/9725321.

[7] S.Y. Li, L. Taillefer, D.G. Hawthorn, M.A. Tanatar, J. Paglione, M. Sutherland, R.W. Hill, C.H. Wang, X.H. Chen, Giant Electron-Electron Scattering in the Fermi-Liquid State of $Na_{0.7}CoO_2$, Physical Review Letters. 93 (2004). doi.org/10.1103/physrevlett.93.056401.

[8] D. D. Le Pevelen, "Small Molecule X-Ray Crystallography, Theory and Workflow" *Encyclopedia of Spectroscopy and Spectrometry*, pp. 2559–2576, 2010, https://doi.org/10.1016/b978-0-12-374413-5.00359-6.

[9] J. Epp, "X-ray diffraction (XRD) techniques for materials characterisation," *Materials Characterisation Using Nondestructive Evaluation (NDE) Methods*, pp. 81–124, 2016, https://doi.org/10.1016/b978-0-08-100040-3.00004-3.

[10] H. Liu, H. Liu, S. H. Lapidus, Y. S. Meng, P. J. Chupas, and K. W. Chapman, “Sensitivity and Limitations of Structures from X-ray and Neutron-Based Diffraction Analyses of Transition Metal Oxide Li-Battery Electrodes,” *Journal of the Electrochemical Society*, vol. 164, no. 9, Jun. 2017, https://doi.org/10.1149/2.0271709jes.

[11] C. Michaelsen, “On the structure and homogeneity of solid solutions: The limits of conventional X-ray diffraction,” *Philosophical Magazine A*, vol. 72, no. 3, pp. 813–828, Sep. 1995, https://doi.org/10.1080/01418619508243802.

[12] P.F. Fewster, The Limits of X-ray Diffraction Theory, Crystals. 13 (2023) 521–521. https://doi.org/10.3390/cryst13030521.

[13] G. Crawley and A. Malcolmson, (2004). Online particle sizing as a route to process optimisation: Consider the potential advantages and design limitations to determine if a switch is right for you. *Chemical Engineering*, *111*(9), 37-42.

[14] I. Callesen, H. Keck, T.J. Andersen, Particle size distribution in soils and marine sediments by laser diffraction using Malvern Mastersizer 2000—method uncertainty including the effect of hydrogen peroxide pre-treatment, Journal of Soil and Sediments. 18 (2018) 2500–2510. doi.org/10.1007/s11368-018-1965-8

[15] H. Kami and L. Ying, “Scanning Electron Microscopy @UNIMAP.” http://emicroscope.blogspot.com/2019/02/hubungi-kami.html

[16] J. M. Ruíz-Vargas, N. Siredey-Schwaller, P. Noyrez, S. Mathieu, P. Bocher, N. Gey, Potential and limitations of microanalysis SEM techniques to characterise borides in brazed Ni-based superalloys, Materials Characterization. 94 (2014) 46–57. doi.org/10.1016/j.matchar.2014.04.009.

[17] J. Arenas-Alatorre, Y. Silva-Velazquez, A. Alva Medina, M. Rivera, Advantages and limitations of OM, SEM, TEM and AFM in the study of ancient decorated pottery, Applied Physics A. 98 (2009) 617–624. doi.org/10.1007/s00339-009-5451-4.

[18] M. Hunkel, H. Surm, & M. Steinbacher, “Dilatometry,” *Recent Advances, Techniques and Applications*, pp. 103–129, 2018, doi.org/10.1016/b978-0-444-64062-8.00019-x.

[19] J. E. Daw, J. L. Rempe, D. L. Knudson, K. G. Condie, and J. C. Crepeau, “Viability of Pushrod Dilatometry Techniques for High-Temperature In-Pile Measurements,” Mar. 2008, https://doi.org/10.2172/926333.

[20] M. Hunkel, H. Surm, M. Steinbacher, Dilatometry, Recent Advances, Techniques & Applications. (2018) 103–129. doi.org/10.1016/b978-0-444-64062-8.00019-x.

[21] N. Emmanuel, R. B. Nair, B. Abraham, and K. Yoosaf, “Fabricating a Low-Cost Raman Spectrometer to Introduce Students to Spectroscopy Basics and Applied Instrument Design,” *Journal of Chemical Education*, vol. 98, no. 6, pp. 2109–2116, May 2021, https://doi.org/10.1021/acs.jchemed.0c01028.

[22] S. Nair, A Review on Raman Rays with respect to Raman Spectroscopy, International Jour of Forensic Sci. 4 (2019).doi.org/10.23880/ijfsc-16000158.

[23] E. Dumont, C. De Bleye, P.-Y. Sacré, L. Netchacovitch, P. Hubert, E. Ziemons, From near-infrared and Raman to surface-enhanced Raman spectroscopy: progress, limitations and perspectives in bioanalysis, Bioanalysis. 8 (2016) 1077–1103. https://doi.org/10.4155/bio-2015-0030.

[24] P.Y. Hou, J. Ager, J. Mougin, A. Galerie, Limitations and Advantages of Raman Spectroscopy for the Determination of Oxidation Stresses, Oxidation of Metals. 75 (2011) 229–245. https://doi.org/10.1007/s11085-011-9235-9.

[25] G. Toscano, S. Raza, S. Xiao, M. Wubs, A.-P. Jauho, S.I. Bozhevolnyi, N.A. Mortensen, Surface-enhanced Raman spectroscopy: nonlocal limitations, Optics Letters. 37 (2012) 2538. https://doi.org/10.1364/ol.37.002538.

[26] E. Capuano & S. M. van Ruth, “Infrared Spectroscopy: Applications,” Encyclopedia *of Food and Health*, pp. 424–431, 2016, doi.org/10.1016/b978-0-12-384947-2.00644-9.

[27] A. Subramanian, V. Prabhakar, and L. Rodriguez-Saona, “Analytical Methods: Infrared Spectroscopy in Dairy Analysis,” *Reference Module in Food Science*, 2016, https://doi.org/10.1016/b978-0-08-100596-5.00602-8.

[28] S. C. Edington, S. Liu, and C. R. Baiz, “Infrared spectroscopy probes ion binding geometries,” *Methods in Enzymology*, pp. 157–191, 2021, https://doi.org/10.1016/bs.mie.2020.12.028.

[29] T. Theophanies, “Introduction to Infrared Spectroscopy,” *Infrared Spectroscopy – Materials Science, Eng. and Technology*, Apr. (2012). doi.org/10.5772/49106

[30] M.A. Mohamed, J. Jaafar, A.F. Ismail, M.H.D. Othman, M.A. Rahman, Fourier Transform Infrared (FTIR) Spectroscopy, Membrane Characterization. (2017) 3–29. https://doi.org/10.1016/b978-0-444-63776-5.00001-2.

[31] M. Öhman, D. Persson, ATR-FTIR Kretschmann spectroscopy for interfacial studies of a hidden aluminium surface coated with a silane film and epoxy II. Analysis by integrated ATR-FTIR and EIS during exposure to electrolyte with complementary

studies by in situ ATR-FTIR and in situ Surface and Interface Analysis. 44 (2011) 105–113. https://doi.org/10.1002/sia.3780.

[32] M.O. Guerrero-Pérez, G.S. Patience, Experimental methods in chemical engineering: Fourier transform infrared spectroscopy—FTIR, The Canadian Journal of Chemical Engineering. 98 (2019) 25–33. doi.org/10.1002/cjce.23664.

[33] J. T. S. Irvine, D. C. Sinclair, and A. R. West, “Electroceramics: Characterisation by Impedance Spectroscopy,” *Advanced Materials*, vol. 2, no. 3, pp. 132–138, Mar. 1990, https://doi.org/10.1002/adma.19900020304.

[34] J.R. Macdonald, Impedance spectroscopy: old problems and new developments, Electrochimica Acta. 35 (1990) 1483–1492. https://doi.org/10.1016/0013-4686(90)80002-6.

[35] J. Hwang, Experimental limitations in impedance spectroscopy: Part IV. Electrode contact effects, Solid State Ionics. 98 (1997) 93–104. doi.org/10.1016/s0167-2738(97)00075-1.

[36] D.D. Edwards, Jin Ha Hwang, S. Ford, T.O. Mason, Experimental limitations in impedance spectroscopy: Part V. Apparatus contributions and corrections, Solid State Ionics. 99 (1997) 85–93. doi.org/10.1016/s0167-2738(97)00206-3.

[37] F. Jensen, Activation energies and the Arrhenius equation, Quality and Reliability Engineering International. 1 (1985) 13–17. doi.org/10.1002/qre.4680010104.

[38] H. Weinstock, A review of SQUID Magnetometry applied to nondestructive evaluation, IEEE Transactions on Magnetics. 27 (1991) 3231–3236. doi.org/10.1109/20.133898.

[39] M. Sawicki, W. Stefanowicz, A. Ney, Sensitive SQUID Magnetometry for studying nano-magnetism, Semiconductor Science and Technology. 26 (2011) 064006. doi.org/10.1088/0268-1242/26/6/064006.

[40] K. Gramm, L. Lundgren, O. Beckman, SQUID Magnetometer for Mangetisation Measurements, Physica Scripta. 13 (1976) 93–95. doi.org/10.1088/0031-8949/13/2/004.

[41] J. Wooldridge, D.M. Paul, G. Balakrishnan, M.R. Lees, Investigation of the spin density wave in Na_xCoO_2, Journal of Physics: Condensed Matter. 17 (2005) 707–718. https://doi.org/10.1088/0953-8984/17/4/013.

[42] D. Prabhakaran, A.T. Boothroyd, R. Coldea, L.M. Helme, D. Alan Tennant, Magnetic Studies of Polycrystalline and Single-Crystal Na_xCoO_2, ArXiv (Cornell University). (2003). https://doi.org/10.48550/arxiv.cond-mat/0312493.

[43] J. Li, T. Malis, S. Dionne, Recent advances in FIB–TEM specimen preparation techniques, Materials Characterization. 57 (2006) 64–70. doi.org/10.1016/j.matchar.2005.12.007.

[44] X. Ke, S. Bals, Ainhoa Romo Negreira, T. Hantschel, H. Bender, Gustaaf Van Tendeloo, TEM sample preparation by FIB for carbon nanotube interconnects, Ultramicroscopy. 109 (2009) 1353–1359. https://doi.org/10.1016/j.ultramic.2009.06.011.

[45] F.A. Stevie, R.B. Irwin, T.L. Shofner, S.R. Brown, J.L. Drown, L.A. Giannuzzi, Plan view TEM sample preparation using the focused ion beam lift-out technique, (1998). https://doi.org/10.1063/1.56881.

[46] X. Ke, C. Bittencourt, G. Van Tendeloo, Possibilities and limitations of advanced transmission electron microscopy for carbon-based nanomaterials, Beilstein Journal of Nanotechnology. 6 (2015) 1541–1557. doi.org/10.3762/bjnano.6.158.

[47] K. Gnanasekaran, R. Snel, G. de With, H. Friedrich, Quantitative nanoscopy: Tackling sampling limitations in (S)TEM imaging of polymers and composites, Ultramicroscopy. 160 (2016) 130–139. doi.org/10.1016/j.ultramic.2015.10.004.

[48] N. Jiang, On the limitation of quantitative measurements using transmission electron microscopy, Journal of Non-Crystalline Solids. 358 (2012) 119–123. https://doi.org/10.1016/j.jnoncrysol.2011.09.004.

Chapter 4

4.1 Characterisation of $Na_3Zr_{2-x}Si_2PO_{12-2x}$ prepared by the solid-state method.

This section discusses the results of the conventionally sintered NZSP series. The data obtained from each characterisation technique of the NZSP (x = 0.0 and 0.60) were compared and contrasted against literature data. The overall aim of this section is to suppress the formation of the *m*-ZrO_2 secondary phase and characterise single-phase NZSP.

4.1.1 X-ray Diffraction

The XRD patterns of $Na_3Zr_{2-x}Si_2PO_{12-2x}$ ($0.0 \leq x \leq 0.6$) sintered at 1250 °C for 6 hours are shown in Figures 4.1.1 and 4.1.2. Prior to choosing these densification conditions, various sintering temperatures (1000, 1100 and 1230 °C) were investigated. The x-ray diffraction patterns of NZSP sintered at different temperatures (1000, 1100 and 1230 °C) are shown in Figure S1 (supplementary section 4.2 of Chapter 4). The diffraction plots in Figure 4.1.1 revealed the impact of decreasing the mole fraction of the ZrO_2 reactant on NZSP. The x-ray diffraction pattern of NZSP (x = 0.0, 0.10, 0.20, 0.30 and 0.40) all exhibited a high percentage of *m*-ZrO_2 impurity phase (* symbol) at 2θ degree value of 24.27 and 28.30, and the patterns are similar to reported data [1-12]. For NZSP (x = 0.50 and 0.60), the *m*-ZrO_2 impurity phase was either suppressed (x = 0.50) or absent (x = 0.60), Figure 4.1.1. Therefore, NZSP (x = 0.60) was selected as our standard, investigated, and compared with NZSP (x = 0.0) and literature data. In Figure 4.1.2, the diffraction patterns of NZSP (x = 0.0 and 0.60) are matched against data files from the International Centre for Diffraction Data (ICDD): *m*-ZrO_2 (PDF N° 00-065-0728) and monoclinic and rhombohedral NZSP (PDF N° 00-035-0412 and 01-076-1449, respectively). Most peaks for NZSP (x = 0.0) matched monoclinic NZSP (PDF N° 00-035-0412) except peaks at 24.27 and 28.30, 2θ degree, corresponding to *m*-ZrO_2. In contrast, most peaks in NZSP (x = 0.60) could be indexed to rhombohedral NZSP symmetry with associated changes in peak height and shape at 19.87 and 23.11, 2θ degrees. However, the peak at 27.96, 2θ degrees matching monoclinic symmetry, Figure 4.1.2 [10-13]. It was concluded, therefore, that $Na_3Zr_{2-x}Si_2PO_{12-2x}$ (x = 0.60) was dominantly rhombohedral (*R-3c*).

Furthermore, the diffraction data of NZSP (x = 0.0 and 0.60) were analysed using Topas 5 software to gain further insight into the crystal structure and phase formation of NZSP compositions, Figure 4.1.3 (a & b). NZSP (x = 0.0) reveals a distribution of 92.0 % *m*-NZSP and 8. 0 % *m*-ZrO_2 with *a*, *b* and *c* values consistent with the literature, Figure 4.1.3a [13-17]. The refinement for NZSP (x = 0.60) confirms it is composed of two phases, 53.0 % rhombohedral (*R-3c*) and 47.0 % monoclinic (*C12/c*), with no evidence of *m*-ZrO_2 impurity phase, Figure 4.1.3(b, c & d). The parameters for NZSP (x = 0.0) agree with those reported in the literature [6-10, 13], but NZSP (x = 0.60) to our knowledge, has not been previously synthesised. Table 4.1 summarises the lattice parameters, theoretical density, good of fits (GoF), unit cell volume and the percentage composition of the distinct phases identified during the refinement. The complete sets of the refined parameters for NZSP (x = 0.0 and 0.60) are shown in Tables S2 - S4 in the supplementary section 4.2 of this chapter.

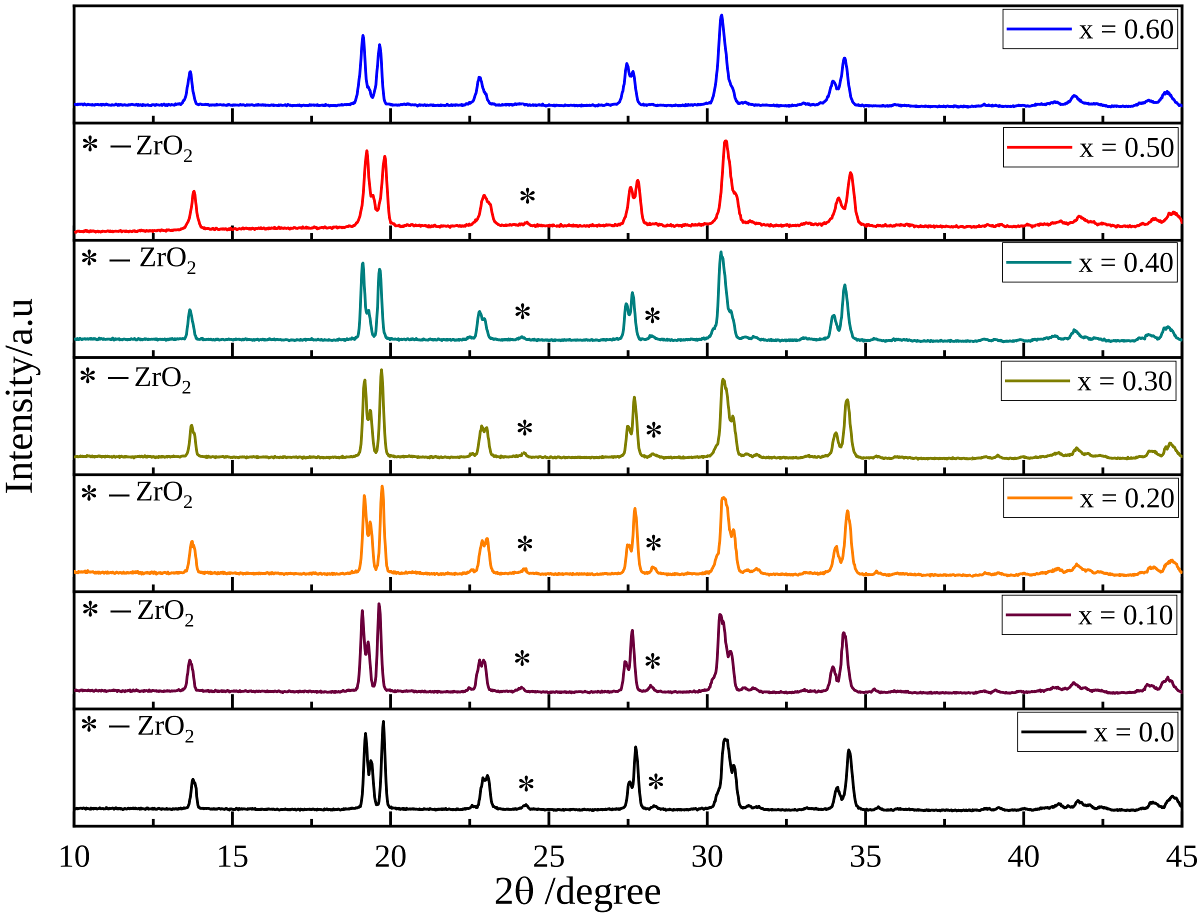

Figure 4.1.1 XRD patterns of $Na_3Zr_{2-x}Si_2PO_{12-2x}$ compositional series (0.0 ≤ x ≤ 0.60) with (*) depicting the *m*-ZrO_2 secondary phase in the series.

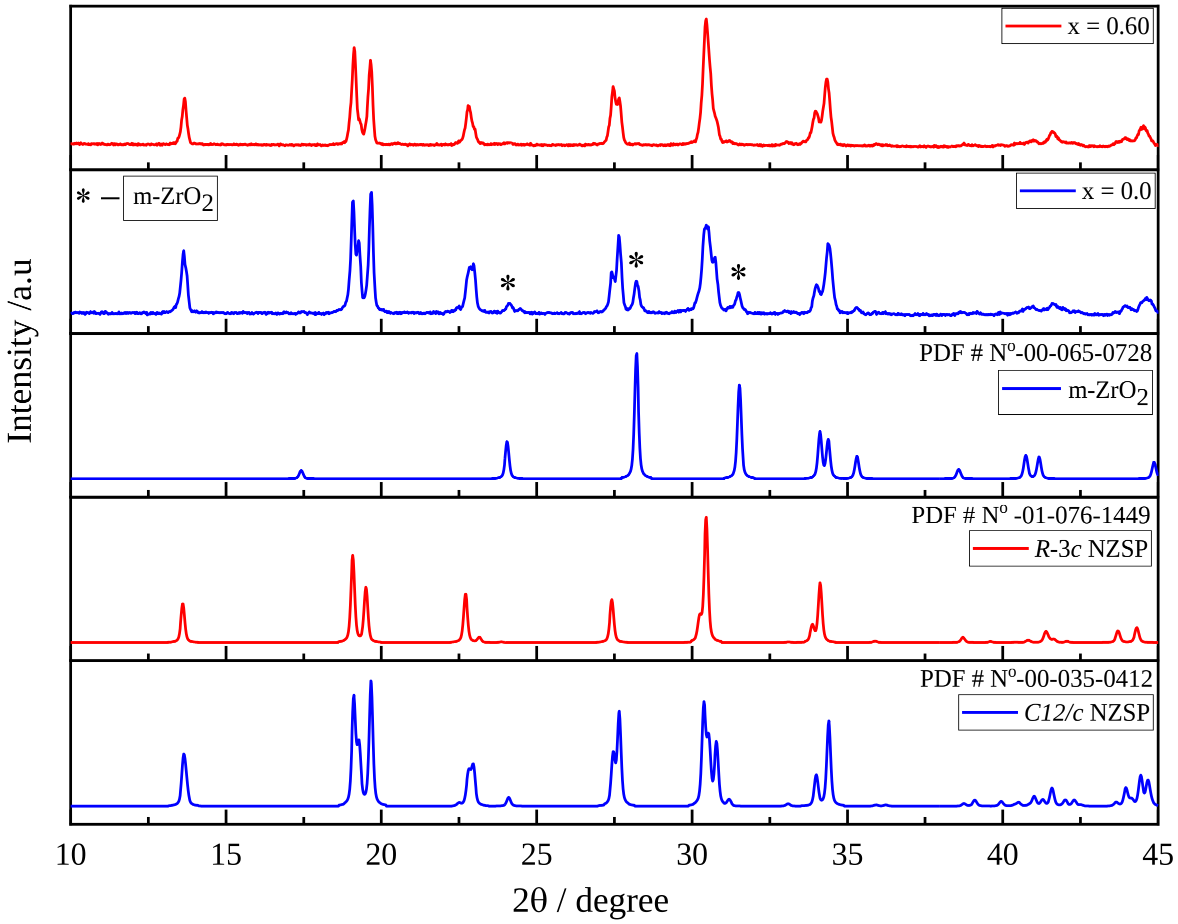

Figure 4.1.2 XRD patterns matching the composition of $Na_3Zr_{2-x}Si_2PO_{12-2x}$ (x = 0.0 and 0.60) against the PDF card N° of monoclinic and rhombohedral NZSP and monoclinic ZrO_2.

Table 4.1

Refined parameters, phase fractions, the goodness of fit (GoF), cell volume, theoretical and relative density of NZSP (x =0.0 and 0.60). *R*-rhombohedral and *M*-monoclinic.

NZSP	Phase fraction (%)			Lattice parameters (Å)			β (°)	GoF	Unit cell volume	$\rho_{(th)}$	Relative density (%)
	C12/c	*R-3c*	*m*-ZrO_2	a	b	c					
x = 0.0	92.0	0.0	8.0	15.634 ±0.0063	9.043 ±0.005	9.23 ±0.0025	123.63	2.50	1086.6	3.24	95.06
x = 0.60	*C12/c* 47.0	*R-3c* 53.0	0.0	9.072 (*R*) 15.651 (*M*)	9.055	23.138 (*R*) 9.219 (*M*)	123.77	2.12	1086.1	3.20	94.30

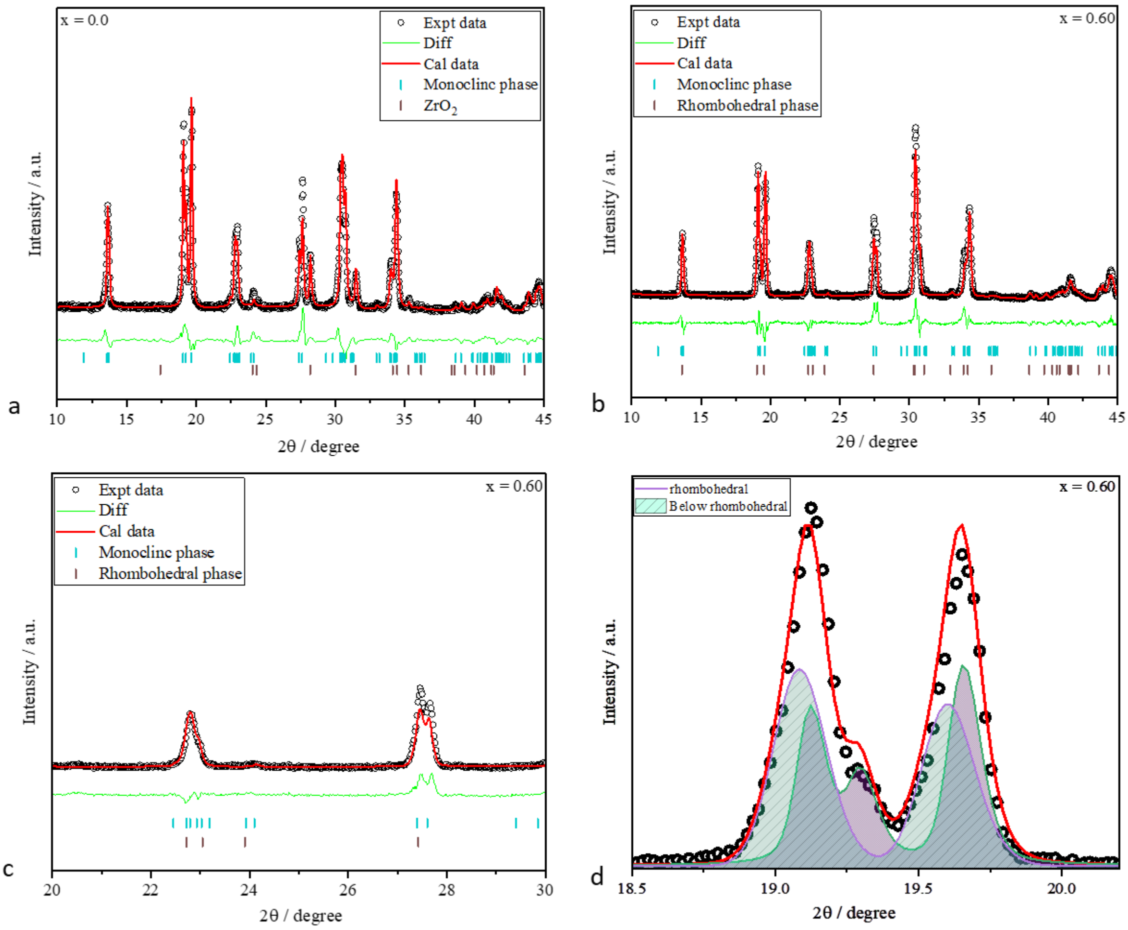

Figures 4.1.3 (a-d). Full pattern Rietveld refinement of $Na_3Zr_{2-x}Si_2PO_{12-2x}$ (a) x = 0.0, (b) x = 0.60, (c) enlargement plot of x = 0.60 without impurity peaks, and (d) peaks representing the composition of rhombohedral and monoclinic phase in x = 0.60.

4.1.2 Relative density

The experimental density of $Na_3Zr_{2-x}Si_2PO_{12-2x}$ (x = 0.0 and 0.60) sintered pellets was measured using Archimedes' method, and the results were compared with their theoretical density obtained from the refinements studies. From our refinements, the theoretical density of NZSP (x = 0.0) is 3.24 gcm^{-3} as shown in Table 4.2, which agrees with literature values [13-15]. To determine the experimental density of the NZSP ceramic, the average of three different measurements were taken. The theoretical density of NZSP (x = 0.60) obtained from the XRD refinements was 3.20 gcm^{-3} as shown in Table 4.2. The relative density (ρ_r) of the NZSP (x = 0.0 and 0.60) was calculated according to equation 3.8 (chapter 3), with the relative density of both NZSP (x = 0.0 and 0.60) > 94.0 %.

In the supplementary section, Table S1 (section 4.2), the ρ_r of conventional sintered $Na_3Zr_2Si_2PO_{12}$ at different sintering temperatures (1000, 1100, and 1230 °C) and time (12 hours) are reported. It is important to note that although at these temperatures (1000, 1100, and 1230 °C), NZSP has higher ρ_r than at 1250 °C /6 hr. There are > 10 vol% *m*-ZrO_2 and Na_3PO_4 phases, and hence, the project criteria of minimising impurity phases are not satisfied. Unreacted ZrO_2 and Na_3PO_4 mostly likely contributed to the high ρ_r of NZSP at these lower temperatures.

Table 4.2
The relative density of $Na_3Zr_{2-x}Si_2PO_{12-2x}$ compositional series (x = 0.0 and 0.60)

NZSP	Sintered temperature (°C) and time (hours)	Actual density (g/cm^3)	Theoretical density (g/cm^3)	Relative density
x = 0.0	1250 / 6	3.08	3.24	95.06
x = 0.60	1250 / 6	3.02	3.20	94.30

4.1.3 Dilatometry

The changes in the volume of the green $Na_3Zr_{2-x}Si_2PO_{12-2x}$ (x = 0.0 and 0.60) pellets as a function of temperature are shown in Figure 4.1.4. The two compositions of the NZSP (x = 0.0 and 0.60) show similar volume contraction over a wide temperature range. The volume changes were measured between 0 and 1200 °C to study the 'melt pool phase' temperature in NZSP as observed by Chakraborty *et. al*. [13]. The 'melt pool phase' for the NZSP (x = 0.0 and 0.60) was observed at a temperature range of 905 – 1086 °C in the dilatometer. Melt pool phase temperature is the temperature range at which the NZSP volume is contracted/shrunk. The melt pool phase temperature should not be confused with the sintering temperature of NZSP, which is ≥ 1200 °C. Regardless of the compositional changes in the mole fraction of the ZrO_2 reactant, the volume of the green NZSP pellets contracted similarly.

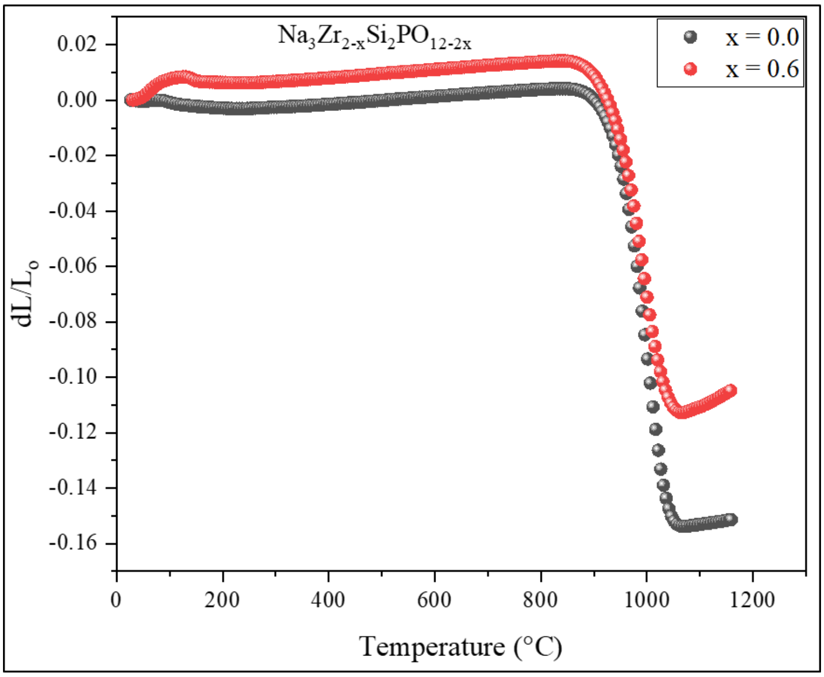

Figure 4.1.4. The dilatometry plot of $Na_3Zr_{2-x}Si_2PO_{12-2x}$ (x = 0.0 & 0.60) shows the change in volume as a function of Temperature.

4.1.4 Scanning electron microscopy

SEM micrographs of the fractured surface of the sintered pellets of $Na_3Zr_{2-x}Si_2PO_{12-2x}$ (x = 0.0 and x = 0.60) are shown in Figures 4.1.5 and 4.1.6, respectively. The micrographs for both NZSP (x = 0.0 and 0.60) reveal micron-sized, cuboid and homogeneous grain structures that are well-sintered and tightly compacted, supporting ceramics with $\rho_r \geq$ 94.0% and results comparable to the literature [6-8 and 13-16]. The average grain size of the NZSP (x = 0.0 and 0.60) was calculated using the line intercept technique on image J software. Equation 4.1 is used to calculate the grain size of the NZSP ceramic.

$$\text{Grain size} = \frac{\text{Length of the SEM micrograph } (\mu\text{m})}{\text{Number of grain intercept}} \qquad 4.1$$

Tables 4.3 and 4.4 recorded the grain sizes of the NZSP (x = 0.0 and 0.60), respectively. Lines were drawn across the SEM micrograph using Image J software, and the number of grains was counted. The average grain size of the NZSP (x = 0.0) is ~1.28 μm with few voids, consistent with a material of ρ_r ~ 95.0%. The average grain size of NZSP (x = 0.60) is ~ 2.12 μm with few voids and consistent with a material of ρ_r ~ 94.0%. Overall, the grain size of the NZSP (x = 0.60) is larger than that of the NZSP (x = 0.0). The larger grain size of NZSP (x = 0.60) could be attributed to inconsistent milling during preparation. Nonetheless, the impact of the larger grain size of NZSP (x = 0.60) will be investigated on the electrical properties of the ceramic. Figure S2 (section 4.2) shows the SEM micrograph of the polished surface of NZSP sintered at 1100 °C for 12 hours.

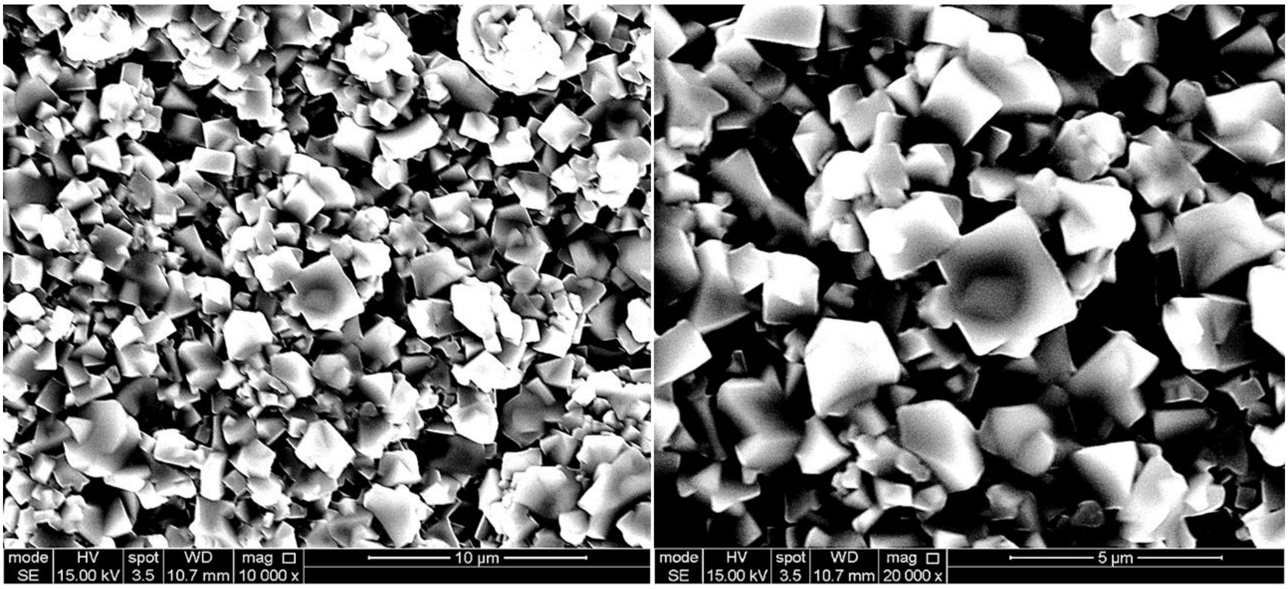

Figure 4.1.5. SEM images of the fractured surface of sintered $Na_3Zr_{2-x}Si_2PO_{12-2x}$ (x = 0.0).

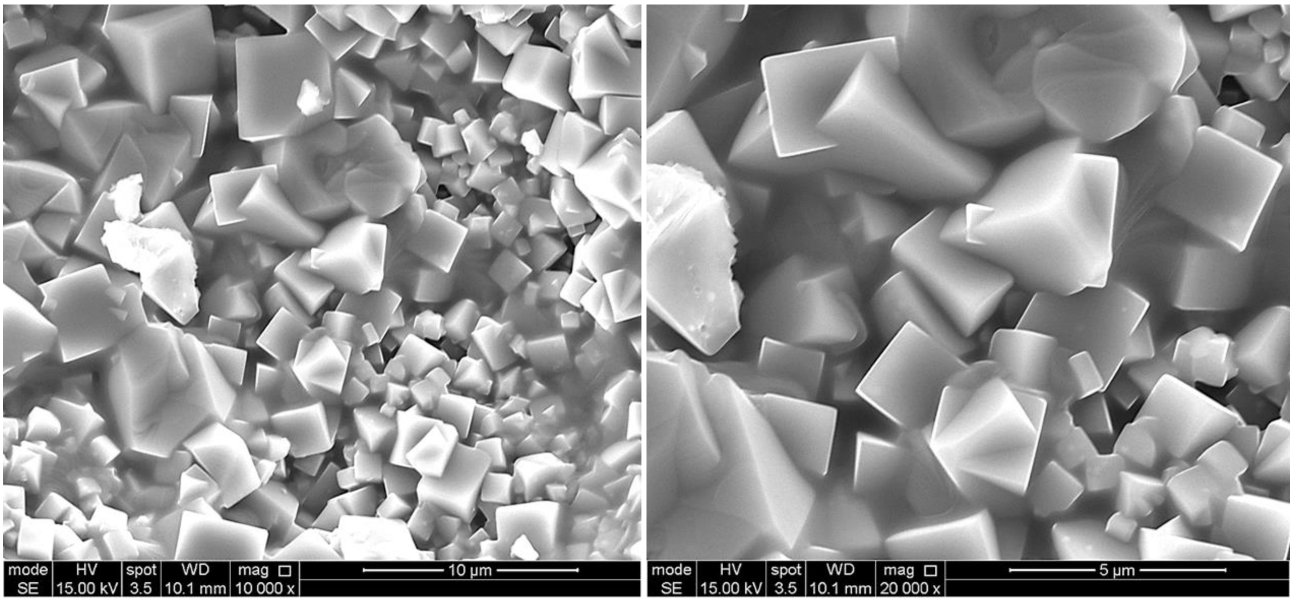

Figure 4.1.6. The SEM images of the fractured surface of sintered $Na_3Zr_{2-x}Si_2PO_{12-2x}$ (x = 0.60).

Table 4.3

Grain size measurement of NZSP (x = 0.0) by line intercept method.

NZSP (x = 0.0)	Area	Mean	length	No of grain intercept	Length/no of grains
1	0.42	171.96	7.40	6	1.23
2	0.53	134.84	9.32	7	1.33
3	0.70	175.58	12.27	8	1.53
4	1.14	138.64	20.00	16	1.25
5	0.94	145.28	16.53	13	1.27
6	0.51	182.78	8.87	7	1.27
7	0.56	124.86	9.72	9	1.08

Table 4.4

Grain size measurement of NZSP (x = 0.60) by line intercept method.

NZSP (x = 0.60)	Area	Mean	length	No of grain intercept	Length/no of grains
1	0.91	123.57	15.45	6	2.58
2	1.14	125.10	19.50	8	2.44
3	0.57	138.67	9.63	7	1.37
4	1.62	124.06	27.67	11	2.52
5	1.02	123.14	17.39	12	1.45
6	0.63	145.22	10.76	5	2.15
7	0.81	154.34	13.88	6	2.31

4.1.5 Fourier Transform Infra-red spectroscopy.

FTIR spectra of $Na_3Zr_{2-x}Si_2PO_{12-2x}$ (x = 0.0 and 0.60) are shown in Figure 4.1.7. The vibrational and stretching frequencies between the two compositions of NZSP (x = 0.0 and 0.60) show no observable differences. Transition metal-oxygen bonds have unique fingerprints at frequencies < 1000 cm^{-1}, with Zr-O stretching/vibration bands dominant in this region [14, 19]. Thus, the 534 and 600 cm^{-1} peaks can be attributed to the Zr–O bond. The P–O bond's vibrational frequency lies between 1100 – 1300 cm^{-1}; hence, the peak at 1130 cm^{-1} can be assigned to the P–O bond. Si–O bond has a unique signature between 900 – 1100 cm^{-1}; therefore, the peaks observed at 928 and 1028 cm^{-1} can be predicted to be that of the Si–O bond. Nonetheless, it is worth noting that the vibrational frequency of metal-oxygen can vary based on the atom's coordination environment, surrounding functional groups, and molecular structure.

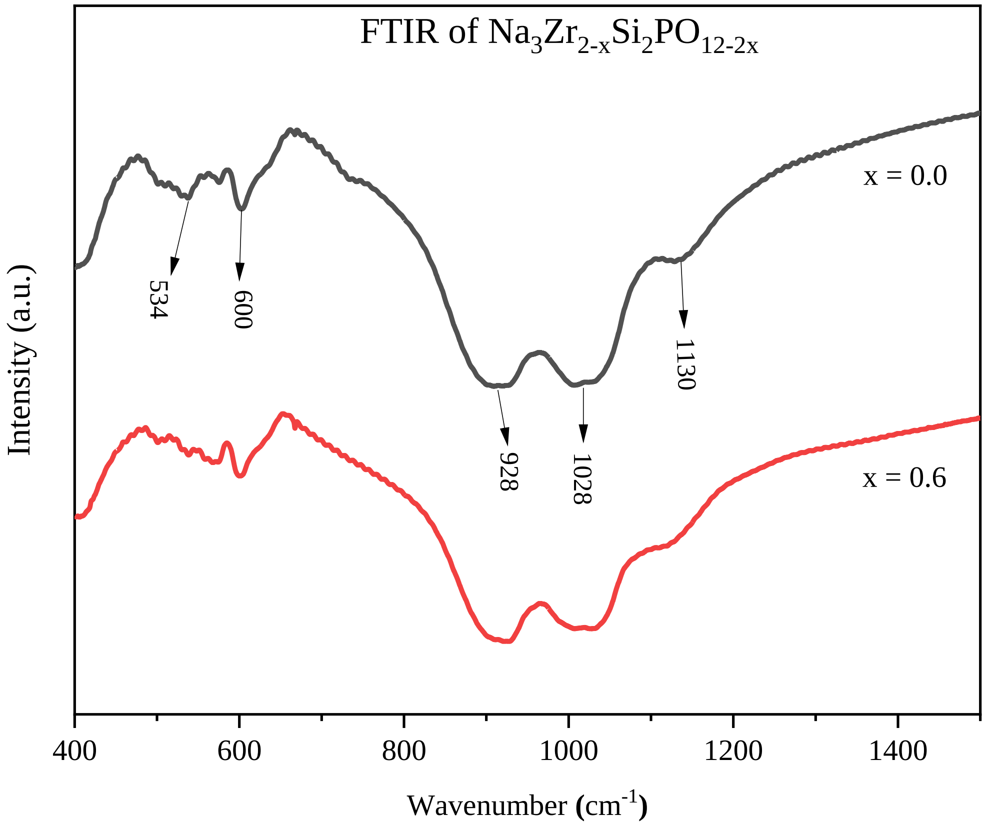

Figure 4.1.7. The FTIR images of $Na_3Zr_{2-x}Si_2PO_{12-2x}$ (x = 0 & 0.6)

4.1.6 Raman Spectroscopy

Raman plot of NZSP (x = 0.0 and 0.60) and *m*-ZrO_2 are shown in Figure 4.1.8. The NZSP spectra are similar to those obtained from a NASICON reported by Barj *et al.*, [20]. Based on the x-ray diffraction data refinement, it is reasonable to assume that all the peaks for NZSP (x = 0.60) arise only from the matrix phase with none matching *m*-ZrO_2, which supports our premise that this composition does not contain the *m*-ZrO_2 impurity phase. The peak at 960 cm^{-1} in NZSP (x = 0.60) does not match *m*-ZrO_2, and it is absent in the monoclinic crystal symmetry of NZSP (x = 0.0). It is likely related to the rhombohedral symmetry or Zr-O site occupancy changes.

Nonetheless, it requires further study. For NZSP (x = 0.0), all modes match either *m*-ZrO_2 or NZSP (x = 0.60), supporting the XRD data from NZSP (x = 0.0) in which peaks associated with *m*-ZrO_2 were observed.

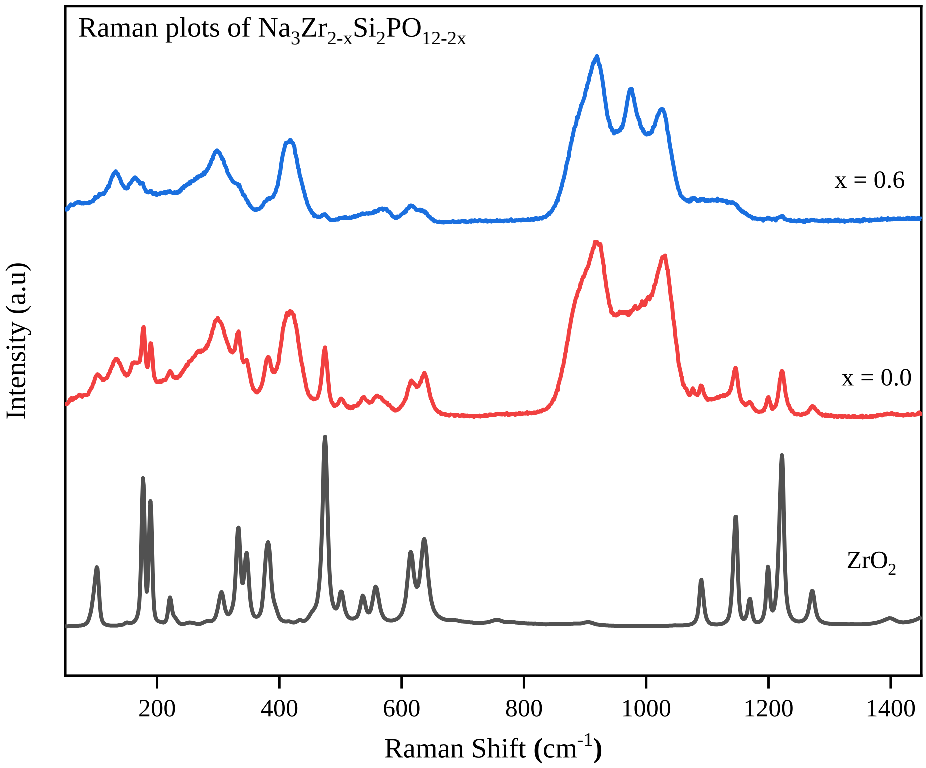

Figure 4.1.8. Raman spectra of $Na_3Zr_{2-x}Si_2PO_{12-2x}$ (x = 0.0 & 0.60). The spectrum of ZrO_2 (monoclinic) is shown for comparison.

4.1.7 Impedance Spectroscopy

Complex impedance plane (Z*) plots at various temperatures for $Na_3Zr_{2-x}Si_2PO_{12-2x}$ ceramics (x = 0.0 and 0.60) sintered at 1250 °C are shown in Figure 4.1.9 & 4.1.10 (a). A low-frequency spike and a partial arc with a non-zero intercept at high frequencies are observed in Figures 4.1.9(a) & 4.1.10(a) “insert”. However, the arc rapidly disappears at higher temperatures, and only a non-zero intercept on the Z’ axis of the spike was observed. The low-frequency spike is consistent with ionic conduction, with the charge carriers being Na^+ ions. Therefore, only the total resistivity of the ceramics could be determined based on the intercept of the spike with the Z' axis. However, the total resistivity of $Na_3Zr_{2-x}Si_2PO_{12-2x}$ (x = 0.0) is slightly lower than that of $Na_3Zr_{2-x}Si_2PO_{12-2x}$ (x = 0.60) at room and higher temperatures, and its order of magnitude agrees with reported literature [6-13].

Sub-ambient measurements were performed to probe the electroactive contributions to the total conductivity. Impedance (Z*) plots at 160 K revealed both NZSP (x= 0.0 and 0.60) to display two arcs, Figure 4.1.9a and 4.1.10a. The bulk, grain boundary and total resistivity of the NZSP (x = 0.0 and 0.60) at 160K based on the intercept of the spike with the Z' axis is shown in Figure 4.1.11. Also, the time-dependent frequency response of the impedance plots of the NZSP (x = 0.0 and 0.60) to external stimulus “relaxation frequency” is shown in Figure 4.1.12, with the associated bulk, grain boundary and total relaxation frequencies measured at 160 and 295 K.

To quantify and interpret the sub-ambient (Z*) data, an equivalent circuit based on two parallel Resistor-Capacitor elements connected in series was used. The high and low-frequency arcs had associated capacitance values in the range pF/cm and nF/cm, as shown in Table 4.5. Therefore, the bulk (R_bC_b) and grain boundary ($R_{gb}C_{gb}$) responses are consistent with compounds with charged Na^+ ions. The imaginary component of the electric modulus (M'') was studied to determine the bulk conductivities (σ_b), and the results support our assumption of the bulk and grain boundary contribution and agree with the reported literature [6-13]. The total, bulk, and grain boundary ionic conductivity at 160 and 295 K are shown in Table 4.5. The capacitance (C'), imaginary components (Z'') of the impedance, and the electric modulus (M'') responses of the NZSP (x = 0.0 and 0.60) at 160 and 295 K are shown in Figures 4.1.9 & 4.1.10 (b-d).

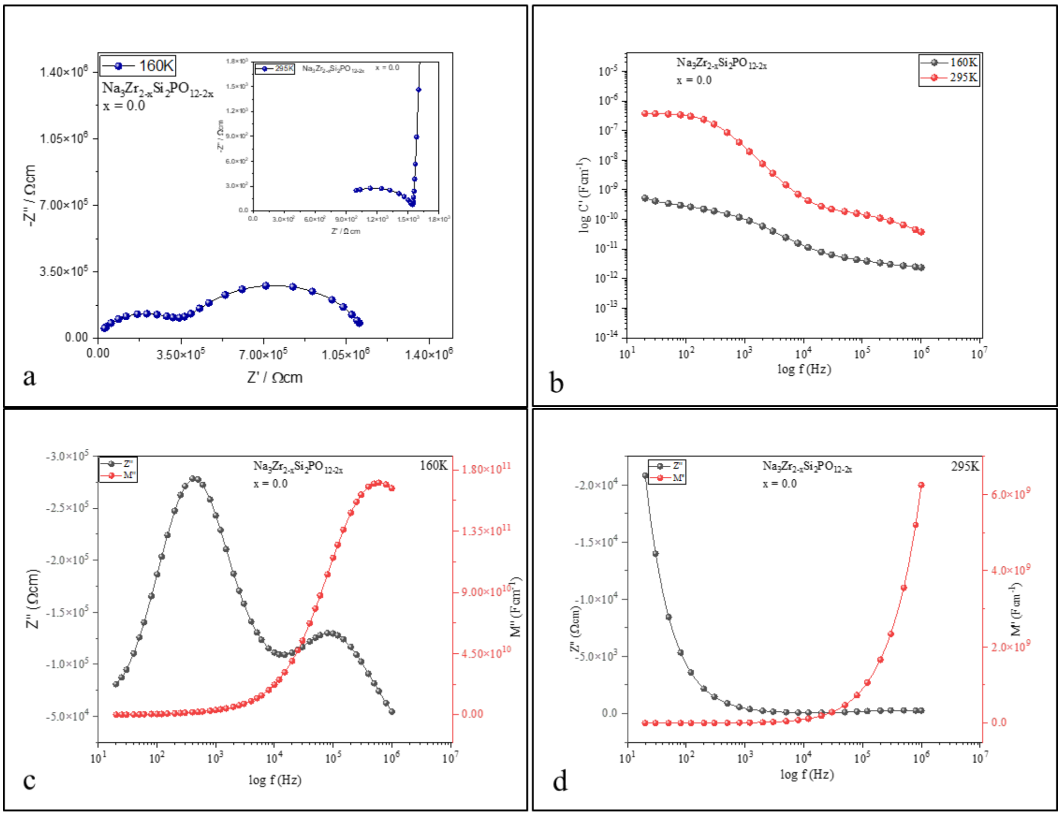

Figure 4.1.9. The complex impedance and spectroscopic plots of $Na_3Zr_{2-x}Si_2PO_{12-2x}$ (x = 0.0) at 160K and 295K (insert). (a) Z'/Z'' (b) capacitance (c & d) Z''/M''.

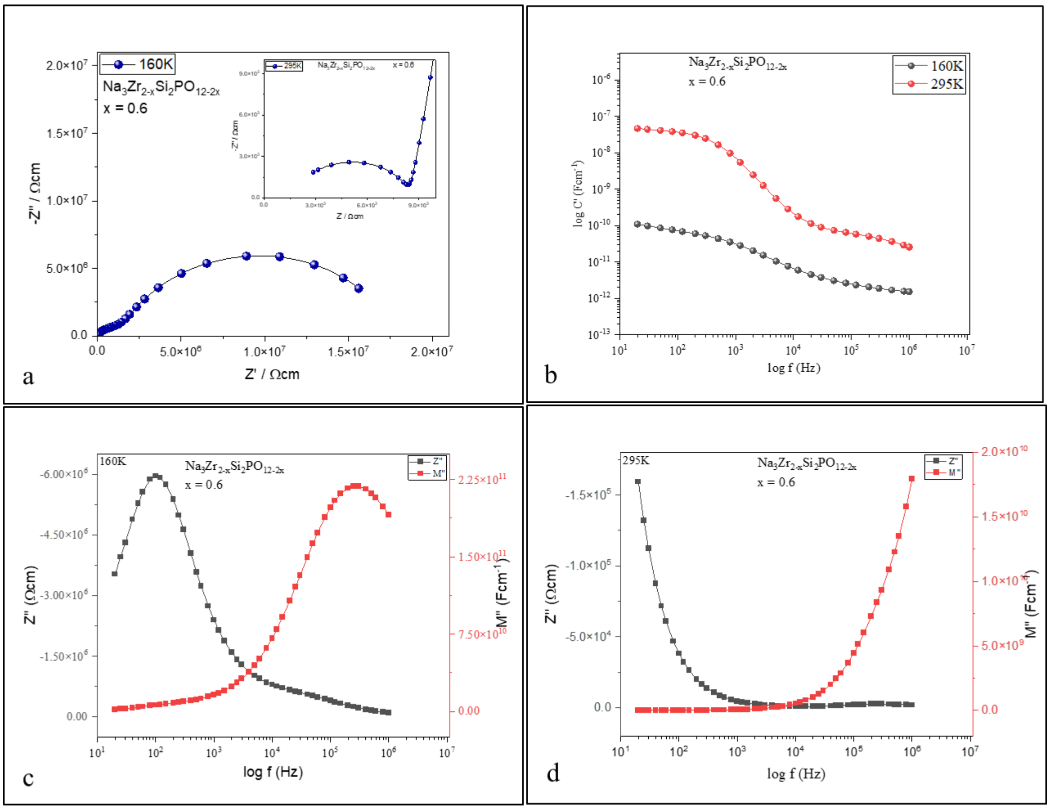

Figure 4.1.10. The complex impedance and spectroscopic plots of $Na_3Zr_{2-x}Si_2PO_{12-2x}$ (x = 0.60) at 160K and 295K (insert). (a) Z'/Z'' (b) capacitance (c & d) Z''/M''.

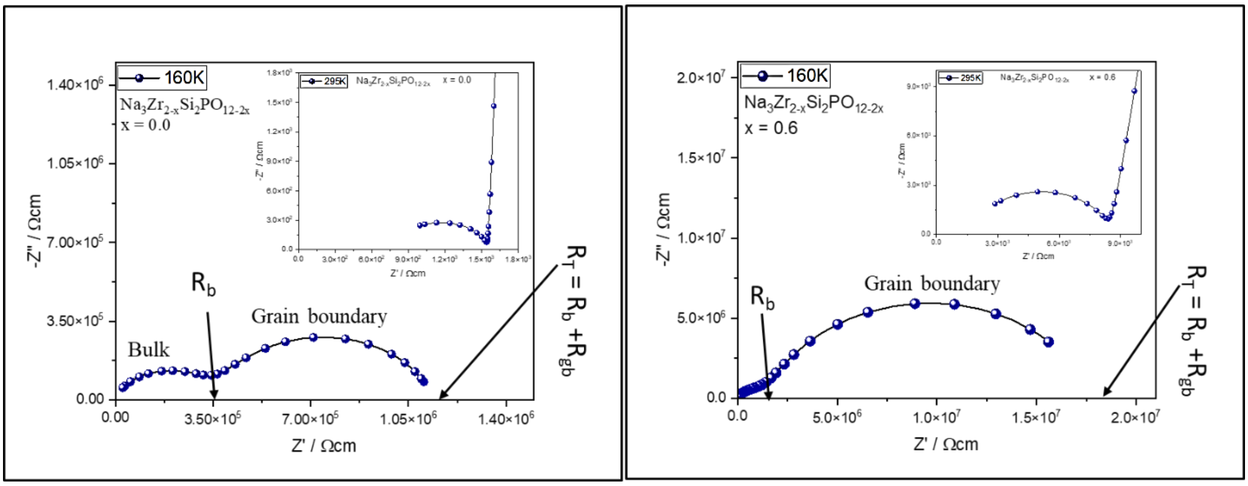

Figure 4.1.11. The complex impedance plots of $Na_3Zr_{2-x}Si_2PO_{12-2x}$ (x = 0.0 and 0.60) at 160 and 295 K (insert) show the bulk and grain boundary conductions. [R_b: Bulk resistance, R_{gb}: Grain boundary resistance and R_T: Total resistance].

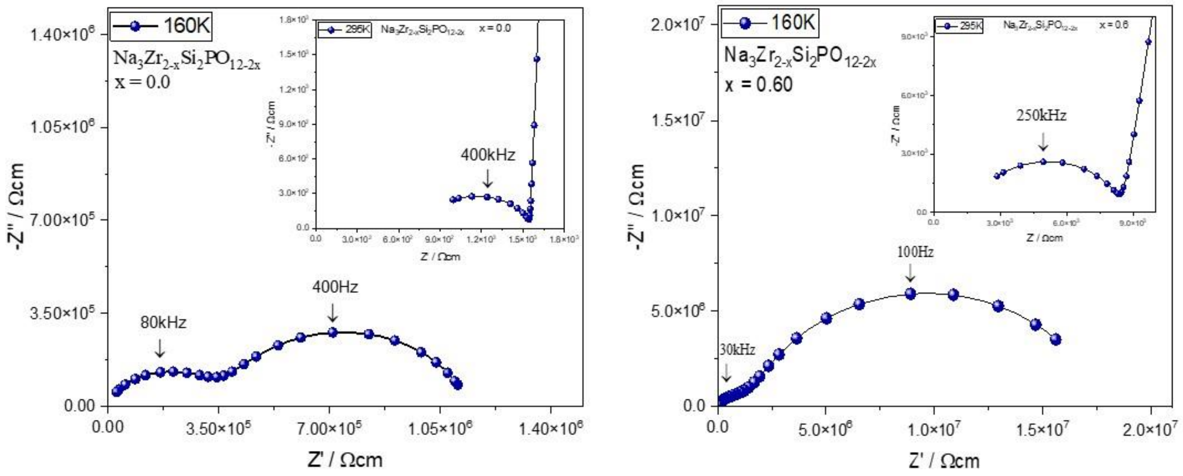

Figure 4.1.12. The complex impedance plots of $Na_3Zr_{2-x}Si_2PO_{12-2x}$ (x = 0.0 and 0.60) at 160 and 295 K (insert) show the bulk and grain boundary relaxation frequency.

Table 4.5.

The bulk and grain boundary capacitance at 160 K and the bulk, grain boundary and total ionic conductivities of the conventional sintered $Na_3Zr_{2-x}Si_2PO_{12-2x}$ (x = 0.0 & 0.6) ceramic at 160 and 295 K.

NZSP	Capacitance (F/cm) = $1/2\pi f_{max}R$ at160 K		Conductivity (S/cm) at 160 K			Conductivity (S/cm) at 295 K		
	C_{bulk}	C_{gb}	σ_{bulk}	σ_{gb}	σ_{total}	σ_{bulk}	σ_{gb}	σ_{total}
x = 0.0	$4.20*10^{-12}$	$47.30*10^{-9}$	$2.32*10^{-6}$	$8.75*10^{-7}$	$6.35*10^{-6}$	$1.30*10^{-3}$	$1.20*10^{-3}$	$6.32*10^{-4}$
x = 0.60	$2.34*10^{-12}$	$11.20*10^{-9}$	$7.35*10^{-7}$	$5.64*10^{-8}$	$1.00*10^{-7}$	$6.54*10^{-4}$	$1.39*10^{-4}$	$1.15*10^{-4}$

4.1.8 Arrhenius plot.

The temperature-dependent data of the (bulk, grain boundary and total) conductivities of the NZSP (x = 0.0 and 0.60) at different temperatures are shown in Table 4.6. The data were extrapolated to calculate the gradient of the Arrhenius plot. The standard least square method was used to obtain the gradients of the temperature-dependent data of the NZSP (x = 0.0 and 0.60) in Origin software, and the uncertainty associated with each gradient and activation energy was recorded.

Table 4.6

Temperature-dependent conductivity (bulk, grain boundary and total) of the NZSP (x = 0.0 and 0.60)

		NZSP (x = 0.0)			NZSP (x = 0.60)		
Temperature (K)	1000/T (K)	log σ_t	log σ_b	log σ_{gb}	log σ_t	log σ_{gb}	log σ_b
320	3.13	-2.783	-2.528	-2.430	-3.552	-3.462	-2.825
295	3.39	-3.199	-2.876	-2.919	-3.940	-3.856	-3.185
280	3.57	-3.480	-3.112	-3.237	-4.208	-4.135	-3.398
260	3.85	-3.886	-3.470	-3.676	-4.616	-4.557	-3.714
240	4.17	-4.226	-3.740	-4.055	-4.980	-4.935	-3.974
220	4.55	-4.648	-4.037	-4.526	-5.452	-5.419	-4.316
200	5.00	-5.150	-4.547	-5.026	-6.013	-5.976	-4.923
180	5.56	-5.706	-5.178	-5.554	-6.636	-6.598	-5.558

The Activation energy (E_a) was calculated according to Equation 3.35 (chapter 3), and the results are shown in Table 4.7. The Arrhenius plot of the total conductivity of the NZSP (x = 0.0 and 0.60), where $\sigma_T = 1/R_T$ are shown in Figures 4.1.13 (a & b), where the E_a is ~ 0.23 eV for NZSP (x = 0.0) and ~ 0.25 eV for NZSP (x = 0.60). These values were comparable and lower than the literature values [5-8]. Arrhenius plots of the bulk ($\sigma_b = 1/R_b$) and grain boundary ($\sigma_{gb} = 1/R_{gb}$) are shown in Figures 4.1.14 (a & b) and 4.1.15 (a & b), respectively. The E_a associated with σ_b is ~ 0.21 eV for both ceramics, suggesting a similar conduction mechanism in both materials, with the difference in σ_b being attributed to a lower carrier concentration in NZSP (x = 0.60). These values agree with the literature [15-17]. The E_a associated with σ_{gb} in both NZSP (x = 0.0 & 0.60) is in the range of ~ 0.24 – 0.25 eV, Figures 4.1.15 (a & b). These values are similar to that obtained for the total E_a, suggesting similar conduction mechanisms. The activation energy (bulk, grain boundary and total) of NZSP (x = 0.0 & 0.60) are lower than the values reported in the literature [13-18]. The low E_a values could be attributed to the conductivity of the NZSP (x = 0.0 & 0.60) recorded at sub-ambient conditions.

Table 4.7

Activation energy associated with the bulk, grain boundary and total activation energy of NZSP (x = 0.0 and 0.60)

NZSP	The activation energy (eV)		
	E_a(bulk)	E_a(gb)	E_a(total)
x = 0.0	0.21 ±0.029	0.24 ±0.05	0.23 ±0.034
x = 0.60	0.21 ±0.031	0.25 ±0.027	0.25 ±0.023

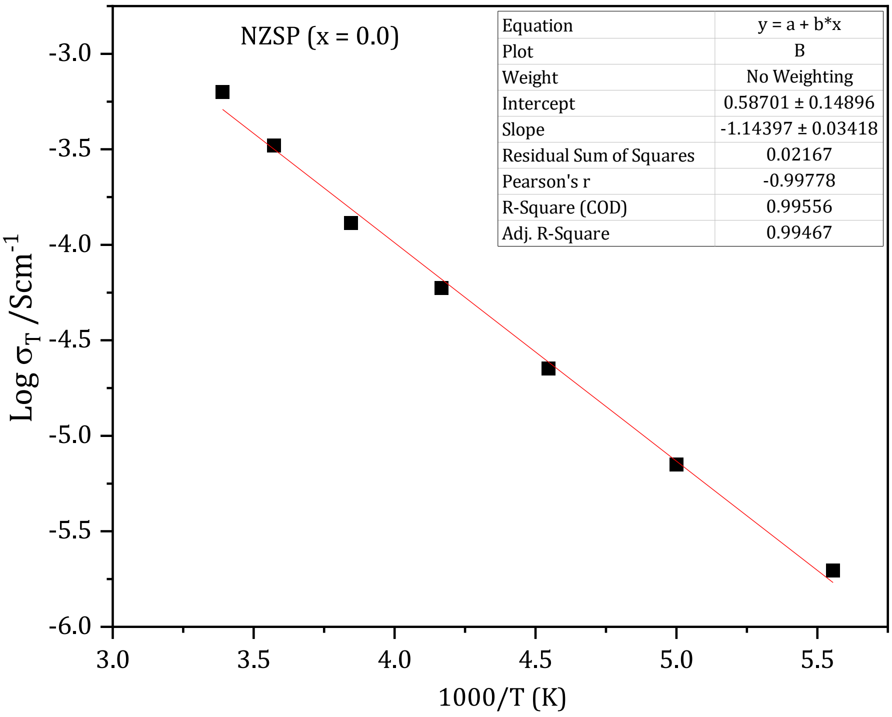

Equation	y = a + b*x
Plot	B
Weight	No Weighting
Intercept	0.58701 ± 0.14896
Slope	-1.14397 ± 0.03418
Residual Sum of Squares	0.02167
Pearson's r	-0.99778
R-Square (COD)	0.99556
Adj. R-Square	0.99467

Figure 4.1.13a. Arrhenius plot of the total conductivity for NZSP (x = 0.0) ceramics.

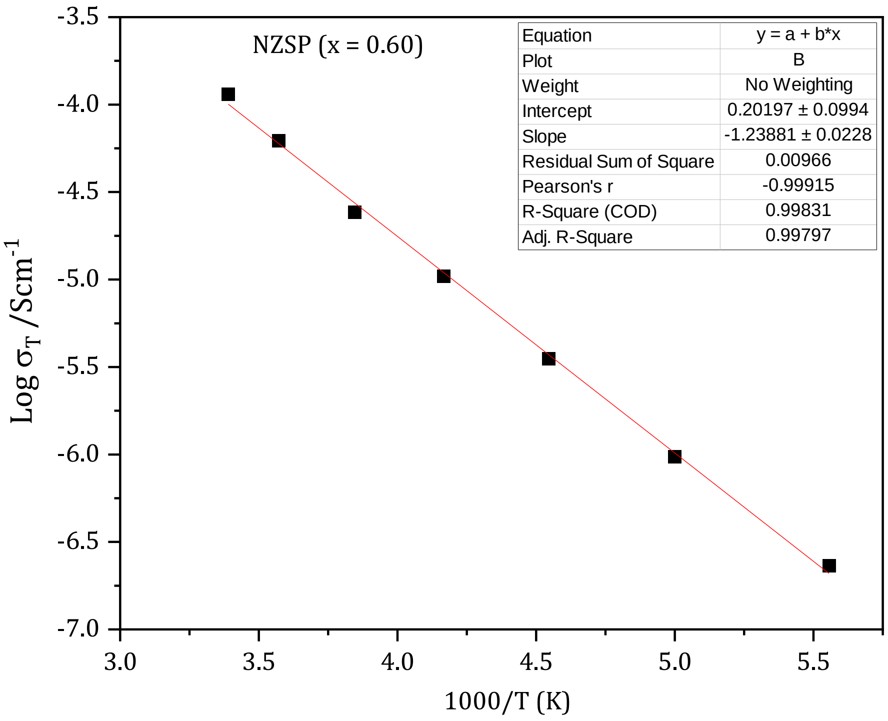

Figure 4.1.13b. Arrhenius plot of the total conductivity for NZSP (x = 0.60) ceramics.

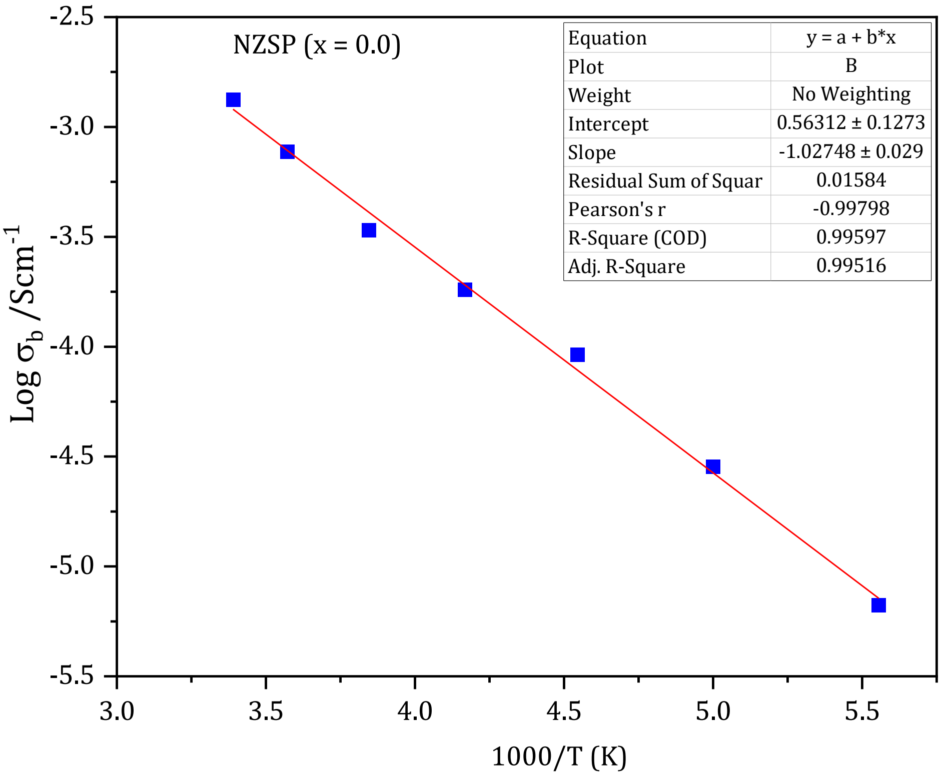

Figure 4.1.14a. Arrhenius plot of the bulk conductivity (σ_b) for NZSP (x = 0.0).

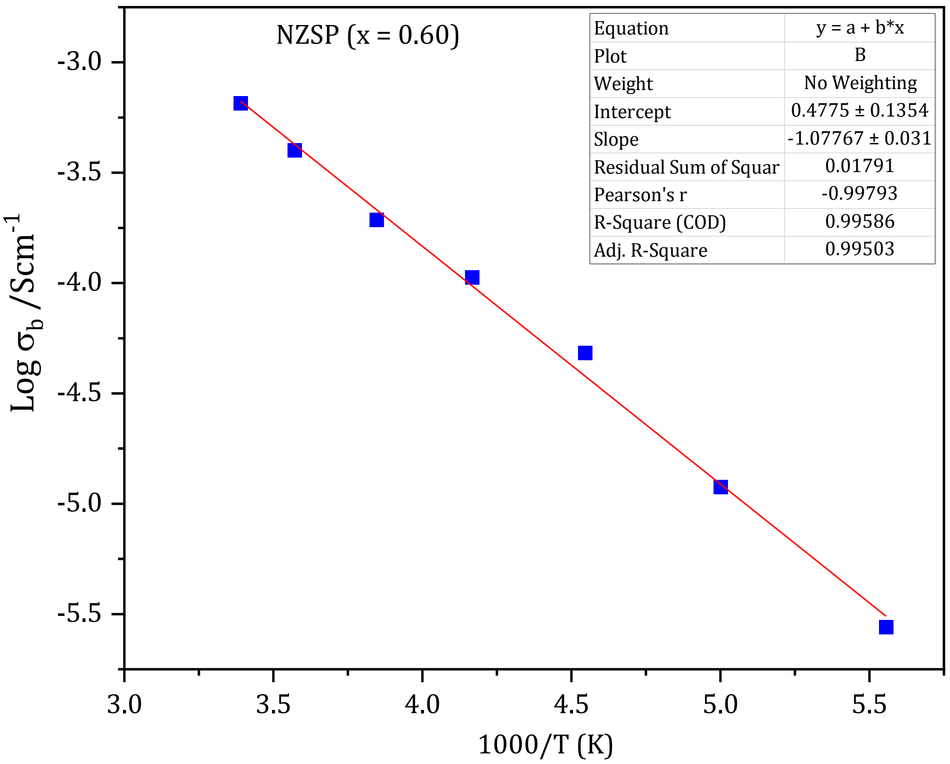

Equation	y = a + b*x
Plot	B
Weight	No Weighting
Intercept	0.4775 ± 0.1354
Slope	-1.07767 ± 0.031
Residual Sum of Squar	0.01791
Pearson's r	-0.99793
R-Square (COD)	0.99586
Adj. R-Square	0.99503

Figure 4.1.14b. Arrhenius plot of the bulk conductivity (σ_b) for NZSP (x = 0.60).

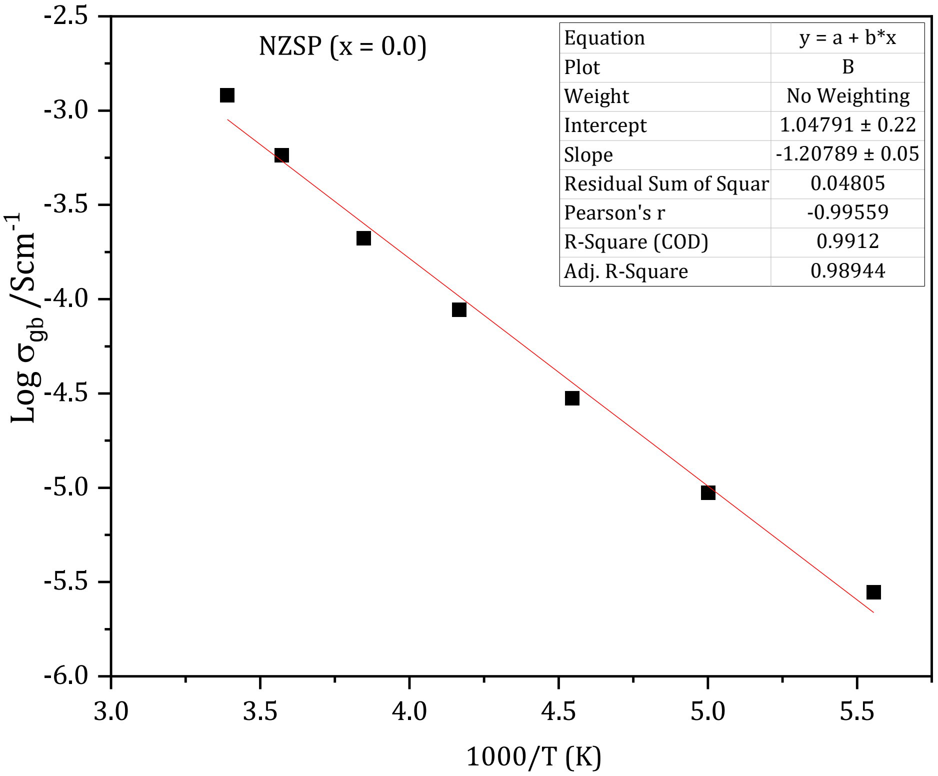

Equation	y = a + b*x
Plot	B
Weight	No Weighting
Intercept	1.04791 ± 0.22
Slope	-1.20789 ± 0.05
Residual Sum of Squar	0.04805
Pearson's r	-0.99559
R-Square (COD)	0.9912
Adj. R-Square	0.98944

Figure 4.1.15a. Arrhenius plot of the grain boundary conductivity (σ_{gb}) for NZSP (x = 0.0).

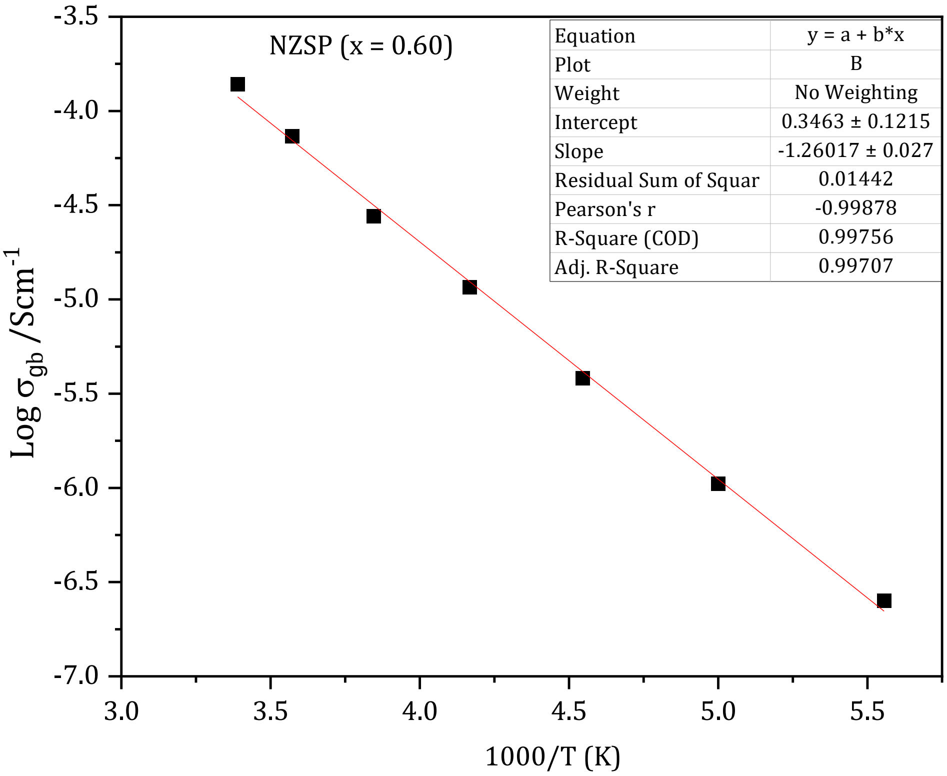

Figure 4.1.15b. Arrhenius plot of the grain boundary conductivity (σ_{gb}) for NZSP (x = 0.60).

4.2 Supplementary data

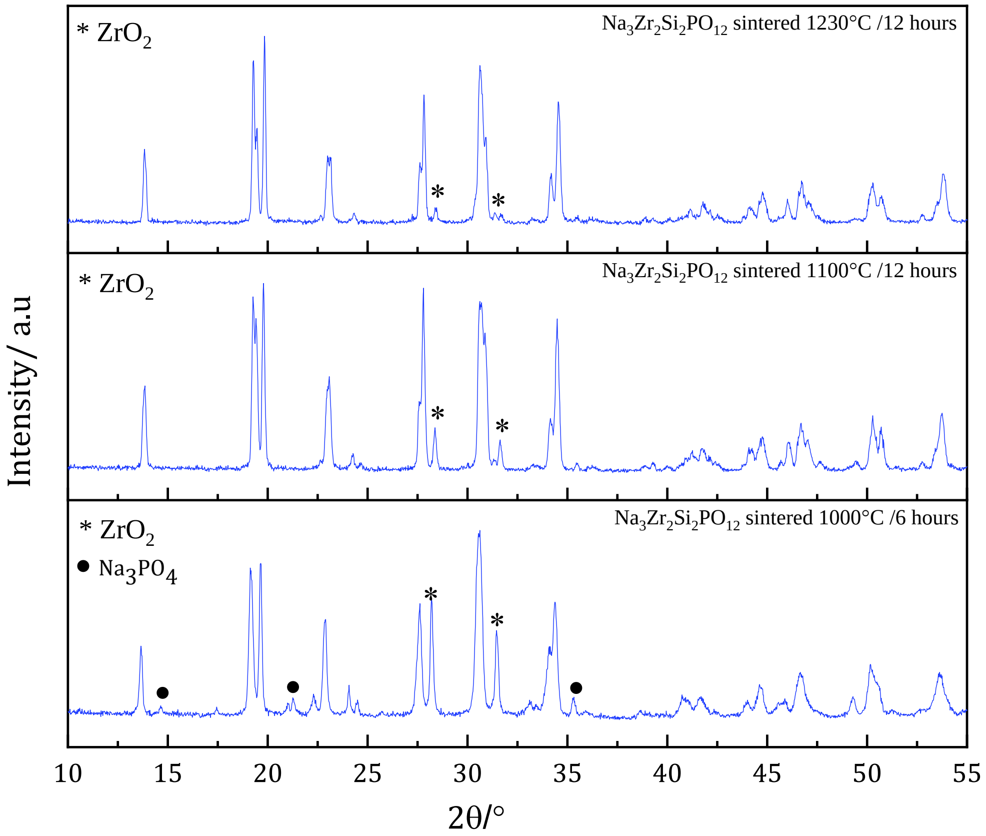

Figure S1. XRD pattern of $Na_3Zr_{2-x}Si_2PO_{12-2x}$ sintered at various temperatures for 12 hours.

Tables S1

Sintering temperature, time, experimental, theoretical, and relative density of NZSP

S/N	NZSP	Sintering Temperature (°C)	Time (Hrs)	Density (g/cm³)	Theoretical Density (g/cm³)	ρ_r
1	$Na_3Zr_2Si_2PO_{12}$	1100	12	3.025	3.27	92.51
2	$Na_3Zr_2Si_2PO_{12}$	1230	3	3.032	3.27	92.72
3	$Na_3Zr_2Si_2PO_{12}$	1000	6	3.181	3.27	97.28
4	$Na_3Zr_2Si_2PO_{12}$	1250	6	3.184	3.27	97.37

Table S2

Monoclinic *C12/c* NZSP (x = 0.0)

NZSP (x=0.0)	GOF=2.5	92% NZSP + 8% ZrO_2
Structure 1		
Phase name	*C12/c*	
R-Bragg	5.664	
Space group	C12/c1	
Scale	0.000199(5)	
Cell Mass	2123.024	
Cell Volume (Å^3)	1086.6(6)	
Wt% - Rietveld	93(5)	
Crystal Linear Absorption Coeff. (1/cm)	217.70(12)	
Crystal Density (g/cm^3)	3.2445(18)	
PV_MOD peak type: a + b Tan(Th) + c / Cos(Th)		
FWHM a	0.0(16)	
b	0.2(4)	
c	0.1(16)	
Lorentzian mix a	0(15)	
b	1(3)	
c	0(15)	
Lattice parameters		
a (Å)	15.634(5)	
b (Å)	9.043(3)	
c (Å)	9.230(3)	
beta (°)	123.630(6)	

Site	Np	x	y	z	Atom	Occ	Beq
P1	4	0.00000	0.03920	0.25000	P	0.33	0(70)
Na1	4	0.25000	0.25000	0.50000	Na+1	0.81	5.0(16)
Na2	4	0.50000	0.89100	0.25000	Na+1	1	5(2)
P2	8	0.35690	0.11170	0.25860	P	0.33	5(30)
Zr1	8	0.10150	0.24720	0.05390	Zr+4	1	1.2(6)
Si2	8	0.35690	0.11170	0.25860	Si+4	0.67	0(14)
Na3	8	0.83600	0.07900	0.84200	Na+1	0.6	5(3)
O6	8	0.08060	0.14750	0.24440	O-2	1	0(2)
O5	8	0.44910	0.18090	0.43690	O-2	1	1.9(19)
O1	8	0.14660	0.43660	0.22260	O-2	1	5(2)
Si1	4	0.00000	0.03920	0.25000	Si+4	0.67	0(40)
O4	8	0.38120	0.13370	0.11160	O-2	1	1.7(19)
O2	8	0.43740	0.44390	0.08210	O-2	1	0(2)
O3	8	0.25270	0.18120	0.20280	O-2	1	4(2)

Table S3

Monoclinic *C12/c* NZSP (x = 0.60)

NZSP (x=0.6)	M phase	GOF=2.12		47% *M*-NZSP + 53% R-NZSPO
Phase name	*C12/c*			
R-Bragg	8.872			
Space group	C12/c1			
Scale	0.00004(18)			
Cell Mass	2123.024			
Cell Volume (Å^3)	1086.1(9)			
Wt% - Rietveld	50(180)			
Crystal Linear Absorption Coeff. (1/cm)	217.80(17)			
Crystal Density (g/cm^3)	3.246(3)			
PV_MOD peak type: a + b Tan(Th) + c / Cos(Th)				
FWHM a	0.0(18)			
b	0.0(5)			
c	0.1(19)			
Lorentzian mix a	1(40)			
b	0(9)			
c	0(40)			
Lattice parameters				
a (Å)	15.651(7)			
b (Å)	9.055(4)			
c (Å)	9.219(4)			
beta (°)	123.776(13)			

Site	Np	x	y	z	Atom	Occ	Beq
P1	4	0.00000	0.03920	0.25000	P	0.33	0(140)
Na1	4	0.25000	0.25000	0.50000	Na+1	0.81	5(20)
Na2	4	0.50000	0.89100	0.25000	Na+1	1	0(20)
P2	8	0.35690	0.11170	0.25860	P	0.33	0(90)
Zr1	8	0.10150	0.24720	0.05390	Zr+4	1	0(20)
Si2	8	0.35690	0.11170	0.25860	Si+4	0.67	0(60)
Na3	8	0.83600	0.07900	0.84200	Na+1	0.6	0(20)
O6	8	0.08060	0.14750	0.24440	O-2	1	0(20)
O5	8	0.44910	0.18090	0.43690	O-2	1	1(20)
O1	8	0.14660	0.43660	0.22260	O-2	1	5(20)
Si1	4	0.00000	0.03920	0.25000	Si+4	0.67	0(80)
O4	8	0.38120	0.13370	0.11160	O-2	1	0(20)
O2	8	0.43740	0.44390	0.08210	O-2	1	0(20)
O3	8	0.25270	0.18120	0.20280	O-2	1	5(20)

Table S4

Rhombohedral *R-3c* NZSP (x = 0.60)

NZSP (x=0.6)	
Phase name	*R-3c*
R-Bragg	9.581
Space group	R-3c:H
Scale	0.00002(9)
Cell Mass	3181.777
Cell Volume (Å^3)	1649.2(18)
Wt% - Rietveld	50(180)
Crystal Linear Absorption Coeff. (1/cm)	215.1(2)
Crystal Density (g/cm^3)	3.204(3)
PV_MOD peak type: a + b Tan(Th) + c / Cos(Th)	
FWHM a	0(2)
b	0.6(5)
c	0(2)
Lorentzian mix a	0(40)
b	0(8)
c	0(40)
Lattice parameters	
a (Å)	9.072(4)
c (Å)	23.138(12)

Site	Np	x	y	z	Atom	Occ	Beq
Zr1	12	0.00000	0.00000	0.14690	Zr+4	1	0(20)
P1	18	0.28830	0.00000	0.25000	P	0.33	0(80)
Si1	18	0.28830	0.00000	0.25000	Si+4	0.67	0(50)
O1	36	0.17620	0.03600	0.19440	O-2	1	0(20)
Na1	6	0.00000	0.00000	0.00000	Na+1	1.01	5(20)
O2	36	0.19390	0.17070	0.09290	O-2	1	5(20)
Na2	18	0.62920	0.00000	0.25000	Na+1	0.66	0(20)

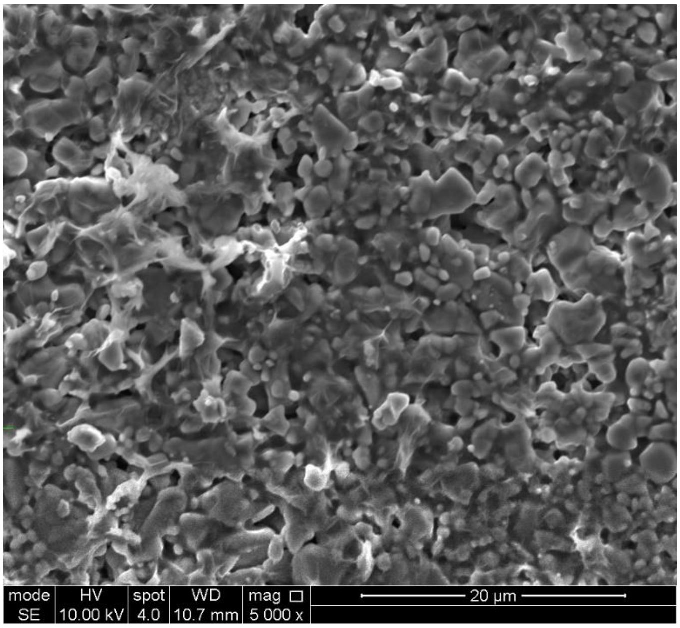

Figure S2. SEM image of the polished surface of $Na_3Zr_{2-x}Si_2PO_{12-2x}$ sintered at 1100°C/12 hours.

4.3 Characterisation of Aqueous cold-sintered $Na_3Zr_2Si_2PO_{12}$

4.3.1 X-ray Diffraction

Following the densification of NZSP by the cold sintering technique, The XRD patterns of the densified pellets at different pressing pressures (125-500 MPa), constant time (1hr) and temperature (120 °C) are shown in Figure 4.3.1a. The X-ray diffraction patterns were matched against NZSP (x = 0.0) samples sintered conventionally, and there were no observable changes to the peaks relating to NZSP except for the presence of the m-ZrO_2 impurity phase at 2θ° values of 28.30 and 31.52 consistent with the literature data [1-10, 21]. The impact of pressing pressure and post-annealing studies on the crystal symmetry of the cold-sintered NZSP ceramic was investigated to understand phase changes associated with these physical properties (pressure and temperature). It was observed that the pressure had an impact on the crystal symmetry of the cold-sintered NZSP as it increased the peak height of the m-ZrO_2 impurity phase of the cold-sintered NZSP, Figure 4.3.1a. The peak height of the m-ZrO_2 impurity phase at 2θ° values of 28.30 and 31.52 were higher than those observed in the conventionally sintered NZSP, Figure 4.3.1a. The increase in the peak height of the m-ZrO_2 impurity phase was observed at all the pressing pressures (125-500 MPa) and constant time (1 hour) and temperature (120 °C) on all the cold-sintered NZSP samples, Figures 4.3.1 (a & b). The increase in the peak height of the m-ZrO_2 was ~ equal at all the pressing pressures. Also, studies on the impact of post-annealing on the cold-sintered NZSP ceramic showed no effect on the crystal symmetry of the ceramic, Figure 4.3.1b. Rather, it improves the densification (section 4.3.2). Post-annealing at 400 °C, however, did not impact the ceramic relative density (see later Table 4.8). Therefore, it can be concluded that an increase in the post-annealing temperature does not alter the crystal symmetry of the cold-sintered NZSP ceramic; rather, it alters the peak height of the m-ZrO_2 in the cold-sintered NZSP.

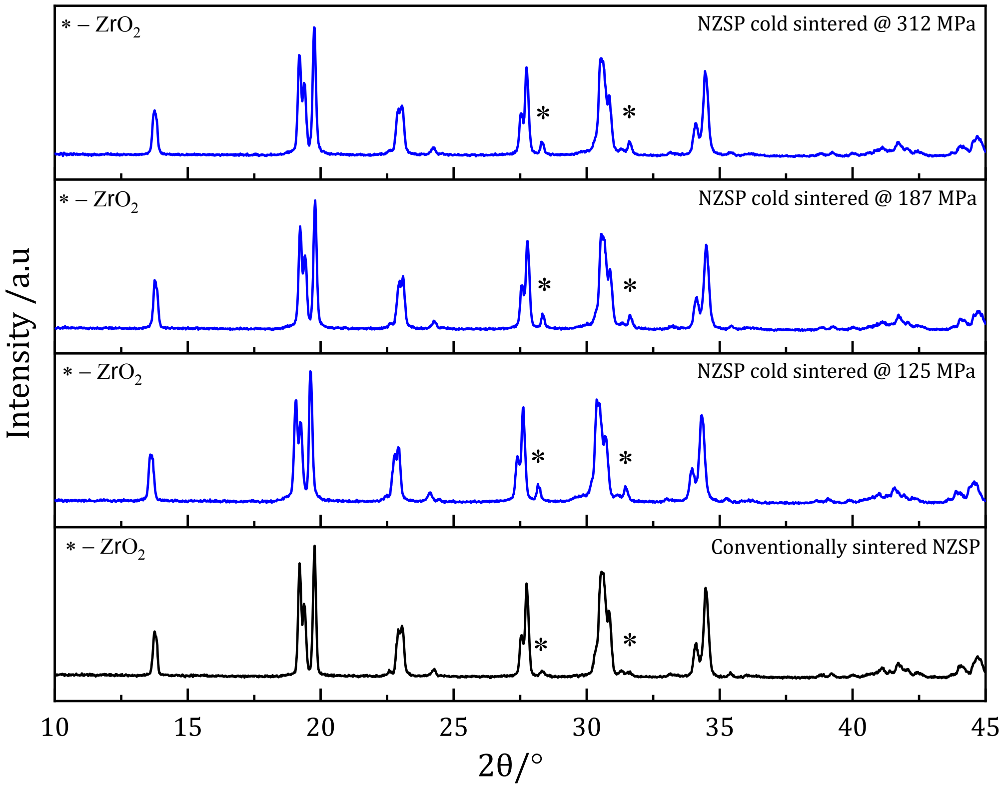

Figure 4.3.1a. XRD patterns of $Na_3Zr_2Si_2PO_{12}$ cold-sintered at 120 °C/1hr at different pressures (MPa)

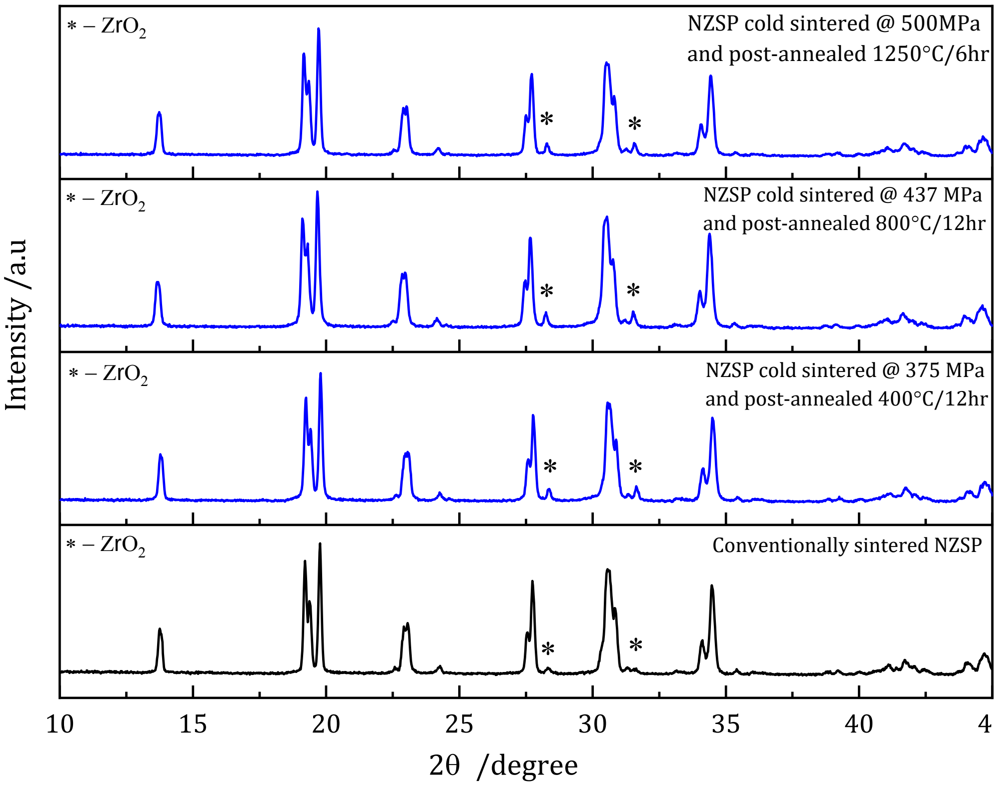

Figure 4.3.1b. XRD patterns of cold-sintered NZSP at different post-annealing temperatures and pressures

4.3.2 Relative density

The relative density of the cold-sintered $Na_3Zr_2Si_2PO_{12}$ was calculated according to equation 3.8 (chapter 3), and the results are shown in Table 4.8. The theoretical density of the conventional sintered NZSP, as obtained from our refinement studies (3.24 gcm^{-3}), was used to calculate the ρ_r. The experimental densities ($\rho_{ex.}$) of the green and post-annealed cold-sintered NZSP were calculated, and the values are recorded in Table 4.8. The relative density of the green cold-sintered NZSP was ~ 80.0%, irrespective of the pressing pressure (MPa), and these values agree with similar cold-sintered reports in the literature [21-25]. The effect of post-annealing at 400 °C on the cold-sintered NZSP did not impact densification, Table 4.8. However, increasing the post-annealing to 800 °C increases the relative density of the cold-sintered NZSP by over 40.0%. A further increase in the post-annealing to 1250 °C was comparable to NZSP sintered conventionally.

Table 4.8

The relative density of cold-sintered $Na_3Zr_2Si_2PO_{12}$

		post-annealed cold-sintered NZSP		
Pressure (MPa)	ρ_r (%) of cold-sintered green NZSP	ρ_r (%) 400°C/12hr	ρ_r (%) 800°C/12hr	ρ_r (%) 1250°C/12hr
125	75.0	77.2		
187.4	80.0	-		
250	80.0	78.7		
312	80.2		89.5	
375	80.6	-	91.0	
437	79.6	-	88.9	
500	80.0	-		95.7
625	80.0	82.0		

4.3.3 Scanning electron microscopy

SEM images of the lightly polished surface of the cold-sintered $Na_3Zr_2Si_2PO_{12}$ ceramic are shown in Figures 4.3.2 - 4.3.4. All the cold-sintered samples were densified at a constant temperature (120 °C) and time (1 hr). The impact of post-annealing could be observed within the SEM micrographs of cold-sintered pellets, Figures 4.3.3 - 4.3.4. Due to the fragile nature and the reactivity (NZSP react with SEM solvents and water) of the cold-sintered NZSP ceramics, the pellets were lightly polished for SEM analysis. Figure 4.3.2 shows a micrograph of the cold-sintered NZSP without post-annealing. The micrograph reveals porous, loose, non-compacted regions with a low agglomeration of NZSP particles supporting a ceramic with $\rho_r \sim 80.0\%$. The results agree with SEM micrographs in the literature on the cold sintering of similar materials [21, 26]. The SEM micrograph shown in Figure 4.3.3 depicts a cold-sintered ceramic that has undergone post-annealing at 400 °C. The micrographs show a low compaction of the particles with fewer pores and weakly bonded particles. Post-annealing at 400°C did impact ceramic densification with $\rho_r \sim 82.0\%$. The micrographs in Figure 4.3.4 revealed the impact of post-annealing at 1250 °C on the cold-sintered NZSP ceramic. The micrographs show well-compacted ceramic with closely clustered grains with $\rho_r \sim 95.0\%$, comparable to conventionally sintered NZSP except for the clustered grains.

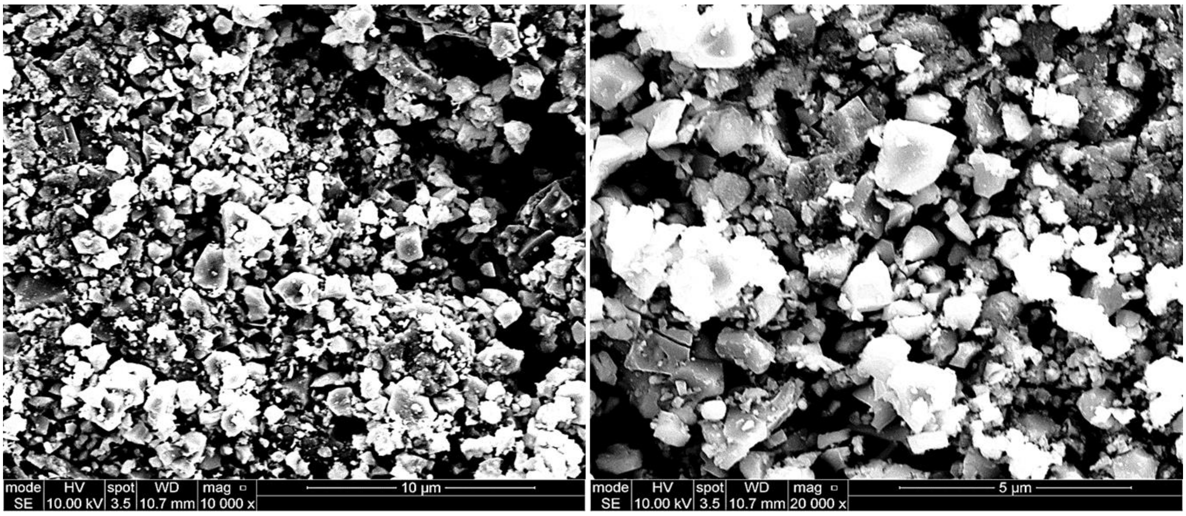

Figure 4.3.2 SEM images of the polished surface of cold-sintered NZSP without post-annealed

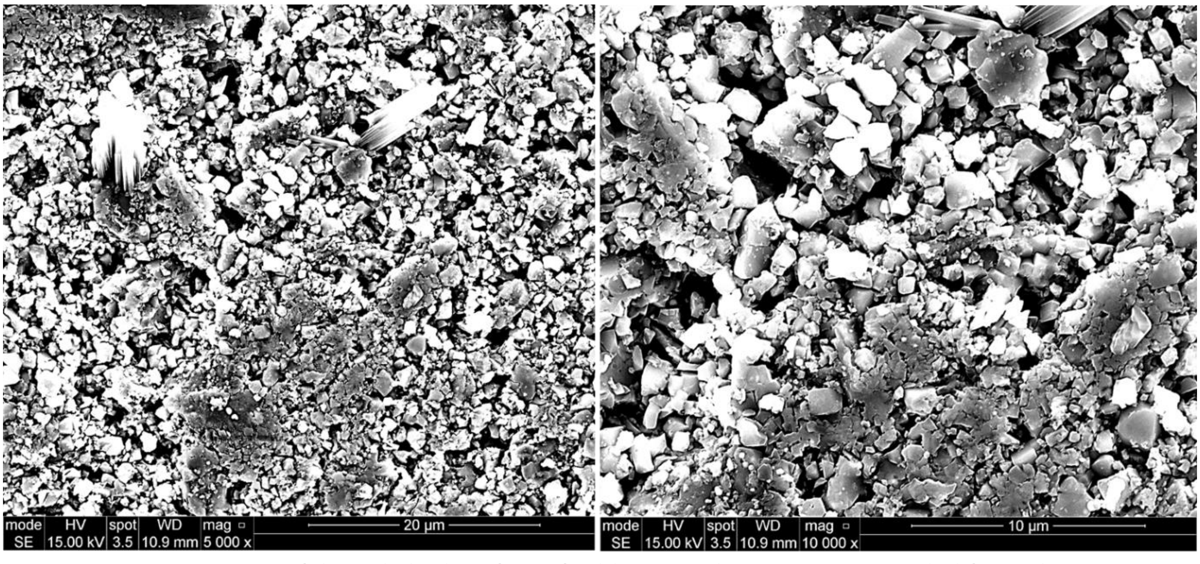

Figure 4.3.3 SEM images of the polished surface of cold-sintered NZSP, post-annealed for 12 hours at 400°C

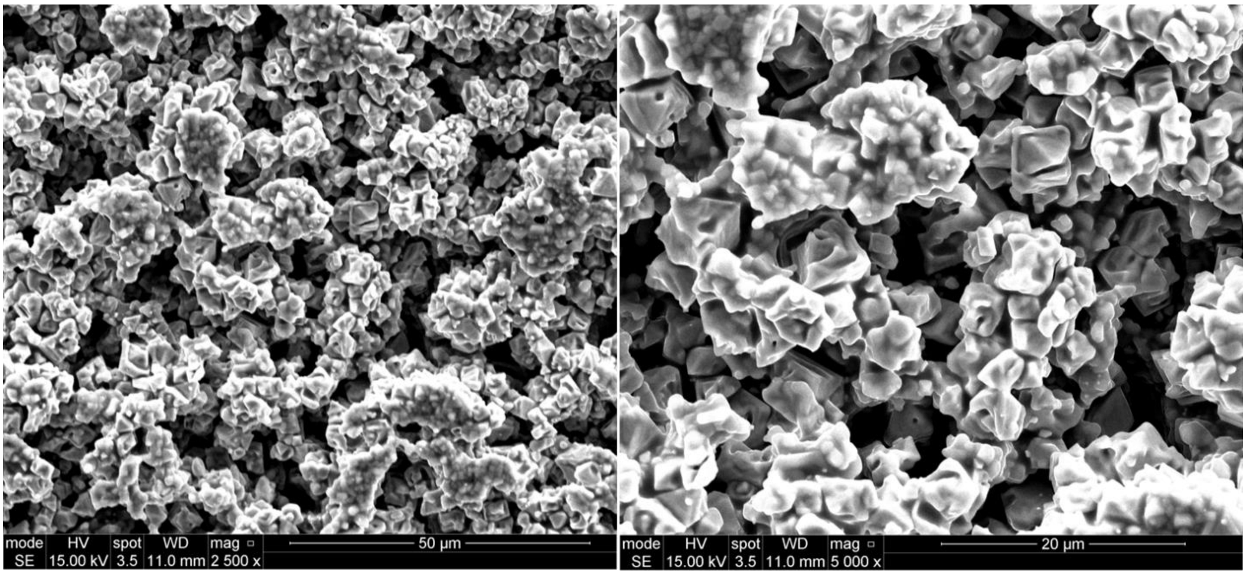

Figure 4.3.4 SEM images of the polished surface of cold-sintered NZSP, post-annealed for 6 hours at 1250°C.

The average grain size of the cold-sintered NZSP was calculated using the line intercept method with image J software. The grain size of the cold-sintered NZSP was calculated according to equation 4.1 (section 4.1.4). Tables 4.9, 4.10 and 4.11 reveal the grain sizes of the cold-sintered NZSP with no post-annealing and post-annealing at 400 °C and 1250 °C, respectively. Lines were drawn across the SEM micrographs using Image J software, and the number of grain intercepts was counted. The average of seven lines drawn across the micrographs and the grain intercepts were estimated. The average grain size of the NZSP with no post-annealing was ~1.24 µm, Table 4.9. The average grain size of NZSP post-annealing at 400 °C was ~ 1.38 µm, Table 4.4. However, the average grain size of the cold-sintered NZSP, post-annealed at 1250 °C was ~7.03 µm. This value is higher than those without post-annealing and 400 °C due to the agglomeration of the grains. Estimating the grains from the agglomerated particles of the 1250 °C NZSP cold sintered samples revealed the grains are between 1.20 and 1.40 µm.

Table 4.9
Grain size of NZSP cold-sintered without post annealing using the line intercept method.

No post-annealing	Area	Mean	Length	grain intercept	Length/no of grains
1	0.46	112.32	10.58	11	0.96
2	0.32	214.86	7.22	7	1.03
3	0.51	97.18	11.57	7	1.65
4	0.26	171.02	5.96	5	1.19
5	0.40	152.03	9.09	8	1.14
6	0.44	130.21	10.10	6	1.68
7	0.26	91.51	6.01	6	1.00

Table 4.10
Grain size of NZSP cold-sintered with post-annealing at 400 °C using the line intercept method.

Post-anneal 400°C	Area	Mean	Length	grain intercept	Length/no of grains
1	0.38	209.93	8.81	7	1.26
2	0.48	167.36	11.10	8	1.39
3	0.41	191.54	9.42	8	1.18
4	0.24	158.33	5.57	4	1.39
5	0.50	130.87	11.37	7	1.62
6	0.52	108.33	12.04	8	1.51
7	0.46	98.79	10.63	8	1.33

Table 4.11
Grain size of NZSP cold-sintered with post-annealing at 1250 °C using the line intercept method.

Post-anneal 1250°C	Area	Mean	Length	grain intercept	Length/no of grains
1	10.47	135.07	65.55	10	6.56
2	10.02	156.74	62.81	11	5.71
3	10.68	114.23	66.89	8	8.36
4	10.50	128.35	65.73	9	7.30
5	3.42	125.37	21.26	3	7.09
6	4.59	135.38	28.61	4	7.15
7	6.77	134.19	42.39	6	7.07

4.3.4 Impedance spectroscopy

The impedance and spectroscopic data at 25 °C of the cold-sintered $Na_3Zr_2Si_2PO_{12}$ post-annealed at different temperatures (400, 800 and 1250 °C) are shown in Figures 4.3.5 – 4.3.7. The complex impedance plane plot of the cold-sintered NZSP pressed at (125 and 250 MPa) and post-annealed for 12 hours at 400 °C is shown in Figure 4.3.5a, and the associated spectroscopic plots are shown in Figures 4.3.5 (b-d). A low-temperature spike and semicircle with a non-zero intercept on the Z' axis were observed, and the total ionic conductivities at 25 °C were $2.73x10^{-5}$ and $2.45x10^{-5}$ S/cm for samples pressed at a pressure of 125 and 250 MPa, respectively. The low-frequency spike is consistent with the charge carriers being Na^+ ions, but the contributions from the bulk and grain boundary responses could not be determined due to the frequency range of the Impedance analyser (Agilent 4294A). The spectroscopic plot of the capacitance is shown in Figure 4.3.5b with values in the range of 10^{-10} Fcm^{-1}, and the spectroscopic plots of the imaginary components M'' and Z'' are shown in Figure 4.3.5 (c & d). Table 4.12 summarises the conductivity value at 25 °C at different pressing pressures and post-annealing. The impedance (Z*) data are similar to those obtained from our conventionally sintered NZSP and the literature [21, 26]. The impact of pressing pressure and post-annealing at 400 °C did not have much effect on the conductivity of the cold-sintered NZSP.

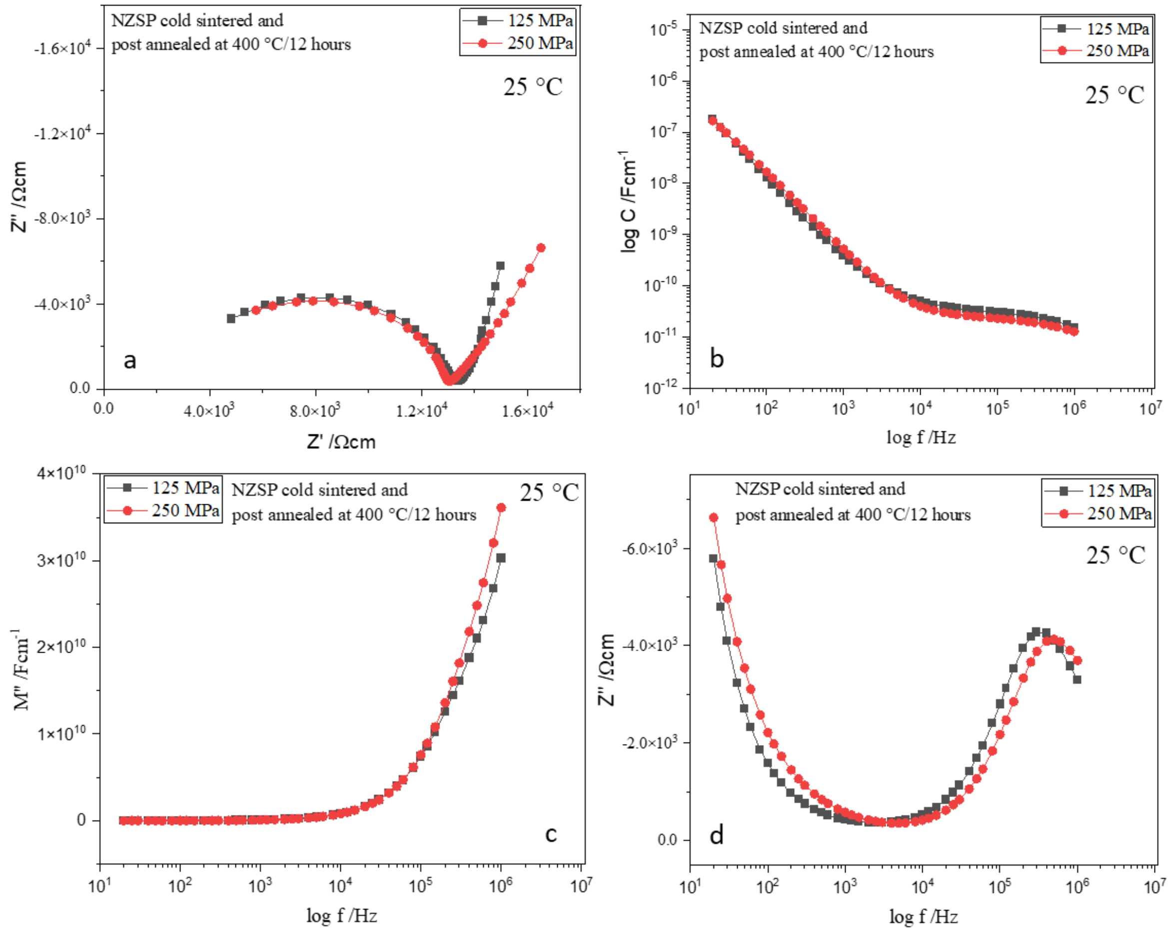

Figure 4.3.5 (a) Impedance complex plane plot and spectroscopic plots at 25 °C of cold-sintered $Na_3Zr_2Si_2P_1O_{12}$ post-annealed for 12 hours at 400 °C (b) capacitance (c) M'' and (d) Z''.

The complex (Z*) impedance plane plot of the cold-sintered NZSP post-annealed at 800 °C is shown in Figure 4.3.6a, and the associated spectroscopic plots are shown in Figure 4.3.6 (b-d). The effect of pressing pressure (312, 375 and 437 MPa) was studied on the conductivity of the cold-sintered ceramic. A low-temperature spike and arc with a non-zero intercept on the Z' axis were observed, and the total ionic conductivity at 25°C were $1.25*10^{-4}$, $1.43*10^{-4}$ and $1.10x10^{-4}$ S/cm for 312, 375 and 437 MPa, respectively. The low-frequency spike is consistent with the charge carriers being Na^+ ions, and the contributions from the bulk and grain boundary responses could not be determined due to the frequency range of the Impedance (Agilent 4294A). The total ionic conductivity of the cold-sintered NZSP pressed was similar and higher than those reported for post-annealing at 400 °C. The spectroscopic plot of the capacitances is shown in Figure 4.3.6b with values in the range of 10^{-10} Fcm^{-1}, and the Z'' plot contains a single peak corresponding to the partial arc in 4.3.6a. The spectroscopic plots of the imaginary components M'' and Z'' are shown in Figure 4.3.6 (c & d).

Overall, post-annealing at 800 °C has much impact on the conductivity of the cold-sintered NZSP as it increases the conductivity by 10-fold compared to those post-annealed at 400 °C.

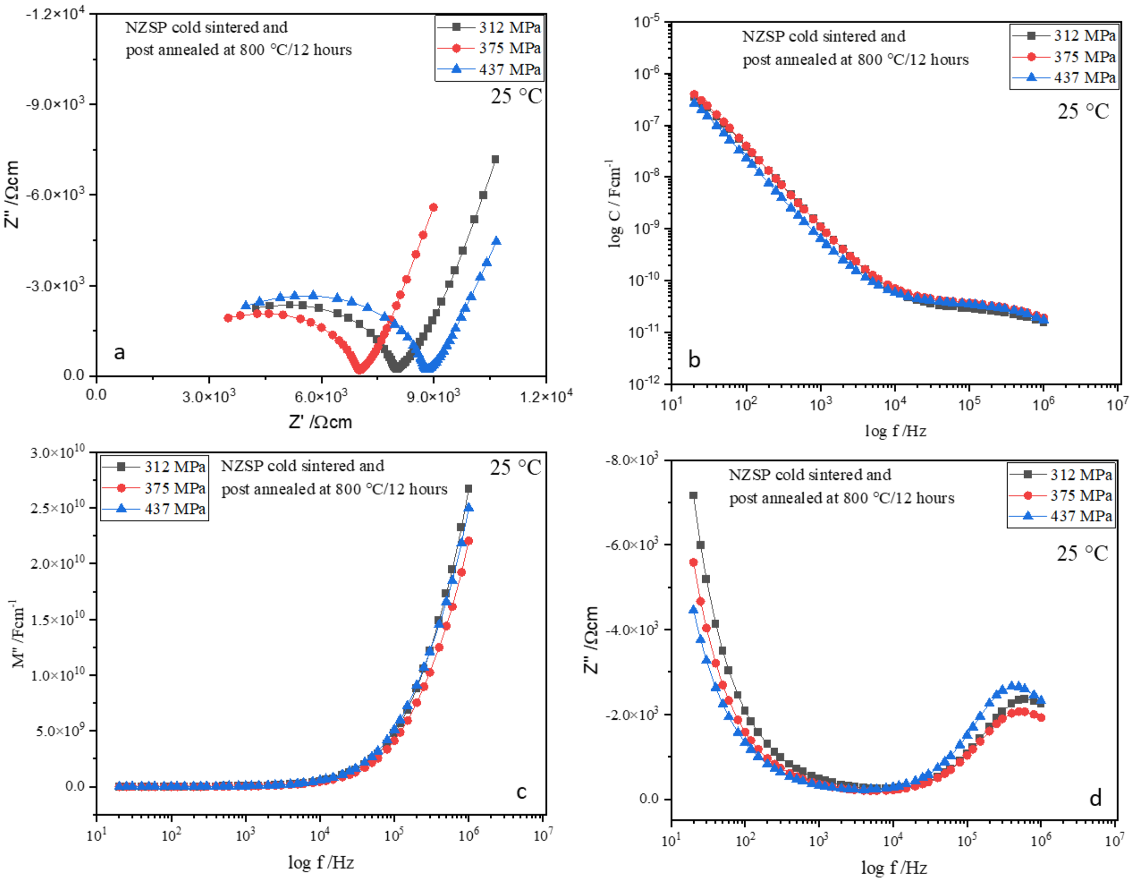

Figure 4.3.6 (a) Impedance complex plane plot and spectroscopic plots at 25 °C of cold-sintered $Na_3Zr_2Si_2P_1O_{12}$ post-annealed for 12 hours at 800 °C (b) capacitance (c) M'' and (d) Z''.

Figure 4.3.7 compares the complex impedance plane and spectroscopic plots of the cold-sintered NZSP (post-annealed at 1250 °C) and conventionally sintered NZSP. A low-temperature spike and arc with a non-zero intercept on the Z' axis were observed, and the total ionic conductivity at 25 °C were 8.75x10^{-4} and 6.32x10^{-4} S/cm for the cold and conventional sintered NZSP, respectively. The low-frequency spike is consistent with the charge carriers being Na^+ ions. The spectroscopic plot of the capacitances is shown in Figure 4.3.7b with values in the range of 10^{-9} Fcm^{-1}. The spectroscopic plots of the imaginary components M'' and Z'' are shown in Figure 4.3.7 (c and d).

Overall, the impact of post-annealing studies on the conductivity of the cold-sintered ceramic revealed that an increase in the post-annealing temperature increases the conductivity. In addition, increasing the post-annealing temperature from 400 to 800 °C increases the conductivity by over 10-fold, while increasing the post-annealing from 800 to 1250 °C did not have much impact on the conductivity. The results obtained agreed with similar studies in the literature [21, 26].

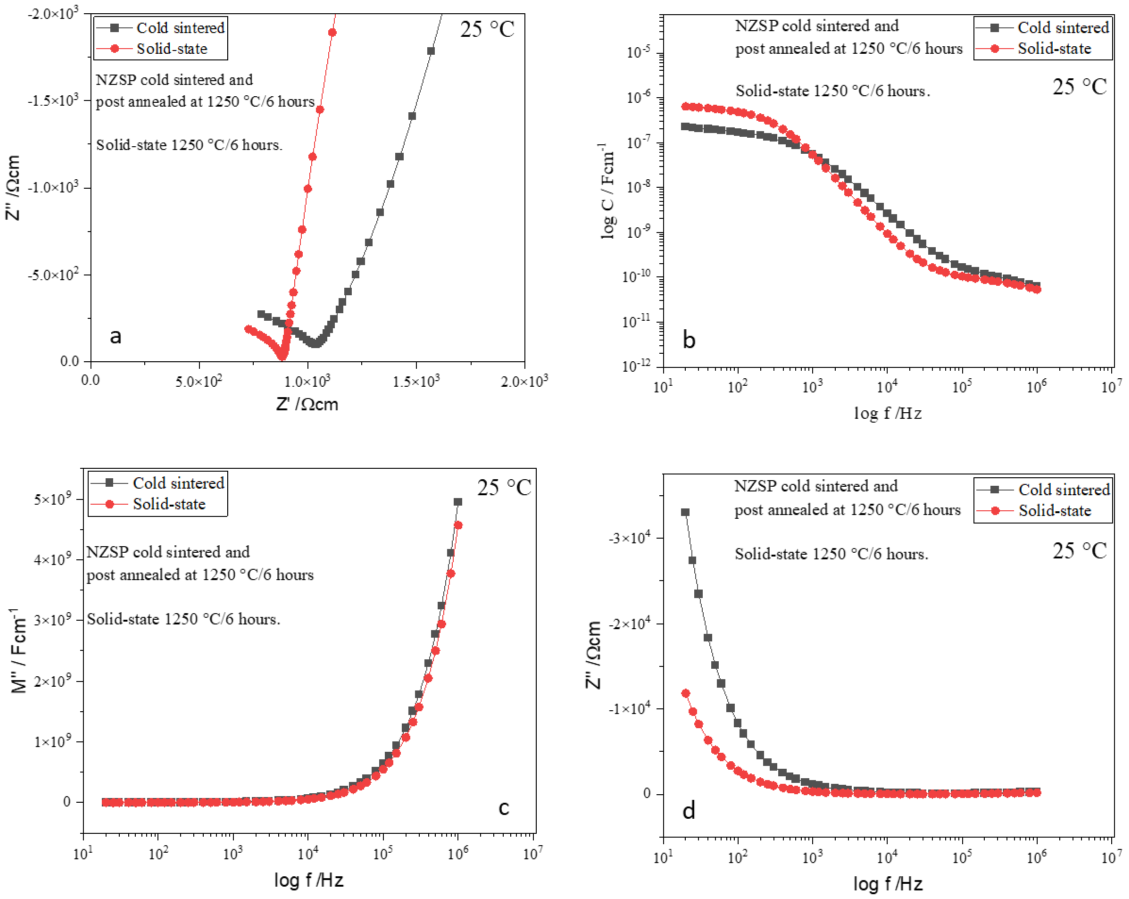

Figure 4.3.7 (a) Impedance complex plane plot and spectroscopic plots at 25 °C of cold-sintered $Na_3Zr_2Si_2P_1O_{12}$ post-annealed for 6 hours at 1250 °C (b) capacitance (c) M'' and (d) Z''.

Table 4.12

Ionic conductivity of cold-sintered $Na_3Zr_2Si_2PO_{12}$ at 25 °C

Pressure (MPa)	Post-annealed conductivity (S/cm) at 25 C		
	400 °C/12hr	800 °C/12hr	1250 °C/6hr
125	$2.73*10^{-5}$		
250	$2.45*10^{-5}$		
312		$1.25*10^{-4}$	
375		$1.43*10^{-4}$	
437		$1.10*10^{-4}$	
500			$8.75*10^{-4}$

4.3.5 Arrhenius plot of the cold-sintered $Na_3Zr_2Si_2PO_{12}$

To calculate the Activation energy (E_a), we utilise equation 3.35 (chapter 3). The gradient of the plot was obtained by the least square method, and the results are shown in Table 4.13. Arrhenius plot of the total conductivity of the cold-sintered NZSP (where $\sigma_T = 1/R_T$) is shown in Figures 4.3.8 (a - f). The E_a associated with the cold-sintered NZSP pressed at 125 and 250 MPa and post-annealed at 400 °C have similar high E_a values of 0.41 eV, Figures 4.3.8 (a and b). These values were higher than those reported for conventional sintered NZSP (section 4.1.8) and the literature values [10-14, 21 and 26]. Furthermore, the E_a associated with cold-sintered NZSP pressed at 312, 375 and 437 MPa and post-annealed at 800 °C have similar E_a values ~ 0.34 eV, Figures 4.3.8 (c-e). The E_a values are similar to the literature data [10-14, 21 and 26]. Finally, the E_a of NZSP pressed at 500MPa and post-annealing at 1250 °C is (~0.35 eV), Figure 4.3.8f, similar to the literature data. Tables 4.13 and 4.14 show the data for plotting the gradients and the associated activation energy and uncertainty values.

In summary, the activation energy of the cold-sintered NZSP is inversely proportional to pressing pressure and post-annealing temperature. As the pressing pressure and temperature increase, the activation energy decreases.

Table 4.13
Temperature-dependent conductivity table of cold-sintered NZSP and the pressing pressure

		Post annealed 400 °C/ 12hr				Post annealed 800 °C/12hr			Post annealed 1250°C/6hr
		125MPa	250MPa			312MPa	375MPa	437MPa	500MPa
Temperature (°C)	1000/T (K)	Log σ_t	Log σ_t	Temperature (°C)	1000/T (K)	Log σ_t	Log σ_t	Log σ_t	Log σ_t
80	2.83	-3.27	-3.27	40	3.19	-3.72	-3.65	-3.78	-2.77
120	2.54	-2.60	-2.57	80	2.83	-3.05	-3.02	-3.12	-2.30
160	2.31	-2.15	-2.13	120	2.54	-2.57	-2.54	-2.45	-1.76
200	2.11	-1.80	-1.78	160	2.31	-2.12	-2.04	-2.18	-1.55
				200	2.11	-1.88	-1.74	-1.97	

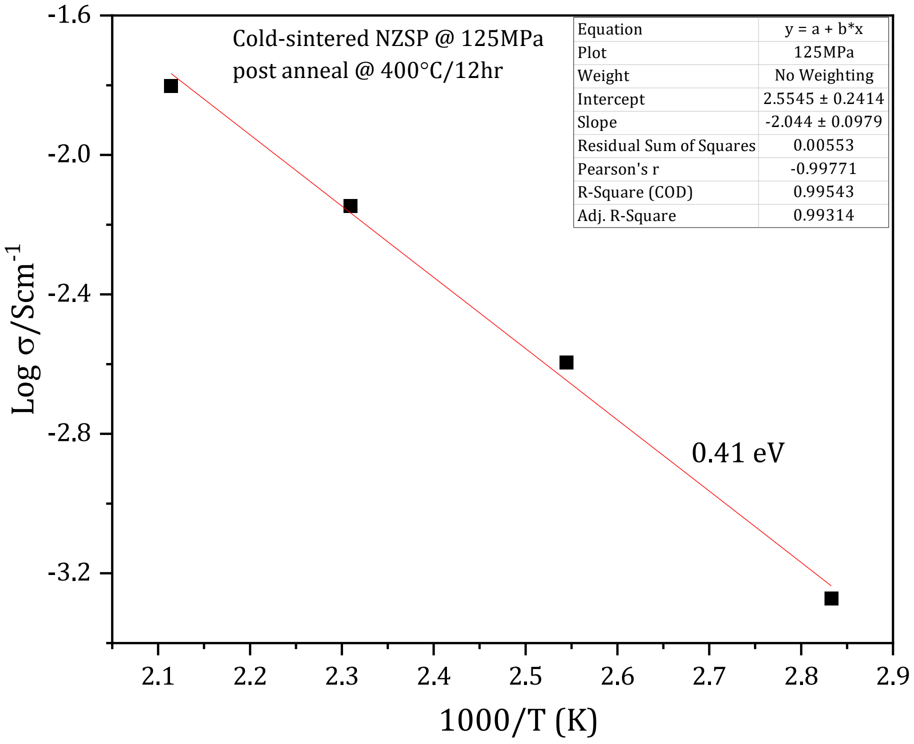

Figure 4.3.8a. Arrhenius plot of the total conductivity of cold-sintered NZSP after post-annealing at 400°C

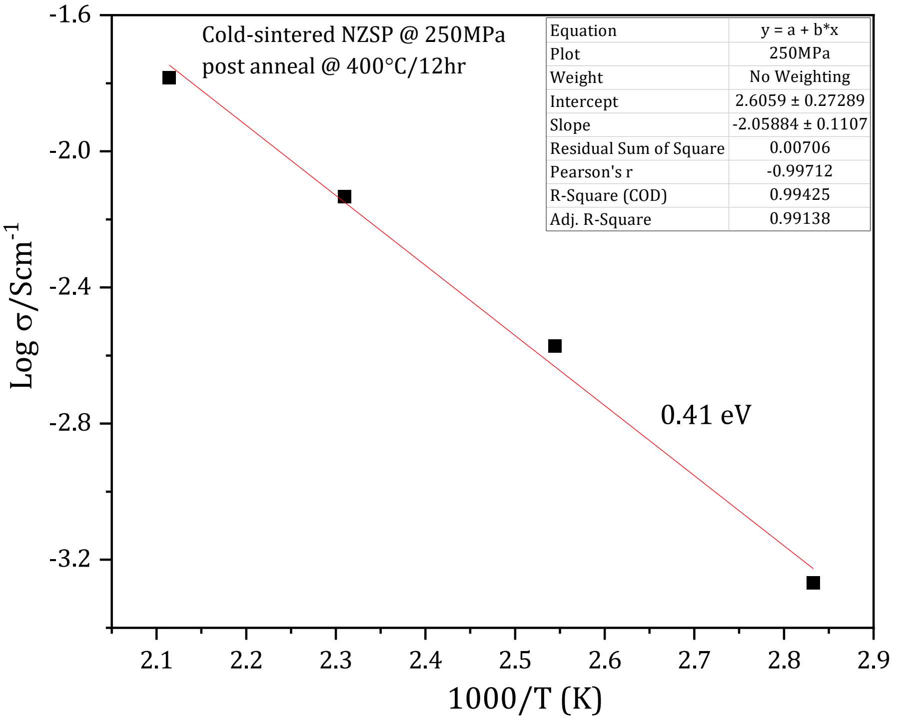

Equation	y = a + b*x
Plot	250MPa
Weight	No Weighting
Intercept	2.6059 ± 0.27289
Slope	-2.05884 ± 0.1107
Residual Sum of Square	0.00706
Pearson's r	-0.99712
R-Square (COD)	0.99425
Adj. R-Square	0.99138

Figure 4.3.8b. Arrhenius plot of the total conductivity of cold-sintered NZSP after post-annealing at 400°C

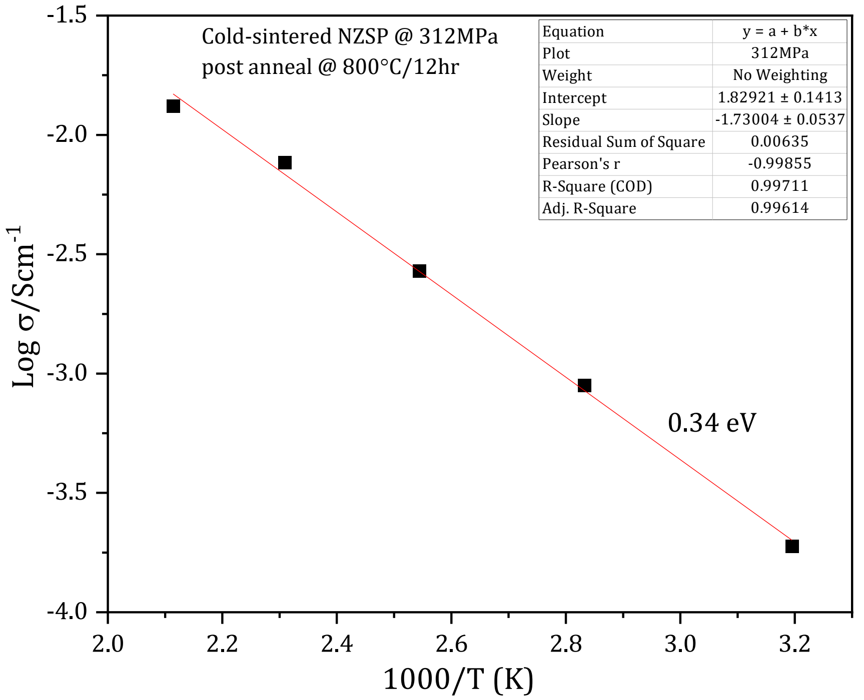

Equation	y = a + b*x
Plot	312MPa
Weight	No Weighting
Intercept	1.82921 ± 0.1413
Slope	-1.73004 ± 0.0537
Residual Sum of Square	0.00635
Pearson's r	-0.99855
R-Square (COD)	0.99711
Adj. R-Square	0.99614

Figure 4.3.8c. Arrhenius plot of the total conductivity of cold-sintered NZSP after post-annealing at 800°C

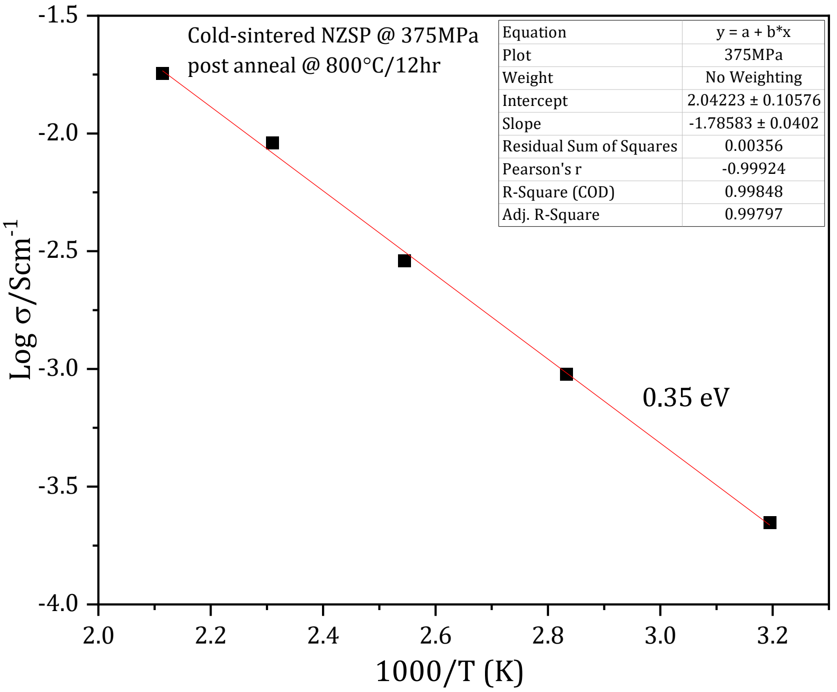

Figure 4.3.8d. Arrhenius plot of the total conductivity of cold-sintered NZSP after post-annealing at 800°C

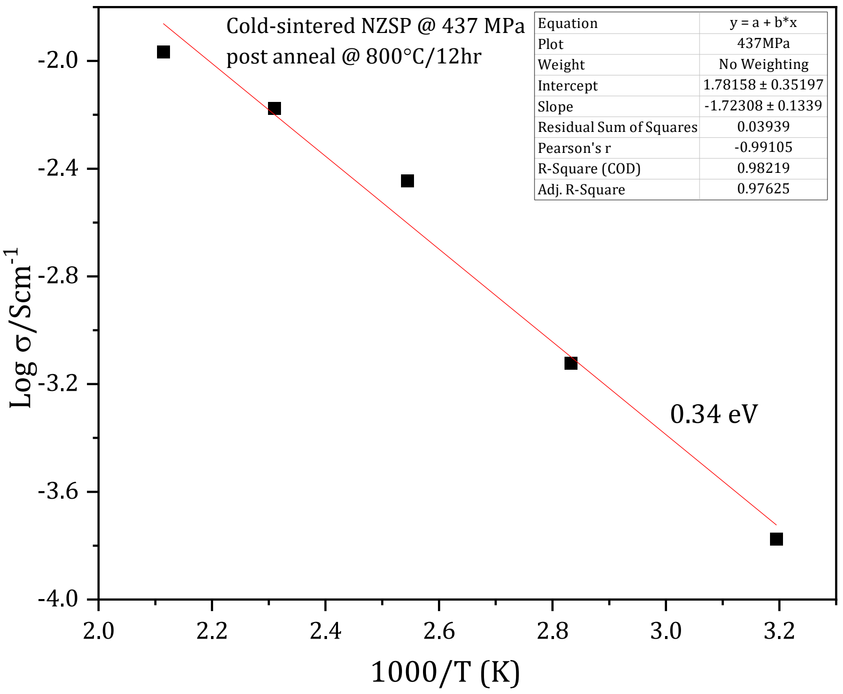

Figure 4.3.8e. Arrhenius plot of the total conductivity of cold-sintered NZSP after post-annealing at 800°C

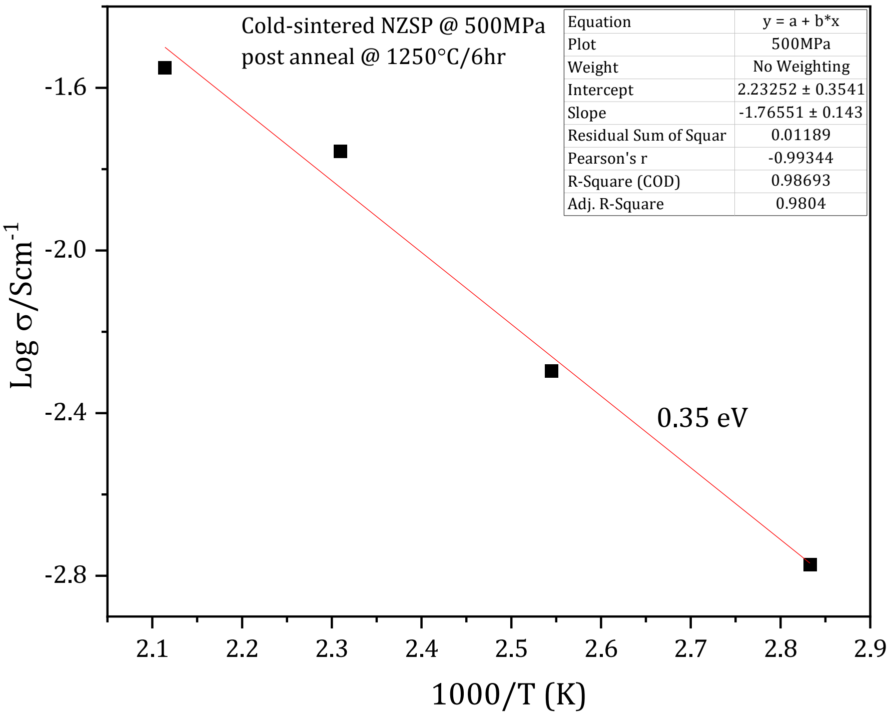

Figure 4.3.8f. Arrhenius plot of the total conductivity of cold-sintered NZSP after post-annealing at 1250°C

Table 4.14

Ionic conductivity of cold-sintered $Na_3Zr_2Si_2PO_{12}$ at 25 °C and the associated E_a.

The activation energy of cold-sintered NZSP			
Pressure MPa	Post-annealed (°C)	Post-annealed time (hours)	(Ea)/ eV
125	400	12	0.41 ± 0.09
250	400	12	0.41 ± 0.11
312	800	12	0.34 ± 0.05
375	800	12	0.35 ± 0.04
437	800	12	0.34 ± 0.13
500	1250	6	0.34 ± 0.14

4.4 Conclusion

The sodium superionic conductor $Na_{x+1}Zr_2Si_xP_{3-x}O_{12}$ ($0.0 \le x \le 3.0$) was investigated as a solid electrolyte. Several compositions of $Na_xZr_{2-x}Si_xP_{3-x}O_{12-2x}$ (x = 0.0, 0.10, 0.20, 0.30, 0.40, 0.50 and 0.60) with altered mole fractions of ZrO_2 reactant were prepared, and various sintering studies were investigated. Raman spectroscopy and X-ray diffraction studies confirmed a single-phase without *m*-ZrO_2 impurity for NZSP (x = 0.60), and *m*-ZrO_2 impurity phase observed in all other compositions of NZSP (x = 0.0, 0.10, 0.20, 0.30, 0.40 and 0.50). Refinement studies of the X-ray diffraction data confirmed phases of 43.0 % monoclinic (*C12/c*) and 57.0 % rhombohedral (*R-3c*) for NZSP (x = 0.60). SEM images revealed a dense, cuboid grain morphology for both compositions (x = 0.0 and 0.60) typical of NASICONs. However, the average grain size of NZSP (x = 0.60) is ~ 55.0 % greater than NZSP (x = 0.0), and all NZSP compositions have $\rho_r > 92.0$ %. Studies on the volume change as a function of temperature on NZSP (x = 0.0 and 0.60) provided insight into the melt-pool phase of the ceramic. The bulk, grain boundary and total ionic conductivity of the NZSP (x = 0.0 and 0.60) were investigated at 160 and 295 K using impedance spectroscopy. NZSP (x = 0.0) with a monoclinic crystal structure has a higher RT bulk conductivity of $\sim 1.3 \times 10^{-3}$ Scm^{-1}. In contrast, NZSP (x = 0.60) with mixed rhombohedral and monoclinic phases gave a slightly lower RT bulk conductivity of ~ 6.5×10^{-4} Scm^{-1}, but both were comparable with literature values.

The cold-sintering studies on the densification of NZSP revealed that the results were only comparable with the conventional sintered NZSP upon post-annealing at higher temperatures. There were no changes to the phase assemblage except for the increase in the peak height of the *m*-ZrO_2 impurity phase of the cold compared to the conventional sintered ceramics, as revealed by XRD. The SEM images showed the impact of post-annealing on the morphology of the ceramic, and samples without post-annealing contained loose particles of NZSP. All the cold-sintered NZSP's ionic conductivities were lower even after post-annealing at higher temperatures, and the activation energies were higher compared to the conventional and literature values. The cold sintering process of NZSP is energy-intensive in its present form and not worth exploring. Using more aggressive inorganic solvents such as dimethylformamide may improve the process but with more significant concerns over health and safety.

4.5 References

[1] A. Ignaszak, P. Pasierb, R. Gajerski, S. Komornicki, Synthesis and properties of Nasicon-type materials, Thermochimica Acta. 426 (2005) 7–14. https://doi.org/10.1016/j.tca.2004.07.002.

[2] A. Jalalian-Khakshour, C.O. Phillips, L. Jackson, T.O. Dunlop, S. Margadonna, D. Deganello, Solid-state synthesis of NASICON ($Na_3Zr_2Si_2PO_{12}$) using nanoparticle precursors for optimisation of ionic conductivity, Journal of Materials Science. 55 (2019) 2291–2302. https://doi.org/10.1007/s10853-019-04162-8.

[3] S. Narayanan, S. Reid, S. Butler, and V. Thangadurai, “Sintering temperature, excess Na, and phosphorous dependencies on morphology and ionic conductivity of $Na_3Zr_2Si_2PO_{12}$ *Solid State Ionics*, vol. 331, Mar. 2019, doi.org/10.1016/j.ssi.2018.12.003.

[4] S. Naqash, Q. Ma, F. Tietz, O. Guillon, $Na_3Zr_2(SiO_4)_2(PO_4)$ prepared by a solution-assisted solid-state reaction, Solid State Ionics. 302 (2017) 83–91. https://doi.org/10.1016/j.ssi.2016.11.004.

[5] A. Parejiya, R. Essehli, R. Amin, J. Liu, N. Muralidharan, H.M. Meyer, D.L. Wood, I. Belharouak, $Na_{1+x}Mn_{x/2}Zr_{2-x/2}(PO_4)_3$ as a Li^+ and Na^+ Super Ion Conductor for Solid-State Batteries, ACS Energy Letters. 6 (2021) 429–436. doi.org/10.1021/acsenergylett.0c02513.

[6] Z. Deng, G. Sai Gautam, S.K. Kolli, J.-N. Chotard, A.K. Cheetham, C. Masquelier, P. Canepa, Phase Behavior in Rhombohedral NaSiCON Electrolytes and Electrodes, Chemistry of Materials. 32 (2020) 7908–7920. doi.org/10.1021/acs.chemmater.0c02695.

[7] P. Yadav and M. C. Bhatnagar, “Structural studies of NASICON material of different compositions by sol-gel method,” *Ceramics International*, vol. 38, no. 2, pp. 1731–1735, Mar. 2012, https://doi.org/10.1016/j.ceramint.2011.09.022.

[8] M. Guin and F. Tietz, “Survey of the transport properties of sodium superionic conductor materials for use in sodium batteries,” *Journal of Power Sources*, vol. 273, pp. 1056–1064, Jan. 2015. doi.org/10.1016/j.jpowsour.2014.09.137.

[9] M. Samiee, B. Radhakrishnan, Z. Rice, Z. Deng, Y.S. Meng, S.P. Ong, J. Luo, Divalent-doped $Na_3Zr_2Si_2PO_{12}$ natrium superionic conductor: Improving the ionic conductivity via simultaneously optimising the phase and chemistry of the

primary and secondary phases, Journal of Power Sources. 347 (2017) 229–237. https://doi.org/10.1016/j.jpowsour.2017.02.042.

[10] S.K. Pal, R. Saha, G.V. Kumar, S. Omar, Designing High Ionic Conducting NASICON-type $Na_3Zr_2Si_2PO_{12}$ Solid-Electrolytes for Na-Ion Batteries, The Journal of Physical Chemistry C. 124 (2020) 9161–9169. https://doi.org/10.1021/acs.jpcc.0c00543.

[11] J.-S. Lee, C.-M. Chang, Y.I. Lee, J.-H. Lee, S.-H. Hong, Spark Plasma Sintering (SPS) of NASICON Ceramics, Journal of the American Ceramic Society. 87 (2004) 305–307. https://doi.org/10.1111/j.1551-2916.2004.00305.x.

[12] K. Okubo, H. Wang, K. Hayashi, M. Inada, N. Enomoto, G. Hasegawa, T. Osawa, H. Takamura. A dense NASICON sheet prepared by tape-casting and low-temperature sintering, Electrochimica Acta. 278 (2018) 176–181. https://doi.org/10.1016/j.electacta.2018.05.020.

[13] A. Chakraborty, Raghunayakula Thirupathi, S. Bhattacharyya, K. Singh, S. Omar, Mg-doped NASICON-type electrolyte for rechargeable solid-state Na-ion batteries, 572 (2023) 233092-233092. doi.org/10.1016/j.jpowsour.2023.233092.

[14] Y.B. Rao, L.N. Patro, Influence of synthesis methodology and excess Na on the ionic transport properties of natrium superionic conductor, $Na_3Zr_2Si_2PO_{12}$, Materials Letters. 301 (2021) 130267. https://doi.org/10.1016/j.matlet.2021.130267.

[15] R. Rajagopalan, Z. Zhang, Y. Tang, C. Jia, X. Ji, H. Wang, Understanding crystal structures, ion diffusion mechanisms and sodium storage behaviour of NASICON materials, Energy Storage Materials. (2021) 171–193. doi.org/10.1016/j.ensm.2020.09.007.

[16] M. Avdeev, Crystal Chemistry of NASICONs: Ideal Framework, Distortion, and Connection to Properties, Chemistry of Materials. 33 (2021) 7620–7632. https://doi.org/10.1021/acs.chemmater.1c02695.

[17] R. Rajagopalan, Z. Zhang, Y. Tang, C. Jia, X. Ji, H. Wang, Understanding crystal structures, ion diffusion mechanisms and sodium storage behaviours of NASICON materials, Energy Storage Materials. 34 (2021) 171–193. doi.org/10.1016/j.ensm.2020.09.007.

[18] D.A. Edelman, T.G. Brandt, E. Temeche, R.M. Laine, Sodium-based solid electrolytes and interfacial stability. Towards solid-state sodium batteries, Materials Today Communications. 32 (2022) 104009. doi.org/10.1016/j.mtcomm.2022.104009.

[19] K. Ren, Y. Cao, Y. Chen, G. Shao, J. Dai, and Y. Wang, “Flash sintering of $Na_3Zr_2(SiO_4)_2(PO_4)$ solid-state electrolyte at a furnace temperature of 700 °C.” *Scripta Materialia*, vol. 187, Oct. 2020, doi.org/10.1016/j.scriptamat.2020.06.055.

[20] M. Barj, G. Lucazeau, and C. Delmas, “Raman and infrared spectra of some chromium Nasicon-type materials: Short-range disorder characterisation,” *Journal of Solid State Chemistry*, vol. 100, no. 1, pp. 141–150, Sep. 1992, https://doi.org/10.1016/0022-4596(92)90164-q.

[21] H. Leng, J. Huang, J. Nie, and J. Luo, “Cold sintering and ionic conductivities of $Na_{3.256}Mg_{0.128}Zr_{1.872}Si_2PO_{12}$ solid electrolytes,” *Journal of Power Sources*, vol. 391, pp. 170–179, Jul. 2018, https://doi.org/10.1016/j.jpowsour.2018.04.067.

[22] B. Nie, T. Liu, Mataz Alcoutlabi, S. Basu, Soundar Kumara, M. Li, J. Lian, H. Sun, Cold sintering-enabled interface engineering of composites for solid-state batteries, 11 (2023). https://doi.org/10.3389/fenrg.2023.1149103.

[23] S. S. Berbano, J. Guo, H. Guo, M. T. Lanagan, and C. A. Randall, “Cold sintering process of $Li_{1.5}Al_{0.5}Ge_{1.5}(PO_4)_3$ solid electrolyte,” *Journal of the American Ceramic Society*, vol. 100, no. 5, pp. 2123–2135, Mar. 2017, doi.org/10.1111/jace.14727.

[24] Y. Liu, J. Liu, Q. Sun, D. Wang, K.R. Adair, J. Liang, C. Zhang, L. Zhang, S. Lu, H. Huang, X. Song, X. Sun, Insight into the Microstructure and Ionic Conductivity of Cold Sintered NASICON Solid Electrolyte for Solid-State Batteries, ACS Applied Materials & Interfaces. 11 (2019) 27890–27896. doi.org/10.1021/acsami.9b08132.

[25] J. Yun Seo, K. Verlinde, R. Rajagopalan, E. D. Gomez, T. E. Mallouk, and C. A. Randall, “Cold sintering process for fabrication of a high volumetric capacity $Li_4Ti_5O_{12}$ anode,” vol. 250, pp. 114435, Nov. 2019, doi.org/10.1016/j.mseb.2019.114435.

[26] Z. Grady, K. Tsuji, A. Ndayishimiye, J. Hwan-Seo, C.A. Randall, Densification of a Solid-State NASICON Sodium-ion Electrolyte Below 400 °C by Cold Sintering with a Fused Hydroxide Solvent, ACS Applied Energy Materials. 3 (2020) 4356–4366. https://doi.org/10.1021/acsaem.0c00047.

Chapter 5

5.0 Densification of $Na_{1.3}Al_{0.3}Ti_{1.7}P_3O_{12}$ by conventional and cold sintering.

This chapter discusses the results of the conventional and cold-sintered NATP. The results from each characterisation technique were compared and contrasted against each other and the literature. The NATP powdered was sourced from a commercial vendor (NEI Corporations, U.S.A.) and used without further processing.

5.1 NATP powder

The NATP powder was studied to understand its phase, grain size distribution and morphology.

5.1.1 Grain Size Distribution

The size distribution of the NATP green powder was analysed using a Malvern Mastersizer particle analyser 3000. Prior to the measurement, the refractive index of the dispersant (H_2O) and NATP was determined to ensure accurate measurements. Ten different measurements were taken to ensure the reliability of the data. The grain sizes of the NATP were recorded at various Dx values (Dx refer to the diameter of the grain at a certain percentile point in a size distribution curve, and the number in parentheses represents the percentile point. The Dx values are used to assess the grain size distribution and provide information about the size range and distribution of grains in the sample.). The grain distribution of the NATP powder shows a bimodal size distribution, Figure 5.1.1. Suggesting that the grains were agglomerated and irregular. Table 5.1 shows the average grain size and the different Dx size distributions of NATP. Dx (10) refers to the diameter at which 10% of the grains in the sample are smaller than the average grain size. Dx (50) represents the median diameter at which 50% of the grains in the sample are smaller than the average grain size, and Dx (90) indicates the diameter below which 90% of the grains in the sample are smaller than the average grain size. The Mastersizer only provides an estimate of the size distribution of the NATP and not the actual grain size of the NATP.

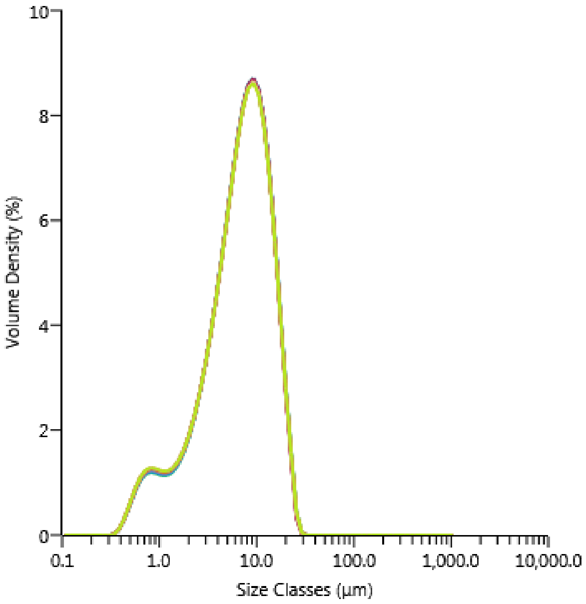

Figure 5.1.1. Grain size distribution of NATP powder.

Table 5.1

The grain size distribution of the $Na_{1.3}Al_{0.3}Ti_{1.7}P_3O_{12}$ green powder.

Record Number	Sample Name	Dx (10) (µm)	Dx (50) (µm)	Dx (90) (µm)
1	$Na_{1.3}Al_{0.3}Ti_{1.7}P_3O_{12}$	1.46	6.89	15.3
2	$Na_{1.3}Al_{0.3}Ti_{1.7}P_3O_{12}$	1.43	6.87	15.2
3	$Na_{1.3}Al_{0.3}Ti_{1.7}P_3O_{12}$	1.41	6.85	15.2
4	$Na_{1.3}Al_{0.3}Ti_{1.7}P_3O_{12}$	1.40	6.84	15.2
5	$Na_{1.3}Al_{0.3}Ti_{1.7}P_3O_{12}$	1.38	6.82	15.0
6	$Na_{1.3}Al_{0.3}Ti_{1.7}P_3O_{12}$	1.37	6.80	14.9
7	$Na_{1.3}Al_{0.3}Ti_{1.7}P_3O_{12}$	1.36	6.80	14.9
8	$Na_{1.3}Al_{0.3}Ti_{1.7}P_3O_{12}$	1.36	6.80	14.9
9	$Na_{1.3}Al_{0.3}Ti_{1.7}P_3O_{12}$	1.36	6.83	15.2
10	$Na_{1.3}Al_{0.3}Ti_{1.7}P_3O_{12}$	1.35	6.80	14.9
Mean		**1.39**	**6.83**	**15.1**
Std. Dev		0.03	0.03	0.15

5.1.2 X-ray diffraction

The XRD pattern of the NATP green powder is shown in Figure 5.1.2. The diffraction peaks were matched to a rhombohedral $Na_{1.3}Al_{0.3}Ti_{1.7}P_3O_{12}$ with space group *R-3c* and PDF Nº 01-014-7800. There were no observable differences in the peaks, and all peaks match the rhombohedral NATP phase except for an unknown peak at 22.4, 2θ degrees.

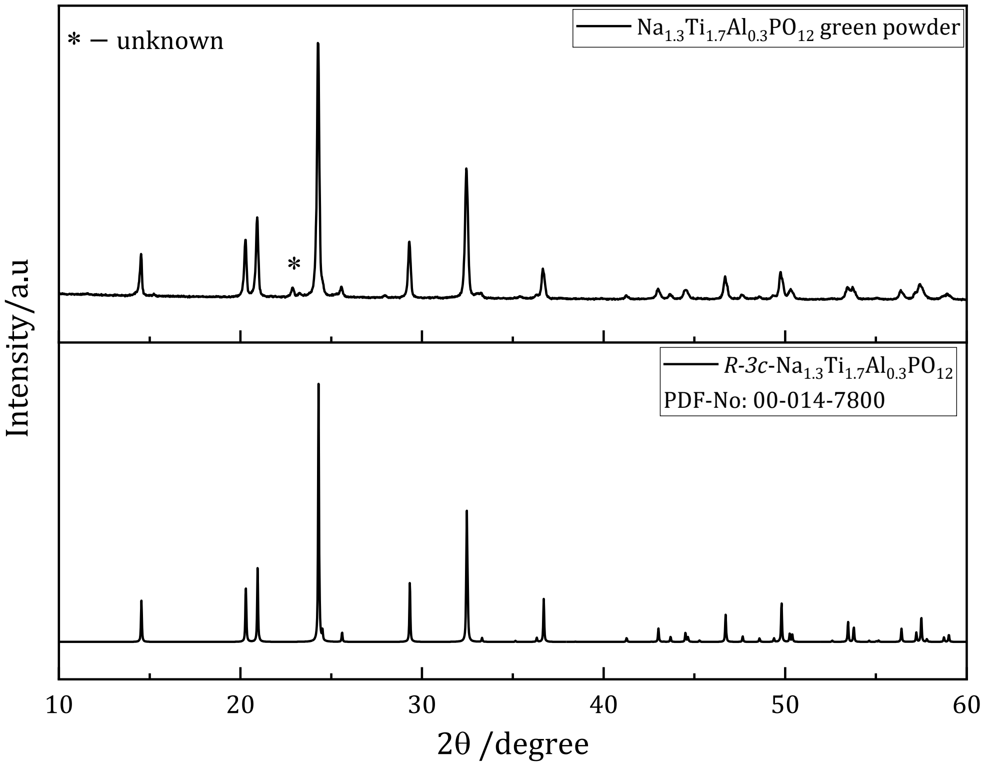

Figure 5.1.2. XRD patterns of the NATP green powder matched against *R-3c* NATP.

5.1.3 Dilatometry

The changes in the volume of the green NATP pellets as a function of temperature are shown in Figure 5.1.3. There was insignificant volume contraction (0.01 m^3) over a wide temperature range up to 900 °C, unlike NZSP (chapter 4). A change in the volume contraction of the NATP was observed at above 900 °C, which is higher than the sintering temperature of the ceramic. Investigation into the melt pool phase of NATP, as observed in NZSP, resulted in a burnt NATP ceramic, indicating there are no such phases present in the NATP. However, the volume contraction studies allow us to predict the optimum sintering temperature of the ceramic.

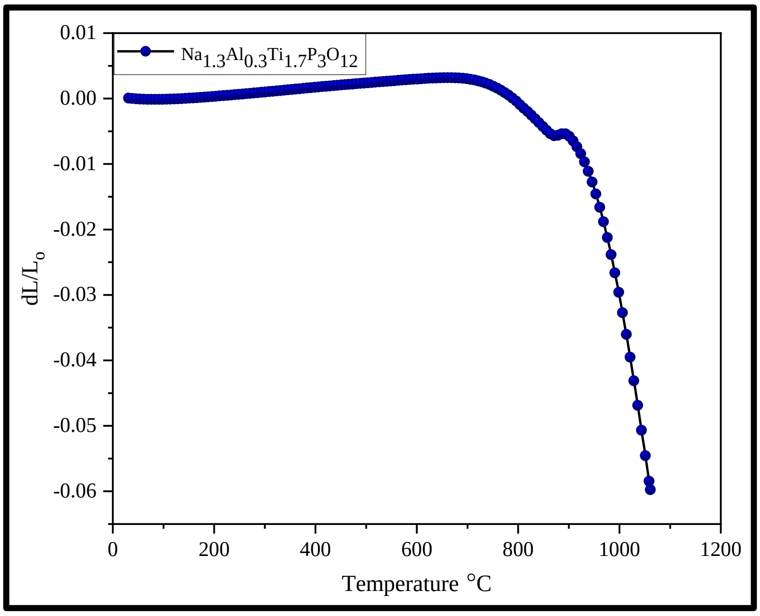

Figure 5.1.3. The dilatometry plot of $Na_{1.3}Al_{0.3}Ti_{1.7}P_3O_{12}$ showing the volume contraction as a function of Temperature.

5.1.4 Scanning electron microscopy

SEM micrographs of the green NATP powder are shown in Figure 5.1.4. The image shows powder that is agglomerated with nano-grain sizes. The grain sizes are irregular and non-uniform, supporting the size distribution obtained from the particle size analyser.

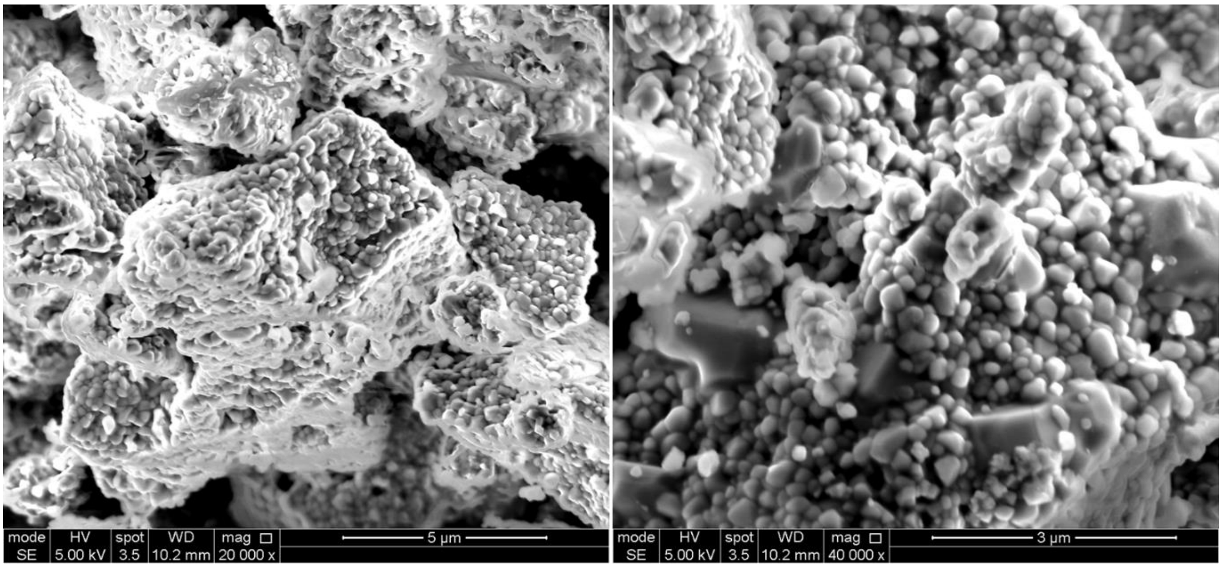

Figure 5.1.4. SEM micrographs of the green NATP powder.

5.2 Conventional sintered NATP

5.2.1 X-ray Diffraction

X-ray diffraction patterns of the conventional sintered $Na_{1.3}Al_{0.3}Ti_{1.7}P_3O_{12}$ are shown in Figure 5.2.1a. Prior to the sintering, NATP pellets were buried in green NATP powder and sintered between 900 - 1000 °C to investigate the optimum sintering temperature for this ceramic. The x-ray diffraction patterns of NATP pellets sintered at 900, 950 and 1000 °C were matched against the diffraction pattern of the $Na_{1.3}Al_{0.3}Ti_{1.7}P_3O_{12}$ green powder with PDF N° 00-014-7800 and compared with the literature. All the XRD patterns of NATP sintered at different temperatures and times have an impurity phase of $AlPO_4$ peaks (x-symbol) at 22.4, 2θ degree value, similar to the literature [1-6, 8]. Upon further studies, we discovered the $AlPO_4$ impurities phase was minimal at 900 °C for 12 hours and had the highest relative density (see later). Also, the unknown peak at 22.4.0, 2θ degrees, which was present in the NATP green powder, disappeared at this temperature (900 °C for 12 hours), Figure 5.2.1b.

Different sintering temperatures (950 and 1000 °C) and times (6-12 hours) were investigated to suppress the $AlPO_4$ impurity phase. Decreasing the sintering time to 6 hours at 900 °C suppressed the formation of the unknown phase but did not minimise the $AlPO_4$ impurity phase, Figure 5.2.1a. The NATP pellet was fragile with poor relative density (see later). Increasing the sintering temperature of NATP to 950 and 1000 °C for 12 hours increases the formation of $AlPO_4$ (22.4, 2θ degree) and re-introduces the unknown peak (23.0, 2θ degrees), which had disappeared at 900 °C, Figure 5.2.1a. All efforts to suppress the $AlPO_4$ impurity phase were unsuccessful and followed a similar trend in the literature (1, 8). The formation of the $AlPO_4$ impurity phase is suggested to be due to the volatilisation of the lighter elements (Na).

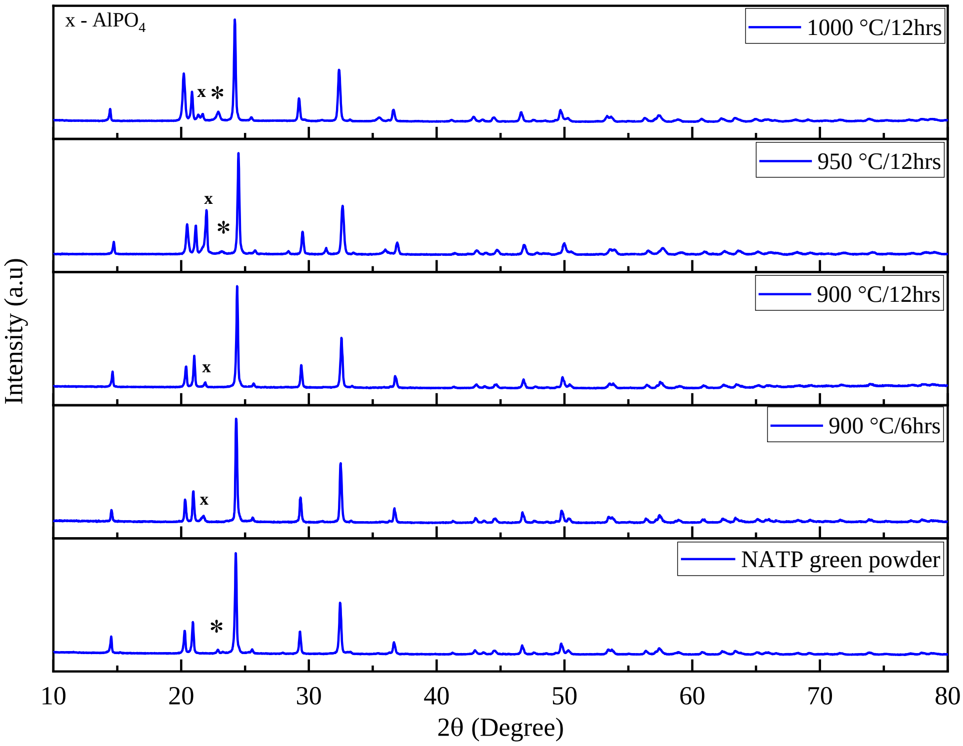

Figure 5.2.1a. XRD patterns of NATP powder and conventional sintered NATP at different temperatures and holding times.

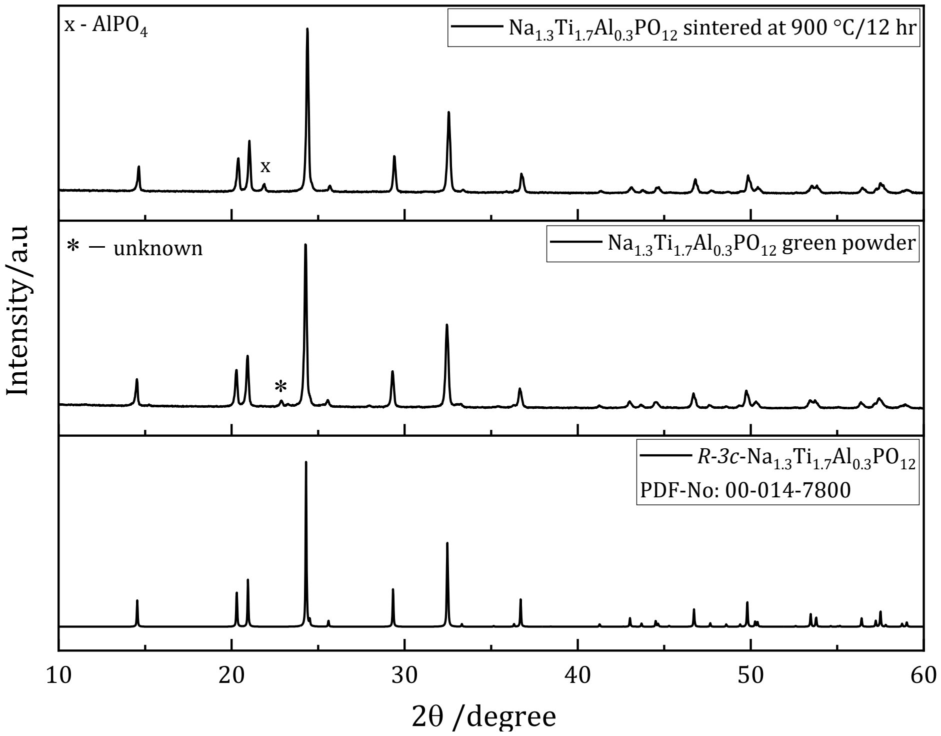

Figure 5.2.1b. XRD patterns of NATP green powder and sintered pellets (900 °C/12 hr) matched against *R-3c* NATP with PDF No: 00-014-7800.

5.2.2 Relative density

The experimental density of NATP sintered pellets was measured using the Archimedes and geometric methods, and the results were compared with their theoretical density of NATP obtained from the literature and ICDD database. The theoretical density of NATP is 2.97 g/cm^3, and the relative density (ρ_r) of NATP was calculated according to equation 3.8 (chapter 3). To determine the density of the NATP ceramic, the average of three different measurements were taken. Table 5.2 shows the relative density of NATP sintered at different temperatures and times. A small increase in the ρ_r of the NATP ceramic was observed as the sintering temperature increased. The reasons for the poor densification of this material are not understood. However, the ρ_r of the NATP ceramic sintered at 900 °C for 12 hours is comparable to the literature [1, 8] using the geometric technique.

Table 5.2.

Relative density of NATP using Archimedes technique

Compound	Sintering temperature and time (°C & hour)	Archimedes (A), (g/cm^3)	Geometric (G), (g/cm^3)	ρ_r (A) %	ρ_r (G) %
$Na_{1.3}Al_{0.3}Ti_{1.7}PO_{12}$	900/6	2.38		80.1	
$Na_{1.3}Al_{0.3}Ti_{1.7}PO_{12}$	900/12	2.51	2.75	84.6	93.2
$Na_{1.3}Al_{0.3}Ti_{1.7}PO_{12}$	950/12	2.55		86.2	
$Na_{1.3}Al_{0.3}Ti_{1.7}PO_{12}$	1000/12	2.56		86.4	

5.2.3 Scanning electron microscopy

SEM images of the fractured surface of the conventional sintered pellets of NATP are shown in Figures 5.2.2 - 5.2.4. The SEM micrograph shown in Figure 5.2.2 belongs to the fractured surface of NATP ceramic sintered at 900 °C for 6 hours. The micrograph reveals porous and agglomerated grains supporting a material with a relative density of 80 %. Figure 5.2.3 revealed the fractured surface SEM micrographs of NATP sintered at 900 °C for 12 hours. The micrographs show porous, nano-sized grains similar to the SEM micrographs reported by Rhode *et al.*, [1]. The SEM micrograph suggests a ceramic with a densification of approximately 92.0 %, supporting the geometric relative density. Figure 5.2.4 (a & b) show the SEM micrographs of the fractured surface of the NATP sintered conventionally at 950 and 1000 °C for 12 hours, respectively. The SEM micrographs both revealed porous agglomerated grains which support ceramic with ~ 85 % relative density. Due to the agglomeration of the grains, we estimated the grain size of the conventional sintered NATP to be ~ 300-500 nm.

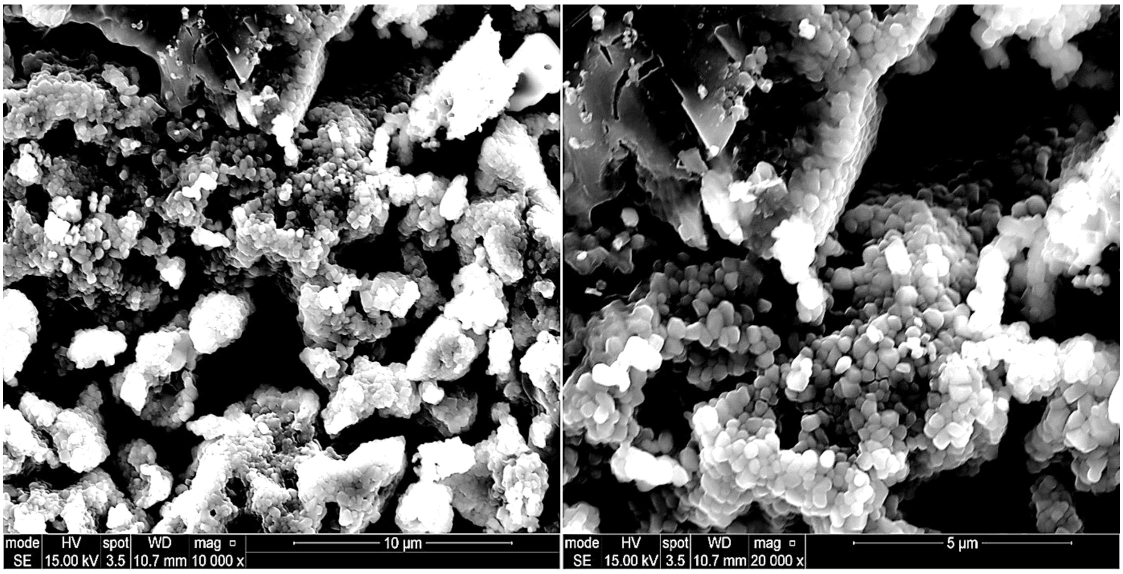

Figure 5.2.2. SEM images of the fractured surface of NATP sintered at 900°C for 6 hours.

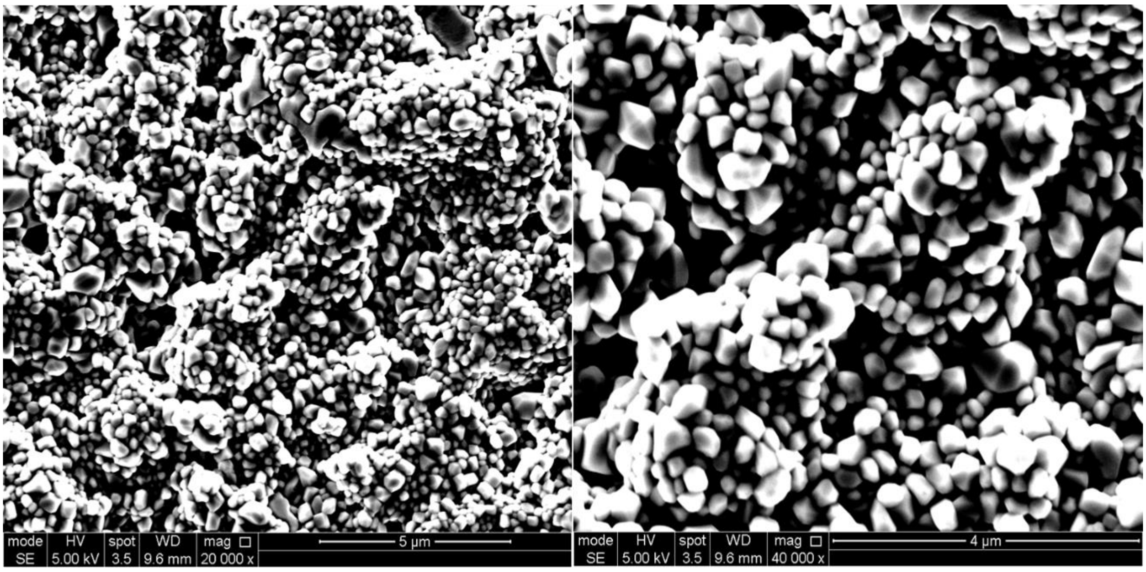

Figure 5.2.3. SEM images of the fractured surface of NATP sintered at 900°C for 12 hours.

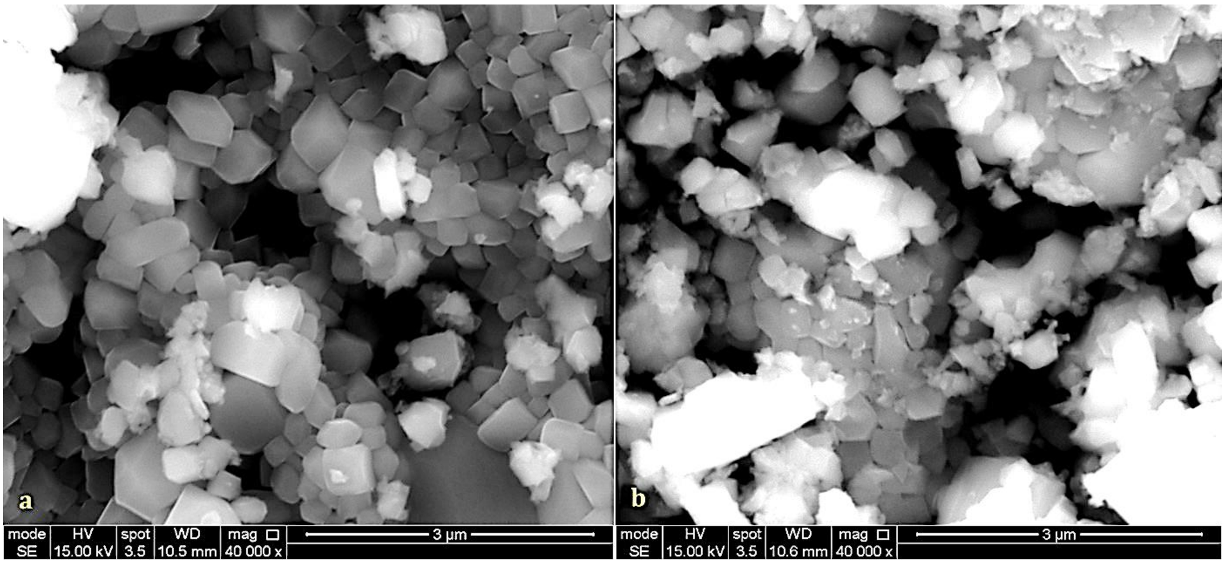

Figure 5.2.4. SEM images of the fractured surface of NATP sintered for 12 hrs at (a) 950 °C (b) 1000 °C.

5.2.4 Impedance Spectroscopy

The impedance plots of $Na_{1.3}Al_{0.3}Ti_{1.7}P_3O_{12}$ ceramics subjected to a 12-hour sintering at 900°C are shown in Figure 5.2.3. The ionic conductivity of the ceramic was measured at room different temperatures up to 450 °C, but due to substantial noise in the impedance data, we limited the plots to 100 °C. The total resistivity of the ceramic was $4.21*10^{-6}$ and $9*10^{-5}$ Ωcm at 20 °C and 100 °C, respectively, as shown in Figure 5.2.3 (a-b), which was similar to the literature [1 & 4]. The imaginary part of the impedance (Z' and Z") formed a semicircle, and the conducting species in the sample could be determined by comparing the Z' and Z" plots to existing data. Figure 5.2.3 (c-d) shows the spectroscopic data (capacitance) in the pico-Farad (10^{-12} F) range and has no low-frequency electrode spike. Figure 5.2.3 (e-f) depicts the spectroscopic plot of M" and Z" imaginary components at 20 °C and 100 °C, respectively. It was determined that no impedance barrier to charge transfer existed between the ceramic and the electrode. Electrons are the conducting species in the system instead of ions [1, 10].

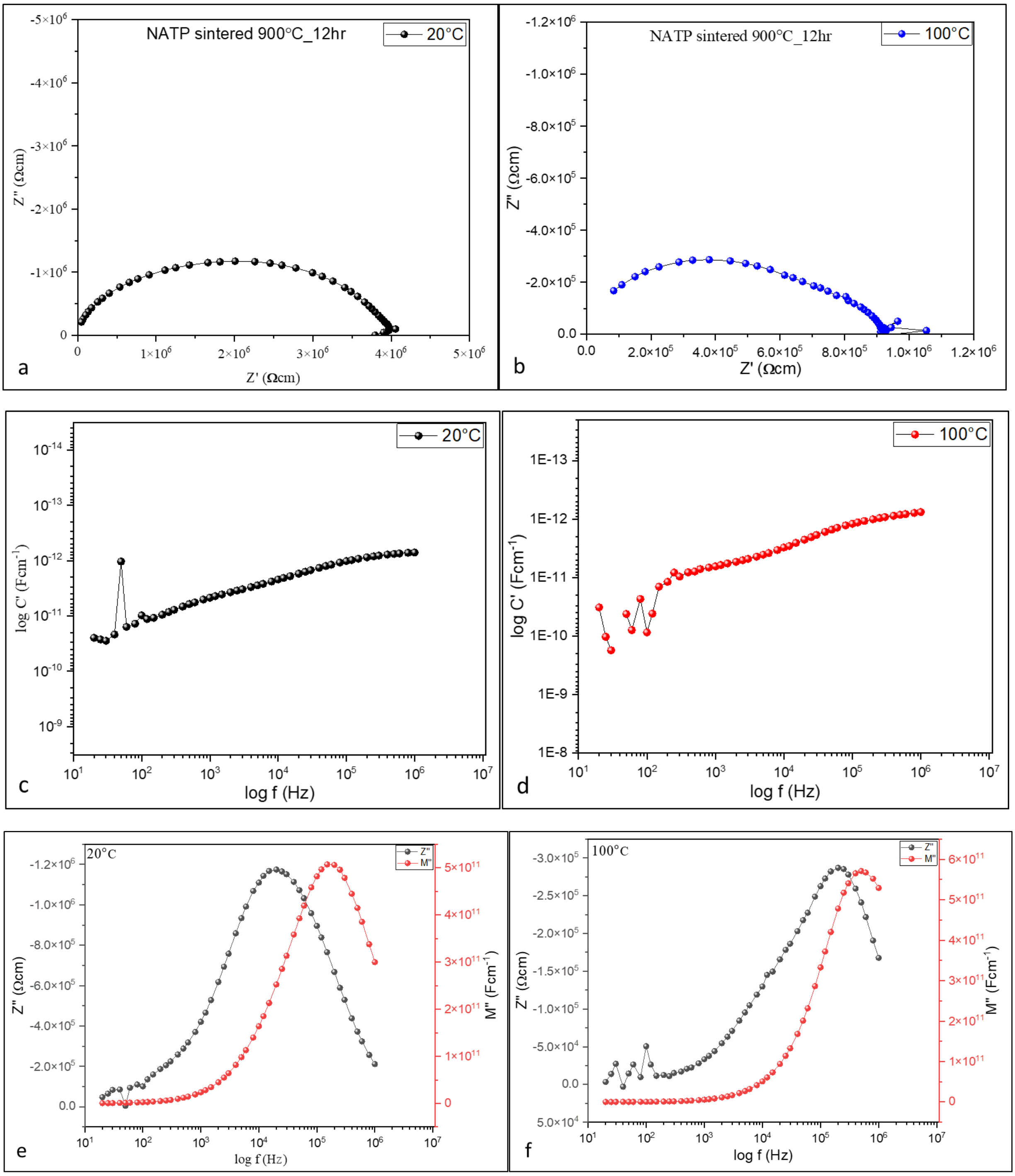

Figure 5.2.3 Complex impedance plots and the spectroscopic plots of $Na_{1.3}Al_{0.3}Ti_{1.7}P_3O_{12}$ sintered at 900 °C for 12 hours (a-b) Z'/Z" (c-d) capacitance (e-f) Z"/M" at 20 °C and 100 °C.

5.2.5 Activation Energy (E_a)

The temperature-dependent data of the total conductivities of the NATP at different temperatures is shown in Table 5.3. The data were extrapolated to calculate the gradient of the Arrhenius plot. The standard least square method was used to obtain the gradients of the temperature-dependent data of the NATP in Origin software, and the uncertainty associated with the gradient and activation energy was recorded.

The activation energy (E_a) was calculated according to Equation 3.35 (chapter 3), and the result is shown in Table 5.3. The Arrhenius plot of the total conductivity of the NATP, where $\sigma_T = 1/R_T$, is shown in Figure 5.2.4, where the E_a is ~ 0.52 ± 0.13 eV. These values were comparable to the literature values [2].

Table 5.3.

The temperature, total resistance, the logarithm of the conductivity and the capacitance for calculating the activation energies of the conventional sintered $Na_{1.3}Al_{0.3}Ti_{1.7}P_3O_{12}$.

Temp (°C)	Temp (K)	1000/T (K)	R_t (Ωcm)	$1/R_t = \sigma$ (Scm^{-1})	log σ	Capacitance (Fcm^{-1})
20	293	3.41	4.21E+06	2.37E-07	-6.62E+00	1.55E-12
28.6	301.6	3.32	5.69E+06	1.76E-07	-6.76E+00	1.73E-12
52	325	3.08	7.41E+06	1.35E-07	-6.87E+00	1.38E-12
96.5	369.5	2.71	1.06E+06	9.46E-07	-6.02E+00	6.86E-13
201.5	474.5	2.11	23137	4.32E-05	-4.36E+00	-

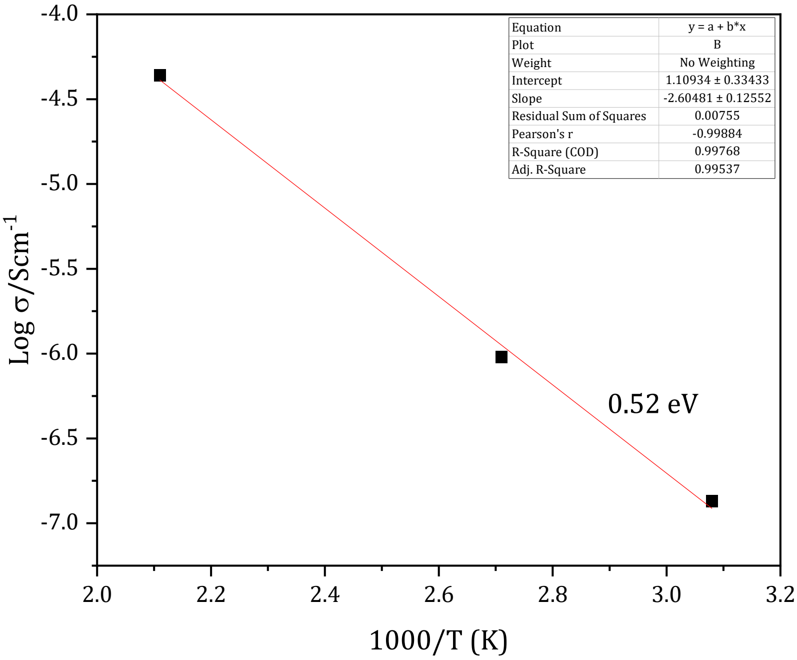

Equation	y = a + b*x
Plot	B
Weight	No Weighting
Intercept	1.10934 ± 0.33433
Slope	-2.60481 ± 0.12552
Residual Sum of Squares	0.00755
Pearson's r	-0.99884
R-Square (COD)	0.99768
Adj. R-Square	0.99537

5.2.4. Temperature-dependent total conductivity plots of conventionally sintered NATP at 900 °C/12hr.

5.3 Cold-sintered NATP

5.3.1 X-ray Diffraction

Following the densification of the NATP by the cold sintering method, The XRD patterns of the densified pellets using different transient solvents {Isopropanol (IPA), sodium hydroxide and acetic acid} at constant pressing pressures (500 MPa), time (1hr) and temperature (200 °C) are shown in Figure 5.3.1. The X-ray diffraction patterns were matched against green NATP powder, and there were no observable changes to the peaks relating to the cold-sintered NATP. The effect of the transient solvents on the densified NATP pellets was studied, and it was confirmed from the diffraction patterns in Figure 5.3.1 that there were no extra peaks relating to the transient solvents. The formation of $AlPO_4$ at 22.4 (2θ°) was observed in the conventional sintered NATP, and the literature [1-8] was absent for all cold-sintered NATP. There were no phase alterations, as all peaks in the cold-sintered NATP matched the corresponding NATP green powder. This suggests the cold sintering method is a benign technique for densifying phase-pure ceramics. In addition, the unknown peak present in the NATP green powder was present in all the cold-sintered NATP.

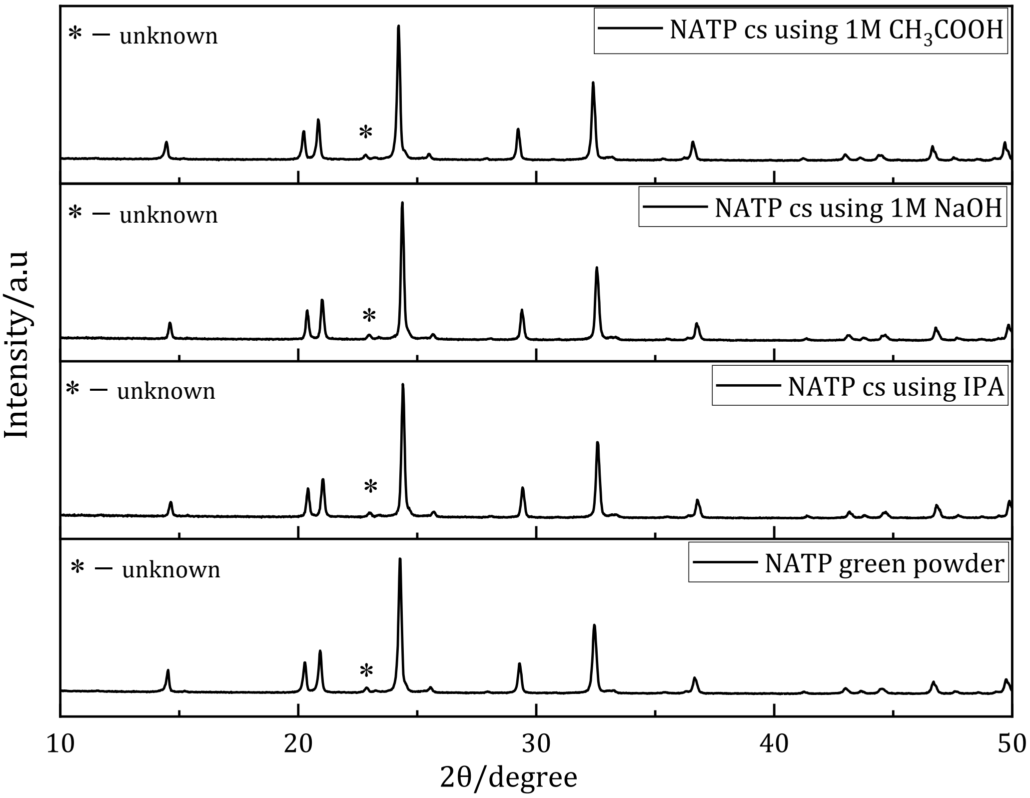

Figure 5.3.1 XRD patterns of cold-sintered NATP using different transient solvents.

5.3.2 Relative density

The relative density of the cold-sintered NATP was calculated according to equation 3.8 (chapter 3). The experimental densities ($\rho_{ex.}$) of the cold-sintered samples are calculated using Archimedes method (Ethanol was used in the Archimedes method due to the reactivity of NATP with H_2O), and the values are recorded in Table 5.4. The theoretical density of NATP, as obtained in the literature and ICDD database, is 2.97 g/cm^3. The relative density of all cold-sintered NATP is ~ 75.0% without post-annealing, pertinent to similar cold-sintered samples reported in the literature [7, 9]. Due to the fragile nature and poor densification of the cold-sintered NATP, post-annealing studies on the NATP ceramic were investigated, and the results are shown in Table 5.4. The highest ρ_r ~ 96.0 % was obtained for 1M CH_3COOH after post-annealing at 800 °C for 12 hours. Aqueous solvents are poor transient solvents for the densification of NATP by cold sintering.

Table 5.4

Cold sintering of NATP using IPA, Acetic acid and 1M NaOH as transient solvents.

$Na_{1.3}Al_{0.3}Ti_{1.7}PO_{12}$	Post annealed °C /time (hrs)	Archimedes density (Ethanol) gcm^{-1}	Relative density (%)
H_2O	600/12	2.57	86.53
1M NaOH	600/12	2.57	86.53
IPA	600/8	2.66	89.56
1M CH_3COOH	600/8	2.56	86.20
1M CH_3COOH	800/12	2.84	95.62

5.3.3 Scanning electron microscopy

SEM micrographs of the fractured surface of the cold-sintered NATP using 1M NaOH, 1M CH_3COOH and isopropanol as the transient solvents are presented in Figures 5.3.2. – 5.3.4. The SEM micrographs of cold-sintered NATP using 1M NaOH as the transient solvent and post-annealed for 12 hours at 200 °C are shown in Figure 5.3.2. The fracture surface shows agglomeration of the grains separated by pores. There is no evidence of the formation of 120° triple points, suggesting limited sintering. Figure 5.3.3. shows the SEM micrographs of the fractured surface of NATP cold-sintered with an organic solvent (1M CH_3COOH) and post-annealed for 8 hours at 600 °C. Although porosity is evident, the dense regions show 120° triple points, indicating that some sintering rather than just consolidation occurs under these conditions. Figure 5.3.4 shows the SEM image of the fractured surface of cold-sintered NATP with isopropanol as the transient solvent and post-annealed at 600 °C for 12 hours. The micrograph is qualitatively similar to Figure 5.3.3. Suggesting that weak organic solvents have similar SEM micrographs.

Overall, the SEM micrographs (Figures 5.3.2 – 5.3.4) suggest a ceramic with low relative density, and there is no microstructural evidence that the NATP cold-sintered using acetic acid as the transient solvent achieved ~ 94%, as recorded by Archimedes measurements, which might suggest that this value is abnormal. Nonetheless, there is some evidence of densification when samples are post-annealed at 600 °C. The low density may relate to an inhomogeneous distribution of the liquid medium during cold sintering. Currently, samples are hand-mixed with the liquid medium in a pestle and mortar. Ball milling with the transient solvent may improve mixing.

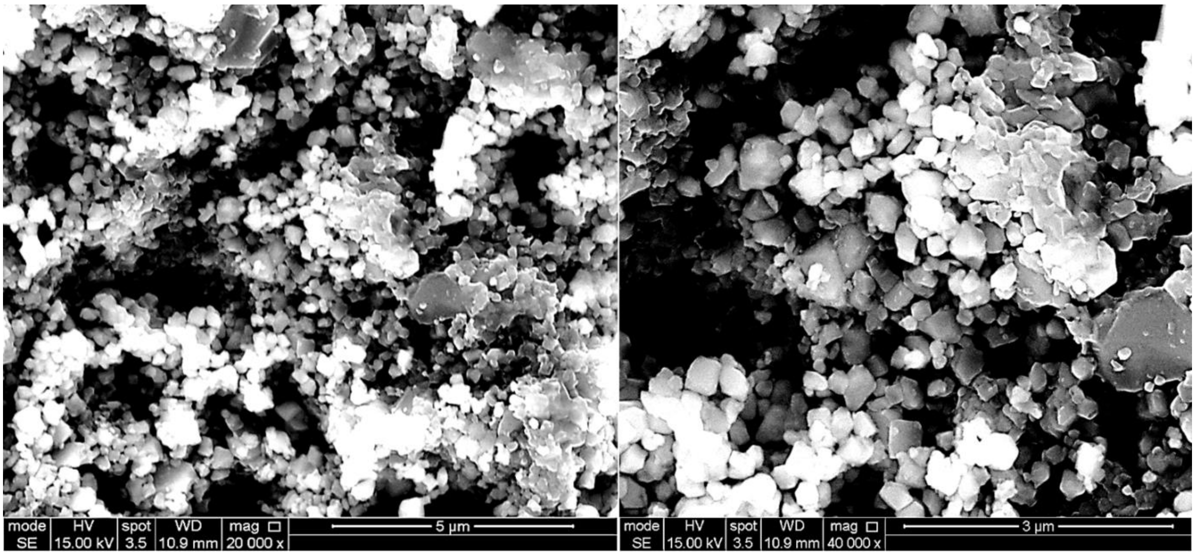

Figure 5.3.2 SEM image of cold-sintered NATP with 1M NaOH, post-annealed 200°C/12hrs.

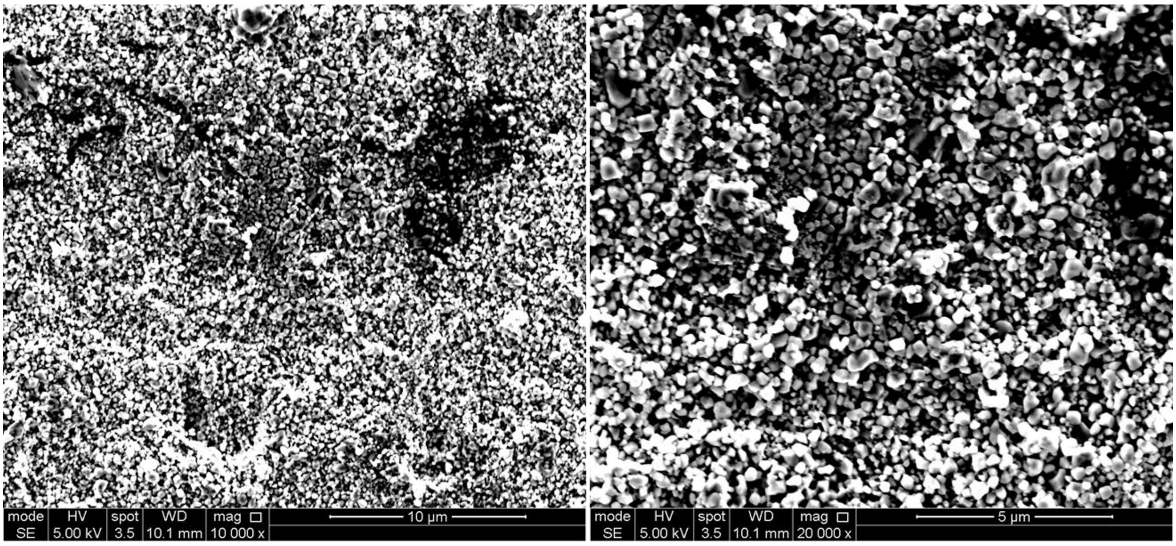

Figure 5.3.3 SEM image of cold-sintered NATP with 0.1M acetic acid, post-annealed 600°C /8hrs.

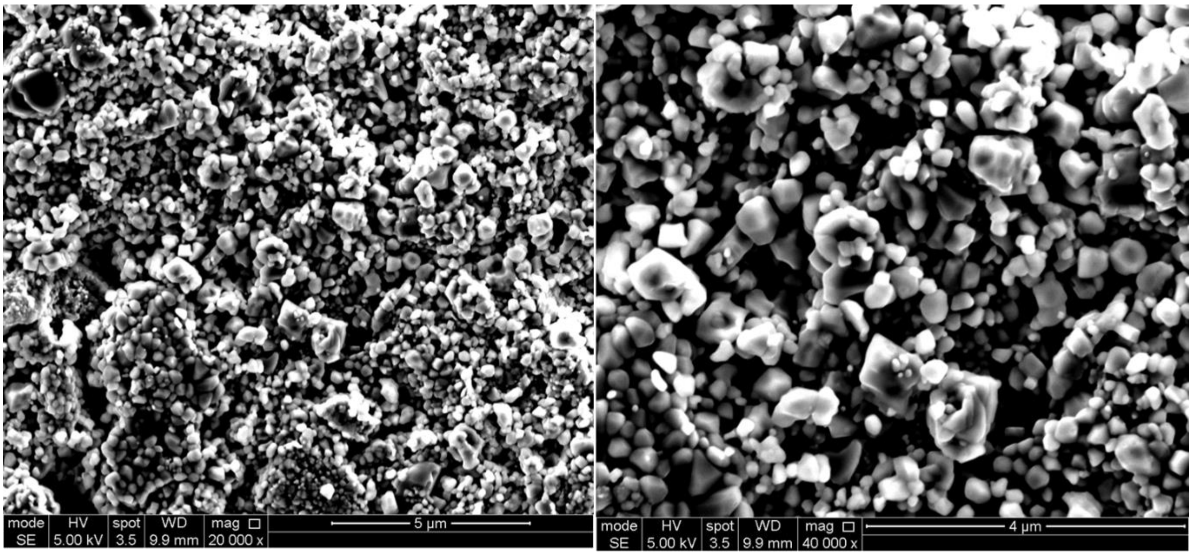

Figure 5.3.4 SEM image of cold-sintered NATP with Isopropanol post-annealed 600°C/8hrs.

5.3.4 Impedance Spectroscopy

Attempts were unsuccessful in measuring the conductivity of cold-sintered NATP ceramics. A significant challenge arose when a gold electrode was applied to the ceramic surfaces and baked for 2 hours at 850 °C (standard Au electrode paste baking temperature but above the post-anneal temperature). Unfortunately, peeling of the Au electrode frequently occurred, and some NATP ceramics fractured. Even when the Au electrode adhered to the surface, there were excessive noise levels in the measured electrical properties, rendering it impossible to obtain accurate readings. Given that the Au electrode paste was baked at 850 °C (higher than the post-anneal at 600 °C), it may have been possible to utilise low-temperature pastes (In-Ga alloys) or sputtered electrodes. However, the poor densities, microstructure and the absence of Na-ion conduction in conventionally sintered NATP suggested that other experiments should be pursued in the available limited time.

5.4 Conclusions.

NATP was densified using conventional and cold sintering methods, and the relative density of the ceramic was comparable to that reported in the literature. The ceramic exhibited R-3c symmetry with an $AlPO_4$ impurity phase observed for the conventionally sintered sample. SEM micrographs of the conventional sintered NATP show a porous agglomerated ceramic with a nano-grain size, and the impedance studies show a room temperature conductivity of 10^{-7} S/cm. Densification of NATP by cold-sintering method resulted in a low relative density ceramic pertinent to similar ceramic densify by cold-sintering. However, post-annealing at elevated temperatures exhibited some evidence of densification in parts of the ceramics. It was observed that aqueous solvents are poor transient solvents for the densification of NATP. X-ray diffraction studies demonstrated that the cold sintering technique on NATP produces an impurity-free ceramic. There were no $AlPO_4$ impurity phases commonly present in the conventionally sintered ceramics. Electrical measurements were not performed due to difficulties in finding a suitable electrode and the limited time to pursue alternative experiments, given that conventionally sintered NATP showed no evidence of ionic conduction.

5.5 References.

[1] M. Rohde, I. U. I. Mohsin, C. Ziebert, and H. J. Seifert, “Ionic and Thermal Transport in Na-ion conducting Ceramic Electrolytes” *International Journal of Thermophysics* vol. 42, no. 10, Jul. 2021, https://doi.org/10.1007/s10765-021-02886-x.

[3] Q. Zhang, X. Zhang, Y. Zhang, and Q. Shen, “Influence of lithium phosphate on the structural and lithium-ion conducting properties of lithium aluminium titanium phosphate pellets,” *Ionics*, vol. 27, no. 6, pp. 2473–2481, Mar. 2021, https://doi.org/10.1007/s11581-021-04011-2.

[4] M. Gellert, Enkhetsetseg Dashjav, D. Grüner, Q. Ma, and F. Tietz, “Compatibility study of oxide and olivine cathode materials with lithium aluminium titanium phosphate,” vol. 24, no. 4, pp. 1001–1006, Sep. 2017, doi.org/10.1007/s11581-017-2276-6.

[5] E. Dashjav, Q. Ma, Q. Xu, C.-L. Tsai, M. Giarola, G. Mariotto, F. Tietz, The influence of water on the electrical conductivity of aluminum-substituted lithium titanium phosphates, 321 (2018) 83–90. https://doi.org/10.1016/j.ssi.2018.04.010.

[6] H. Cai, T. Yu, D. Xie, B. Sun, J. Cheng, L. Li, X. Bao, H. Zhang, Microstructure and ionic conductivities of NASICON-type $Li_{1.3}Al_{0.3}Ti_{1.7}(PO_4)_3$ solid electrolytes produced by cold sintering assisted process, 939 (2023) 168702–168702. https://doi.org/10.1016/j.jallcom.2023.168702.

[7] J. Y. Seo, K. Verlinde, R. Rajagopalan, E. D. Gomez, T. E. Mallouk, and C. A. Randall, “Cold sintering process for fabrication of a high volumetric capacity $Li_4Ti_5O_{12}$ anode,” vol. 250, pp. 114435–114435, Nov. 2019, doi.org/10.1016/j.mseb.2019.114435

[8] M.Y. Sengul, Arnaud Ndayishimiye, W. Lee, Joo Yun Seo, Z. Fan, Yun Kyung Shin, E.D. Gomez, C.A. Randall, van Duin, Atomistic level aqueous dissolution dynamics of $Li_{1+x}Al_xTi_{2-x}(PO_4)_3$ (LATP), (2022) 4125–4130. doi.org/10.1039/d1cp05360d.

[9] J.-H. Seo, H. Nakaya, Y. Takeuchi, Z. Fan, H. Hikosaka, R. Rajagopalan, E.D. Gomez, M. Iwasaki, C.A. Randall, Broad temperature dependence, high conductivity, and structure-property relations of cold sintering of LLZO-based composite electrolytes, Journal of the European Ceramic Society. 40 (2020) 6241–6248. https://doi.org/10.1016/j.jeurceramsoc.2020.06.050.

[10] J. T. S. Irvine, D. C. Sinclair, and A. R. West, “Electroceramics: Characterisation by Impedance Spectroscopy,” *Advanced Materials*, vol. 2, no. 3, pp. 132–138, Mar. 1990, https://doi.org/10.1002/adma.19900020304.

Chapter 6

6.0 Densification of $Na_{0.7}CoO_2$ (NCO) by conventional and cold sintering.

This chapter discusses the results of the conventional and cold-sintering of NCO. The results from each characterisation technique were compared and contrasted against each other and the literature. The NCO powder was sourced from a commercial vendor (NEI Corporation, U.S.A.) and used without further processing. The objective is to densify NCO using cold and conventional and investigate its conductivity (electrolyte/cathode) and magnetic properties.

6.1 NCO powder

The NCO powder was studied to understand its structure, grain size distribution, phase assemblage and morphology.

6.1.1 Grain size distribution

The NCO green powder was analysed for grain size distribution using the Malvern Mastersizer particle analyser 3000. The refractive indices of the dispersant (water) and the NCO were measured to be 1.33 and 1.870, respectively, prior to conducting the measurements. To ensure data reliability, ten measurements were taken. The NCO grain sizes were measured at different Dx values, and the results showed a uniform, single peak size distribution, indicating that the grains are mostly uniform in size. The size uniformity value of 0.71 was relatively high, indicating that the grains are well distributed. Figure 6.1.1 shows the size distribution of the NCO powder, while Table 6.1 displays the average grain size at different percentiles. The Dx information and what it means is reported in section 5.1.1.

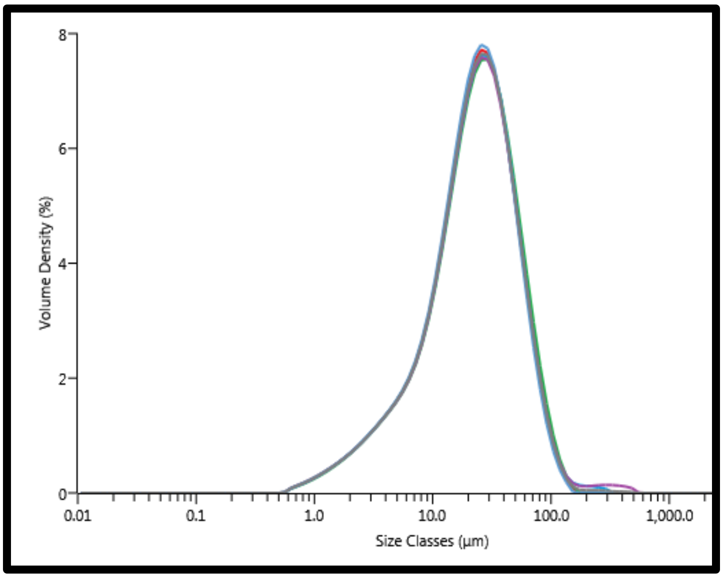

Figure 6.1.1. Grain size distribution of NCO green powder

Table 6.1

The grain size distribution and uniformity index of $Na_{0.7}CoO_2$ green powder.

Record Number	Sample Name	Dx (10) (μm)	Dx (50) (μm)	Dx (90) (μm)	Uniformity
1	$Na_{0.7}CoO_2$	5.40	22.86	57.30	
2	$Na_{0.7}CoO_2$	5.40	22.85	57.20	
3	$Na_{0.7}CoO_2$	5.40	22.83	57.20	
4	$Na_{0.7}CoO_2$	5.40	22.83	57.20	
5	$Na_{0.7}CoO_2$	5.30	22.82	57.00	
6	$Na_{0.7}CoO_2$	5.30	22.80	55.90	
7	$Na_{0.7}CoO_2$	5.30	22.80	55.90	
8	$Na_{0.7}CoO_2$	5.24	22.80	55.90	
9	$Na_{0.7}CoO_2$	5.20	22.43	55.90	
10	$Na_{0.7}CoO_2$	5.20	22.40	55.90	
Mean		**5.31**	**22.74**	**57.30**	**0.71**
Std. Dev		0.05	0.025	0.46	

6.1.2 X-ray diffraction

The XRD pattern of the NCO green powder is shown in Figure 6.1.2. The diffraction peaks were matched and indexed to a hexagonal $Na_{0.71}CoO_2$ with space group $P6_3/mmc$ and PDF N^{o} 00-078-2822. Due to the peak heights of the NCO green powder, the diffraction patterns were modified to reveal the peaks at higher 2θ degree values. After the modification, it was observed that peaks matching Co_3O_4 at 2θ degree values of 14.61 and 17.20 were not present in the indexed P2-phase hexagonal $Na_{0.71}CoO_2$.

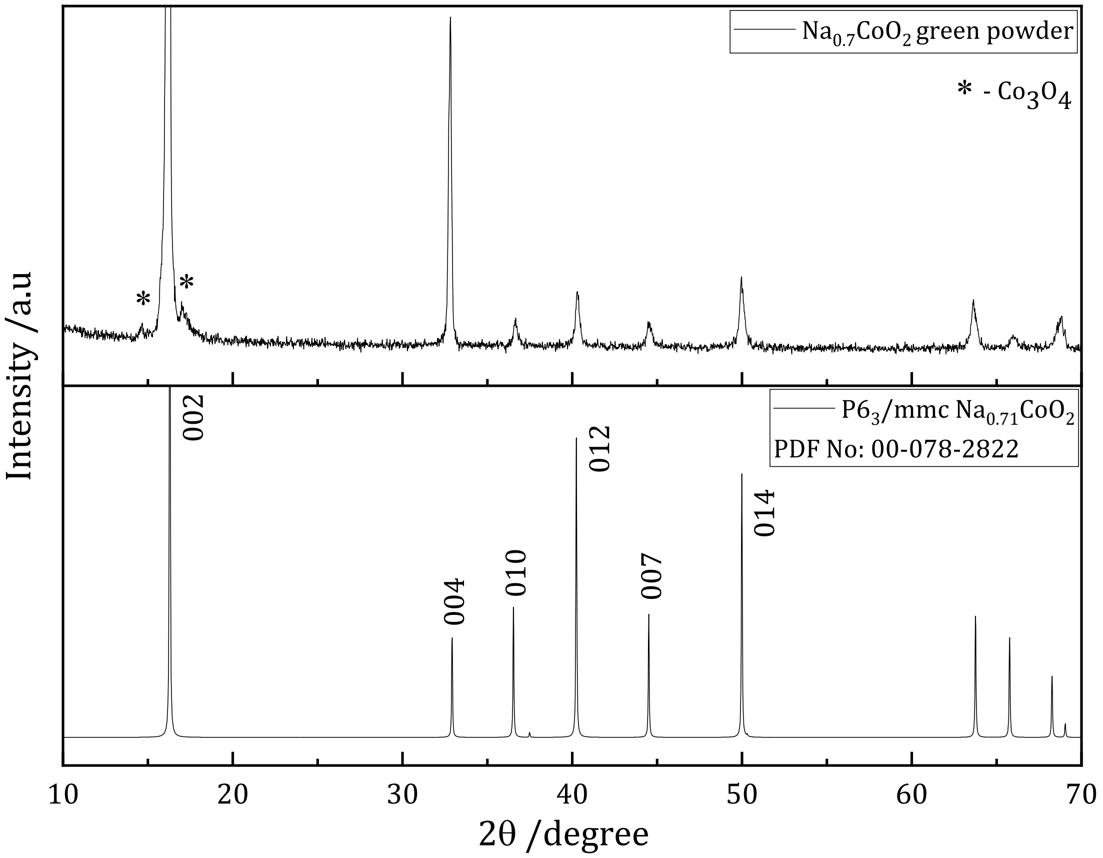

Figure 6.1.2 Room temperature X-ray diffraction patterns of the NCO green powder and indexed P2-phase $Na_{0.71}CoO_2$ with space group *$P6_3/mmc$*.

6.1.3 Scanning electron microscopy

SEM micrographs of the NCO green powder are shown in Figure 6.1.3. It was evident that the powder particles were agglomerated with different size ranges, supporting the size distribution shown in Table 6.1. The particles resemble a rock-like material.

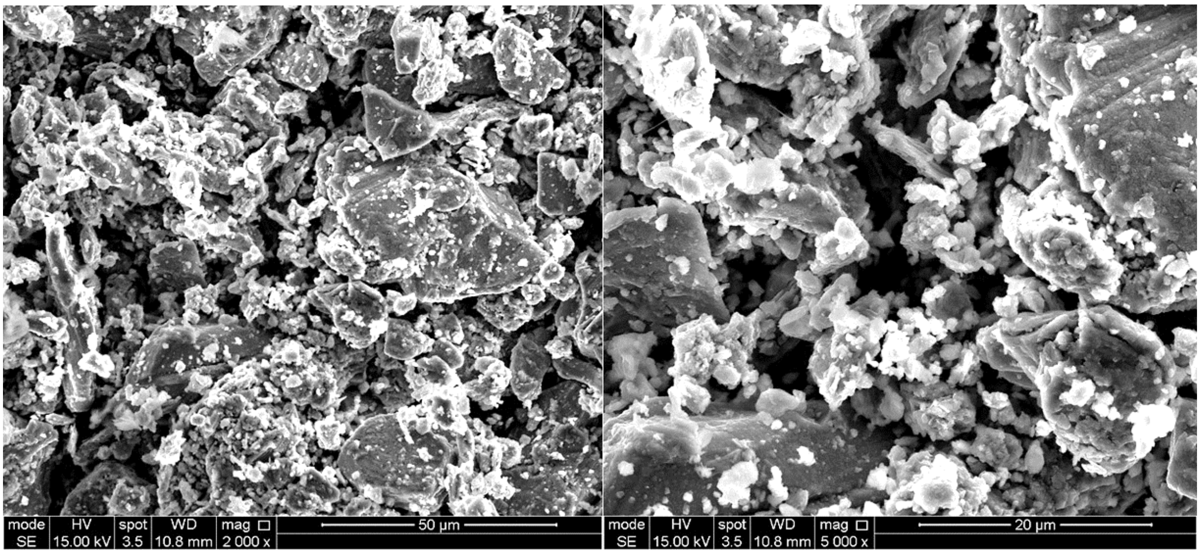

Figure 6.1.3 SEM micrograph of NCO green powder.

6.2 Conventionally sintered NCO

6.2.1 X-ray diffraction

X-ray diffraction patterns of the sintered pellets of $Na_{0.7}CoO_2$ are shown in Figures 6.2.1 (a & b) and 6.2.2. Prior to the sintering, NCO pellets were buried in green NCO powder and sintered between 700 - 900 °C to investigate the optimum sintering temperature for the material. The X-ray diffraction patterns of the NCO pellets sintered at 750, 800 and 900 °C were matched against the diffraction pattern of the $Na_{0.7}CoO_2$ green powder that had earlier been matched to the PDF N° 00-078-2822.

To accurately match the diffraction patterns and reveal the smaller peaks at higher 2θ values, XRD plots were modified to reveal the smaller peaks of NCO and possible impurity peaks. Figure 6.2.2 shows the XRD plots of NCO green powder and conventional sintered NCO ceramic without modification. From Figure 6.2.2, it is impossible to accurately label the CoO/Co_3O_4 impurity peaks, as they are not visible. Among the X-ray diffraction patterns, the pellets sintered at 700 and 800 °C for 12 hours resulted in a sample without extra peaks of cobalt (II) oxide except for those present in the NCO green powder, Figure 6.2.1b. The XRD plot of NCO pellets sintered at 700 °C for 12 hours was not reported due to its similarity to the NCO sample sintered at 800 °C for 12 hours. However, NCO pellets sintered at 700 °C were fragile with low relative density (see later). All the peaks in the NCO pellets of the sample sintered at 800 °C matched with the PDF N° 00-078-2822 and were indexed to $P6_3/mmc$ P2 hexagonal structure, which agrees with the literature [1-7]. However, the Co_3O_4 impurity peaks at 14.61 and 17.20 observed in the NCO green powder were sharper in NCO sintered at 800 °C, Figure 6.2.1b. The XRD patterns of the NCO pellets sintered at 750 and 900 °C for 12 hours have impurity phases of CoO/Co_3O_4 (* - symbol) at 30.1, 34.3 and 40.2, 2θ degree values, Figure 6.2.1a. The peaks associated with CoO/Co_3O_4 phases were higher for NCO pellets sintered at 900 °C for 12, suggesting the volatilisation of the Na^+ ion at this temperature. Surprisingly, NCO pellets sintered at 750 °C exhibited CoO/Co_3O_4 impurity peaks at 30.1, 34.3 and 40.2, 2θ but which were absent at 800 °C.

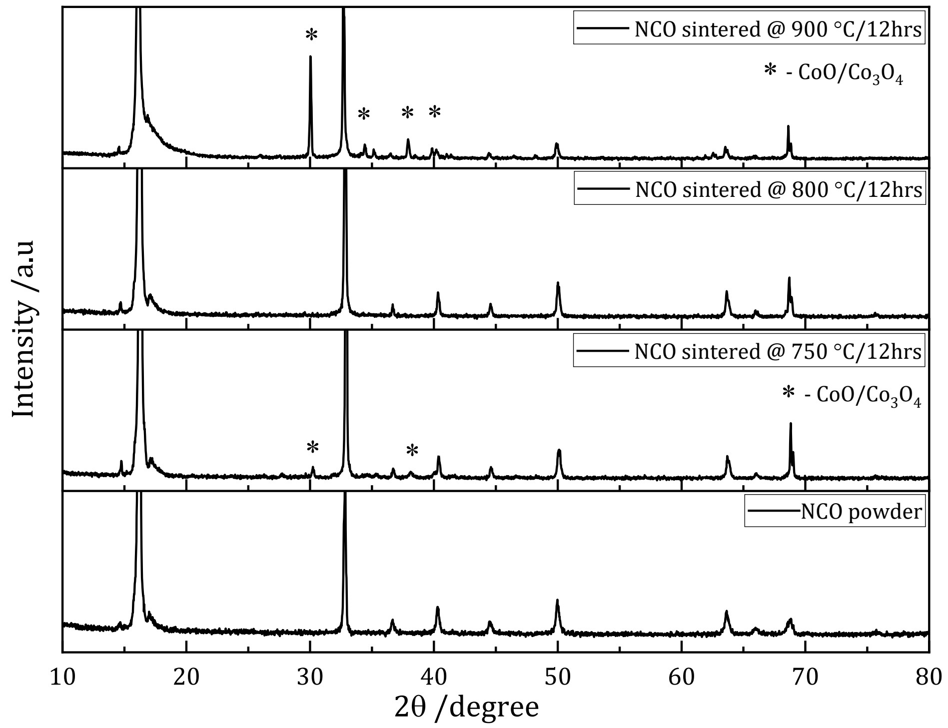

Figure 6.2.1a. Room temperature X-ray diffraction patterns of NCO green powder and conventionally sintered at different sintering temperatures.

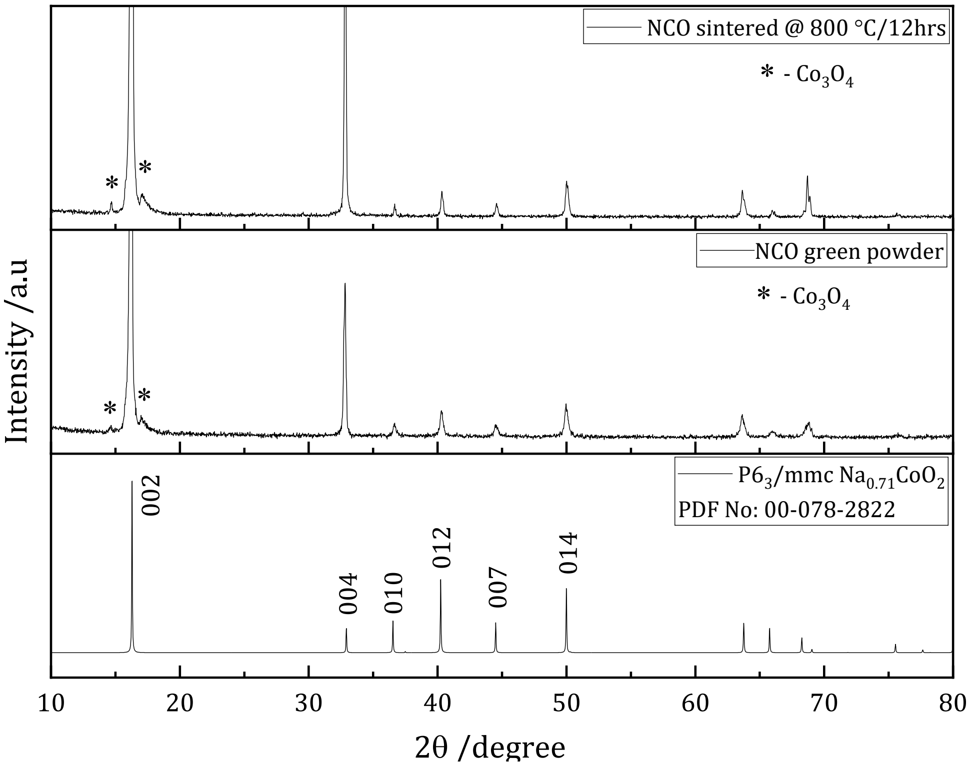

Figure 6.2.1b. Room temperature X-ray diffraction patterns of the conventional sintered NCO at 800 °C, NCO green powder and indexed P2-phase $Na_{0.71}CoO_2$ with space group *P6₃/mmc*.

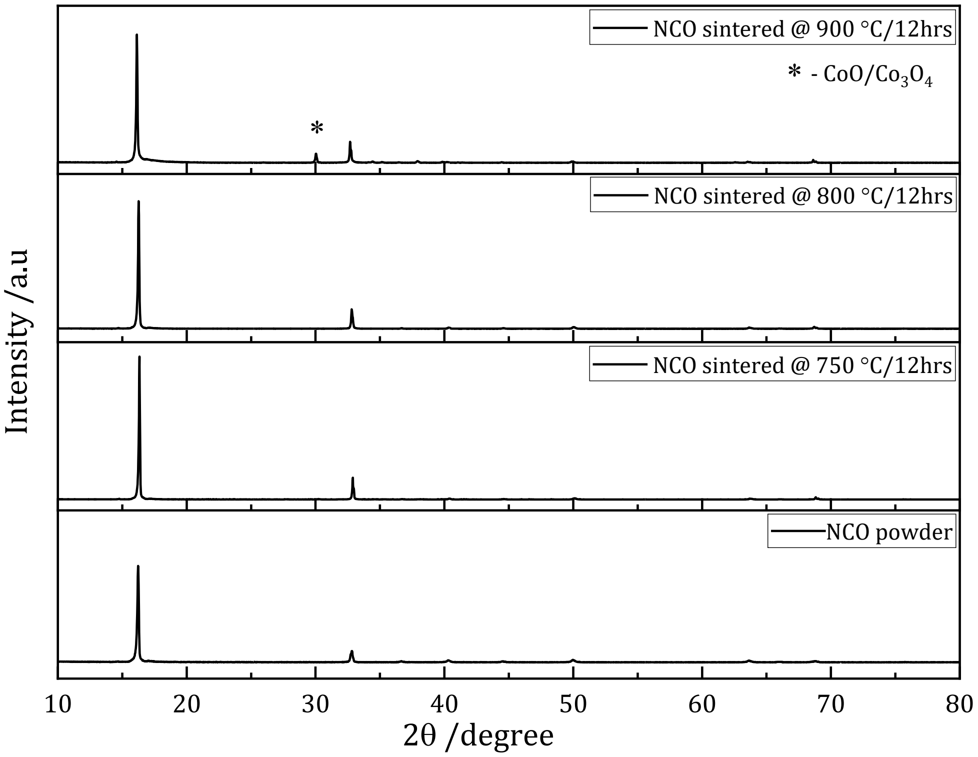

Figure 6.2.2. Room temperature X-ray diffraction patterns of NCO green powder and conventionally sintered NCO without modification.

6.2.2 Relative density

The experimental density of the $Na_{0.7}CoO_2$ pellets sintered conventionally at different temperatures was measured using the Archimedes method, and the results were compared with the $Na_{0.71}CoO_2$ theoretical density obtained from the ICDD database. The theoretical density of $Na_{0.71}CoO_2$ is 4.74 g/cm^3, and the relative density (ρ_r) of NCO was calculated according to equation 3.8 (chapter 3). To determine the experimental density of the NCO ceramic, the average of three different measurements was taken, and the results are shown in Table 6.2 and Figure 6.2.3. The ρ_r of NCO pellets sintered at 700 °C was approximately 80.0 %, and increasing the sintering temperature by 50 °C increases the ρ_r by 10.25 %. A further increase of 50 °C (800 °C) increases the ρ_r by ~ 15.60 %, as shown in Table 6.2. A sharp decrease in the ρ_r of the NCO pellets was observed on increasing the sintering temperature to 900 °C. This ρ_r data confirmed the possible volatilisation of Na^+ ion in the structure of the NCO pellets sintered at 900 °C. There was no literature data to compare these density values, as NCO is used in the slurry form as a cathode material for Na-ion solid-state batteries and requires no densification after preparation.

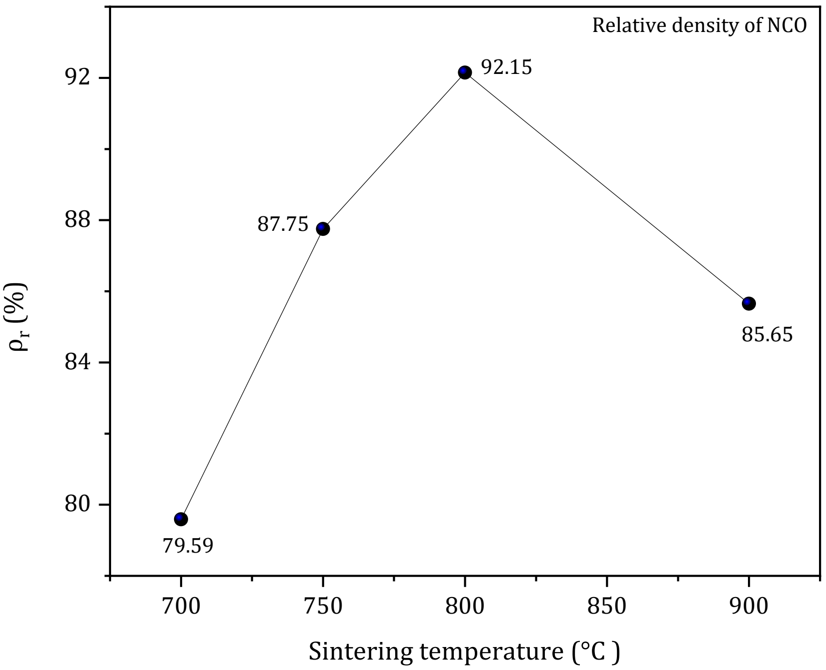

Figure 6.2.3. Relative density of NCO at different sintering temperatures and constant time (12 hr)

Table 6.2.

Density measurement of conventional sintered $Na_{0.7}CoO_2$

Compound	Sintering temperature and time (°C & hrs)	Archimedes (ρ /gcm^{-3})	ρ_r (%)
$Na_{0.7}CoO_2$	700/12	3.71	79.59
$Na_{0.7}CoO_2$	750/12	4.09	87.75
$Na_{0.7}CoO_2$	800/12	4.29	92.15
$Na_{0.7}CoO_2$	900/12	4.06	85.65

6.2.3 Scanning electron microscopy

SEM micrographs of the $N_{0.7}CoO_2$ pellets sintered conventionally at various temperatures are shown in Figures 6.2.4 - 6.2.7. The SEM micrographs of the fractured surface of NCO sintered at 700 °C for 12 hours are shown in Figure 6.2.4. The micrographs show irregular grains with visible pores around the grain intercept, supporting a ceramic with ~ 80.0 % relative density. The SEM micrographs shown in Figure 6.2.5 belong to the fractured surface of NCO ceramic sintered at 750 °C for 12 hours. The grains were more compacted and tightly held with few pores compared to the sample sintered at 700. Figure 6.2.6

shows the SEM micrographs of the lightly polished surface of NCO sintered at 800 °C for 12 hours. The micrographs demonstrate dense, compacted, and tightly held grains with fewer intergranular porosity. Some regions in the micrograph show evidence of triple-point sintering, indicating that there has been a significant sintering. The micrograph is consistent with a ~ 92.0 % dense ceramic. To complete the studies, we investigated the SEM micrograph of the lightly polished surface of NCO sintered at 900 °C for 12 hours, Figure 6.2.7. There were more pores around the grains, with more light and loose grains indicative of cobaltate ions, which was revealed in the XRD plot. The micrographs suggest a ceramic with low ρ_r.

Overall, the SEM micrographs of the conventionally sintered NCO show evidence of triple points due to sintering, and all the micrographs revealed different grain shapes at different sintering temperatures. To our knowledge, there is no literature to compare the SEM micrographs of the conventional sintered NCO.

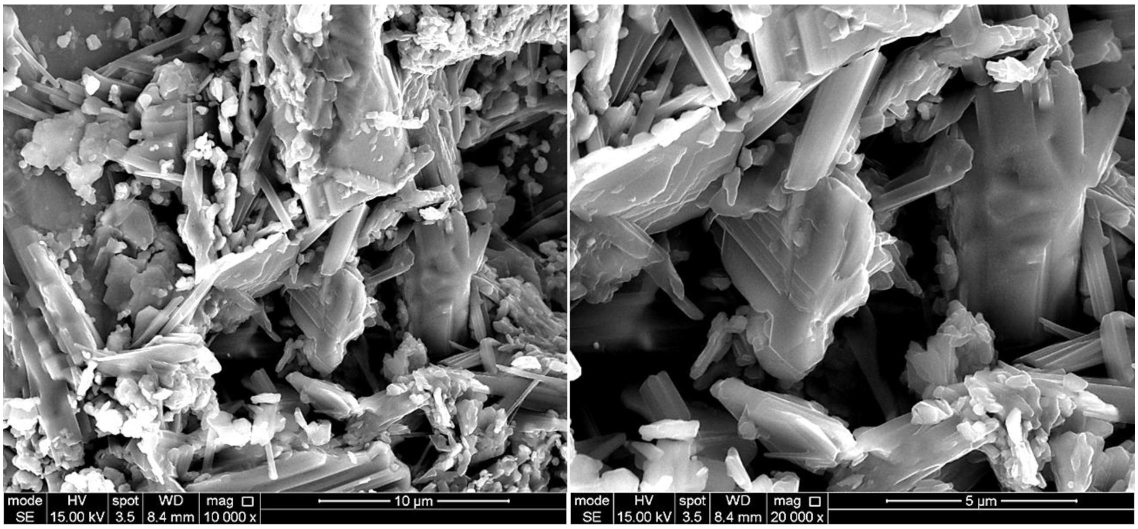

Figure 6.2.4. SEM images of the fractured surface of conventional sintered NCO at 700 °C for 12 hr.

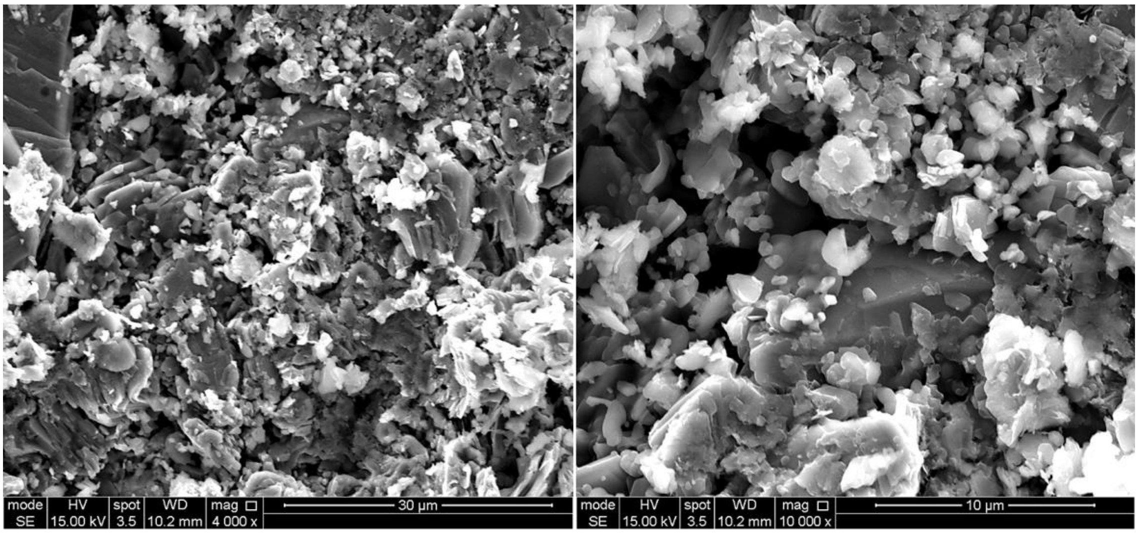

Figure 6.2.5. SEM images of the fractured surface of conventional sintered NCO at 750 °C for 12 hr.

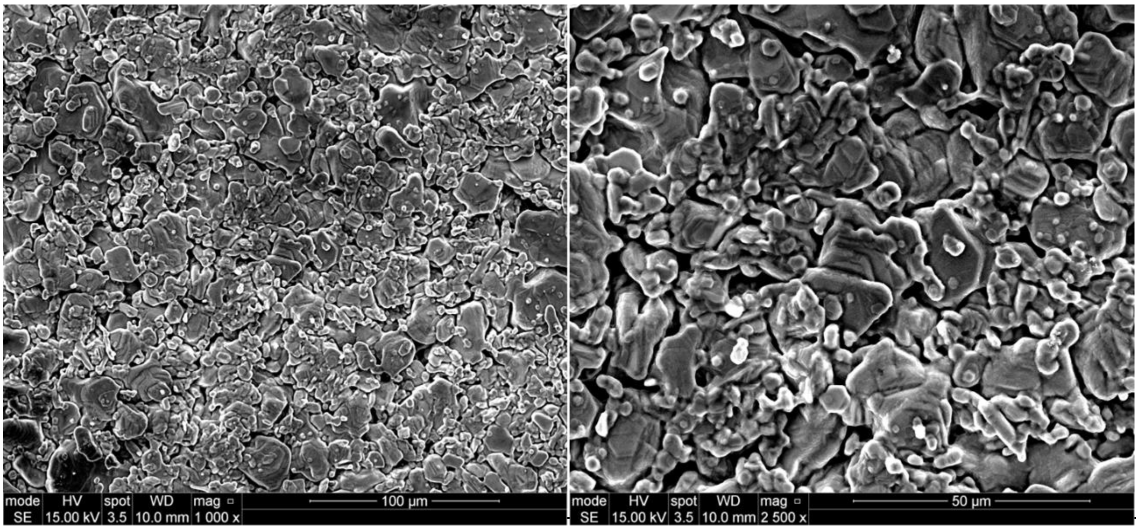

Figure 6.2.6. SEM images of the polished surface of conventional sintered NCO at 800 °C for 12 hr.

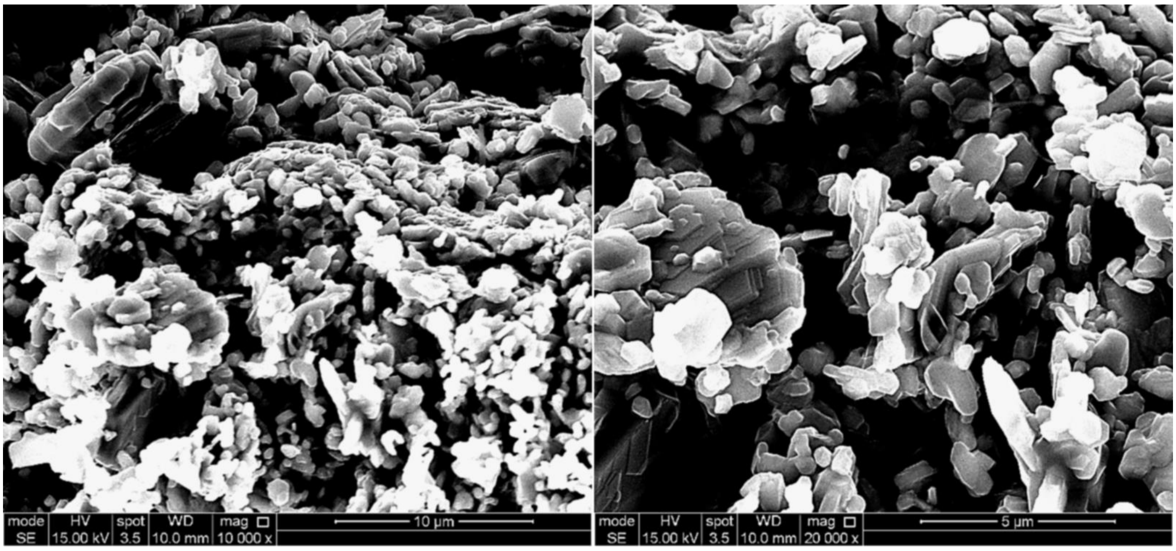

Figure 6.2.7. SEM images of the polished surface of conventional sintered NCO at 900 °C for 12 hr.

6.2.4 Impedance Spectroscopy

For the conductivity measurement, we investigated NCO ceramic that was conventionally sintered at 800 °C for 12 hours due to its high phase purity and greater relative density compared to other conventionally sintered NCO ceramics.

Table 6.3

Impedance spectroscopic data of NCO sintered conventionally at 800 °C for 12 hr. Obt = obtained values, Calc = calculated values, R_s, R_x and R_T = bulk, grain boundary and total resistance, respectively. σ_T = total conductivity, C_T = total capacitance, f_{max} and ω_{max} are the maximum frequency and angular frequency.

SS 800°C/ 12hr	Obt	Obt	Obt	Calc	Obt	Calc	Obt
Temp (K)	R_s	R_x	R_T	σ_T	ω_{max}	f_{max}	C_T
140	124.47	16.20	140.67	0.007	$1.3\text{x}10^{-6}$	$3.0\text{x}10^{2}$	$6.0\text{x}10^{-9}$
160	109.50	16.60	126.06	0.008	$1.4\text{x}10^{-6}$	$4.0\text{x}10^{2}$	$6.4\text{x}10^{-9}$
180	95.60	17.00	112.55	0.009	$1.5\text{x}10^{-6}$	$5.0\text{x}10^{2}$	$7.0\text{x}10^{-9}$
200	82.52	17.40	99.93	0.010	$1.6\text{x}10^{-6}$	$1.0\text{x}10^{3}$	$7.7\text{x}10^{-9}$
220	65.92	18.00	83.89	0.012	$1.7\text{x}10^{-6}$	$4.0\text{x}10^{3}$	$8.7\text{x}10^{-9}$
240	52.73	17.50	70.19	0.014	$1.9\text{x}10^{-6}$	$2.0\text{x}10^{4}$	$9.5\text{x}10^{-9}$
260	42.48	18.00	60.44	0.017	$2.1\text{x}10^{-6}$	$8.0\text{x}10^{3}$	$1.1\text{x}10^{-8}$
273	35.43	17.60	53.03	0.019	$2.2\text{x}10^{-6}$	$3.0\text{x}10^{3}$	$1.2\text{x}10^{-8}$
293	25.32	17.80	43.15	0.023	$2.4\text{x}10^{-6}$	$1.0\text{x}10^{4}$	$1.5\text{x}10^{-8}$

Au alloy was first applied on the NCO ceramic and baked at 850 °C for 2 hours, equivalent to the sintering temperature of the NCO; this affected the properties of the NCO ceramic, and we could only determine the admittance (Y*), which is not an ideal equivalent to the impedance, Figure 6.2.8. The complex impedance plane, Z* plots and the spectroscopic plots of the conventional sintered NCO ceramics using In-Ga alloys are shown in Figure 6.2.9, and the associated data obtained from extrapolating of the Zview software are shown in Table 6.3.

At room temperature, there was only a single, poorly resolved arc with a high-frequency non-zero intercept on the Z' axis. The total (dc) resistivity was based on the low-frequency intercept of the arc in Z* plots and was ~ 40-50 Ωcm, and the non-zero intercept at high frequency was in the range of ~ 20 to 35 Ωcm. Changing the electrodes from In-Ga to Au alloy removed the low-frequency arc in the Z* plots and showed inductive effects (i.e. positive Z'' values) with Z' values remaining in the range < 50 Ωcm, Figure 6.2.8b. These results are consistent with NCO ceramic being highly conductive at room temperature and the low-frequency arc observed with the In-Ga alloy sample is associated with a non-ohmic electrode contact.

The Z* data in Figure 6.2.9 were modelled on an equivalent circuit based on a single resistor connected in series with a parallel Resistor-Capacitor element. The single resistor, which is associated with the high frequency and non-zero intercept on the Z' axis, is attributed to the overall resistivity of the ceramic ($R_{ceramic}$), and the parallel RC element, which is associated with the arc in Z*, is attributed to the electrode effect ($R_{electrode}C_{electrode}$). Performing measurements at sub-ambient temperatures resulted in modest changes in the Z* plots. The arc in the Z* increased in magnitude with decreasing temperature, but there were only minor changes in the non-zero intercept, Figure 6.2.9a. This shows that $R_{electrode}$ increases with decreasing temperature, with $C_{electrode}$ in the range ~ 6 – 15 $nFcm^{-1}$ and $R_{ceramic}$ decrease with decreasing temperature, Table 6.3. Due to the conductive nature of the NCO ceramic, we extrapolated the bulk (R_s) and grain boundary (R_x) resistance to probe their contributions to the overall impedance response of the NCO ceramics. Figure 6.2.9 (b-d) shows the spectroscopic data of the impedance, (b) the capacitance, C" (c) the imaginary component of the impedance, Z" and (d) the electric modulus, M" of the conventional sintered NCO.

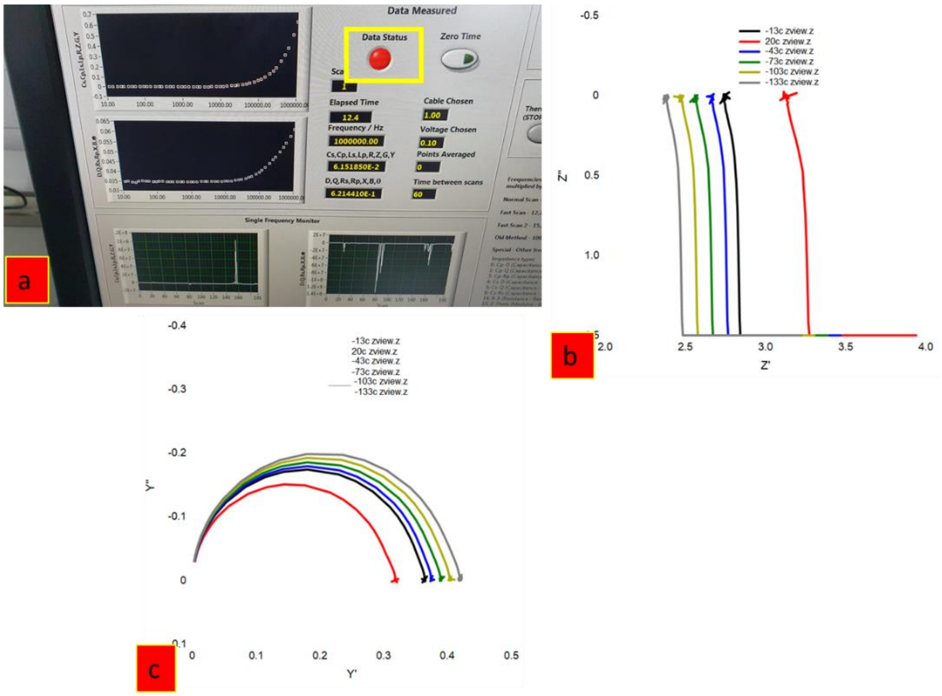

Data Measured

Data Status

Zero Time

Scan: 1

Elapsed Time: 12.4

Frequency / Hz: 1000000.00

Cs,Cp,Ls,Lp,R,Z,G,Y: 6.151850E-2

D,Q,Rs,Rp,X,B,θ: 6.214410E-1

Cable Chosen: 1.00

Voltage Chosen: 0.10

Points Averaged: 0

Time between scans: 60

Figure 6.2.8. (a) Impedance spectroscopy software and the data status in the yellow rectangular box. The red button depicts that the sample under investigation is highly conducting. (b) Z'/Z'' [Impedance] and (c) Y'/Y'' [Admittance], using gold alloy on the ceramic and baked at 850 °C/2 hours.

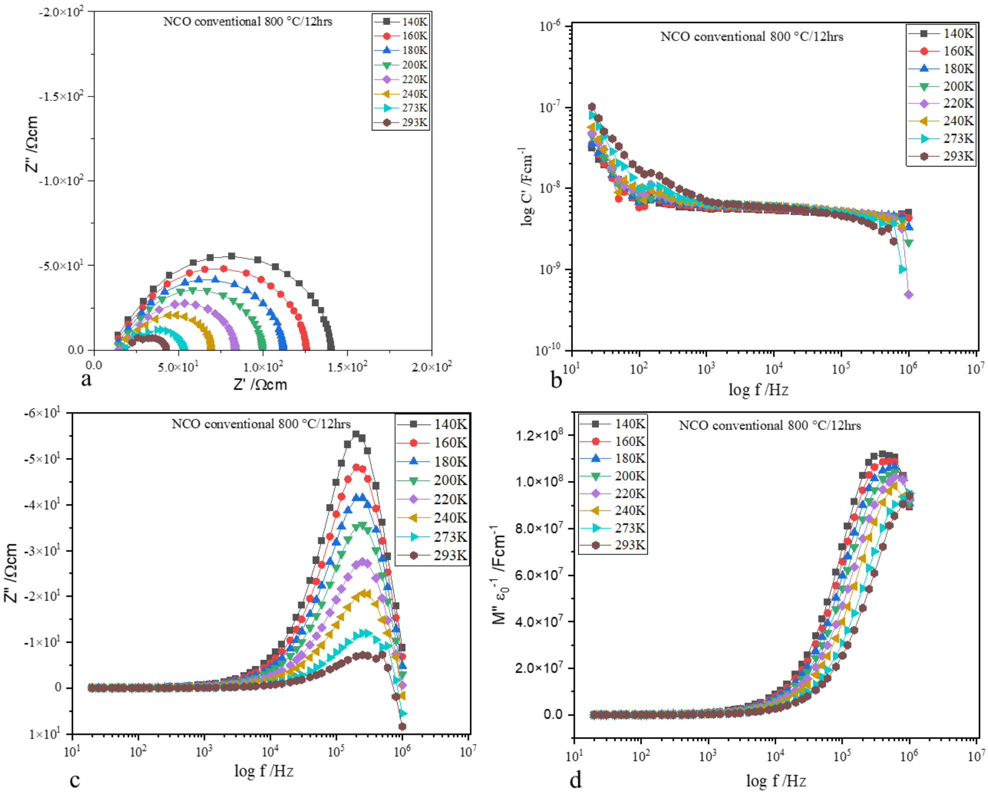

Figure 6.2.9. Impedance (Z*) and the spectroscopic plots of conventional sintered NCO at 140 – 293K (a) Z'/Z'' (b) capacitance (c) Z'' (d) M''.

6.2.5 Arrhenius plot

The temperature-dependent data of the (bulk, grain boundary and total) conductivities of the sintered NCO at different temperatures are shown in Table 6.4. The data were extrapolated to calculate the gradient of the Arrhenius plot. The standard least square method was used to obtain the gradients of the temperature-dependent data of the NCO in Origin software, and the uncertainty associated with each gradient and activation energy was recorded.

The Activation energy (E_a) was calculated according to Equation 3.35 (chapter 3), and the results are shown in Table 6.4. The Arrhenius plot of the total conductivity of the sintered NCO (where $\sigma_T = 1/R_T$) is shown in Figure 6.2.10. The E_a is ~ 0.027 ± 0.015 eV, and the plot deviated from linearity. The plot shows metallic-type conduction and non-Arrhenius-type behaviour for the non-ohmic contacts. In addition, the plot of $T^{-1/3}$ and $T^{-1/4}$ against the total conductivity deviated from linearity, Figures 6.2.11 and 6.2.12, which suggests the conduction mechanism in the conventional sintered sodium cobaltate is in +III/+IV state. Hence, the Na^+ ion migration pathway in the conventional sintered NCO was investigated, Figures 6.2.13. The plots of the log of the ceramic (bulk) and electrode (grain boundary) conductivity against 1000/T show the contribution of each factor to the total conductivity, and it was observed that the Na^+ ion migration favours the electrode (grain boundary). The data could not be compared to the literature, as no data is available to the best of our knowledge on the E_a of NCO, and the low E_a values could be attributed to the conductivity nature of the NCO ceramic.

Table 6.4

Temperature-dependent conductivity of conventional sintered NCO. σ_s, σ_x and σ_t, are the bulk, grain boundary and total conductivity extracted from the bulk (R_x), grain boundary (R_s) and total (R_T) resistance shown in Table 6.3 (above).

Temp (K)	1000/T (K)	$T^{-1/3}$	$T^{-1/4}$	σ_s	Log σ_s	σ_x	Log σ_x	σ_T	Log σ_T
140	7.14	0.1926	0.2907	0.008	-2.095	0.062	-1.210	0.007	-2.15
160	6.25	0.1842	0.2812	0.009	-2.039	0.060	-1.220	0.008	-2.10
180	5.56	0.1771	0.2730	0.010	-1.980	0.059	-1.230	0.009	-2.05
200	5.00	0.1710	0.2659	0.012	-1.917	0.057	-1.241	0.010	-2.00
220	4.55	0.1657	0.2597	0.015	-1.819	0.056	-1.255	0.012	-1.92
240	4.17	0.1609	0.2541	0.019	-1.722	0.057	-1.243	0.014	-1.85

260	3.85	0.1567	0.2490	0.024	-1.628	0.056	-1.255	0.017	-1.78
273	3.66	0.1542	0.2460	0.028	-1.549	0.057	-1.246	0.019	-1.72
293	3.41	0.1506	0.2417	0.039	-1.403	0.056	-1.250	0.023	-1.64

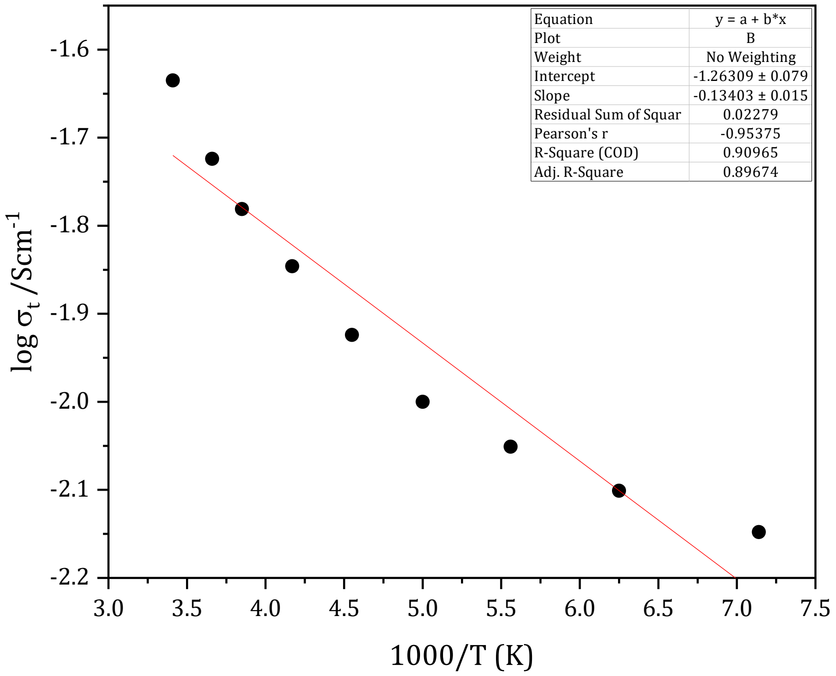

Figure 6.2.10. Arrhenius plot of the total conductivity of the conventional sintered NCO.

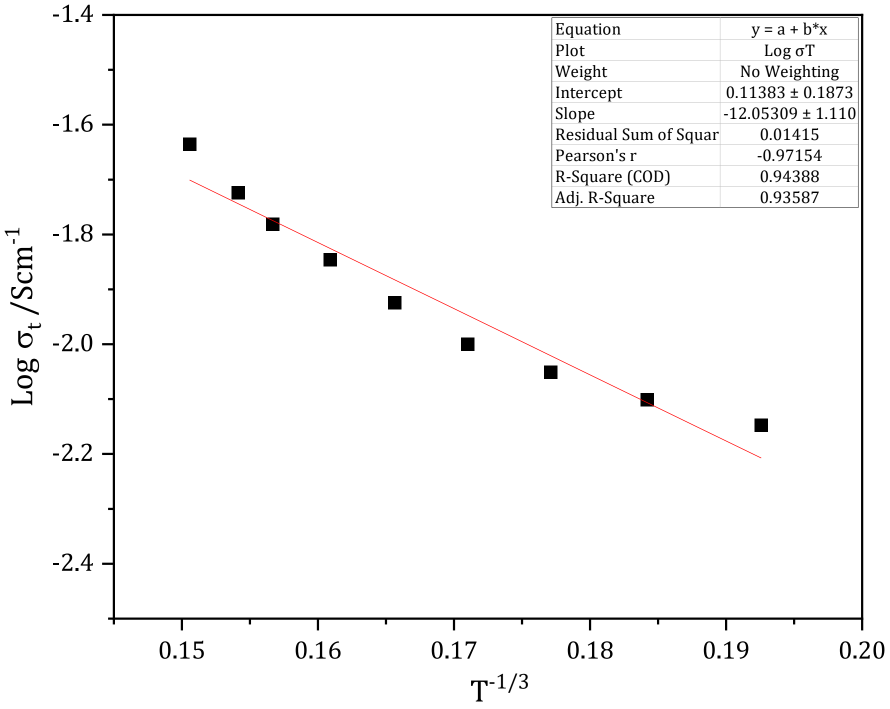

Figure 6.2.11. Arrhenius plot of the total conductivity of sintered NCO against $T^{-1/3}$.

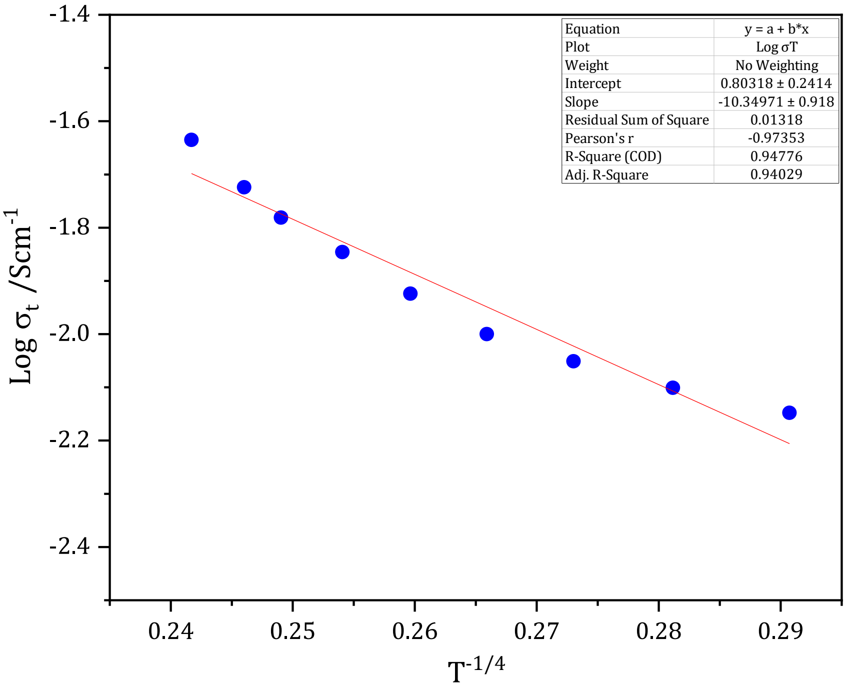

Equation	y = a + b*x
Plot	Log σT
Weight	No Weighting
Intercept	0.80318 ± 0.2414
Slope	-10.34971 ± 0.918
Residual Sum of Square	0.01318
Pearson's r	-0.97353
R-Square (COD)	0.94776
Adj. R-Square	0.94029

Figure 6.2.12. Arrhenius plot of the total conductivity of sintered NCO against $T^{-1/4}$.

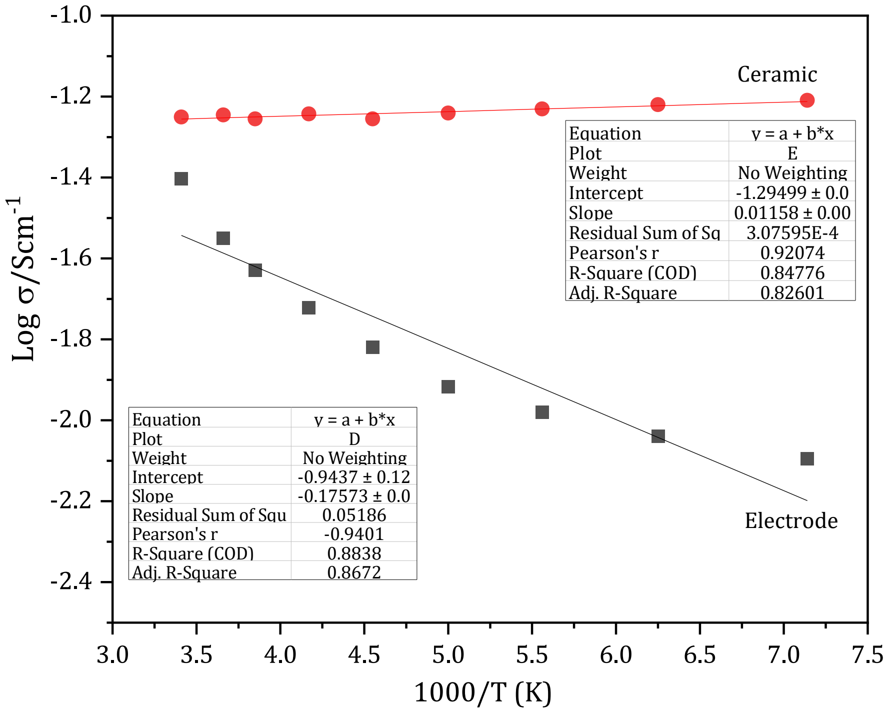

Equation	y = a + b*x
Plot	E
Weight	No Weighting
Intercept	-1.29499 ± 0.0
Slope	0.01158 ± 0.00
Residual Sum of Sq	3.07595E-4
Pearson's r	0.92074
R-Square (COD)	0.84776
Adj. R-Square	0.82601

Equation	y = a + b*x
Plot	D
Weight	No Weighting
Intercept	-0.9437 ± 0.12
Slope	-0.17573 ± 0.0
Residual Sum of Squ	0.05186
Pearson's r	-0.9401
R-Square (COD)	0.8838
Adj. R-Square	0.8672

Figure 6.2.13. Arrhenius plot of the bulk (electrode) and grain boundary (ceramic) conductivity of sintered NCO against 1000/T.

6.3 Cold-sintering of $Na_{0.7}CoO_2$

This section discusses the results of the densification of NCO cold-sintered using different transient solvents: aqueous solvents (H_2O and 1M NaOH solution), Organic solvent (Isopropanol) and organic salts with water of crystallisation (cobalt acetate, sodium acetate and citric acid). The effect of the transient solvents on the phase, morphology and electrical properties of the cold-sintered NCO was studied, and the results are compared to the conventionally sintered NCO and the literature.

6.3.1 Aqueous (distilled water) cold sintering of NCO

In this section, distilled water was used as the transient solvent for the densification of NCO, and the phase, morphology, and electrical properties of the NCO ceramic were investigated and compared to the conventional sintered NCO.

6.3.1.1 X-ray diffraction

The X-ray diffraction pattern of the NCO cold-sintered with distilled H_2O is shown in Figure 6.3.1. The X-ray diffraction peaks were matched against the NCO green powder and PDF N^o: 00-078-2822 of the P2-phase $Na_{0.71}CoO_2$ with space group $P6_3/mmc$. All the peaks in the cold-sintered NCO matched well with the indexed P2-phase $Na_{0.71}CoO_2$ without any impurity peaks [1-5]. The extra/impurity peaks of Co_3O_4 at 14.61 and 17.20, 2θ degrees observed in the NCO green powder were absent in the aqueous cold-sintered NCO. This indicated that the aqueous cold-sintering process is a benign technique for densifying phase-pure ceramic (such as NCO) with high ρ_r (see later, section 6.3.1.2). Comparing the X-ray diffraction pattern of the aqueous cold sintered with conventional sintered, Figure 6.3.2, the peaks in the NCO samples sintered conventionally were sharper and well resolved with extra peaks of Co_3O_4 at 14.61 and 17.20, 2θ degrees. The X-ray diffraction patterns of the NCO were modified to reveal all the peaks present in the diffraction, especially those at high 2θ degree values in the sample. If the X-ray diffraction pattern were to be reported without modification, patterns would resemble Figure 6.3.3, with only two noticeable peaks of NCO at 16.2 and 33.9, 2θ in the diffraction pattern.

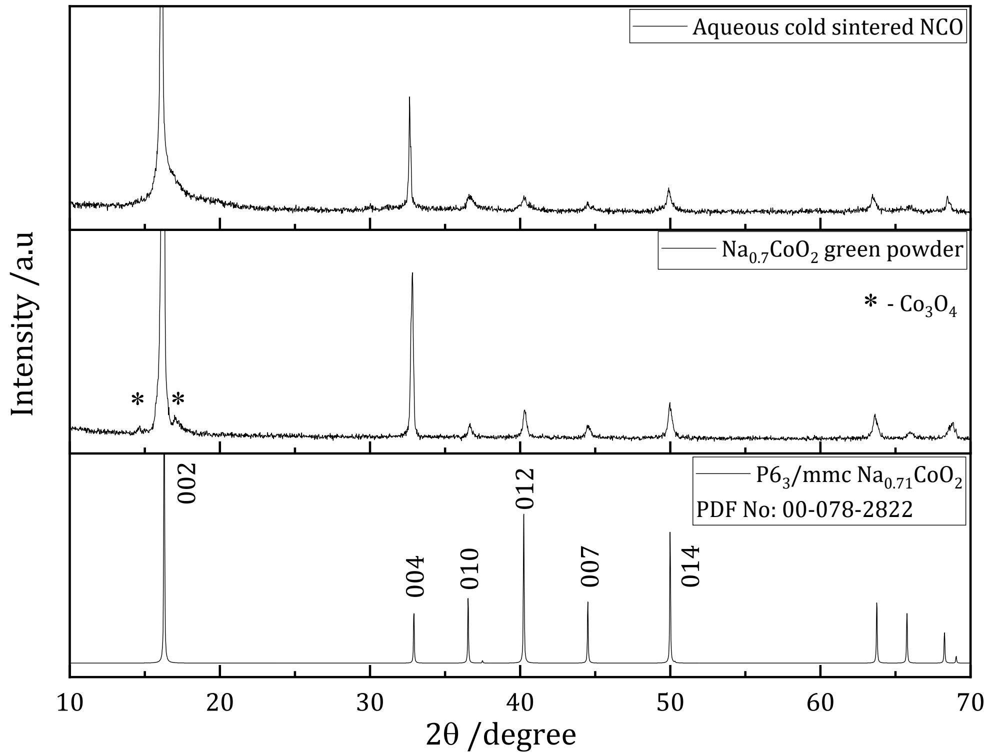

Figure 6.3.1. Room temperature X-ray diffraction patterns of Aqueous cold-sintered NCO, green powder, and indexed P2-phase $Na_{0.71}CoO_2$ with space group *$P6_3/mmc$*.

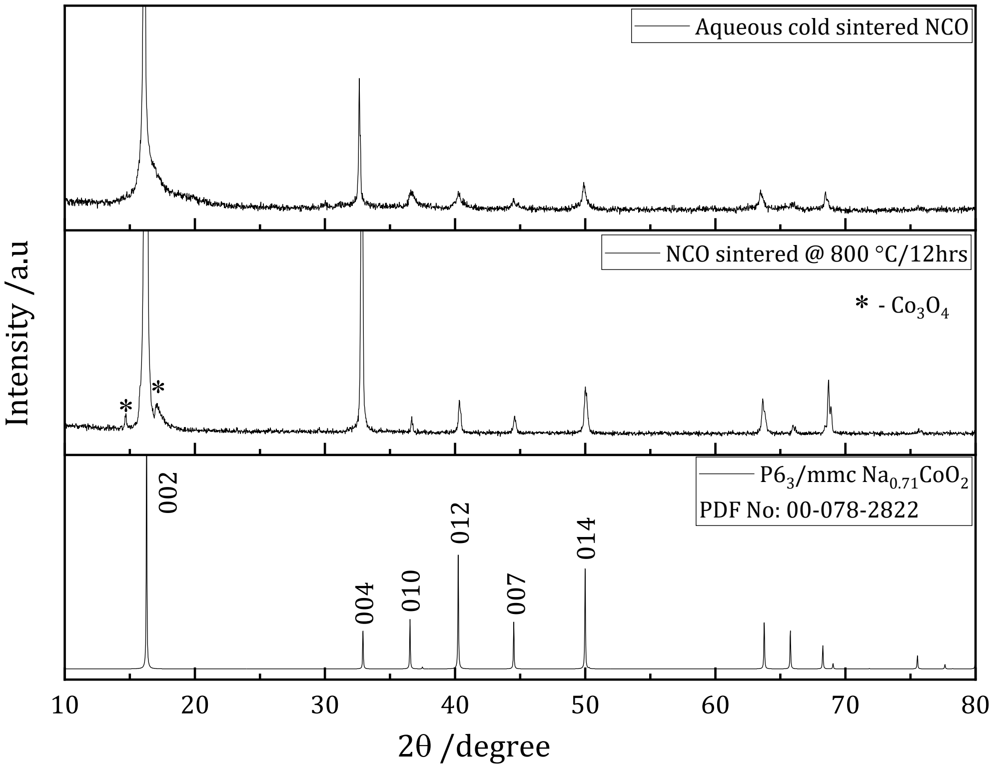

Figure 6.3.2. Room temperature X-ray diffraction patterns of the Aqueous cold-sintered NCO and the conventional sintered NCO against the indexed P2-phase $Na_{0.71}CoO_2$ with space group *$P6_3/mmc$*.

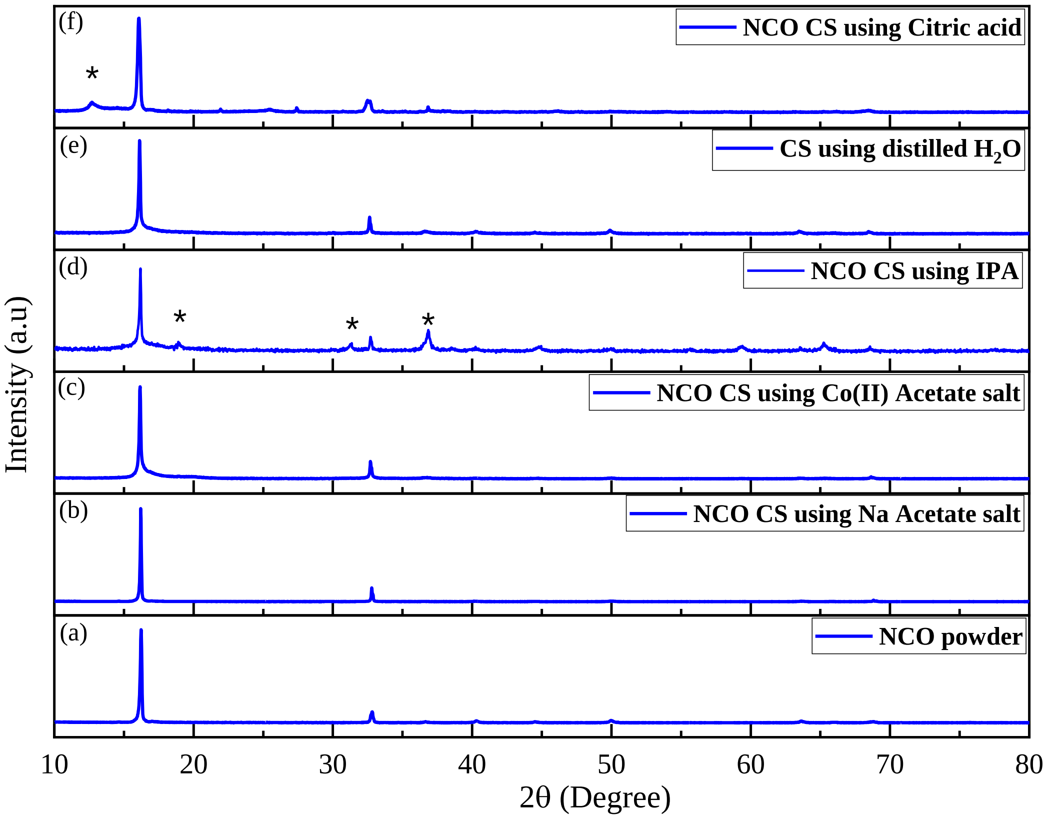

Figure 6.3.3. Room temperature X-ray diffraction patterns of cold-sintered NCO (a) powder (b) Na acetate (c) Co acetate (d) IPA (e) distilled water and (f) citric acid, without extrapolating.

6.3.1.2 Relative density

The experimental density of the aqueous (H_2O) cold-sintered $Na_{0.7}CoO_2$ pellets was measured using the Archimedes method, and the results were compared with $Na_{0.71}CoO_2$ theoretical density obtained from the ICDD database. The theoretical density of $Na_{0.71}CoO_2$ is 4.74 g/cm^3, and the relative density (ρ_r) of NCO was calculated according to equation 3.8 (chapter 3). To achieve the highest NCO experimental density, various parameters (time, temperature, and pressure) were varied, and the average of three readings was recorded, as shown in Table 6.5. Figure 6.3.4 compares the relative densities of aqueous (H_2O) cold-sintered NCO pellets by varying the densification temperature (150 and 200 °C) at different times (minutes) at a constant pressing pressure of (500 MPa). All the NCOs cold-sintered using distilled water as the transient solvent achieved a relative density greater than 92.0% irrespective of the pressing pressure, temperature and time, Table 6.5. Pressing the NCO pellets for 15 and 30 minutes did not have much difference on the experimental density of the NCO ceramic. NCO ceramic pressed at 500 MPa, 150 °C, and 1 hour achieved a relative density of 93.52

% and increasing the pressing temperature by 50 °C (200 °C) increases the relative density by ~ 5.0 %. There was no literature data to compare these density values with as NCO is used in the slurry form as a cathode material for Na-ion solid-state batteries and requires no densification after preparation. Aqueous NCO achieved the highest relative density among the NCO ceramics cold sintered with different transient solvents (see later) and the conventional sintered NCO (section 6.2.2).

Table 6.5

The density (g/cm^3) and relative density (ρ_r) of aqueous cold-sintered NCO by varying the densification parameters

Variable Temp., Time and constant Pressure					Variable Pressure (MPa) and constant Temp. 200 °C & time			
	500 MPa/150 °C		500 MPa/200 °C		250	312	375	437
Time (minutes)	Density (g/cm^3)	ρ_r (%)	Density (g/cm^3)	ρ_r (%)	ρ_r (%)	ρ_r (%)	ρ_r (%)	ρ_r (%)
15	4.301	92.3	4.400	94.42	-	-	-	-
30	4.311	92.51	4.406	94.55	-	-	-	-
45	4.325	92.81	4.539	97.40	-	-	-	-
60	4.358	93.52	4.569	98.05	94.08	95.02	97.17	97.55

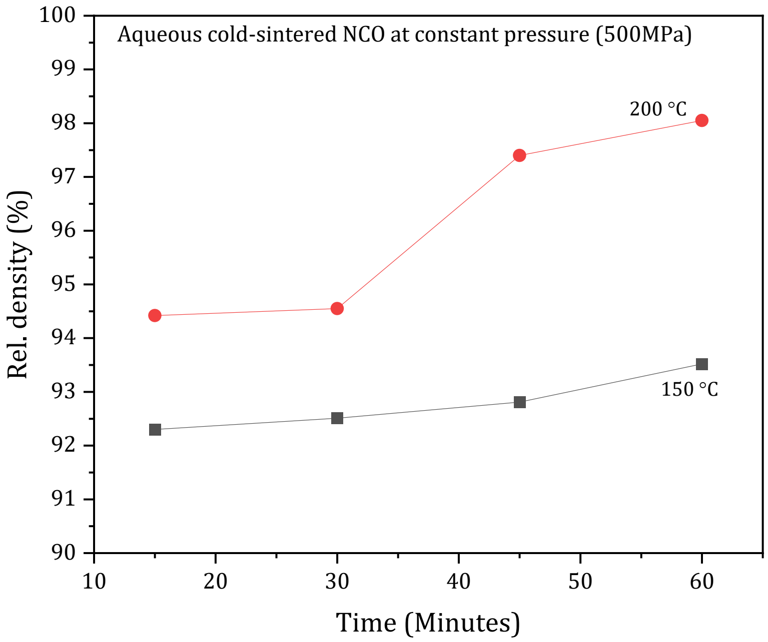

Figure 6.3.4. Relative density of NCO pellets at constant pressure and different temperatures and time.

6.3.1.3 Scanning electron microscopy

SEM micrographs of the lightly polished surface of the aqueous cold-sintered NCO ceramics are shown in Figure 6.3.5. The microstructure appears almost fully dense, with scant evidence of porosity. The grains are firmly interconnected and compressed, which is consistent with ~ 98.0 % relative density. Samples generally react at ambient, and care must be taken not to over-interpret individual features, as artefacts can be readily formed on exposure to the atmosphere and during grinding and polishing as shown in Figure 6.3.6.

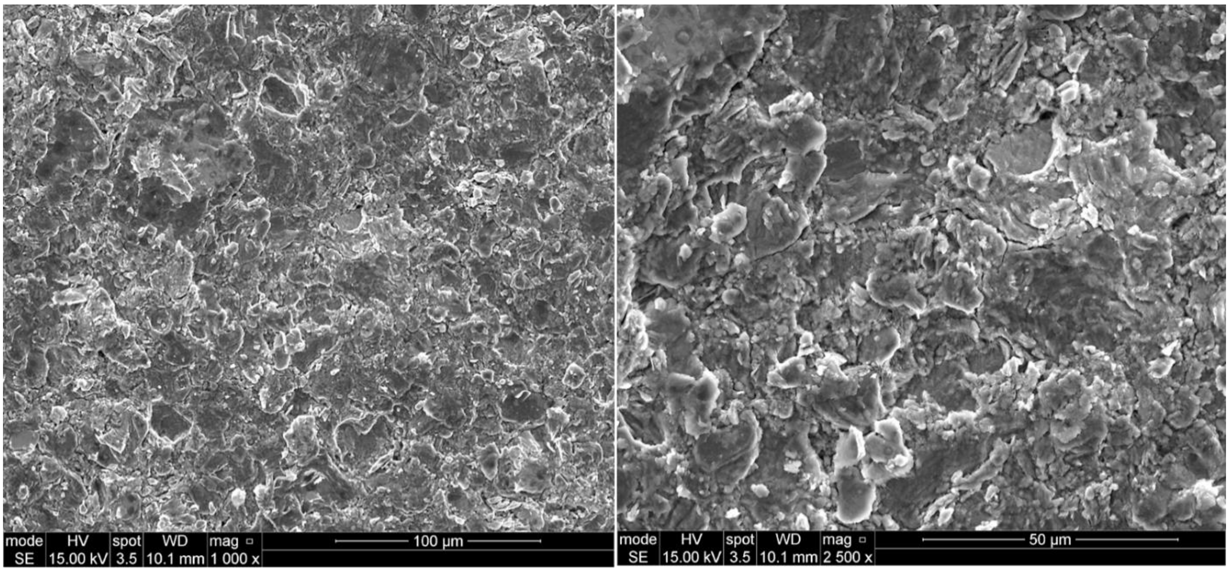

Figure 6.3.5. SEM micrographs of the lightly polished surface of aqueous cold-sintered NCO.

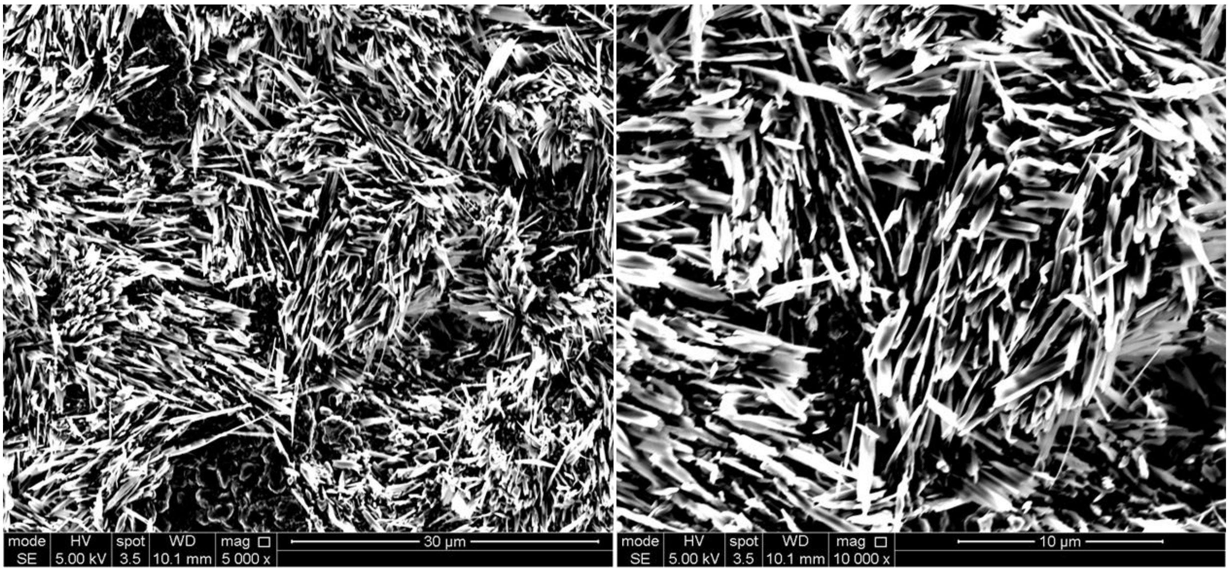

Figure 6.3.6. SEM micrographs of the Artefact formed on the exposed polished surface of the aqueous cold-sintered NCO pellet.

6.3.1.4 Elemental Mapping of the NCO

The elemental mapping of the aqueous (H_2O) cold-sintered NCO is shown in Figure 6.3.7. In the BSD image, there are two distinct areas where there is a high concentration of Na and Co. The two regions were mapped with a red circle in Figure 6.3.7. The dark region (indicated by an arrow) contains a high concentration of Na^+ ions, as shown in Region 2 in the EDX spectra; at the same time, the grey areas have high concentrations of Co3+ ions, as shown in Region 1 in the spectra.

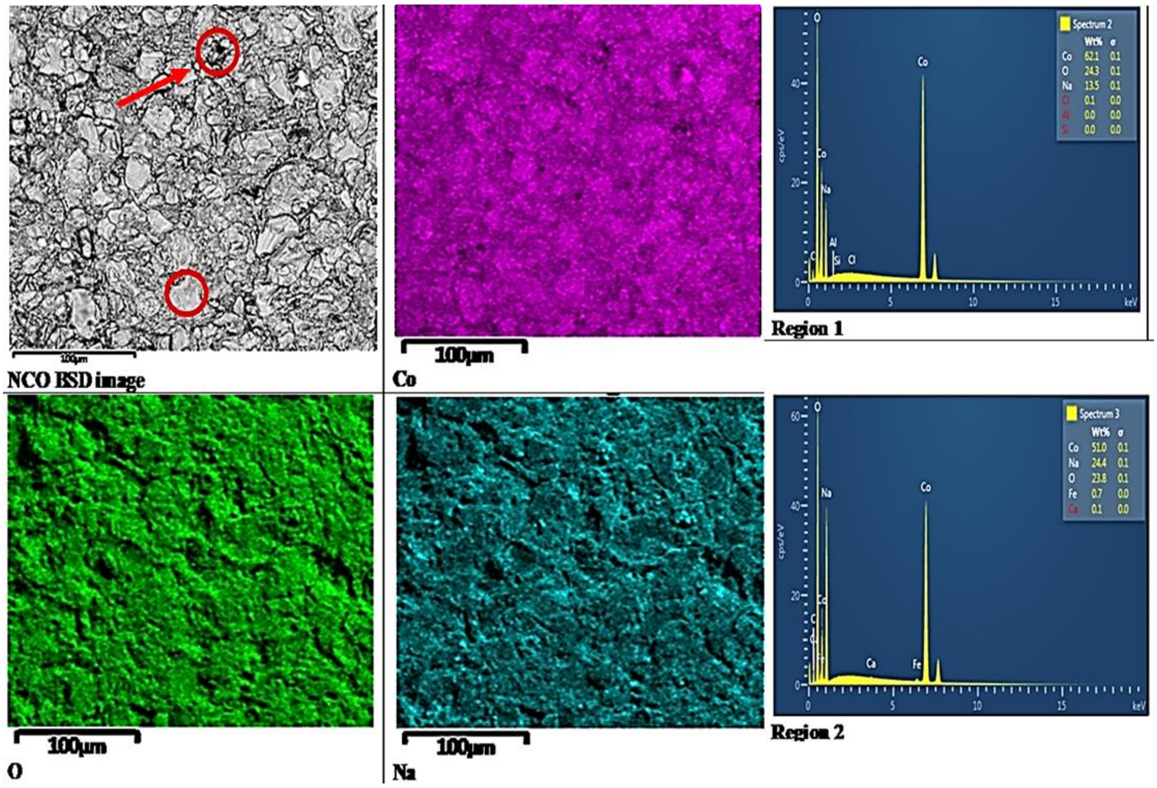

Figure 6.3.7. The elemental mapping of the aqueous cold-sintered NCO.

6.3.1.5 Impedance Spectroscopy

The NCO ceramic cold sintered at 500 MPa, 200 °C for 1 hour, was further investigated for conductivity due to its superior phase purity and high relative density. The complex impedance plane, Z*, and the spectroscopic plots of the aqueous (H_2O) cold-sintered NCO ceramics using In-Ga alloys are shown in Figure 6.3.8, and the associated data obtained from extrapolating the Zview software are shown in Table 6.6.

Table 6.6

Impedance spectroscopic data of the aqueous (H_2O) cold-sintered NCO. Obt = obtained values, Calc = calculated values, R_s, R_x and R_T = bulk, grain boundary and total resistance, respectively. σ_T = total conductivity, C_T = total capacitance, f_{max} and ω_{max} are the maximum frequency and angular frequency.

NCO CS H_2O	Obt	Obt	Obt	Calc	Obt	Calc	Obt
Temp (K)	R_x	R_s	R_T	σ_T	ω_{max}	f_{max}	C_T
140	34.96	140.33	175.61	0.0057	2.1E+06	2.5E+02	3.4E-09
160	33.58	149.08	182.66	0.0055	2.0E+06	3.0E+02	3.3E-09
180	36.12	114.58	150.70	0.0066	2.2E+06	4.0E+02	3.9E-09
200	36.87	87.50	124.36	0.0080	2.4E+06	5.0E+02	4.6E-09
220	38.39	63.79	102.17	0.0098	2.6E+06	1.0E+03	5.8E-09
240	40.05	43.03	83.08	0.0120	3.0E+06	1.5E+03	7.1E-09
273	38.89	19.67	58.56	0.0171	3.2E+06	5.0E+05	1.3E-08

At room temperature, there was only a single, poorly resolved arc with a high-frequency non-zero intercept on the Z' axis, similar to what was observed in the conventional sintered NCO ceramic. The total (dc) resistivity was based on the low-frequency intercept of the arc in Z* plots and was ~ 50-60 Ωcm, and the non-zero intercept at high frequency was in the range of ~ 20 to 40 Ωcm. The results are consistent with NCO ceramic being highly conductive at room temperature and the low-frequency arc observed with the In-Ga alloy sample associated with a non-ohmic electrode contact.

The Z* data in Figure 6.3.8 were modelled on an equivalent circuit based on a single resistor connected in series with a parallel Resistor-Capacitor element. The single resistor, which is associated with the high frequency and non-zero intercept on the Z' axis, is attributed to the overall resistivity of the ceramic ($R_{ceramic}$), and the parallel RC element, which is associated with the arc in Z*, is attributed to the electrode effect ($R_{electrode}C_{electrode}$). Performing measurements at sub-ambient temperatures resulted in modest changes in the Z* plots. The arc in the Z* increased in magnitude with decreasing temperature, but there were only minor changes in the non-zero intercept, Figure 6.3.8a. This shows that $R_{electrode}$ increases with decreasing temperature, with $C_{electrode}$ in the range ~ 3 – 10 $nFcm^{-1}$ and $R_{ceramic}$ decrease with decreasing temperature. Due to the conductive nature of the NCO ceramic, we extrapolated the bulk (R_s) and grain boundary (R_x) resistance to probe their contributions to the overall impedance response of the NCO ceramics, as shown in Table 6.6. Figure 6.3.8 (b-d) shows the spectroscopic data of the impedance, (b) the capacitance, C" (c) the imaginary component of the impedance, Z" and (d) the electric modulus, M" of the aqueous (H_2O) cold-sintered NCO.

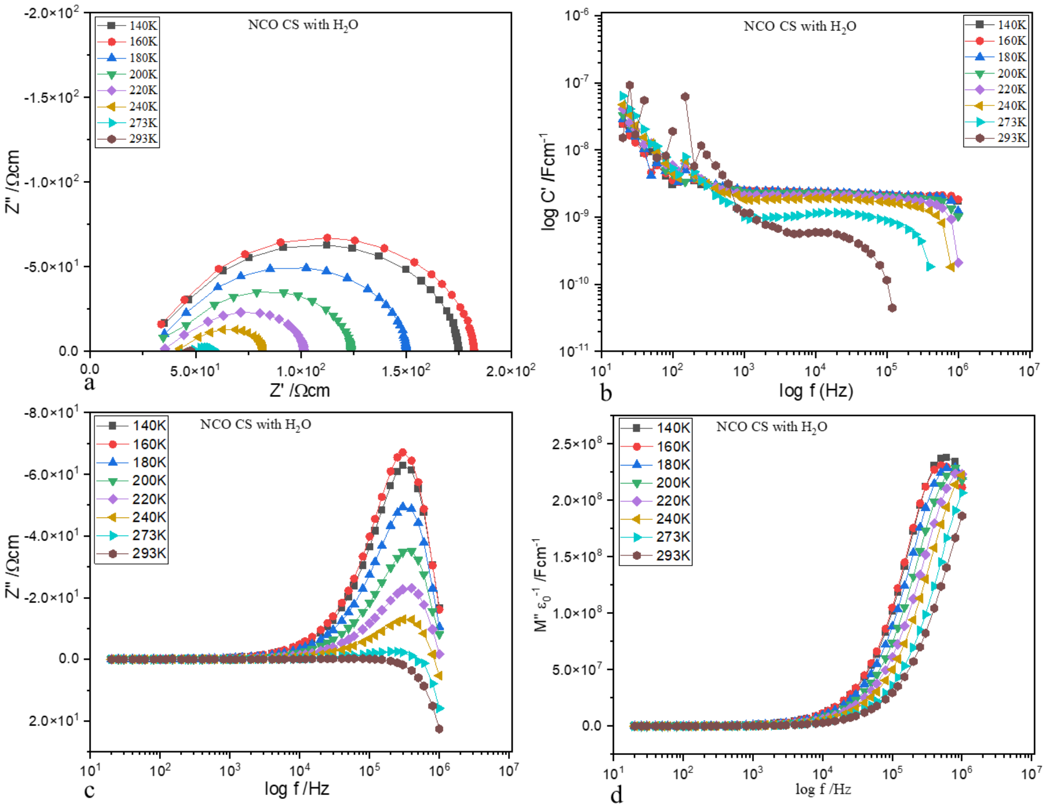

Figure 6.3.8. Impedance (Z*) and the spectroscopic plots of distilled water cold-sintered NCO at 140 – 293K range (a) Z'/Z'' (b) capacitance (c) Z'' (d) M''.

6.3.1.6 Arrhenius plot

The temperature-dependent data of the (bulk, grain boundary and total) conductivities of the aqueous cold sintered NCO at different temperatures are shown in Table 6.7. The data were extrapolated to calculate the gradient of the Arrhenius plot. The standard least square method was used to obtain the gradients of the temperature-dependent data of the aqueous cold-sintered NCO in Origin software, and the uncertainty associated with each gradient and activation energy was recorded.

The Activation energy (E_a) was calculated according to Equation 3.35 (chapter 3), and the results are shown in Table 6.7. The Arrhenius plot of the total conductivity of the aqueous cold-sintered NCO (where $\sigma_T = 1/R_T$) is shown in Figure 6.3.9. The E_a is ~ 0.037 ± 0.017 eV; the plot shows metallic-type conduction and non-Arrhenius-type behaviour for the non-ohmic contacts. In addition, the plot of $T^{-1/3}$ and $T^{-1/4}$ against the total conductivity deviated from linearity, Figures 6.3.10 and 6.3.11.

Hence, the Na^+ ion migration pathway in the aqueous cold-sintered NCO was investigated, Figures 6.3.12. The plots of the log of the ceramic (bulk) and electrode (grain boundary) conductivity against 1000/T show the contribution of each factor to the total conductivity, and it was observed that the Na^+ ion migration favours the electrode (grain boundary). The data could not be compared to the literature, as no data is available to the best of our knowledge on the E_a of NCO, and the low E_a values could be attributed to the conductivity nature of the NCO ceramic. However, the results obtained are comparable to NCO samples sintered conventionally and other aqueous (1M NaOH solution) cold-sintered NCO ceramics (see later).

Table 6.7

Temperature-dependent conductivity of aqueous cold-sintered NCO. σ_s, σ_x and σ_t are the bulk, grain boundary and total conductivity extracted from the bulk (R_x), grain boundary (R_s) and total (R_t) resistance shown in Table 6.6 (above).

Temp (K)	1000/T (K)	$T^{-1/3}$	$T^{-1/4}$	σ_x	Log σ_x	σ_s	Log σ_s	σ_T	Log σ_T
140	7.14	0.193	0.291	0.029	-1.54	0.007	-2.15	0.006	-2.25
160	6.25	0.184	0.281	0.030	-1.53	0.007	-2.17	0.005	-2.26
180	5.56	0.177	0.273	0.028	-1.56	0.009	-2.06	0.007	-2.18
200	5.00	0.171	0.266	0.027	-1.57	0.011	-1.94	0.008	-2.10
220	4.55	0.166	0.260	0.026	-1.58	0.016	-1.80	0.010	-2.01
240	4.17	0.161	0.254	0.025	-1.60	0.023	-1.63	0.012	-1.92
273	3.66	0.154	0.246	0.026	-1.59	0.051	-1.29	0.017	-1.77

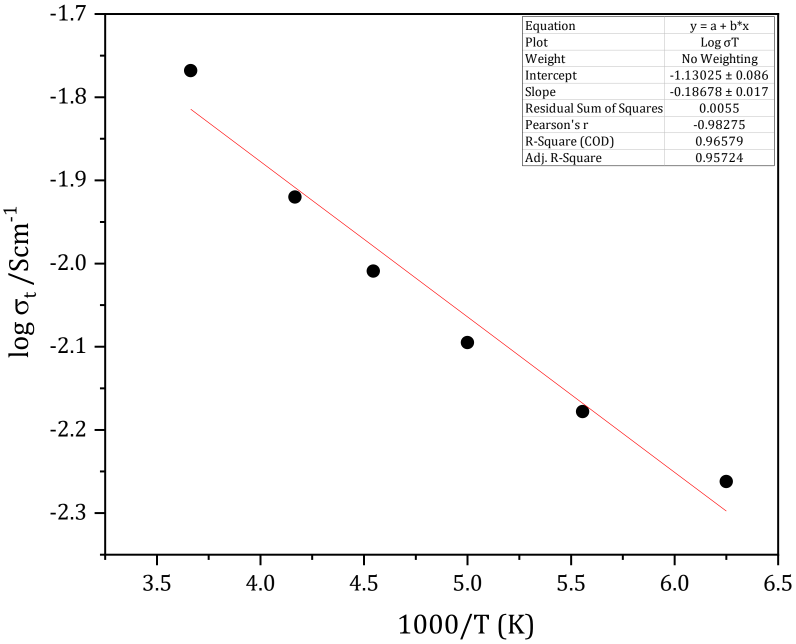

Figure 6.3.9. Arrhenius plot of the total conductivity of the aqueous cold-sintered NCO.

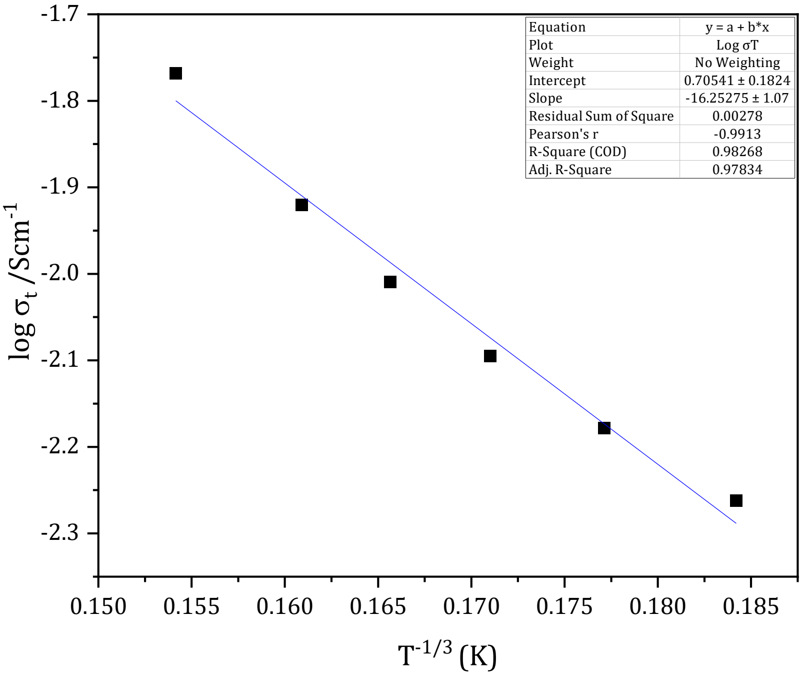

Figure 6.3.10. Arrhenius plot of the total conductivity of the aqueous cold-sintered NCO against $T^{-1/3}$.

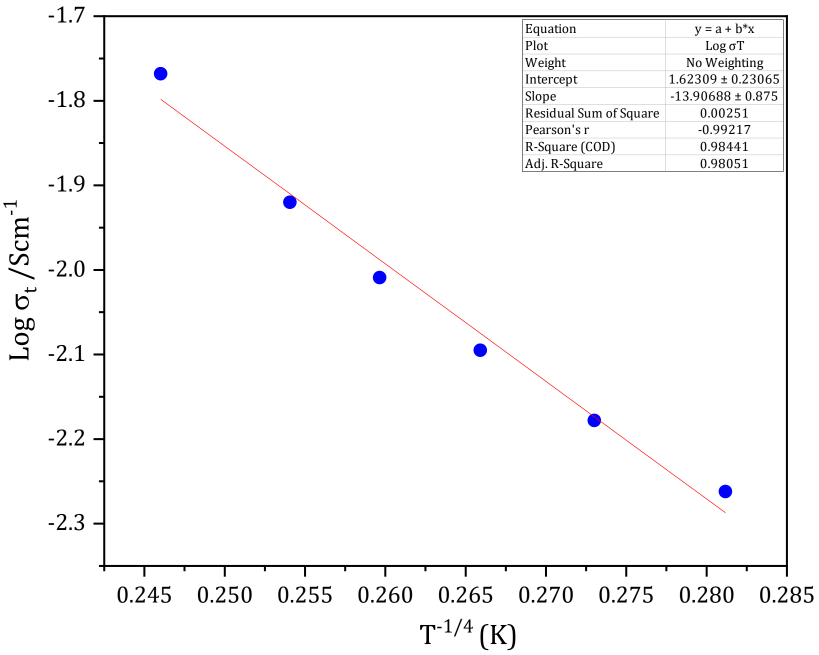

Equation	y = a + b*x
Plot	Log σT
Weight	No Weighting
Intercept	1.62309 ± 0.23065
Slope	-13.90688 ± 0.875
Residual Sum of Square	0.00251
Pearson's r	-0.99217
R-Square (COD)	0.98441
Adj. R-Square	0.98051

Figure 6.3.11. Arrhenius plot of the total conductivity of sintered NCO against $T^{-1/4}$.

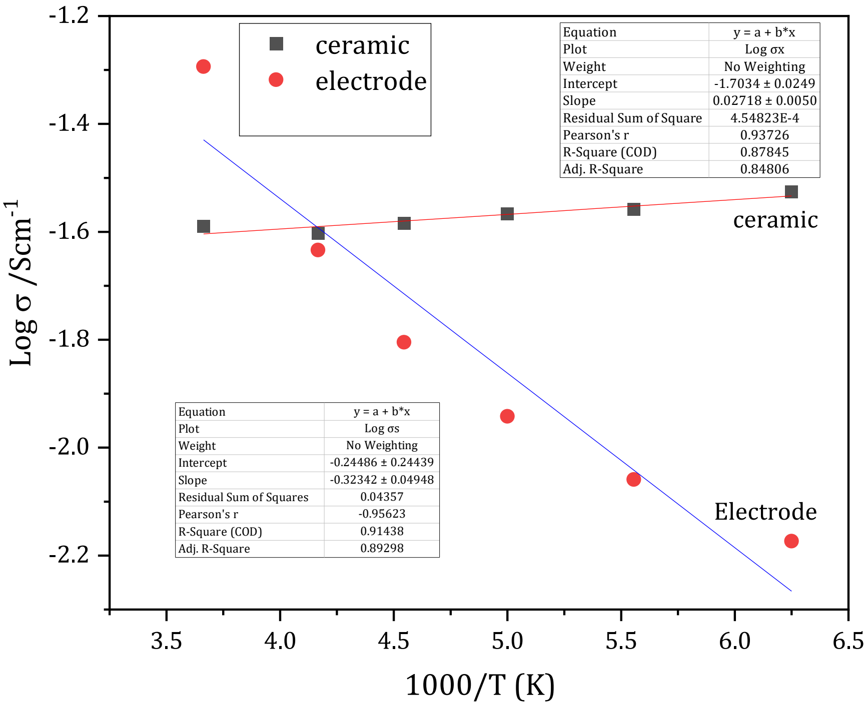

Equation	y = a + b*x
Plot	Log σx
Weight	No Weighting
Intercept	-1.7034 ± 0.0249
Slope	0.02718 ± 0.0050
Residual Sum of Square	4.54823E-4
Pearson's r	0.93726
R-Square (COD)	0.87845
Adj. R-Square	0.84806

Equation	y = a + b*x
Plot	Log σs
Weight	No Weighting
Intercept	-0.24486 ± 0.24439
Slope	-0.32342 ± 0.04948
Residual Sum of Squares	0.04357
Pearson's r	-0.95623
R-Square (COD)	0.91438
Adj. R-Square	0.89298

Figure 6.3.12. Arrhenius plot of the bulk (electrode) and grain boundary (ceramic) conductivity of aqueous cold-sintered NCO against 1000/T.

6.3.2 NCO cold sintered using aqueous 1M NaOH solution.

In this section, NCO powder was cold sintered using 1M NaOH solution as the transient solvent and the phase, morphology and electrical properties were investigated and compared with the H_2O-densified NCO sample.

6.3.2.1 X-ray diffraction

The X-ray diffraction pattern of the cold-sintered NCO using 1M NaOH solution as the transient solvent is shown in Figure 6.3.13. The X-ray diffraction peaks were matched against the NCO green powder and PDF N°: 00-078-2822 of the P2-phase $Na_{0.71}CoO_2$ with space group $P6_3/mmc$ [1-5]. All the peaks in the 1M NaOH cold-sintered NCO indexed according to the P2-phase of $Na_{0.71}CoO_2$. The extra/impurity peaks of Co_3O_4 at 14.61 and 17.20, 2θ degrees observed in the NCO green powder were partially absent in the 1M NaOH cold-sintered NCO. The peak at 14.61, 2θ degrees disappeared, and peaks at higher 2θ degree values were not sharp. Comparing the X-ray diffraction pattern of 1M NaOH cold-sintered NCO with aqueous (H_2O) cold-sintered NCO, Figure 6.3.14, the peaks in the aqueous (H_2O) cold-sintered NCO samples were sharper than that of the 1M NaOH cold-sintered NCO sample. Also, the peaks at higher 2 theta values in the 1M NaOH cold sintered NCO ceramic were less intense, and some were not visible above the background (36.62 and 44.77, 2θ degree).

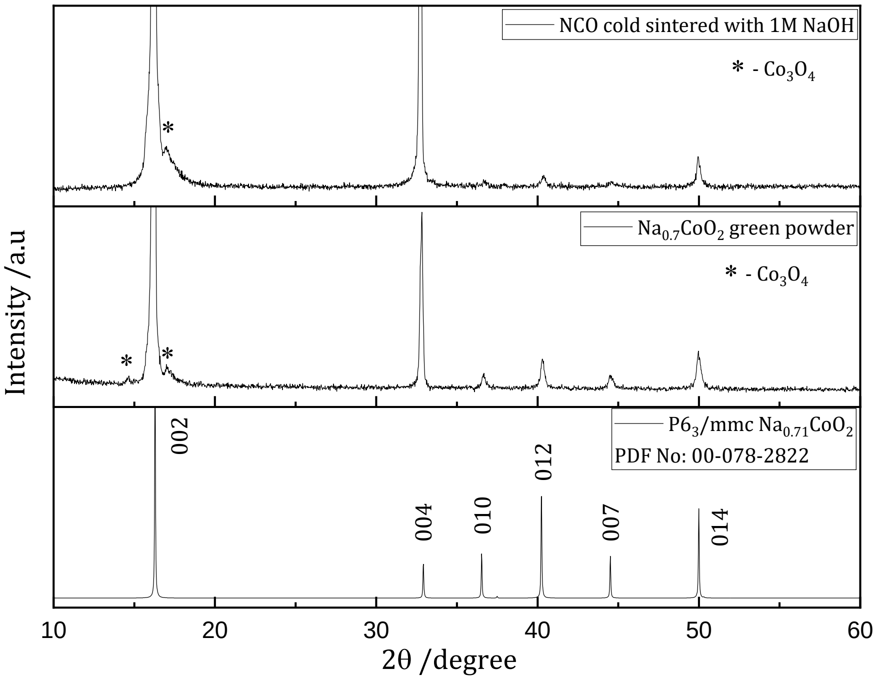

Figure 6.3.13. Room temperature X-ray diffraction patterns of 1M NaOH cold-sintered NCO, green powder NCO, and indexed P2-phase $Na_{0.71}CoO_2$ with space group *$P6_3/mmc$*.

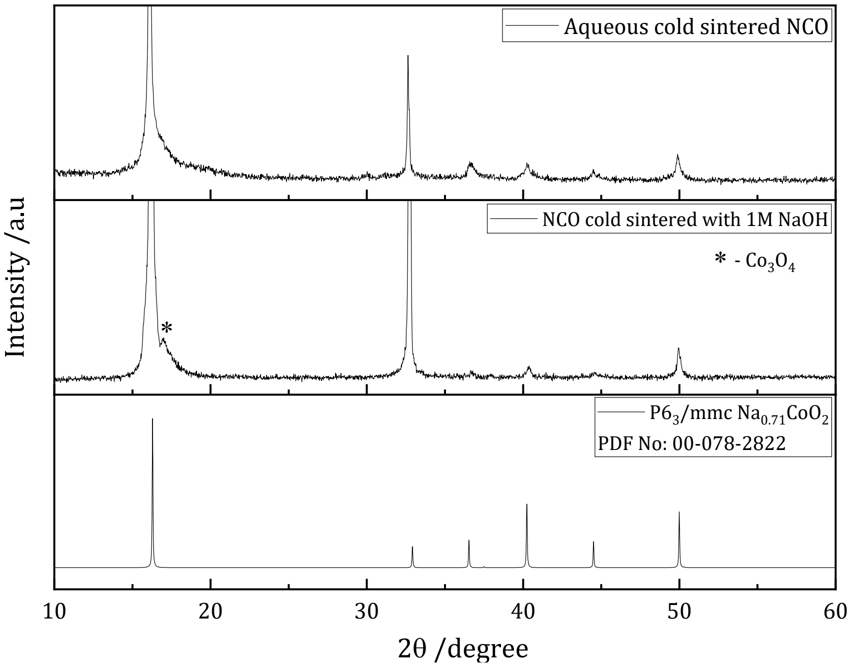

Figure 6.3.14. Room temperature X-ray diffraction patterns comparing 1M NaOH cold-sintered NCO with aqueous cold-sintered NCO and indexed P2-phase $Na_{0.71}CoO_2$ with space group *P6₃/mmc*.

6.3.2.2 Relative density

The experimental density of the 1M NaOH cold-sintered $Na_{0.7}CoO_2$ pellets was measured using the Archimedes method, and the results were compared with $Na_{0.71}CoO_2$ theoretical density obtained from the ICDD database. The theoretical density of $Na_{0.71}CoO_2$ is 4.74 g/cm^3, and the relative density (ρ_r) of NCO was calculated according to equation 3.8 (chapter 3). To achieve the highest experimental density for NCO ceramic, time, temperature and pressure were varied, and the average of three measurements was recorded, as shown in Table 6.8. NCO ceramic pressed at 500 MPa, 200 °C, and 1 hour achieved the highest relative density of 97.40 % for 1M NaOH cold-sintered NCO. Figures 6.3.15 and 6.3.16 compare the relative densities of 1M NaOH cold-sintered NCO with aqueous (H_2O) cold-sintered NCO pellets by varying the densification parameters. All the NCO pellets cold-sintered with (H_2O) as the transient solvent achieved a higher relative density compared to the 1M NaOH cold-sintered NCO pellets. The relative density trend observed for the aqueous (H_2O) cold-sintered NCO was also observed for the 1M NaOH cold-sintered NCO, and all the pellets' relative densities are greater than 93.0 % irrespective of the pressing pressure, temperature and time, Table 6.8.

Table 6.8

The densities and relative densities of 1M NaOH cold-sintered NCO by varying the densification parameters.

Variable Temp., Time, and const. Pressure			Variable Pressure (MPa) and constant 200 °C			
	500 MPa/200 °C		250	312	375	437
Time (minutes)	Density (g/cm^3)	ρ_r (%)	ρ_r (%)	ρ_r (%)	ρ_r (%)	ρ_r (%)
15	4.387	94.14	-	-	-	-
30	4.395	94.31	-	-	-	-
45	4.446	95.4	-	-	-	-
60	4.539	97.4	93.91	94.51	94.83	95.26

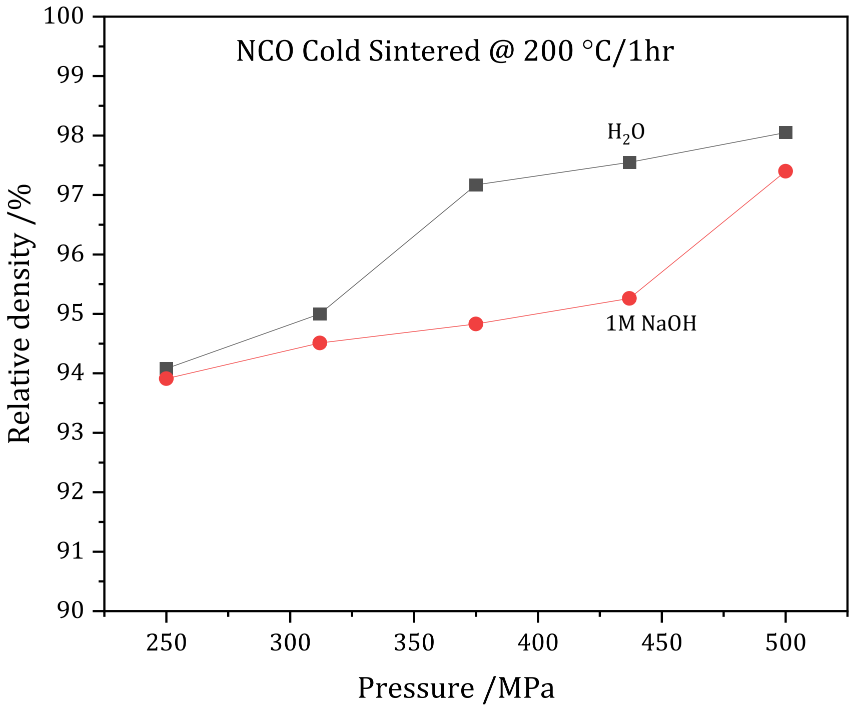

Figure 6.3.15. Comparison of the relative density of 1M NaOH and aqueous cold sintered NCO pellets at variable pressure and constant temperature and time.

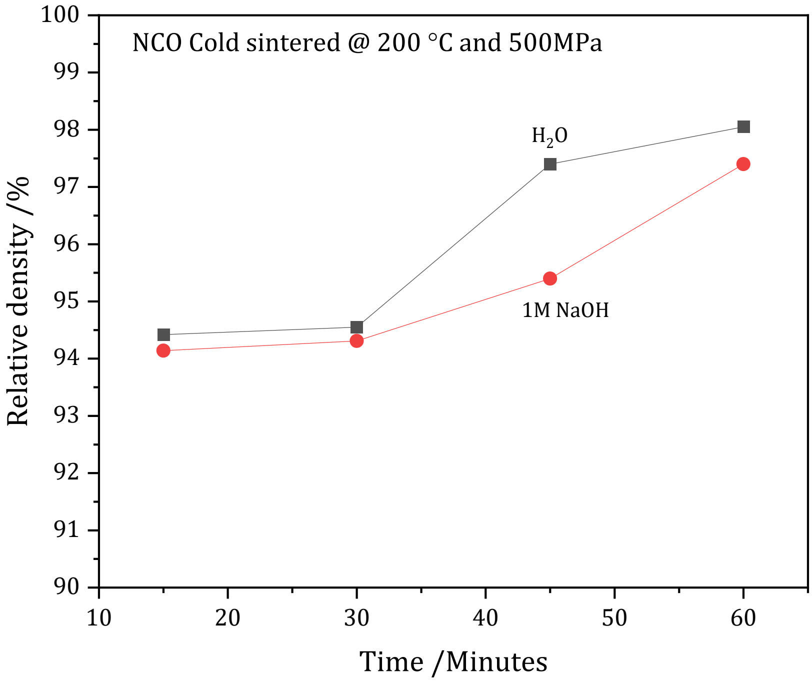

Figure 6.3.16. Comparison of the relative density of 1M NaOH and aqueous cold sintered NCO pellets at variable time and constant temperature and time.

6.3.2.3 Scanning electron microscopy

SEM micrographs of the fractured surface of the 1M NaOH cold-sintered NCO ceramics are shown in Figure 6.3.17. The microstructure appears dense and tightly packed with firmly interconnected grains supporting a dense ceramic with 97.0 % relative density.

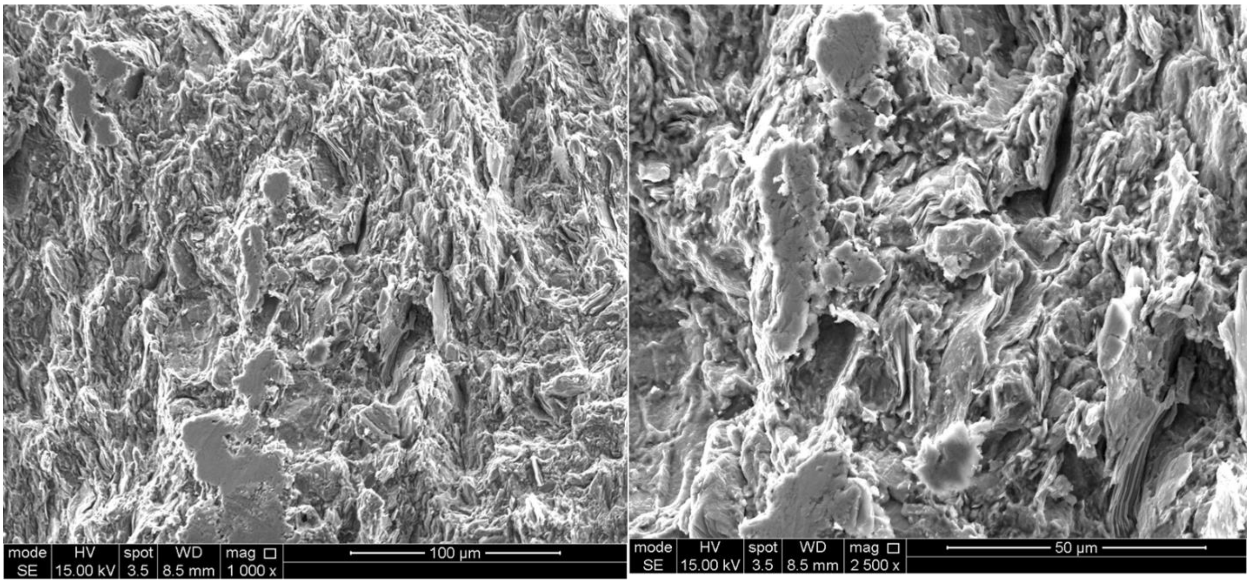

Figure 6.3.17. SEM micrographs of the fractured surface of cold-sintered NCO using 1M NaOH as the transient solvent.

6.3.2.4 Impedance Spectroscopy

The NCO ceramic that was cold sintered with 1M NaOH at 500 MPa, 200 °C for 1 hour was investigated for conductivity measurement due to its high relative density. The complex impedance plane, Z* plots and the spectroscopic plots of the 1M NaOH cold-sintered NCO ceramics using In-Ga alloys are shown in Figure 6.3.18, and the associated data obtained from extrapolating the Zview software are shown in Table 6.9.

Table 6.9

Impedance spectroscopic data of 1M NaOH cold-sintered NCO. Obt = obtained values, Calc = calculated values, R_s, R_x and R_T = bulk, grain boundary and total resistance, respectively. σ_T = total conductivity, C_T = total capacitance, f_{max} and ω_{max} are the maximum frequency and angular frequency.

NCO CS NaOH	Obt	Obt	Obt	Calc	Obt	Calc	Obt
Temp (K)	R_s	R_x	R_t	σ_T	ω_{max}	f_{max}	C_T
140	239.05	90.09	328.95	0.0030	4.2E+06	2.5E+02	9.9E-10
160	211.03	91.68	302.71	0.0033	4.3E+06	8.0E+02	1.1E-09
180	187.84	93.01	280.54	0.0036	4.3E+06	1.0E+03	1.2E-09
200	162.84	99.86	262.71	0.0038	4.4E+06	1.5E+03	1.4E-09
220	126.53	107.60	234.13	0.0043	4.5E+06	2.0E+03	1.8E-09
240	95.17	106.23	201.41	0.0050	4.5E+06	3.0E+03	2.3E-09
260	69.72	106.79	176.52	0.0057	4.2E+06	4.0E+03	3.4E-09
273	52.12	103.15	155.27	0.0064	3.9E+06	8.0E+03	4.7E-09
293	32.44	76.76	109.2	0.0092	1.6E+06	0.0E+00	1.0E-08

At room temperature, there was only a single, poorly resolved arc with a high-frequency non-zero intercept on the Z' axis. The total (dc) resistivity was based on the low-frequency intercept of the arc in Z* plots and was ~ 100 - 110 Ωcm, and the non-zero intercept at high frequency was in the range of ~ 30 to 40 Ωcm. The results are consistent with NCO ceramic being highly conductive at room temperature and the low-frequency arc observed with the In-Ga alloy sample associated with a non-ohmic electrode contact.

The Z* data in Figure 6.3.18 were modelled on an equivalent circuit based on a single resistor connected in series with a parallel Resistor-Capacitor element. The single resistor, which is associated with the high frequency and non-zero intercept on the Z' axis, is attributed to the overall resistivity of the ceramic ($R_{ceramic}$), and the parallel RC element, which is associated with the arc in Z*, is attributed to the electrode effect ($R_{electrode}C_{electrode}$). Performing measurements at sub-ambient temperatures resulted in modest changes in the Z* plots. The arc in the Z* increased in magnitude with decreasing temperature, but there were only minor changes in the non-zero intercept, Figure 6.3.18a. This shows that $R_{electrode}$ increases with decreasing temperature, with $C_{electrode}$ in the range 5 – 10 $nFcm^{-1}$ and $R_{ceramic}$ decrease with decreasing temperature. Due to the conductive nature of the NCO ceramic, we extrapolated the bulk (R_S) and grain boundary (R_X) resistance to probe their contributions to the overall impedance response of the ceramics. Figure 6.3.18 (b-d) shows the spectroscopic data of the impedance, (b) the capacitance, C" (c) the imaginary component of the impedance, Z" and (d) the electric modulus, M" of the 1M NaOH cold-sintered NCO.

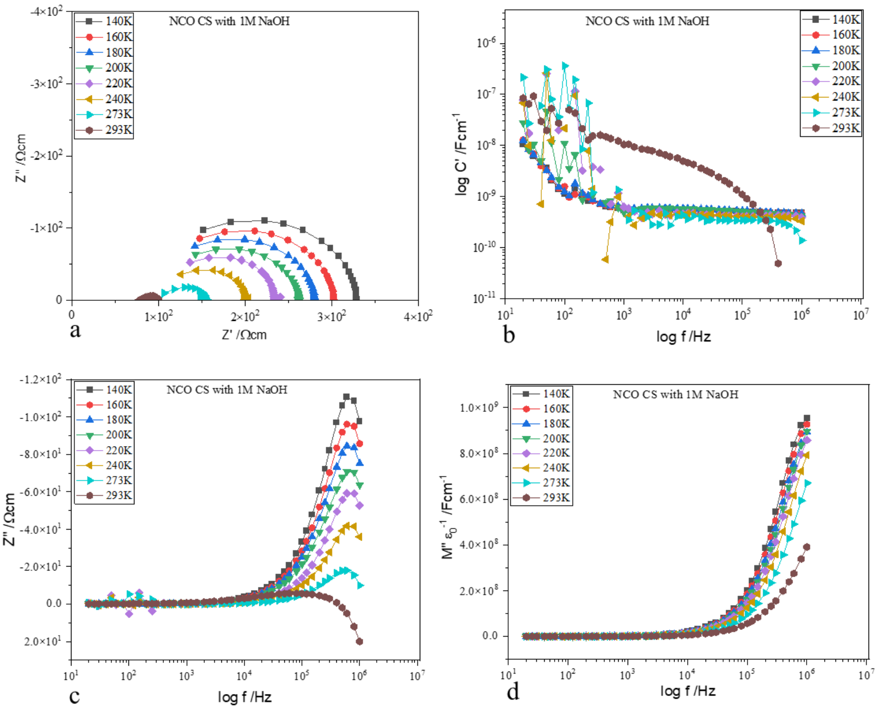

Figure 6.3.18. Z* and the spectroscopic plots of 1M NaOH cold-sintered NCO at 140 – 293K (a) Z'/Z'' (b) capacitance (c) Z'' (d) M''.

6.3.2.5 Arrhenius plot

The temperature-dependent data of the (bulk, grain boundary and total) conductivities of the aqueous 1M NaOH cold sintered NCO at different temperatures are shown in Table 6.10. The data were extrapolated to calculate the gradient of the Arrhenius plot. The

standard least square method was used to calculate the gradients of the temperature-dependent data of the 1M NaOH cold-sintered NCO in Origin software, and the uncertainty associated with each gradient and activation energy was recorded.
The Activation energy (E_a) was calculated according to Equation 3.35 (chapter 3), and the results are shown in Table 6.10. The Arrhenius plot of the total conductivity of the aqueous cold-sintered NCO (where $\sigma_T = 1/R_T$) is shown in Figure 6.3.19. The E_a is ~ 0.011 ± 0.0062 eV; the plot shows metallic-type conduction and non-Arrhenius-type behaviour for the non-ohmic contacts. In addition, the plots of $T^{-1/3}$ and $T^{-1/4}$ against the total conductivity are shown in Figures 6.3.20 and 6.3.21.

Figures 6.3.22 show the plots of the log of the NCO ceramic (bulk) and electrode (grain boundary) conductivity against 1000/T show the contribution of each factor to the total conductivity, and it was observed that the Na^+ ion migration favours the electrode (grain boundary). The results obtained were compared to a sample cold-sintered with distilled water, and it shows a similar mechanism.

Table 6.10
Temperature-dependent conductivity of 1M NaOH cold-sintered NCO. σ_s, σ_x and σ_t are the bulk, grain boundary and total conductivity extracted from the bulk (R_x), grain boundary (R_s) and total (R_t) resistance shown in Table 6.9 (above).

Temp (K)	1000/T (K)	$T^{-1/3}$	$T^{-1/4}$	σ_s	Log σ_s	σ_x	Log σ_x	σ_T	Log σ_T
140	7.143	0.193	0.291	0.0042	-2.38	0.0111	-1.95	0.0030	-2.517
160	6.250	0.184	0.281	0.0047	-2.32	0.0109	-1.96	0.0033	-2.481
180	5.556	0.177	0.273	0.0053	-2.27	0.0108	-1.97	0.0036	-2.448
200	5.000	0.171	0.266	0.0061	-2.21	0.0100	-2.00	0.0038	-2.419
220	4.545	0.166	0.260	0.0079	-2.10	0.0093	-2.03	0.0043	-2.369
240	4.167	0.161	0.254	0.0105	-1.98	0.0094	-2.03	0.0050	-2.304
260	3.846	0.157	0.249	0.0143	-1.84	0.0094	-2.03	0.0057	-2.247
273	3.663	0.154	0.246	0.0192	-1.72	0.0097	-2.01	0.0064	-2.191
293	3.413	0.151	0.242	0.0308	-1.51	0.0130	-1.89	0.0092	-2.038

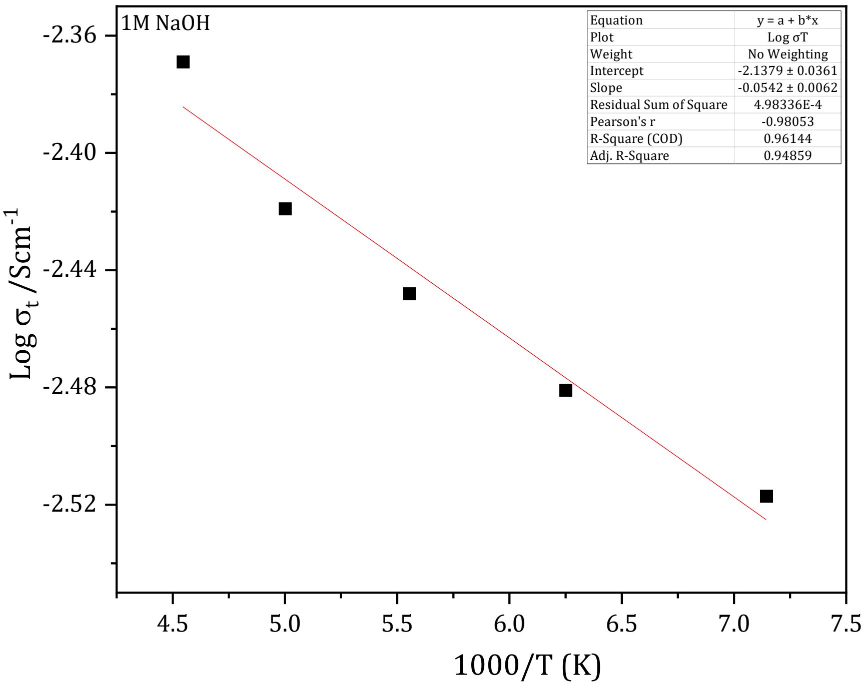

Figure 6.3.19. Arrhenius plot of the total conductivity of 1M NaOH cold-sintered NCO.

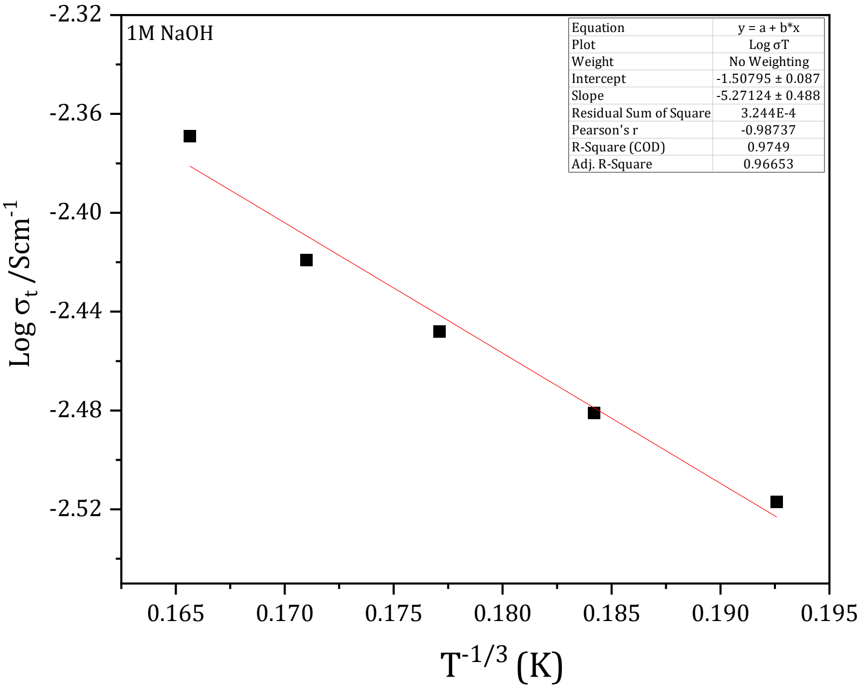

Figure 6.3.20. Arrhenius plot of the total conductivity of 1M NaOH cold-sintered NCO against $T^{-1/3}$.

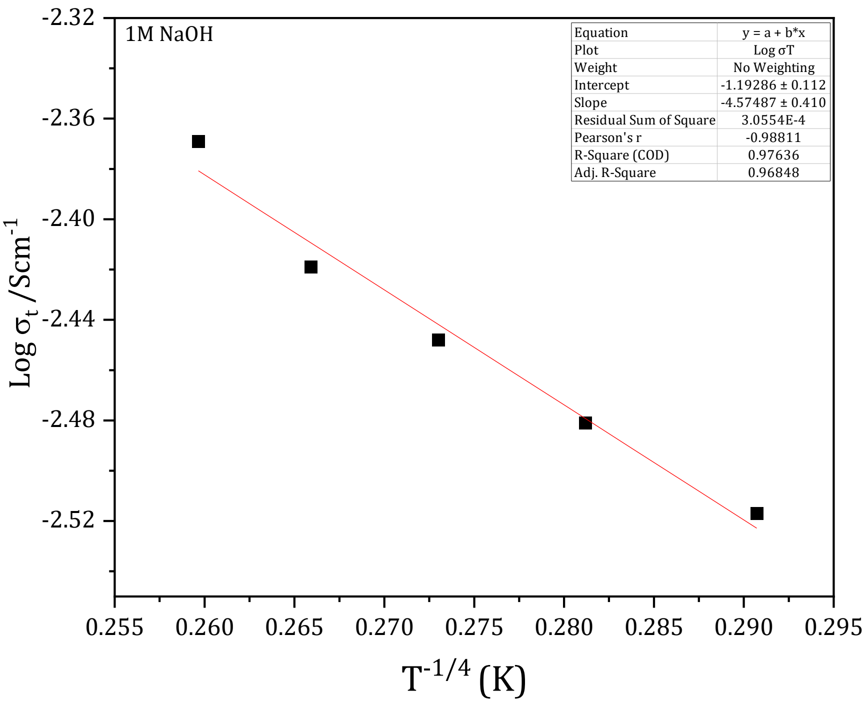

Figure 6.3.21. Arrhenius plot of the total conductivity of 1M NaOH cold-sintered NCO against $T^{-1/4}$.

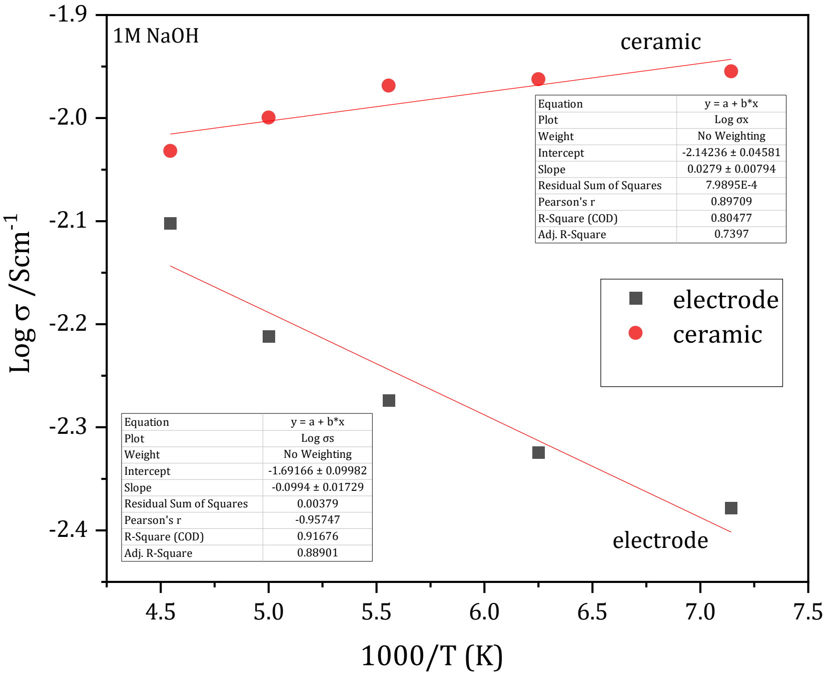

Figure 6.3.22. Arrhenius plot of the bulk (electrode) and grain boundary (ceramic) conductivity of 1M NaOH cold-sintered NCO against 1000/T.

6.3.3 NCO cold sintered using Isopropanol.

In this section, NCO powder was cold-sintered using isopropanol (IPA, an organic solvent) as the transient solvent. The phase, morphology and electrical properties were studied and compared with the H_2O-densified NCO sample.

6.3.3.1 X-ray diffraction

The X-ray diffraction pattern of the cold-sintered NCO using IPA as the transient solvent is shown in Figure 6.3.23. The X-ray diffraction peaks were matched against the NCO green powder and PDF N^{o}: 00-078-2822 of the P2-phase with space group $P6_3$/mmc [1-5]. All the peaks in the IPA-cold-sintered NCO matched with the NCO green powder and indexed according to the P2-phase $Na_{0.71}CoO_2$ phase. The impurity peaks of Co_3O_4 at 14.61 and 17.20, 2θ degrees observed in the NCO green powder were absent in the IPA cold-sintered NCO. However, there were unknown peaks at 18.85 and 31.19, 2θ degrees values. These unknown peaks could be an impurity from the IPA solvent or an unknown source. Efforts to identify the impurity peaks were unsuccessful. Also, the peaks at higher 2θ degree values were not better resolved compared to the samples aqueously cold-sintered.

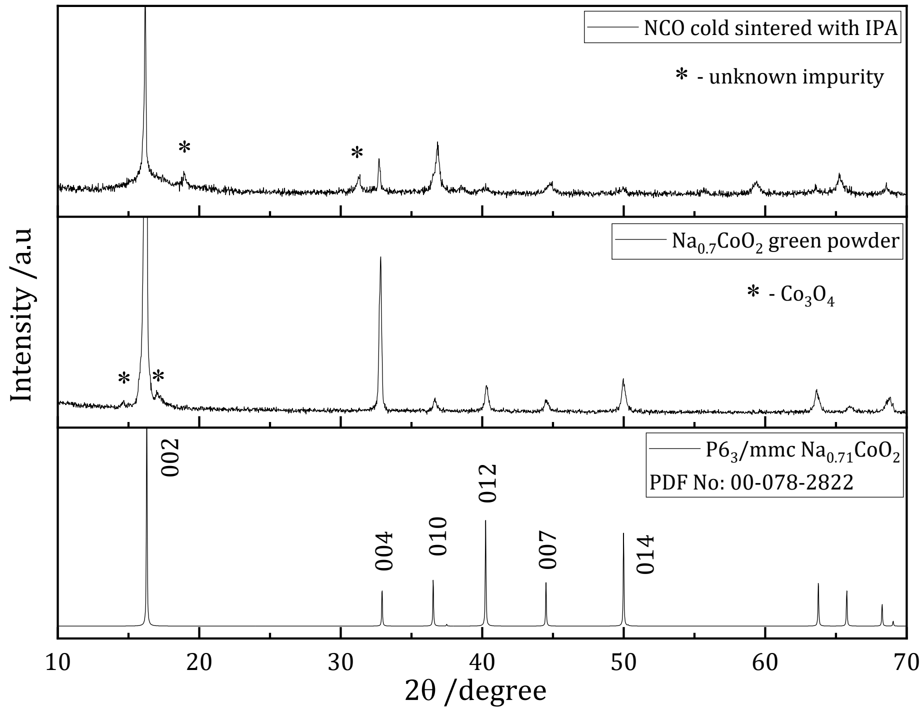

Figure 6.3.23. Room temperature X-ray diffraction patterns of NCO cold-sintered with IPA, the green powder and indexed P2-phase $Na_{0.71}CoO_2$ with space group *$P6_3$/mmc*.

6.3.3.2 Relative density

The experimental density of the IPA cold-sintered $Na_{0.7}CoO_2$ pellets was measured using the Archimedes method, and the results were compared with the $Na_{0.7}CoO_2$ theoretical density obtained from the ICDD database. The theoretical density of $Na_{0.7}CoO_2$ is 4.74 g/cm^3, and the relative density (ρ_r) of NCO was calculated according to equation 3.8 (chapter 3). Based on the densification results from aqueously (H_2O and 1M NaOH) cold-sintered samples, IPA cold-sintered NCO samples were pressed at 500 MPa, 200 °C, and 1 hour and the relative density obtained at these densification parameters was ~ 93.65%, as shown in Table 6.11 The relative density of the organic solvent cold-sintered NCO was lower compared to NCO samples aqueously cold-sintered but higher than NCO sample sintered conventionally.

Table 6.11

The density and relative density of IPA cold-sintered NCO.

Organic solvent	Pressure (MPa)	Temp (°C)	Time (1hr)	Density	ρ_r
10 wt% IPA	500	200	1	4.364	93.65

6.3.3.3 Scanning electron microscopy

SEM micrographs of the lightly polished surface of IPA cold-sintered NCO ceramics are shown in Figure 6.3.24. The micrographs appear dense with firmly interconnected grains. The cracks in the micrograph may be attributed to the applied pressure of (500 MPa) during the densification process. However, evidence of sintering is observed.

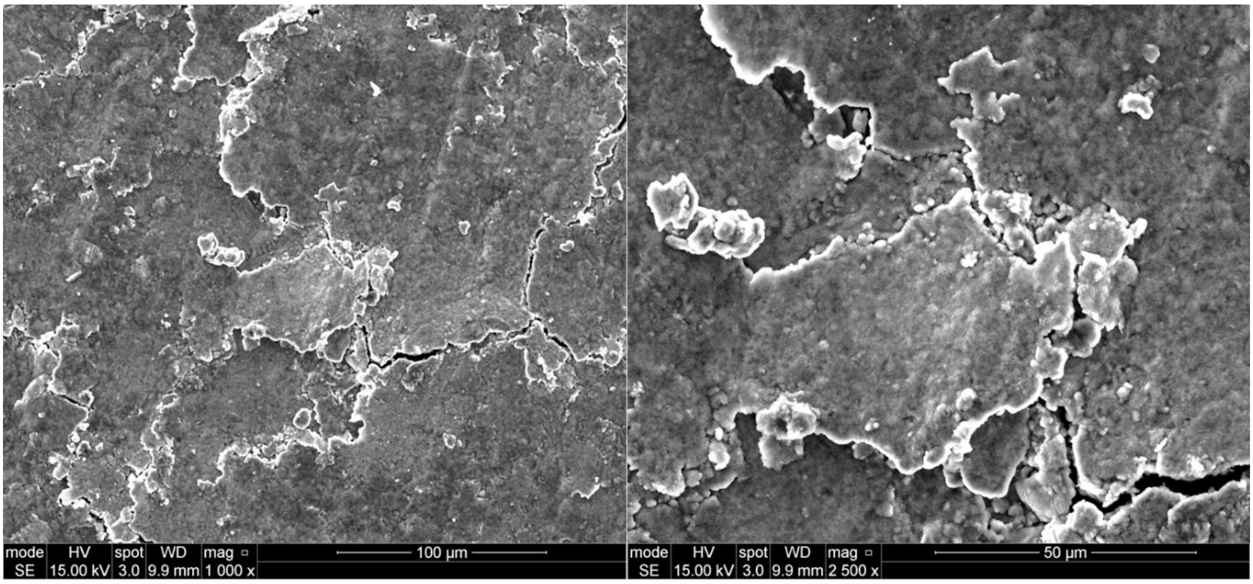

Figure 6.3.24. SEM micrographs of the lightly polished surface of isopropanol cold-sintered NCO.

6.3.3.4 Impedance Spectroscopy

The complex impedance plane, Z* and the spectroscopic plots of the IPA cold-sintered NCO ceramics using In-Ga alloys are shown in Figure 6.3.25, and the associated data obtained from extrapolating of the Zview software are shown in Table 6.12. The Z* data were different from those observed for aqueously cold-sintered NCO and conventional sintered NCO samples.

At room temperature, there was a single resolved arc with a negative intercept on the Z' axis, and the total (dc) resistivity was ~ 5.3 x 10^4 Ωcm. The RT conductivity value of the IPA cold-sintered NCO ceramic was ~ 1000% lower compared to conventional sintered and aqueous cold-sintered NCO samples. Performing measurements at sub-ambient temperatures did not change the Z* plots. The arc in the Z* increased in magnitude with decreasing temperature, Figure 6.3.26a. At temperatures below 25 °C, the single arcs were well resolved, Figure 6.3.25a. The spectroscopic data of the impedance, (b) the capacitance, C" (c) the imaginary component of the impedance, Z" and (d) the electric modulus, M" of the IPA cold-sintered NCO is shown in Figure 6.3.25 (b-d).

Table 6.12

Impedance spectroscopic data of IPA cold-sintered NCO. Obt = obtained values, Calc = calculated values, R_s, R_x and R_T = bulk, grain boundary and total resistance, respectively. σ_T = total conductivity, C_T = total capacitance, f_{max} and ω_{max} are the maximum frequency and angular frequency.

NCO CS IPA	Obt	Obt	Obt	Calc	Obt	Calc	Obt
Temp (K)	R_s	R_x	R_T	σ_T	ω_{max}	f_{max}	C_T
140	2.89E+05	-934.2	2.88E+05	3.47E-06	29755	5.00E+03	1.16E-10
160	2.53E+05	-980.8	2.52E+05	3.97E-06	32607	5.00E+03	1.21E-10
200	1.91E+05	-895.8	1.90E+05	5.25E-06	39546	6.00E+03	1.32E-10
220	1.62E+05	-775.2	1.61E+05	6.21E-06	43911	7.00E+03	1.41E-10
240	1.38E+05	-752.9	1.37E+05	7.30E-06	48256	8.00E+03	1.50E-10
260	1.17E+05	-691	1.16E+05	8.62E-06	54517	9.00E+03	1.57E-10
273	89506	-531.2	88975	1.12E-05	69947	1.20E+04	1.60E-10
293	54908	-1681	53227	1.88E-05	5145	6.00E+02	3.54E-09

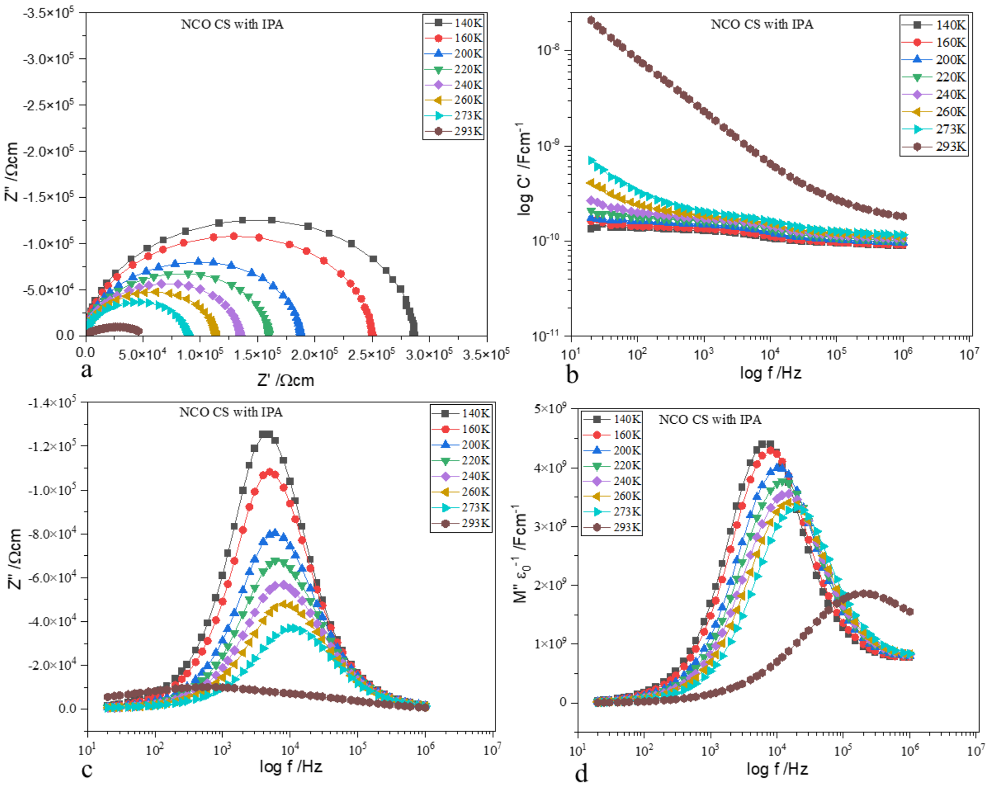

Figure 6.3.25. Z* and the spectroscopic plots of IPA cold-sintered NCO at 140 – 293K (a) Z'/Z'' (b) capacitance (c) Z'' (d) M''.

Due to the low conductivity of the IPA cold-sintered NCO samples compared to aqueously cold-sintered NCO, we decided to apply heat (850 °C/2hr) to the IPA cold-sintered NCO pellets and study the electrical properties, Figure 6.3.26. The associated Zview software data obtained from extrapolating the (IPA + heat) cold-sintered NCO ceramic is shown in Table 6.13. The total dc resistivity was increased by over 1000% by the application of heat to the NCO ceramic. The arc at 0 and 25 °C were well resolved and performing measurements at sub-ambient temperatures resulted in modest changes in the Z* plots. The arc in the Z* increased in magnitude with decreasing temperature, Figure 6.3.26a. The spectroscopic data of the impedance, (b) the capacitance, C" (c) the imaginary component of the impedance, Z" and (d) the electric modulus, M" of the IPA + heat NCO cold-sintered are shown in Figures 6.3.26 (b-d).

Table 6.13

Impedance spectroscopic data of Isopropanol cold-sintered (NCO + heat) at 850 °C/2hr. Obt = obtained values, Calc = calculated values, R_s, R_x and R_T = bulk, grain boundary and total resistance, respectively. σ_T = total conductivity, C_T = total capacitance, f_{max} and ω_{max} are the maximum frequency and angular frequency.

NCO CS IPA + heat (850 °C /2HR)	Obt	Obt	Obt	Calc	Obt	Calc	Obt
Temp (K)	R_s	R_x	R_T	σ_T	ω_{max}	f_{max}	C_T
140	215.98	75.90	291.88	0.0034	4.0E+06	2.0E+03	1.2E-09
160	178.70	79.05	257.75	0.0039	4.4E+06	3.0E+03	1.3E-09
180	139.91	83.72	223.53	0.0045	4.6E+06	4.0E+03	1.6E-09
200	108.28	87.76	196.03	0.0051	4.8E+06	5.0E+03	1.9E-09
220	87.91	89.95	177.86	0.0056	4.9E+06	6.0E+03	2.3E-09
240	135.93	80.80	216.73	0.0046	4.6E+06	6.0E+03	1.6E-09
260	446.50	59.04	505.54	0.0020	2.0E+06	6.0E+03	1.1E-09
273	759.72	53.58	813.30	0.0012	1.1E+06	1.0E+03	1.2E-09
293	1361.50	48.27	1409.80	0.0007	6.2E+05	5.0E+03	1.2E-09

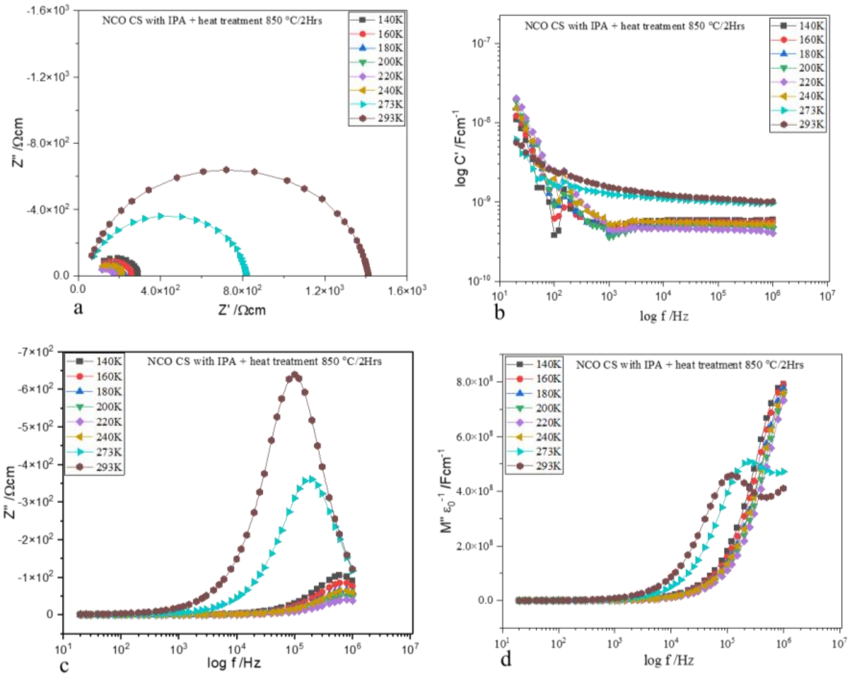

Figure 6.3.26. Z* and the spectroscopic plots of IPA cold-sintered NCO (plus heat at 850 °C/2hr) at 140 – 293K (a) Z'/Z'' (b) capacitance (c) Z'' (d) M''.

6.3.3.5 Arrhenius plot

The temperature-dependent data of the (bulk, grain boundary and total) conductivities of the IPA cold sintered NCO at different temperatures is shown in Table 6.14. The data were extrapolated to calculate the gradient of the Arrhenius plot. The standard least square method was used to calculate the gradients of the temperature-dependent data of the IPA cold-sintered NCO in Origin software, and the uncertainty associated with each gradient and activation energy was recorded.

Due to the improved conductivity of heat-treated IPA NCO ceramic, the activation energy was determined (E_a) according to Equation 3.35 (chapter 3), and the results are shown in Table 6.14. The Arrhenius plot of the total conductivity of IPA cold-sintered NCO (where $\sigma_t = 1/R_t$) is shown in Figure 6.3.27. The E_a is ~ 0.017 ± 0.005 eV, and the plot shows similar metallic-type conduction and non-Arrhenius-type behaviour for the non-ohmic contacts. In addition, the plots of $T^{-1/3}$ and $T^{-1/4}$ against the total conductivity are shown in Figures 6.3.28 and 6.3.29. The plots of the log of the ceramic (bulk) and electrode (grain boundary) conductivity against 1000/T show the contribution of each factor to the total conductivity, and it was observed that the Na^+ ion migration favours the electrode (grain boundary), Figure 6.3.30. The results obtained were comparable to the NCO sample aqueously cold-sintered only after heating the IPA cold-sintered NCO ceramic.

Table 6.14

Temperature-dependent conductivity of IPA + heat cold-sintered NCO. σ_s, σ_x and σ_t are the bulk, grain boundary and total conductivity extracted from the bulk (R_x), grain boundary (R_s) and total (R_t) resistance shown in Table 6.13 (above).

Temp (K)	1000/T (K)	$T^{-1/3}$	$T^{-1/4}$	σ_s	Log σ_s	σ_x	Log σ_x	σ_T	Log σ_T
140	7.14	0.19	0.29	0.005	-2.334	0.013	-1.880	0.0034	-2.465
160	6.25	0.18	0.28	0.006	-2.252	0.013	-1.898	0.0039	-2.411
180	5.56	0.18	0.27	0.007	-2.146	0.012	-1.923	0.0045	-2.349
200	5.00	0.17	0.27	0.009	-2.035	0.011	-1.943	0.0051	-2.292
220	4.55	0.17	0.26	0.011	-1.944	0.011	-1.954	0.0056	-2.25
240	4.17	0.16	0.25	0.007	-2.133	0.012	-1.907	0.0046	-2.336

260	3.85	0.16	0.25	0.002	-2.650	0.017	-1.771	0.0020	-2.704
273	3.66	0.15	0.25	0.001	-2.881	0.019	-1.729	0.0012	-2.91
293	3.41	0.15	0.24	0.001	-3.134	0.021	-1.684	0.0007	-3.149

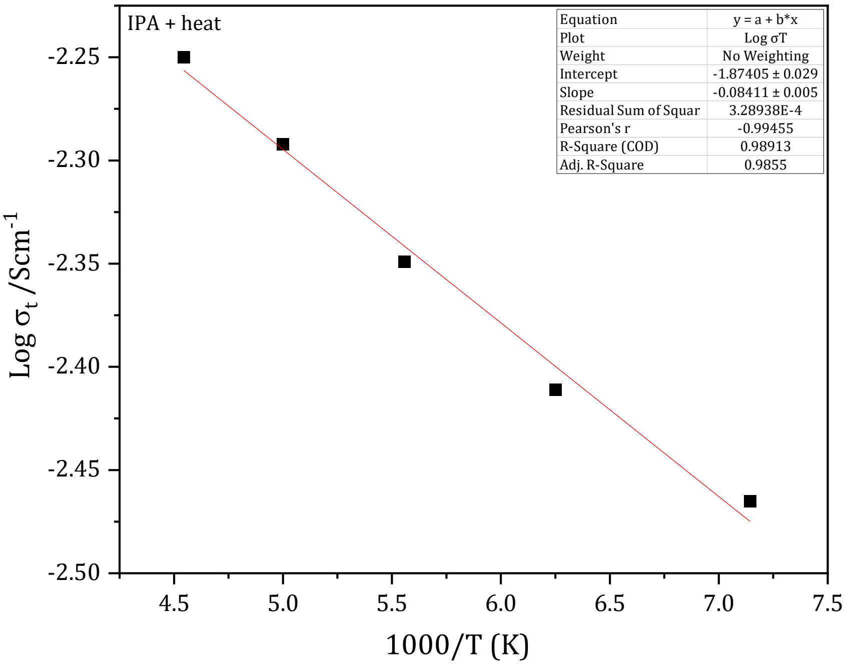

Figure 6.3.27. Arrhenius plot of the total conductivity of IPA + heat cold-sintered NCO.

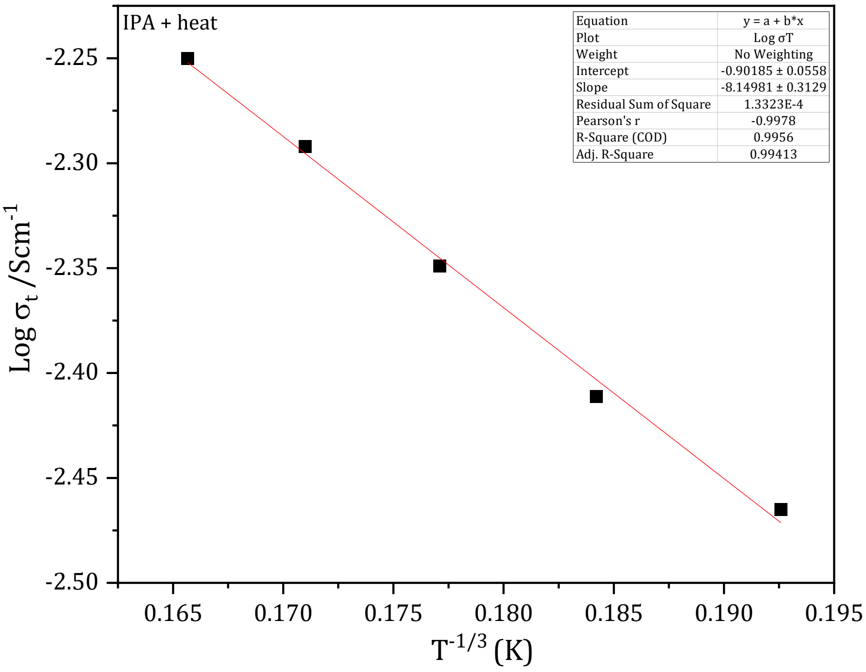

Figure 6.3.28. Arrhenius plot of the total conductivity of IPA cold-sintered NCO against $T^{-1/3}$.

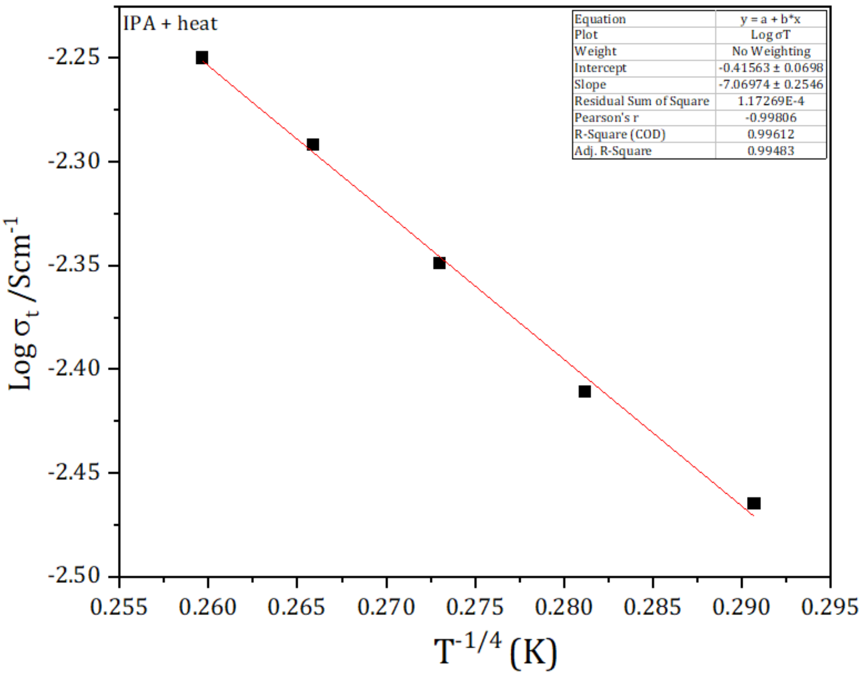

Equation	y = a + b*x
Plot	Log σT
Weight	No Weighting
Intercept	-0.41563 ± 0.0698
Slope	-7.06974 ± 0.2546
Residual Sum of Square	1.17269E-4
Pearson's r	-0.99806
R-Square (COD)	0.99612
Adj. R-Square	0.99483

Figure 6.3.29. Arrhenius plot of the total conductivity of IPA cold-sintered NCO against $T^{-1/4}$.

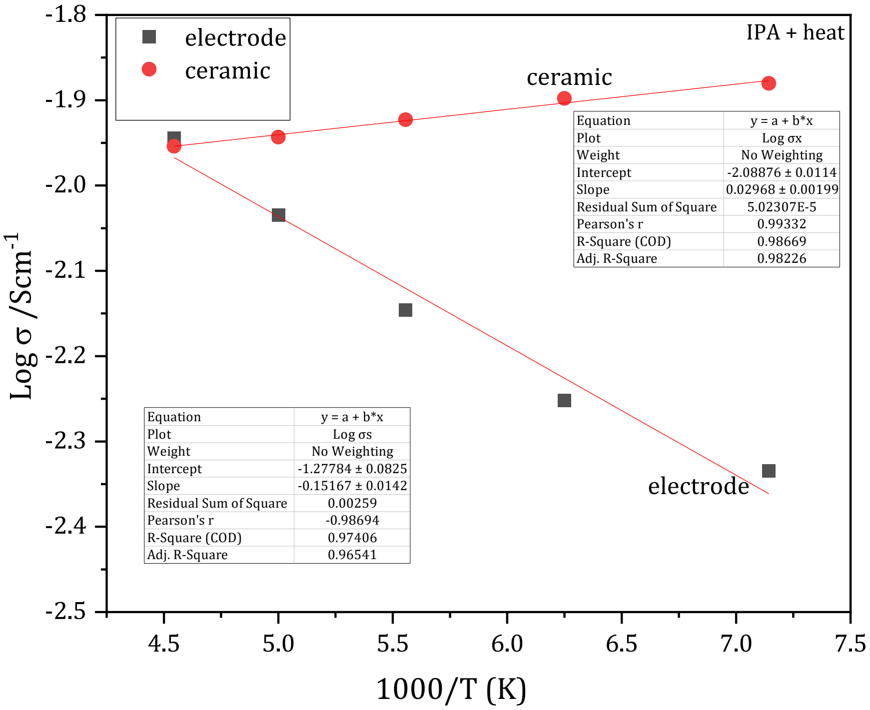

Equation	y = a + b*x
Plot	Log σx
Weight	No Weighting
Intercept	-2.08876 ± 0.0114
Slope	0.02968 ± 0.00199
Residual Sum of Square	5.02307E-5
Pearson's r	0.99332
R-Square (COD)	0.98669
Adj. R-Square	0.98226

Equation	y = a + b*x
Plot	Log σs
Weight	No Weighting
Intercept	-1.27784 ± 0.0825
Slope	-0.15167 ± 0.0142
Residual Sum of Square	0.00259
Pearson's r	-0.98694
R-Square (COD)	0.97406
Adj. R-Square	0.96541

Figure 6.3.30. Arrhenius plot of the bulk (electrode) and grain boundary (ceramic) conductivity of IPA cold-sintered NCO against 1000/T.

6.3.4 NCO cold-sintered using sodium acetate ($CH_3COONa.3H_2O$)

In this section, NCO powder was cold sintered using sodium acetate trihydrate salt ($CH_3COONa.3H_2O$) as the transient solvent. The sodium organic salt was chosen due to the water of crystallisation and the Na^+ ions present in the compound, and it was anticipated that the organic salt would release the crystallized water for the densification of the NCO ceramic. The phase, morphology and electrical properties of the densified NCO were investigated and compared with aqueously densified NCO ceramic.

6.3.4.1 X-ray diffraction

The X-ray diffraction pattern of the cold-sintered NCO using sodium acetate salt as the transient solvent is shown in Figure 6.3.31. The X-ray diffraction peaks were matched against the NCO green powder and PDF N°: 00-078-2822 of the P2-phase $Na_{0.71}CoO_2$ with space group $P6_3/mmc$ [1-5]. All the peaks in the sodium acetate cold-sintered NCO matched with the NCO green powder and the indexed P2-phase $Na_{0.71}CoO_2$. The impurity peaks of Co_3O_4 at 14.61 and 17.20, 2θ degrees observed in the NCO green powder were sharper in the sodium acetate cold-sintered NCO. There were no extra/impurity peaks except for those present in the NCO green powder. The peak at 68.84, 2θ degrees values in the sodium acetate cold-sintered NCO was sharper and higher compared to the NCO green powder. This suggests that the Na^+-ion from the sodium acetate salt may have contributed to the peak height.

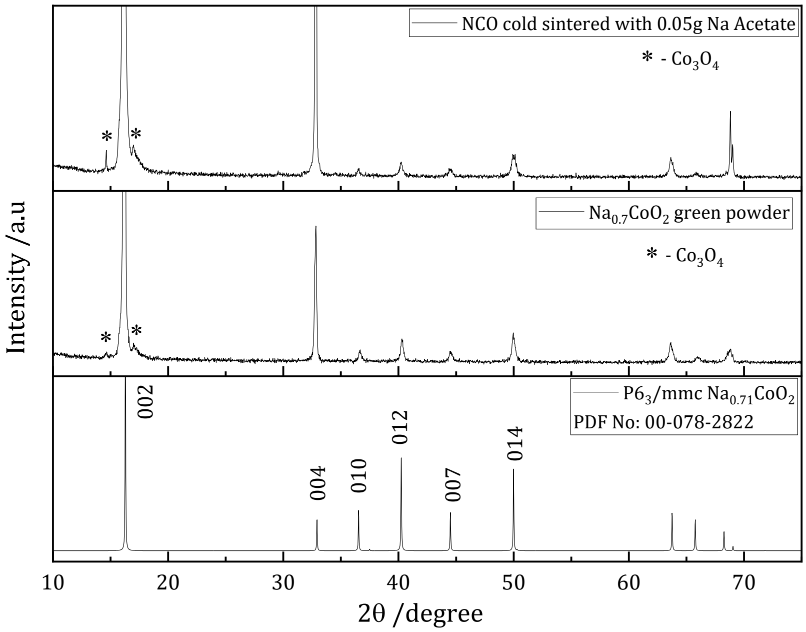

Figure 6.3.31. Room temperature X-ray diffraction patterns of NCO cold-sintered with sodium acetate salt, the green powder, and the indexed P2-phase $Na_{0.71}CoO_2$ with space group *$P6_3/mmc$*.

6.3.4.2 Relative density

The experimental density of the sodium acetate cold-sintered $Na_{0.7}CoO_2$ pellets was measured using the Archimedes method, and the results were compared with the $Na_{0.71}CoO_2$ theoretical density obtained from the ICDD database. The theoretical density of $Na_{0.7}CoO_2$ is 4.74 g/cm^3, and the relative density (ρ_r) of NCO was calculated according to equation 3.8 (chapter 3). Based on the densification results of aqueously (H_2O and 1M NaOH) cold-sintered samples, sodium acetate cold-sintered samples were pressed at 500 MPa, 200 °C, and 1 hour, and the relative density obtained at these densification parameters was ~ 88.24%, as shown in Table 6.15. The relative density of the organic salt cold-sintered NCO was lower compared to NCO samples aqueously and conventional sintered. However, the reason for this low ρ_r could be due to the organic salt with water of crystallisation.

Table 6.15

The density and relative density of sodium acetate cold-sintered NCO.

organic salts	Pressure (MPa)	Temp (°C)	Time (1hr)	Density	RD
0.05g sodium acetate	500	200	1	4.112	88.24

6.3.4.3 Scanning electron microscopy

SEM micrographs of the fractured surface of sodium acetate cold-sintered NCO ceramics are shown in Figure 6.3.32. The microstructure appears dense and interconnected. The grains appear smaller with no evidence of agglomeration.

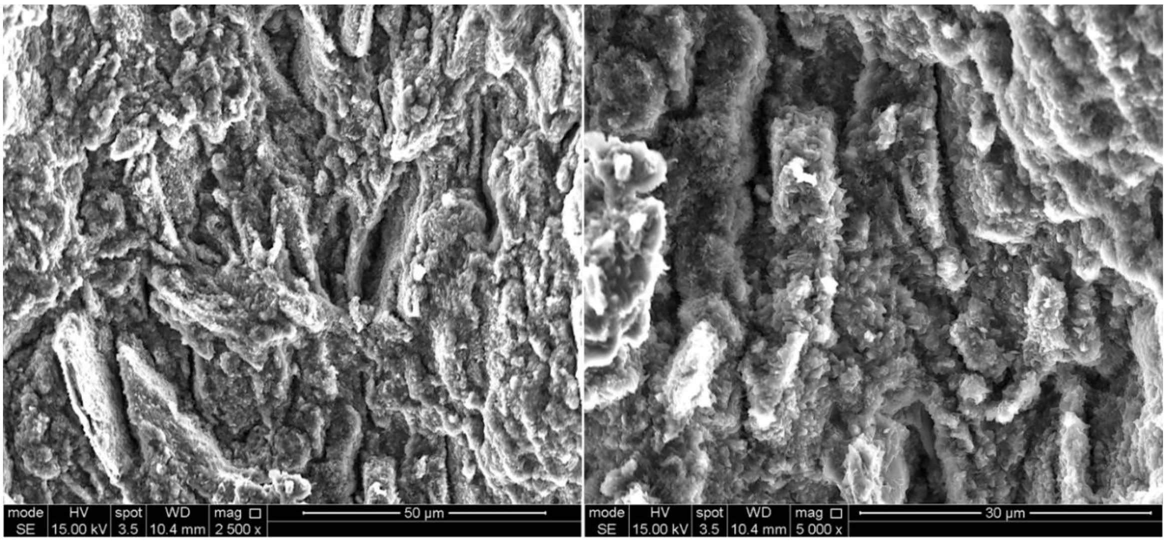

Figure 6.3.32 SEM micrographs of the fractured surface of NCO ceramic cold-sintered with sodium acetate salt as the transient solvent.

6.3.4.4 Impedance Spectroscopy

The complex impedance plane, Z* plots and the spectroscopic plots of the sodium acetate cold-sintered NCO ceramics using In-Ga alloys are shown in Figure 6.3.33. The associated data obtained from extrapolating the Zview software are shown in Table 6.16.

Table 6.16

Impedance spectroscopic data of sodium acetate cold-sintered NCO. Obt = obtained values, Calc = calculated values, R_s, R_x and R_T = bulk, grain boundary and total resistance, respectively. σ_T = total conductivity, C_T = total capacitance, f_{max} and ω_{max} are the maximum frequency and angular frequency.

NCO CS Na acetate	Obt	Obt	Obt	Calc	Obt	Calc	Obt
Temp (K)	R_x	R_s	R_t	σ_T	ω_{max}	F_{max}	C_T
140	567.51	95.86	663.37	0.0015	1.63E+06	2.59E+05	8.99E-10
160	678.81	69.28	748.09	0.0013	1.61E+06	2.55E+05	9.43E-10
180	757.56	47.04	804.56	0.0012	1.58E+06	2.52E+05	9.76E-10
200	861.22	23.44	884.66	0.0011	1.50E+06	2.38E+05	9.25E-10
220	972.94	13.59	986.52	0.0010	1.32E+06	2.10E+05	1.00E-09
240	888.03	11.58	899.61	0.0011	1.37E+06	2.18E+05	1.07E-09
260	756.75	36.28	793.03	0.0013	1.44E+06	2.30E+05	1.16E-09
273	729.48	33.89	763.37	0.0013	1.53E+06	2.43E+05	1.27E-09
293	828.29	34.08	862.37	0.0012	1.15E+06	1.83E+05	1.30E-09

At room and sub-ambient temperatures, there were only single well-resolved arcs with a high-frequency zero intercept on the Z' axis. The total (dc) room temperature resistivity was based on the high-frequency intercept of the arc in Z* plots and was ~ 860 Ωcm. The Z* data in Figure 6.3.33 were modelled on an equivalent circuit based on a single resistor connected in series with a parallel Resistor-Capacitor element. The single resistor, which is associated with the high frequency and zero intercept on the Z' axis, is attributed to the overall resistivity of the ceramic ($R_{ceramic}$), and the parallel RC element, which is associated with the arc in Z*, is attributed to the electrode effect ($R_{electrode}C_{electrode}$). The bulk ($R_s$) and grain boundary ($R_x$) resistance contributions to the overall impedance Z* response of the ceramics were calculated and shown in Table 6.16. Figure 6.3.33 (b-d) shows the spectroscopic data of the impedance, (b) the capacitance, C" (c) the imaginary component of the impedance, Z" and (d) the electric modulus, M" of the sodium acetate cold-sintered NCO.

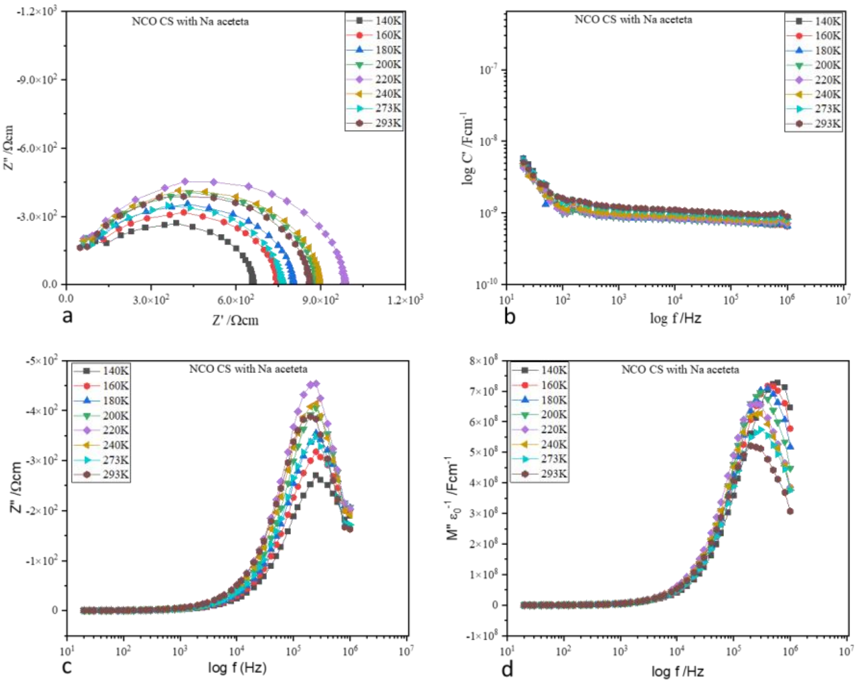

Figure 6.3.33. Z* and the spectroscopic plots of cold-sintered NCO (sodium acetate) at 140 – 313 K (a) Z'/Z'' (b) capacitance (c) Z'' (d) M''.

6.3.4.5 Arrhenius plot

The temperature-dependent data of the (bulk, grain boundary and total) conductivities of the sodium acetate cold sintered NCO at different temperatures is shown in Table 6.17. The standard least square method was used to calculate the gradients of the temperature-dependent data of the sodium acetate cold-sintered NCO in Origin software, and the uncertainty associated with each gradient and activation energy was recorded.

The Activation energy (E_a) was calculated according to Equation 3.35 (chapter 3), and the results are shown in Table 6.17. The Arrhenius plot of the total conductivity of sodium acetate cold-sintered NCO (where $\sigma_T = 1/R_T$) is shown in Figure 6.3.34. The E_a is ~ 0.026 ± 0.010 eV; the plot shows metallic-type conduction and non-Arrhenius-type behaviour for the non-ohmic contacts. In addition, the plots of $T^{-1/3}$ and $T^{-1/4}$ against the total conductivity are shown in Figures 6.3.35 and 6.3.36. The plots of the log of the ceramic (bulk) and electrode (grain boundary) conductivity against 1000/T show the contribution of each factor to the total conductivity is shown in Figure 6.3.37.

Table 6.17

Temperature-dependent conductivity of sodium acetate cold-sintered NCO. σ_s, σ_x and σ_t are the bulk, grain boundary and total conductivity extracted from the bulk (R_x), grain boundary (R_s) and total (R_t) resistance shown in Table 6.16 (above).

Temp (K)	1000/T (K)	$T^{-1/3}$	$T^{-1/4}$	σ_x	Log σ_x	σ_s	Log σ_s	σ_T	Log σ_T
140	7.14	0.193	0.291	0.0018	-2.75	0.010	-1.98	0.0015	-2.822
160	6.25	0.184	0.281	0.0015	-2.83	0.014	-1.84	0.0013	-2.874
180	5.56	0.177	0.273	0.0013	-2.88	0.021	-1.67	0.0012	-2.906
200	5.00	0.171	0.266	0.0012	-2.94	0.043	-1.37	0.0011	-2.947
220	4.55	0.166	0.260	0.0010	-2.99	0.074	-1.13	0.0010	-2.994
240	4.17	0.161	0.254	0.0011	-2.95	0.086	-1.06	0.0011	-2.954
260	3.85	0.157	0.249	0.0013	-2.88	0.028	-1.56	0.0013	-2.899
273	3.66	0.154	0.246	0.0014	-2.86	0.030	-1.53	0.0013	-2.883
293	3.41	0.151	0.242	0.0012	-2.92	0.029	-1.53	0.0012	-2.936

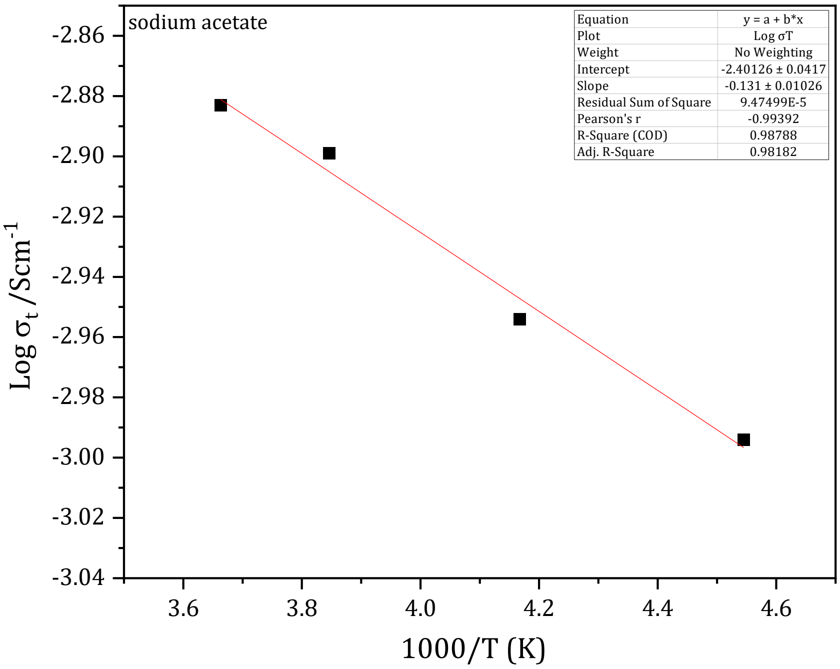

Figure 6.3.34. Arrhenius plot of the total conductivity of sodium acetate cold-sintered NCO.

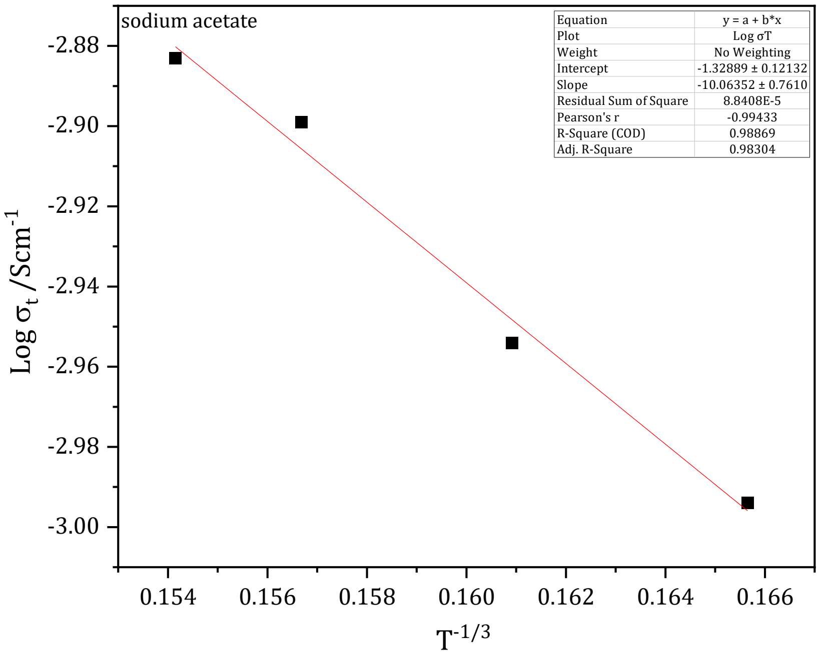

Equation	y = a + b*x
Plot	Log σT
Weight	No Weighting
Intercept	-1.32889 ± 0.12132
Slope	-10.06352 ± 0.7610
Residual Sum of Square	8.8408E-5
Pearson's r	-0.99433
R-Square (COD)	0.98869
Adj. R-Square	0.98304

Figure 6.3.35. Arrhenius plot of the total conductivity of sodium acetate cold-sintered NCO against T$^{-1/3}$.

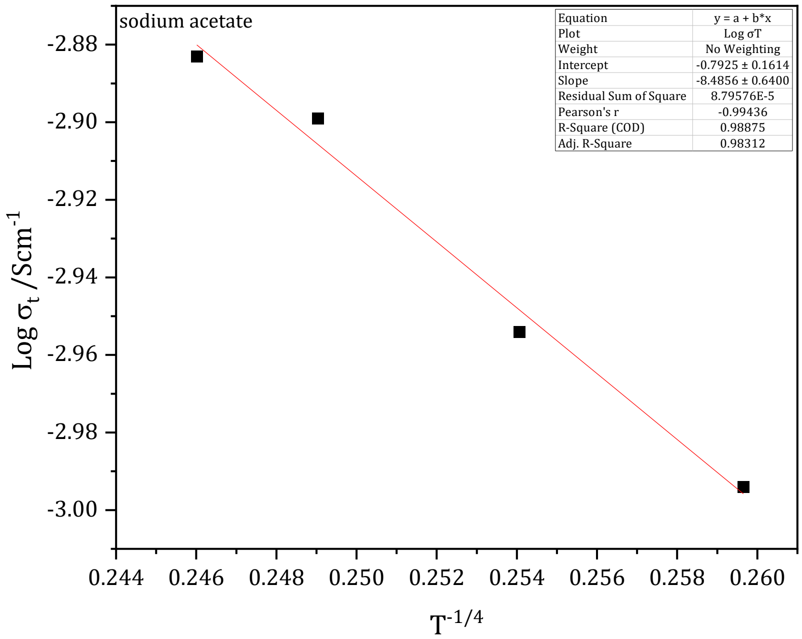

Equation	y = a + b*x
Plot	Log σT
Weight	No Weighting
Intercept	-0.7925 ± 0.1614
Slope	-8.4856 ± 0.6400
Residual Sum of Square	8.79576E-5
Pearson's r	-0.99436
R-Square (COD)	0.98875
Adj. R-Square	0.98312

Figure 6.3.36. Arrhenius plot of the total conductivity of sodium acetate cold-sintered NCO against T$^{-1/4}$.

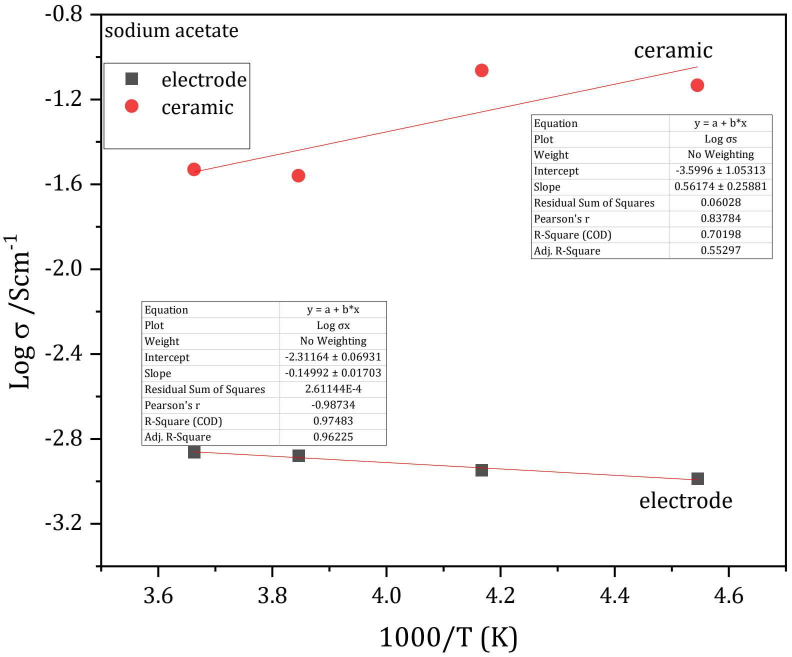

Equation	y = a + b*x
Plot	Log σs
Weight	No Weighting
Intercept	-3.5996 ± 1.05313
Slope	0.56174 ± 0.25881
Residual Sum of Squares	0.06028
Pearson's r	0.83784
R-Square (COD)	0.70198
Adj. R-Square	0.55297

Equation	y = a + b*x
Plot	Log σx
Weight	No Weighting
Intercept	-2.31164 ± 0.06931
Slope	-0.14992 ± 0.01703
Residual Sum of Squares	2.61144E-4
Pearson's r	-0.98734
R-Square (COD)	0.97483
Adj. R-Square	0.96225

Figure 6.3.37. Arrhenius plot of the bulk (electrode) and grain boundary (ceramic) conductivity of sodium acetate cold-sintered NCO against 1000/T.

6.3.5 NCO cold sintered using cobalt (II) acetate tetrahydrate salt.

In this section, NCO powder was cold sintered using cobalt (II) acetate tetrahydrate salt $(CH_3COO)_2Co.4H_2O$ as the transient solvent. The cobalt acetate organic salt was chosen due to the water of crystallisation and cobalt ion present in the compound, and we anticipated that the organic salt would release the crystallized water for the densification of the NCO ceramic. The phase, morphology and electrical properties of the densified NCO were investigated and compared with an aqueously densified NCO.

6.3.5.1 X-ray diffraction

The X-ray diffraction pattern of the cold-sintered NCO using cobalt (II) acetate salt as the transient solvent is shown in Figure 6.3.38. The X-ray diffraction peaks were matched against the NCO green powder and PDF N°: 00-078-2822 of the P2-phase $Na_{0.71}CoO_2$ with space group $P6_3/mmc$ [1-5]. All the peaks in the cobalt acetate cold-sintered NCO matched with the NCO green powder. The impurity peaks of Co_3O_4 at 14.61 and 17.20, 2θ degrees observed in the NCO green powder were absent in the cobalt (II) acetate cold-sintered NCO. However, there was a broad peak at 19.87, 2θ degrees, which corresponds to the CoO peak. The peaks in the cobalt acetate cold-sintered NCO were not sharp, and peaks at higher 2θ degrees values were not visible compared to NCO samples aqueously cold-sintered.

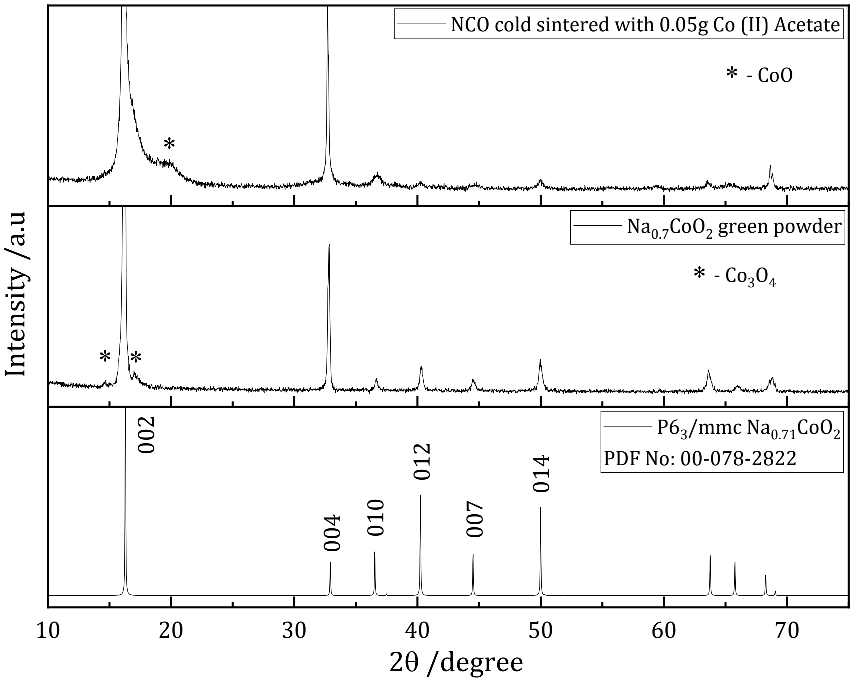

Figure 6.3.38. Room temperature X-ray diffraction patterns of NCO cold-sintered with cobalt (II) acetate salt, the green powder, and the indexed P2-phase $Na_{0.71}CoO_2$ with space group *$P6_3/mmc$*.

6.3.5.2 Relative density

The experimental density of the cobalt (II) acetate cold-sintered $Na_{0.7}CoO_2$ pellets was measured using the Archimedes method, and the results were compared with the $Na_{0.71}CoO_2$ theoretical density obtained from the ICDD database. The theoretical density of $Na_{0.71}CoO_2$ is 4.74 g/cm^3, and the relative density (ρ_r) of NCO was calculated according to equation 3.8 (chapter 3). Based on the densification results of aqueously (H_2O and 1M NaOH) cold-sintered samples, cobalt acetate cold-sintered samples were pressed at 500 MPa, 200 °C, and 1 hour, and the relative density obtained at these parameters is ~ 89.53%, as shown in Table 6.18. The relative density of the organic salt cold-sintered NCO was lower compared to samples aqueously cold-sintered but comparable to NCO samples cold-sintered using organic salt of sodium acetate.

Table 6.18

The density and relative density of cobalt (II) acetate cold-sintered NCO.

organic salts	Pressure (MPa)	Temp (°C)	Time (1hr)	Density	RD
0.05g Co (II) acetate	500	200	1	4.172	89.53

6.3.5.3 Scanning Electron Microscopy

SEM micrographs of the fractured surface of cobalt (II) acetate cold-sintered NCO ceramics are shown in Figure 6.3.39. The grains are loosely packed with agglomerated grains. The lighter grains in the micrograph are possibly Co^{3+} ions grains, and overall, there is triple point sintering of NCO ceramic.

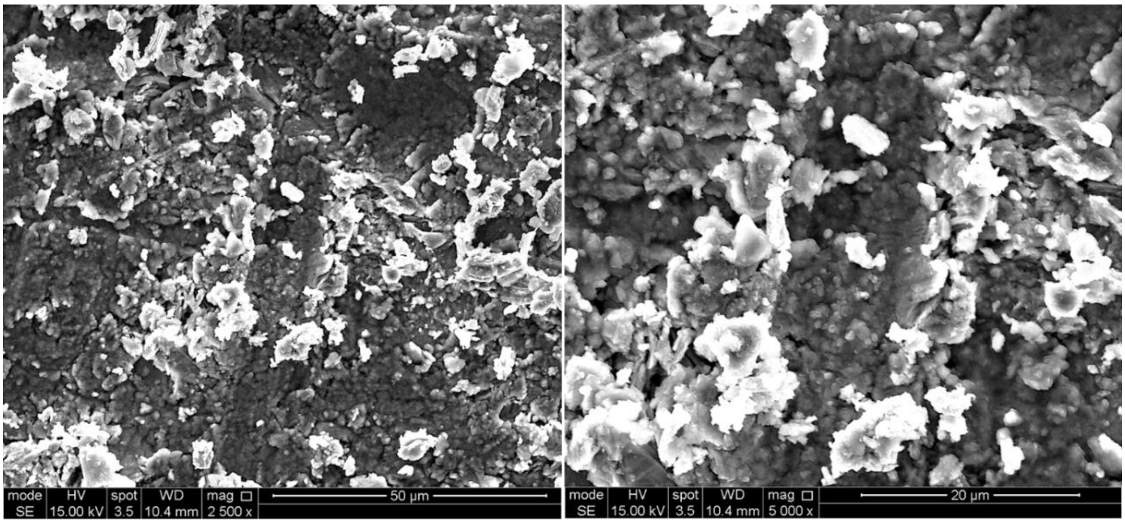

Figure 6.3.39. SEM images of the fractured surface of NCO cold-sintered with cobalt (II) acetate salt as the transient solvent.

6.3.5.4 Impedance Spectroscopy

The complex impedance plane, Z* and the spectroscopic plots of the cobalt acetate cold-sintered NCO ceramics using In-Ga alloys are shown in Figure 6.3.40. The associated data obtained from extrapolating the Zview software are shown in Table 6.19.

Table 6.19

Impedance spectroscopic data of cobalt (II) acetate cold-sintered NCO. Obt = obtained values, Calc = calculated values, R_s, R_x and R_T = bulk, grain boundary and total resistance, respectively. σ_T = total conductivity, C_T = total capacitance, f_{max} and ω_{max} are the maximum frequency and angular frequency.

NCO CS Co (II) Acetate	Obt	Obt	Obt	Calc	Obt	Calc	Obt
Temp (K)	R_x	R_s	R_t	σ_T	ω_{max}	F_{max}	C_T
140	6.96E+07	-2.13E+05	6.94E+07	1.44E-08	188.5	3.00E+01	6.66E-12
160	4.29E+07	-39753	4.28E+07	2.33E-08	157.08	2.50E+01	7.18E-12
180	2.17E+07	-55716	2.16E+07	4.63E-08	130.59	2.08E+01	7.98E-12
200	1.18E+07	33090	1.18E+07	8.44E-08	211.36	3.36E+01	8.87E-12
220	6.17E+06	33181	6.20E+06	1.61E-07	347.61	5.53E+01	1.02E-11
240	3.24E+06	27789	3.27E+06	3.06E-07	536.5	8.54E+01	1.22E-11
260	1.89E+06	17863	1.91E+06	5.24E-07	724.43	1.15E+02	1.46E-11
273	1.18E+06	9427.1	1.19E+06	8.41E-07	693.64	1.10E+02	1.74E-11
313	5.29E+05	4804.2	5.34E+05	1.87E-06	1032.2	1.64E+02	1.19E-09

At room and sub-ambient temperature, Figure 6.3.40, the impedance data gave a distinct plot which was different from those observed with other cold-sintered NCO ceramics. The Z* plot produces bizarre impedance and spectroscopic plots. However, we extrapolated the data and recorded it as obtained. The total (dc) resistivity at 273 K was based on the intercept of the arc in Z* plots and was ~ 1.2×10^6 Ωcm. Figure 6.3.40 (b-d) shows the spectroscopic data of the impedance, (b) the capacitance, C" (c) the imaginary component of the impedance, Z" and (d) the electric modulus, M" of the cobalt acetate cold-sintered NCO.

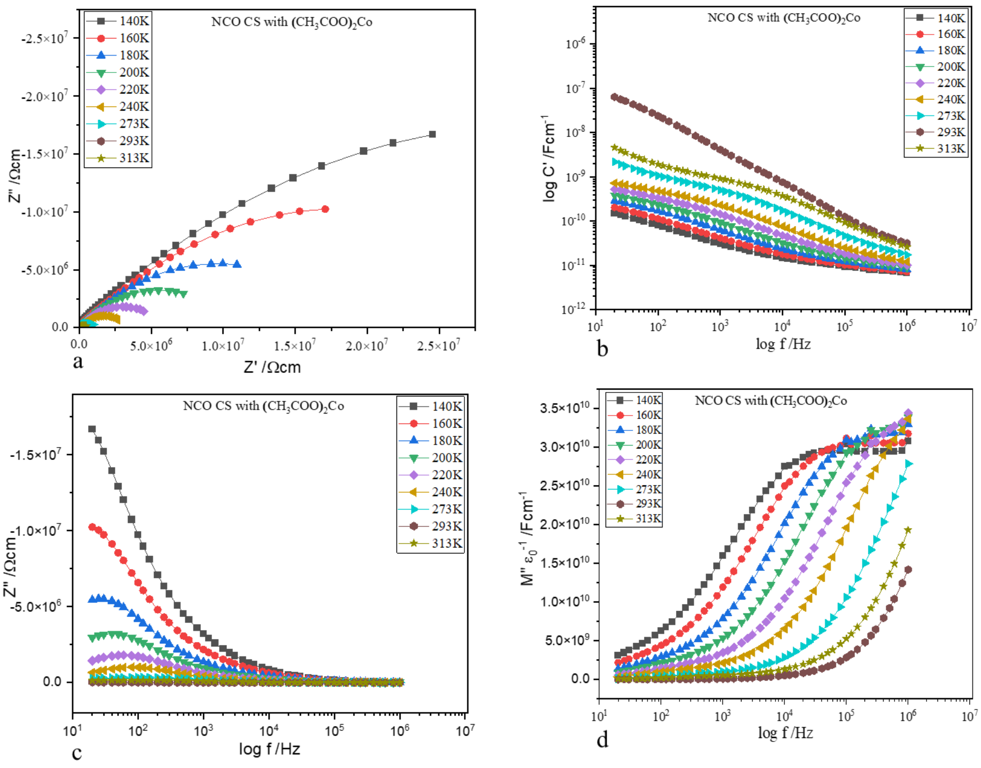

Figure 6.3.40. Z* and the spectroscopic plots of cobalt acetate cold-sintered NCO at 140 – 313 K (a) Z'/Z'' (b) capacitance (c) Z'' (d) M''.

6.3.5.5 Arrhenius plot

The temperature-dependent data of the (bulk, grain boundary and total) conductivities of the cobalt acetate cold sintered NCO at different temperatures is shown in Table 6.20. The standard least square method was used to calculate the gradients of the temperature-dependent data of the cobalt acetate cold-sintered NCO in Origin software, and the uncertainty associated with the gradient and activation energy was recorded.

The Activation energy (E_a) was calculated according to Equation 3.35 (chapter 3), and the results are shown in Table 6.20. The Arrhenius plot of the total conductivity of cobalt (II) acetate cold-sintered NCO (where $\sigma_t = 1/R_t$) is shown in Figure 6.3.41. The E_a is ~ 0.15 ± 0.026 eV. In addition, the plots of $T^{-1/3}$ and $T^{-1/4}$ against the total conductivity are shown in Figures 6.3.42 and 6.3.43. The plots of the log of the ceramic (bulk) and electrode (grain boundary) conductivity against 1000/T show a similar trend, which was different from those observed in other cold-sintered NCO ceramics.

Table 6.20

Temperature-dependent conductivity of Co (II) acetate cold-sintered NCO. σ_s, σ_x and σ_t are the bulk, grain boundary and total conductivity extracted from the bulk (R_x), grain boundary (R_s) and total (R_t) resistance shown in Table 6.19 (above).

Temp (K)	1000/T (K)	$T^{-1/3}$	$T^{-1/4}$	σ_x	Log σ_x	σ_s	Log σ_s	σ_T	Log σ_t
140	7.14	0.193	0.291	1.44E-08	-7.84E+00	-4.69E-06	-	1.44E-08	-7.84
160	6.25	0.184	0.281	2.33E-08	-7.63E+00	-2.52E-05	-	2.33E-08	-7.63
180	5.56	0.177	0.273	4.61E-08	-7.34E+00	-1.79E-05	-	4.63E-08	-7.33
200	5.00	0.171	0.266	8.47E-08	-7.07E+00	3.02E-05	-4.52E+00	8.44E-08	-7.07
220	4.55	0.166	0.260	1.62E-07	-6.79E+00	3.01E-05	-4.52E+00	1.61E-07	-6.79
240	4.17	0.161	0.254	3.09E-07	-6.51E+00	3.60E-05	-4.44E+00	3.06E-07	-6.51
260	3.85	0.157	0.249	5.29E-07	-6.28E+00	5.60E-05	-4.25E+00	5.24E-07	-6.28
273	3.66	0.154	0.246	8.47E-07	-6.07E+00	1.06E-04	-3.97E+00	8.41E-07	-6.08
313	3.20	0.147	0.238	1.89E-06	-5.72E+00	2.08E-04	-3.68E+00	1.87E-06	-5.73

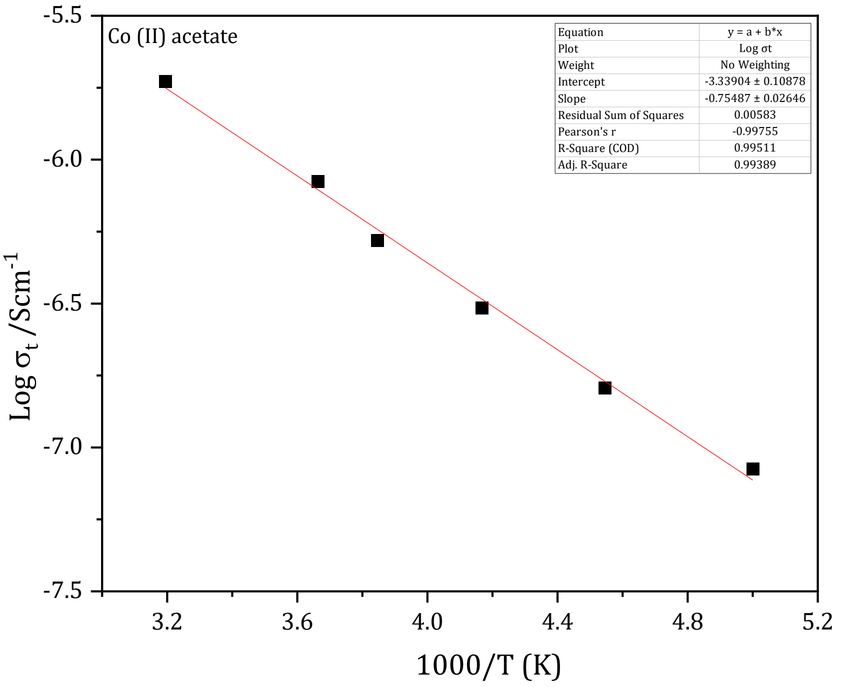

Figure 6.3.41. Arrhenius plot of the total conductivity of cobalt (II) acetate cold-sintered NCO.

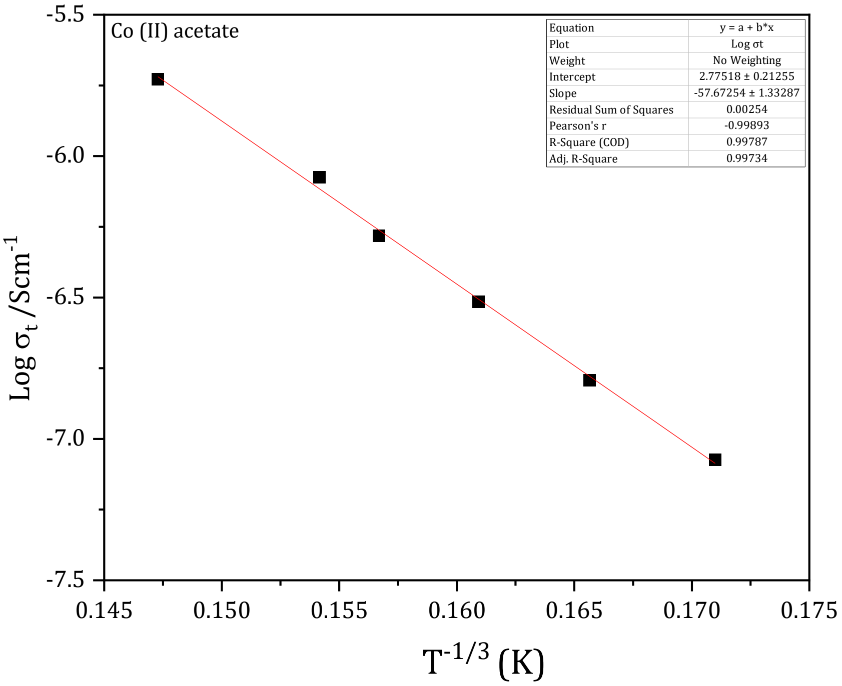

Figure 6.3.42. Arrhenius plot of the total conductivity of cobalt (II) acetate cold-sintered NCO against $T^{-1/3}$.

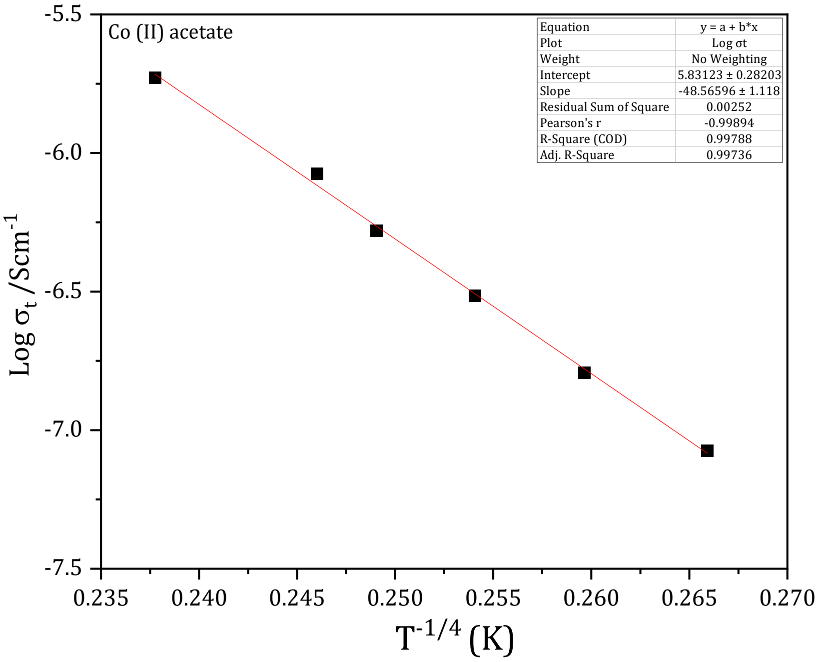

Figure 6.3.43. Arrhenius plot of the total conductivity of cobalt (II) acetate cold-sintered NCO against $T^{-1/4}$.

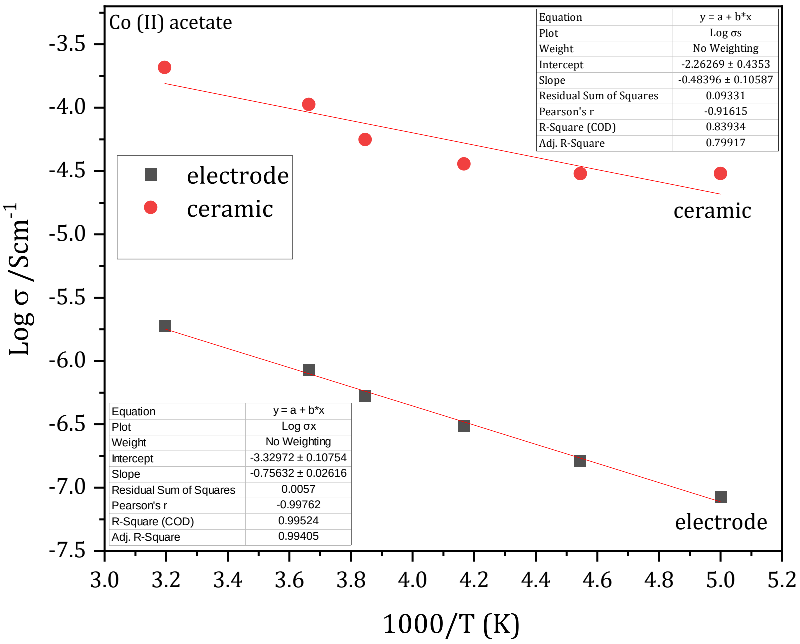

Equation	y = a + b*x
Plot	Log σs
Weight	No Weighting
Intercept	-2.26269 ± 0.4353
Slope	-0.48396 ± 0.10587
Residual Sum of Squares	0.09331
Pearson's r	-0.91615
R-Square (COD)	0.83934
Adj. R-Square	0.79917

Equation	y = a + b*x
Plot	Log σx
Weight	No Weighting
Intercept	-3.32972 ± 0.10754
Slope	-0.75632 ± 0.02616
Residual Sum of Squares	0.0057
Pearson's r	-0.99762
R-Square (COD)	0.99524
Adj. R-Square	0.99405

Figure 6.3.44. Arrhenius plot of the bulk (electrode) and grain boundary (ceramic) conductivity of cobalt (II) acetate cold-sintered NCO against 1000/T.

6.3.6 NCO cold sintered using citric acid.

In this section, NCO powder was cold sintered using citric acid monohydrate salt ($C_6H_8O_7Co.H_2O$) as the transient solvent. The organic salt was chosen due to its water of crystallisation, and we anticipated that the organic salt would release the crystallized water for the densification of the NCO ceramic. The phase, morphology and electrical properties of the densified NCO were investigated.

6.3.6.1 X-ray diffraction

The X-ray diffraction pattern of the cold-sintered NCO using citric acid monohydrate salt as the transient solvent is shown in Figure 6.3.45. The X-ray diffraction peaks were matched against the NCO green powder and PDF N°: 00-078-2822 of the P2-phase $Na_{0.71}CoO_2$ with space group $P6_3/mmc$ [1-5]. There were several impurity peaks at 12.68, 22.00, 25.41, 27.46, 30.69 and 38.00, 2θ degrees matching citric acid. This suggests citric acid is not a good salt for the densification of NCO.

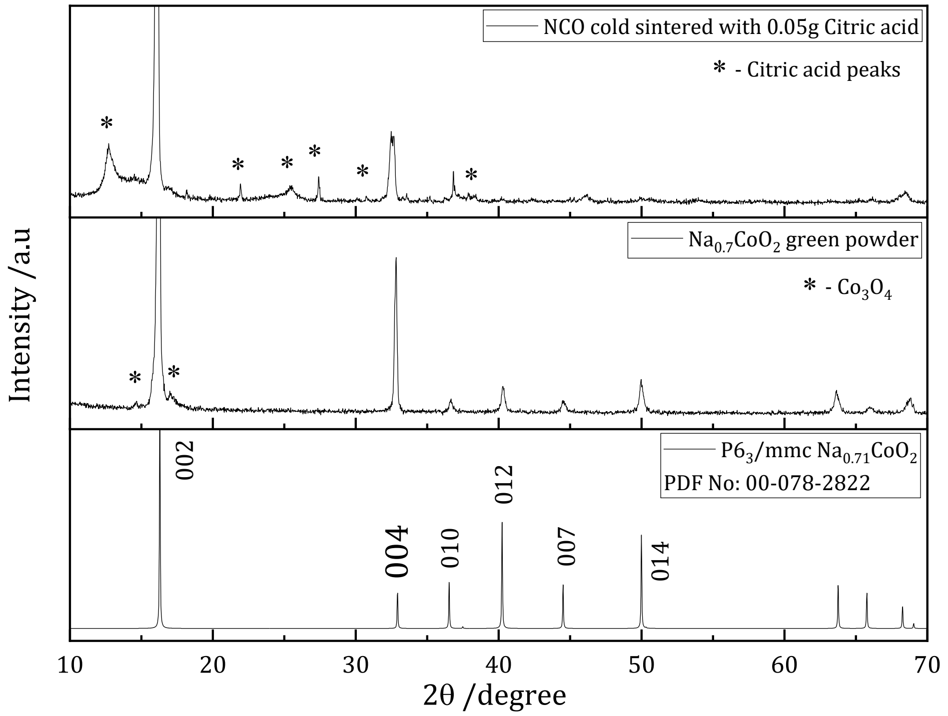

Figure 6.3.45. Room temperature X-ray diffraction patterns of NCO cold-sintered with citric acid salt, the green powder, and the indexed P2-phase $Na_{0.71}CoO_2$ with space group *$P6_3/mmc$*.

6.3.6.2 Relative density

The experimental density of the citric acid cold-sintered $Na_{0.7}CoO_2$ pellets was measured using the Archimedes method, and the results were compared with the $Na_{0.71}CoO_2$ theoretical density obtained from the ICDD database. The theoretical density of $Na_{0.71}CoO_2$ is 4.74 g/cm^3, and the relative density (ρ_r) of NCO was calculated according to equation 3.8 (chapter 3). Based on the densification results of aqueously (H_2O and 1M NaOH) cold-sintered samples, citric acid cold-sintered samples were pressed at 500 MPa, 200 °C, and 1 hour, and the relative density obtained at these densification parameters was ~ 76.42%, as shown in Table 6.21 The relative density of the citric acid cold-sintered NCO was lower compared to other cold-sintered samples.

Table 6.21

The density and relative density of cobalt (II) acetate cold-sintered NCO.

Organic salts	Pressure (MPa)	Temp (°C)	Time (1hr)	Density	ρ_r
0.05g Citric acid	500	200	1	3.561	76.42

6.3.6.3 Scanning Electron Microscopy

SEM micrographs of the lightly polished surface of citric acid cold-sintered NCO ceramics are shown in Figure 6.3.46. The grains are agglomerated with a ribbon-like shape. Suggesting the citric acid may have impacted the NCO grains or possibly it could be an artefact from the ceramic processing. Overall, the micrographs support a ceramic with ~ 75.00 relative density.

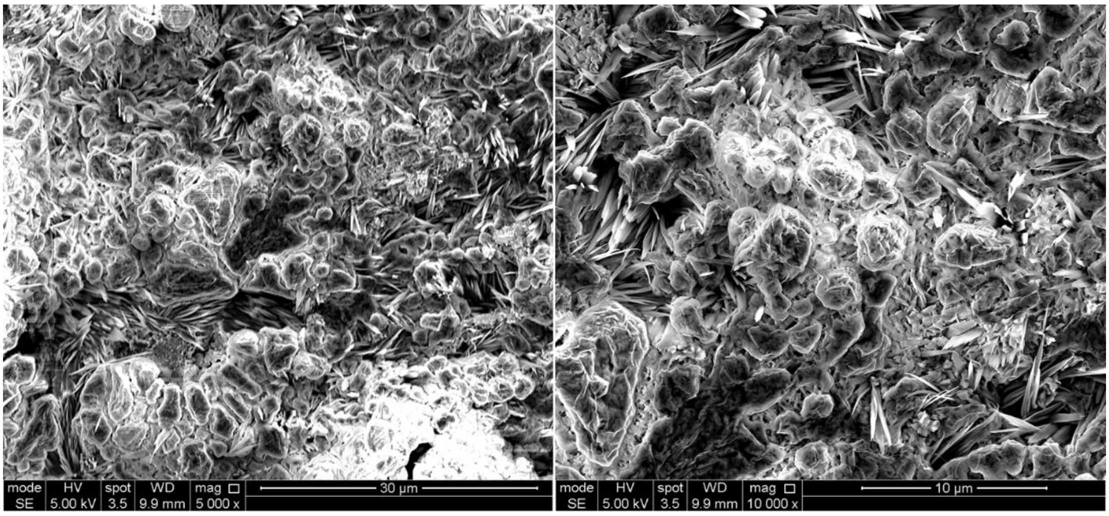

Figure 6.3.46. SEM images of the lightly polished surface of NCO cold-sintered with citric acid salt as the transient solvent.

6.3.6.4 Impedance Spectroscopy

The complex impedance plane, Z* plots and the spectroscopic plots of the citric acid cold-sintered NCO ceramics using In-Ga alloys gave a bizarre reading and could not be interpreted.

6.4 Further comparative studies of cold vs conventional sintered NCO

This section compares the magnetic properties and further examines the microstructure of cold (H_2O) and conventionally sintered NCO

6.4.1 SQUID Magnetometry

The NCO sample was cooled to 2 K under zero field, and the real and imaginary susceptibilities were measured as a function of temperature, between 2 K and 300 K, at zero applied field (due to the remanence on the superconducting magnet, the actual field was ~ –0.4 Oe) for both increasing and decreasing temperature. A field of 100 Oe was then applied, and the measurement was repeated between 2 K and 35 K to study the low-temperature behaviour.

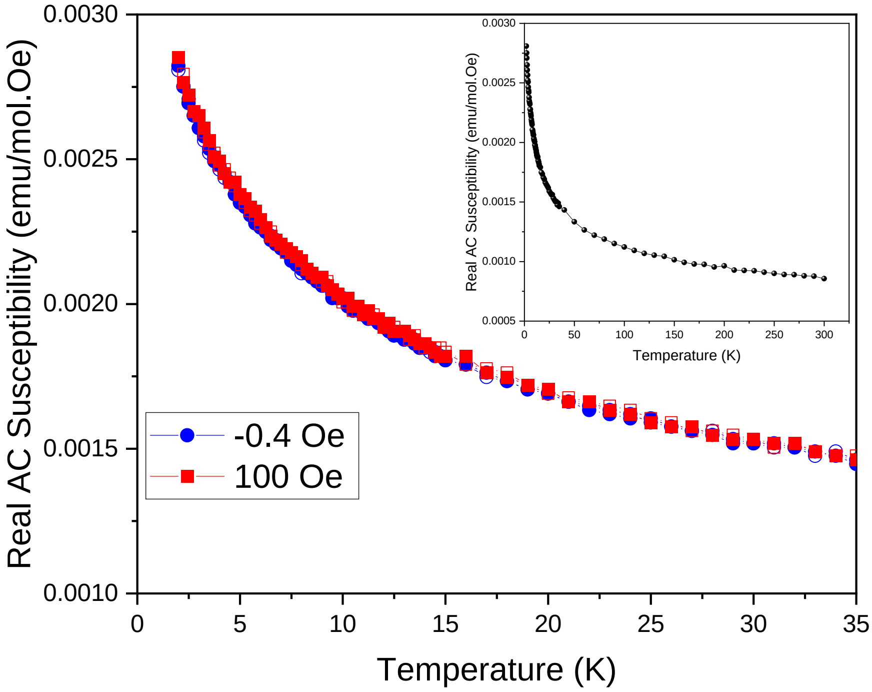

Figure 6.4.1 and insert. Real susceptibility as a function of temperature and applied magnetic field for an AC frequency of 757 Hz. The solid shapes are for increasing temperature, and the open shapes are for decreasing temperature.

Figure 6.4.1 shows the real susceptibility behaviour of the NCO sample as a function of temperature and applied magnetic field. The real susceptibility increases as the temperature decreases, and there were no peaks or plateau regions within the data, even below 20 K, suggesting that the NCO sample {both conventional (red) and cold sintered (blue)} is paramagnetic. Furthermore, there was no difference between the heating and cooling data sets or between the data for different applied magnetic fields, as shown in

Table 6.22. The zero-field measurement was repeated for the conventional NCO sample, and the results are shown in Figure 6.4.2 and Table 6.23.

Table 6.22

The heating and cooling data sets of the cold-sintered NCO at zero-field measurement.

Temp (K)	Real AC Susceptibility (emu/mol.Oe)	Temp (K)	Real AC Susceptibility (emu/mol.Oe)
35.00	0.0015	2.00	0.0029
34.00	0.0015	2.25	0.0028
33.00	0.0015	2.50	0.0027
32.00	0.0015	2.75	0.0027
31.00	0.0015	3.00	0.0027
30.00	0.0015	3.25	0.0026
29.00	0.0016	3.50	0.0026
28.00	0.0016	3.75	0.0025
27.00	0.0016	4.00	0.0025
26.00	0.0016	4.25	0.0025
25.00	0.0016	4.50	0.0024
24.00	0.0016	4.75	0.0024
23.00	0.0017	5.00	0.0024
22.00	0.0017	5.25	0.0024
21.00	0.0017	5.50	0.0023
20.00	0.0017	5.75	0.0023
19.00	0.0017	6.00	0.0023
18.00	0.0018	6.25	0.0023
17.00	0.0018	6.50	0.0022
16.00	0.0018	6.75	0.0022
15.00	0.0018	7.00	0.0022
14.75	0.0019	7.25	0.0022
14.50	0.0019	7.50	0.0022
14.25	0.0019	7.75	0.0022
14.00	0.0019	8.00	0.0022
13.75	0.0019	8.25	0.0021

13.50	0.0019	8.50	0.0021
13.25	0.0019	8.75	0.0021
13.00	0.0019	9.00	0.0021
12.75	0.0019	9.25	0.0021
12.50	0.0019	9.50	0.0021
12.25	0.0019	9.75	0.0020
12.00	0.0019	10.00	0.0020
11.75	0.0020	10.25	0.0020
11.50	0.0020	10.50	0.0020
11.25	0.0020	10.75	0.0020
11.00	0.0020	11.00	0.0020
10.75	0.0020	11.25	0.0020
10.50	0.0020	11.50	0.0020
10.25	0.0020	11.75	0.0020
10.00	0.0020	12.00	0.0019
9.75	0.0020	12.25	0.0019
9.50	0.0021	12.50	0.0019
9.24	0.0021	12.75	0.0019
9.00	0.0021	13.00	0.0019
8.75	0.0021	13.25	0.0019
8.50	0.0021	13.50	0.0019
8.25	0.0021	13.75	0.0019
8.00	0.0021	14.00	0.0019
7.75	0.0022	14.25	0.0019
7.50	0.0022	14.50	0.0018
7.25	0.0022	14.75	0.0018
7.00	0.0022	15.00	0.0018
6.75	0.0022	16.00	0.0018
6.50	0.0023	17.01	0.0018
6.25	0.0023	18.00	0.0018
6.00	0.0023	19.00	0.0017
5.75	0.0023	20.00	0.0017
5.50	0.0023	21.00	0.0017
5.25	0.0024	22.00	0.0017

5.00	0.0024	23.00	0.0016
4.75	0.0024	24.00	0.0016
4.50	0.0024	25.00	0.0016
4.25	0.0025	26.00	0.0016
4.00	0.0025	27.00	0.0016
3.75	0.0025	28.00	0.0016
3.50	0.0026	29.00	0.0015
3.25	0.0026	30.00	0.0015
3.00	0.0027	31.00	0.0015
2.75	0.0027	32.00	0.0015
2.50	0.0027	33.00	0.0015
2.25	0.0028	34.00	0.0015
2.00	0.0029	35.00	0.0015

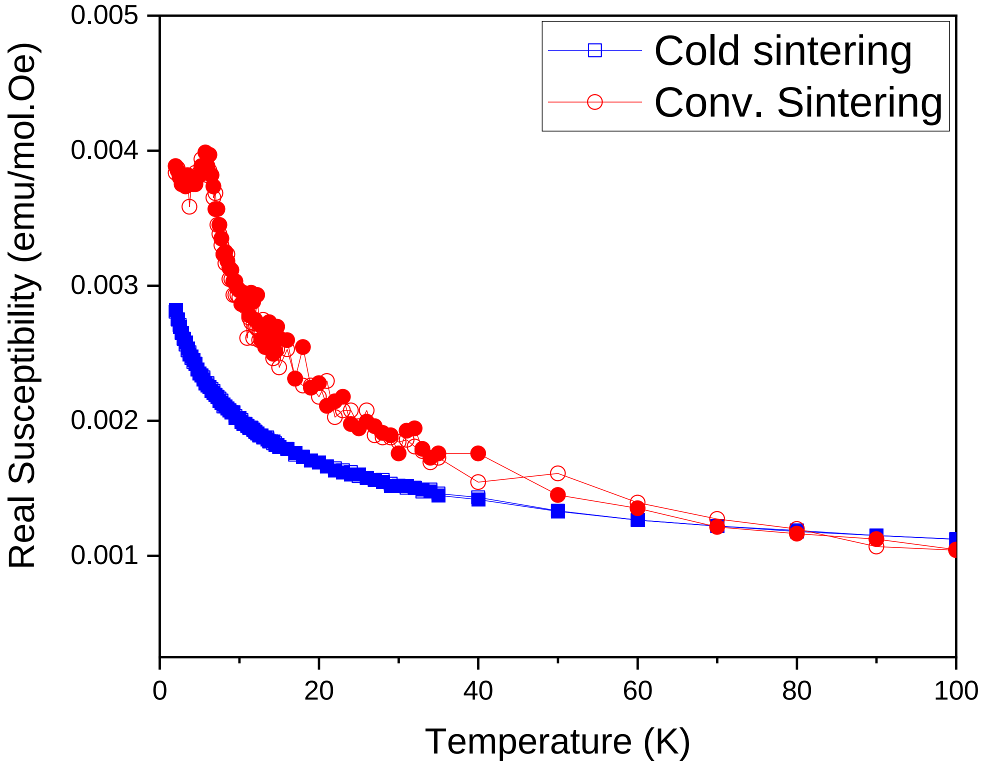

Figure 6.4.2. Real susceptibility as a function of temperature at zero applied fields for an AC frequency of 757 Hz for conventional and cold sintered NCO. The solid shapes are for increasing temperature, and the open shapes are for decreasing temperature.

Table 6.23

The heating and cooling data of the conventional sintered NCO at zero-field measurement.

Temp (K)	Real AC Susceptibility (emu/mol.Oe)	Temp (K)	Real AC Susceptibility (emu/mol.Oe)
2.00	0.0038	300.00	6.4E-04
2.25	0.0039	290.02	6.1E-04
2.50	0.0038	280.01	6.6E-04
2.75	0.0038	270.01	6.4E-04
3.00	0.0038	260.01	6.3E-04
3.25	0.0038	250.01	5.7E-04
3.50	0.0038	240.01	6.7E-04
3.75	0.0036	230.01	7.3E-04
4.00	0.0038	220.01	8.0E-04
4.25	0.0038	210.01	7.1E-04
4.50	0.0038	200.01	7.3E-04
4.75	0.0038	190.00	8.7E-04
5.00	0.0038	180.00	7.8E-04
5.25	0.0039	170.00	8.0E-04
5.50	0.0039	160.00	7.9E-04
5.75	0.0038	150.00	8.7E-04
6.00	0.0038	140.00	9.4E-04
6.25	0.0039	130.00	9.2E-04
6.50	0.0038	120.00	9.6E-04
6.75	0.0037	110.00	9.4E-04
7.00	0.0037	100.00	1.1E-03
7.25	0.0035	90.00	1.1E-03
7.50	0.0034	80.00	1.2E-03
7.75	0.0033	70.00	1.2E-03
8.00	0.0032	60.00	1.4E-03
8.25	0.0032	50.00	1.5E-03
8.50	0.0032	40.00	1.8E-03
8.75	0.0031	35.00	1.8E-03

9.00	0.0031	34.00	1.7E-03
9.25	0.0029	33.00	1.8E-03
9.50	0.0029	32.00	1.9E-03
9.75	0.0029	31.00	1.9E-03
10.00	0.0029	30.00	1.8E-03
10.25	0.0029	29.00	1.9E-03
10.50	0.0029	28.00	1.9E-03
10.75	0.0029	27.00	2.0E-03
11.00	0.0026	26.00	2.0E-03
11.25	0.0028	25.00	1.9E-03
11.50	0.0027	24.00	2.0E-03
11.75	0.0026	23.00	2.2E-03
12.00	0.0027	22.00	2.1E-03
12.25	0.0027	21.00	2.1E-03
12.50	0.0026	20.00	2.3E-03
12.75	0.0027	19.00	2.2E-03
13.00	0.0028	18.00	2.6E-03
13.25	0.0026	17.00	2.3E-03
13.50	0.0026	16.00	2.6E-03
13.75	0.0026	15.00	2.6E-03
14.00	0.0026	14.75	2.7E-03
14.25	0.0025	14.50	2.5E-03
14.50	0.0025	14.25	2.5E-03
14.75	0.0025	14.00	2.6E-03
15.00	0.0024	13.75	2.7E-03
16.00	0.0025	13.50	2.6E-03
17.00	0.0023	13.25	2.6E-03
18.00	0.0023	13.00	2.6E-03
19.00	0.0023	12.75	2.6E-03
20.00	0.0022	12.50	2.7E-03
21.00	0.0023	12.25	2.9E-03
22.00	0.0020	12.00	2.8E-03
23.00	0.0021	11.75	2.9E-03
24.00	0.0021	11.50	3.0E-03

25.00	0.0020	11.25	2.8E-03
26.00	0.0021	11.00	2.9E-03
27.00	0.0019	10.75	2.9E-03
28.00	0.0019	10.50	3.0E-03
29.00	0.0019	10.25	2.9E-03
30.00	0.0018	10.00	3.0E-03
31.00	0.0019	9.75	3.0E-03
32.00	0.0018	9.50	3.0E-03
33.00	0.0018	9.25	3.0E-03
34.00	0.0017	9.00	3.1E-03
35.00	0.0017	8.75	3.1E-03
40.00	0.0016	8.50	3.2E-03
50.00	0.0016	8.25	3.3E-03
60.00	0.0014	8.00	3.2E-03
70.00	0.0013	7.75	3.4E-03
80.00	0.0012	7.50	3.5E-03
90.00	0.0011	7.25	3.6E-03
100.00	0.0010	7.00	3.6E-03
110.00	0.0010	6.75	3.7E-03
120.00	0.0010	6.50	3.8E-03
130.00	0.0009	6.25	4.0E-03
140.00	0.0009	6.00	3.9E-03
150.00	0.0008	5.75	4.0E-03
160.00	0.0008	5.50	3.9E-03
170.00	0.0008	5.25	3.9E-03
180.00	0.0007	5.00	3.8E-03
190.00	0.0008	4.75	3.8E-03
200.00	0.0008	4.50	3.8E-03
210.00	0.0008	4.25	3.8E-03
220.00	0.0006	4.00	3.8E-03
230.00	0.0006	3.75	3.8E-03
240.00	0.0007	3.50	3.8E-03
250.00	0.0007	3.25	3.7E-03
260.00	0.0007	3.00	3.8E-03

270.00	0.0007	2.75	3.8E-03
280.00	0.0007	2.50	3.8E-03
290.00	0.0006	2.25	3.9E-03
300.00	0.0006	2.00	3.9E-03

From Figure 6.4.2, The two different fabrication methods for NCO gave two distinct behaviours as a function of temperature. For the cold-sintered sample, a classic paramagnetic behaviour was observed with no peaks or significant changes in susceptibility as a function of temperature. For the conventional NCO sample, there was a classic paramagnetic behaviour down to 6 K, and at this temperature, a peak was observed, relating to a change in the magnetic behaviour within the NCO sample to either anti-ferromagnetic or spin-glass. Spin glass behaviour is typically characterised by a frequency dispersion in the susceptibility [13-15]. Therefore, to confirm the spin glass state, the conventional sintered NCO powder was subjected to frequency dispersion, as shown in Figure 6.4.3, and the associated data sets are shown in Table 6.24. The peaks for 75.7 Hz and 757 Hz for the conventional sintered NCO sample had peak shifts with frequency, suggesting a transition from a paramagnetic to a spin glass state [8-15].

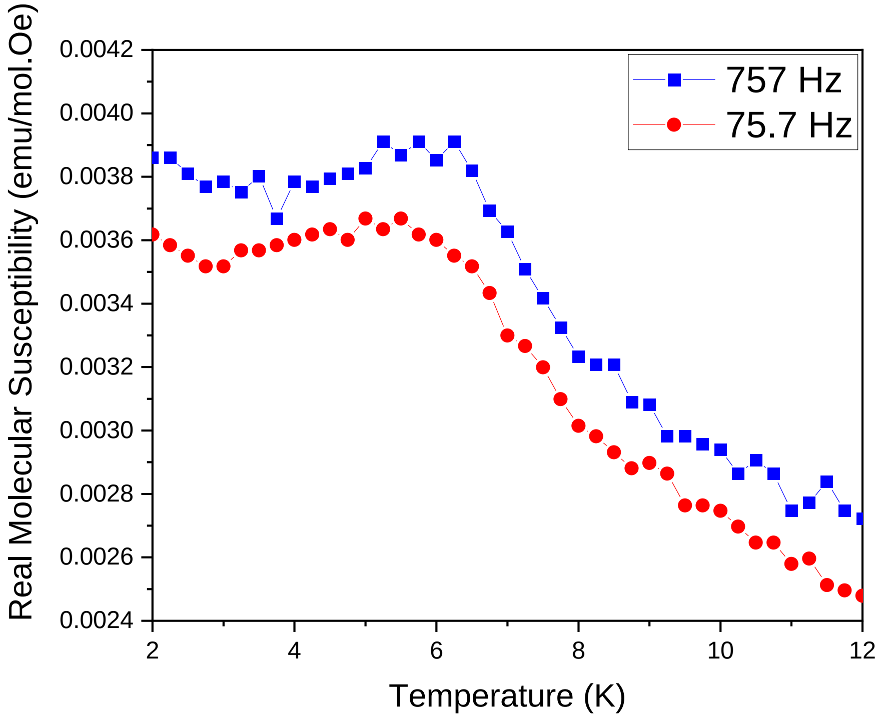

Figure 6.4.3. Real susceptibility as a function of temperature and AC frequency at zero applied fields for the conventional NCO.

Table 6.24

The data sets of the conventional sintered NCO at 75 and 757 Hz.

75 Hz		757 Hz	
Temp (K)	Real AC Susceptibility (emu/mol.Oe)	Temp (K)	Real AC Susceptibility (emu/mol.Oe)
2.00	0.0036	2.00	0.0039
2.25	0.0036	2.25	0.0039
2.50	0.0036	2.50	0.0038
2.75	0.0035	2.75	0.0038
3.00	0.0035	3.00	0.0038
3.25	0.0036	3.25	0.0038
3.50	0.0036	3.50	0.0038
3.75	0.0036	3.75	0.0037
4.00	0.0036	4.00	0.0038
4.25	0.0036	4.25	0.0038
4.50	0.0036	4.50	0.0038
4.75	0.0036	4.75	0.0038
5.00	0.0037	5.00	0.0038
5.25	0.0036	5.25	0.0039
5.50	0.0037	5.50	0.0039
5.75	0.0036	5.75	0.0039
6.00	0.0036	6.00	0.0039
6.25	0.0036	6.25	0.0039
6.50	0.0035	6.50	0.0038
6.75	0.0034	6.75	0.0037
7.00	0.0033	7.00	0.0036
7.25	0.0033	7.25	0.0035
7.50	0.0032	7.50	0.0034
7.75	0.0031	7.75	0.0033
8.00	0.0030	8.00	0.0032
8.25	0.0030	8.25	0.0032
8.50	0.0029	8.50	0.0032
8.75	0.0029	8.75	0.0031

9.00	0.0029	9.00	0.0031
9.25	0.0029	9.25	0.0030
9.50	0.0028	9.50	0.0030
9.75	0.0028	9.75	0.0030
10.00	0.0028	10.00	0.0029
10.25	0.0027	10.25	0.0029
10.50	0.0027	10.50	0.0029
10.75	0.0027	10.75	0.0029
11.00	0.0026	11.00	0.0028
11.25	0.0026	11.25	0.0028
11.50	0.0025	11.50	0.0028
11.75	0.0025	11.75	0.0028
12.00	0.0025	12.00	0.0027
12.25	0.0025	12.25	0.0028
12.50	0.0025	12.50	0.0027
12.75	0.0024		
13.00	0.0024		
13.25	0.0024		
13.50	0.0023		
13.75	0.0023		
14.00	0.0023		
14.25	0.0023		
14.50	0.0023		
14.75	0.0023		
15.00	0.0023		
16.00	0.0023		
17.00	0.0021		
18.00	0.0021		
19.00	0.0020		
20.00	0.0020		
21.00	0.0019		
22.00	0.0019		
23.00	0.0018		
24.00	0.0019		

25.00	0.0018		
26.00	0.0018		
27.00	0.0018		
28.00	0.0017		
29.00	0.0018		
30.00	0.0017		
31.00	0.0017		
32.00	0.0016		
33.00	0.0017		
34.00	0.0016		
35.00	0.0016		
40.00	0.0015		
50.00	0.0013		
60.00	0.0012		
70.00	0.0012		
80.00	0.0011		
90.00	0.0010		
100.00	0.0009		
110.00	0.0009		
120.00	0.0008		
129.99	0.0009		
140.00	0.0008		
149.99	0.0008		
160.00	0.0007		
169.99	0.0008		
179.99	0.0007		
189.99	0.0007		
199.99	0.0007		
209.99	0.0007		
220.00	0.0006		
229.99	0.0006		
240.00	0.0006		
249.99	0.0006		
259.99	0.0006		

269.99	0.0006		
280.00	0.0006		
289.99	0.0006		
300.00	0.0006		

6.4.2 Transmission Electron Microscopy

All the NCO powder (green powder, conventional and aqueous cold sintered) fundamental reflections in electron diffraction patterns were indexed to the hexagonal P6_3/mmc structure, consistent with the X-ray diffraction. Figures 6.4.4 (a and b) are the modulations in the hexagonal plane exhibiting a periodicity of k ≈ 0.125 $[110]^*$ for Figure 6.4.4a and k = ½$[110]^*$ for Figure 6.4.4b, which are the most frequently observed in NCO powder (* represents a reciprocal-space vector). Figure 6.4.4c shows frequently observed grains with complex patterns of diffuse spots in NCO green powder [16]. The correlation length varied from grain to grain for similar types of ordering, and based on literature studies on NCO samples, there is no clear relationship between the types of Na ordering and controlled stoichiometry composition.

The conventional sintered NCO grains revealed an extra weaker reflection compared to the cold sintered NCO grains. NCO grains from both methods revealed sharp and diffuse grains which are attributed to a distinct Na atoms arrangement forming super-lattices. After densification of the NCO by both conventional and cold sintering, a large number of the superstructures were retained. Despite the high temperature of the conventional NCO (800 °C/12 hour), the sample contained grains featuring diffuse super-lattice spots with a distinct periodicity characterised by k = 1/6$[110]^*$, Figure 6.4.4d. This is similar to the super-lattice observed in the NCO green powder (Figure 6.4.4a) and cold-sintered NCO sample (Figures 6.4.4g). Other types of Na ordering observed in the NCO green powder were more prominent in the conventional NCO sample, and these superstructures have their ordering modulation vectors in the hexagonal {0001} plane directed at an angle [e.g., ≈ 23° in Figures 6.4.4c (NCO green powder) and 6.4.4f (NCO conventional sintered) and ≈ 13° in Figure. 6.4.4i (NCO aqueous cold-sintered)] to the axes of the fundamental lattice. These types of ordering patterns with rotated axes but distinct periodicity were reported in $Na_{0.7}CoO_2$ [17]. The superstructure from both methods (conventional and aqueous cold sintered) contributed three sets of super-lattice reflection in [0001] selected area of the NCO diffraction patterns and developed 60° twin domains in the superstructure.

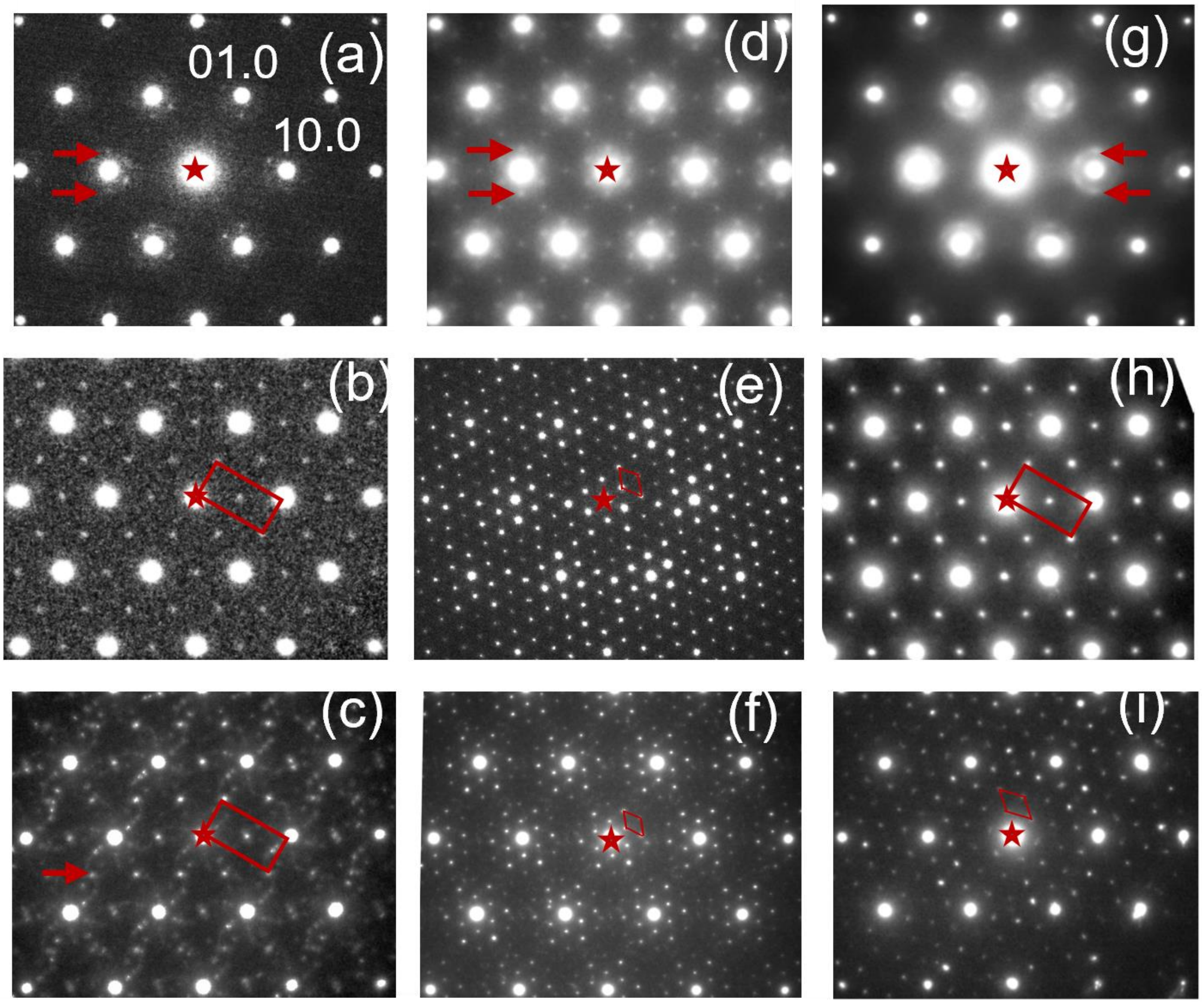

Figures 6.4.4 Tableau of [0001] selected area electron diffraction patterns illustrating different superstructures encountered in the NCO green powder (a-c), conventional sintered NCO (d-f), and cold-sintered NCO(g-i). The superstructure reflections and their repeat units are indicated using red arrows and parallelograms.

In addition, similar to the SEM micrographs, the cold and conventional sintered NCO microstructures reflect different densities. Figure 6.4.5a revealed the cold-sintered NCO sample lamellar morphology with cross-sectional dimensions of 200 nm. These lamellae display a major disorder, which is demonstrated as mesoscale and nanoscale striations in diffraction-contrast images. Figure 6.4.5b shows the conventional sintered lamellae with cross-sectional dimensions of 50 nm. The grain boundaries in the conventional and cold-sintered samples were devoid of secondary phases. However, the boundaries appeared sharper in the conventional ceramics (Figure 6.4.5b) compared to the cold sintered (Figure 6.4.5a.)

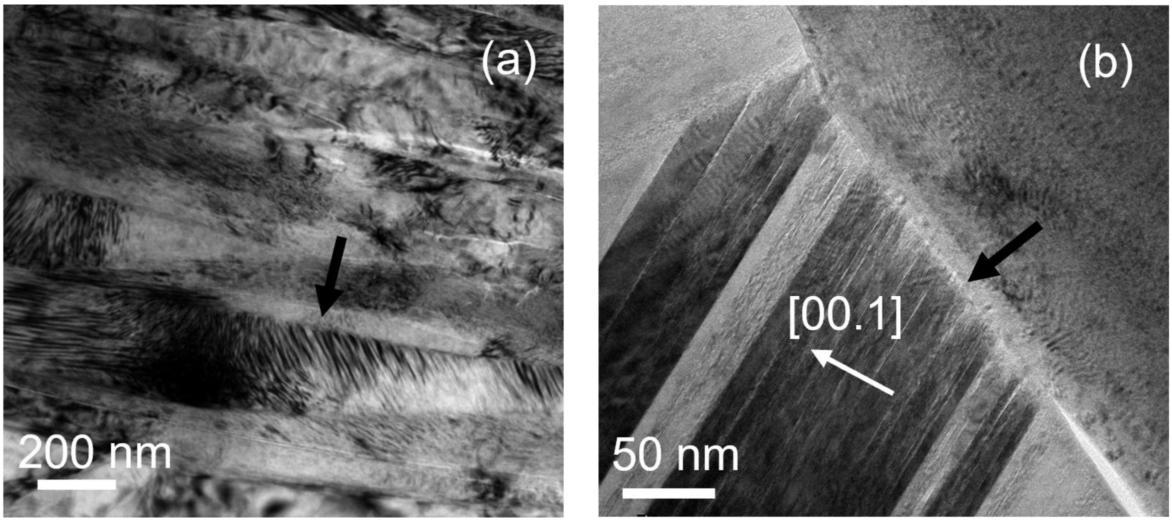

Figures 6.4.5 Bright-field TEM images of the (a) cold-sintered and (b) conventionally sintered NCO. Grain boundaries are indicated with black arrows, and the approximate direction of the hexagonal c-axis is illustrated by the white arrow in (b).

Figure 6.4.6 shows the Fourier filtering of high-resolution TEM (HRTEM) images of the cold-sintered superstructures, confirming that they exist as 60° domain variants. In addition, high-resolution phase-contrast imaging of individual lamellae of the substructure out-of-phase domains and adjacent regions having their *c*-axes misoriented by several degrees confirmed the 60° domain variants. Figure 6.4.7 shows the conventional sintered sample, which was prepared in cross-sectional geometry and contained plate-like but more equiaxed grains and displayed considerable stacking disorder along the *c*-axis and misoriented adjacent domains.

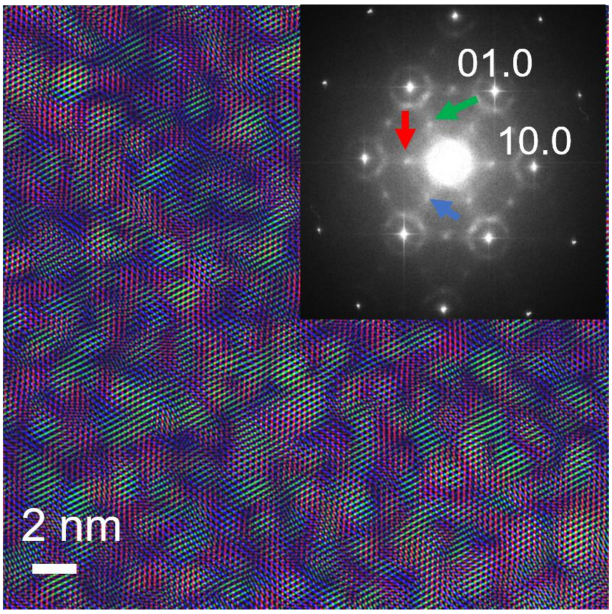

Figure 6.4.6 RGB rendering of a sum of three images obtained via the Fourier filtering of an HRTEM image of a region in the cold-sintered sample featuring the same diffuse super-lattice reflections as in Fig. 6.4.4g. Each of these images was generated using one of the three sets of super-lattice spots indicated using red, green, and blue arrows in the inset, which shows the Fast Fourier Transform of the original HRTEM image. The RGB image displays distinct regions of these colours, indicating that the superstructure forms three spatially distinct 60° domains.

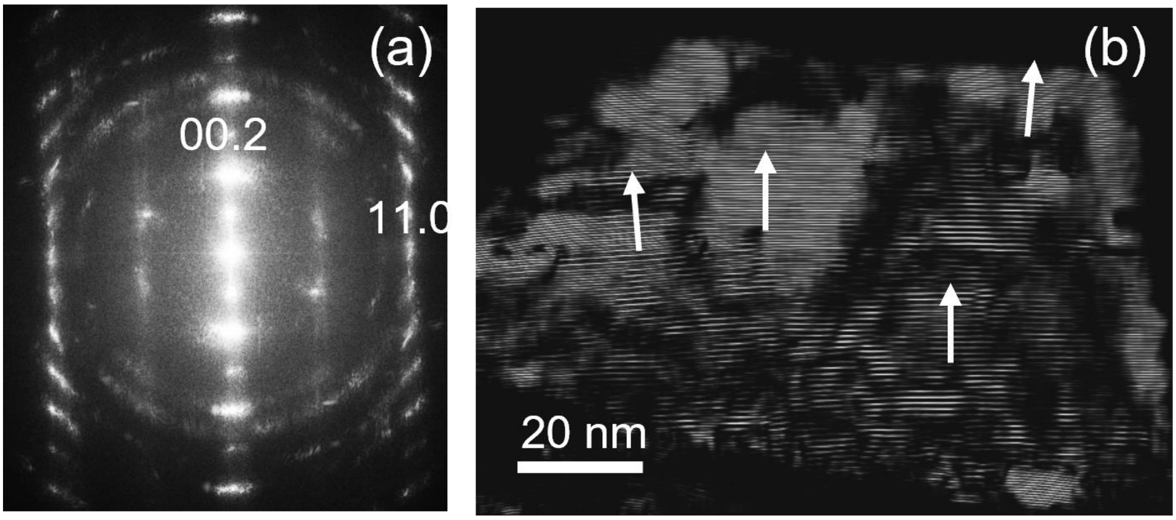

Figure 6.4.7 (a) Fast Fourier Transform of an HRTEM image of a lamellar grain in the conventional sample recorded in [11.0] orientation. A spread of *c*-axis orientations and stacking disorder in the imaged region is evident. (b) Phase-contrast image obtained as the inverse Fourier transform of (a) using 00.1 and 00.2 sets of reflections. The image reveals a high incidence of out-of-phase domains and regions, about 20 nm in size, with slightly different c-axis orientations, indicated using white arrows.

The oxidation state of Cobalt was probed using the L_3/L_2 Co white-line intensity ratio in core-loss EEL spectra, Figure 6.4.8a. Previous studies demonstrated that the ratio of the oxidation state of the Co increases as the ratio of L_3/L_2 decreases [18]. Figure 6.4.8b shows the comparative analysis of EELS and EDS signals recorded simultaneously from the NCO green powder. The analyses confirmed that all three NCO samples (green powder, conventional and cold sintered NCO) demonstrated similar composition and Co oxidation state.

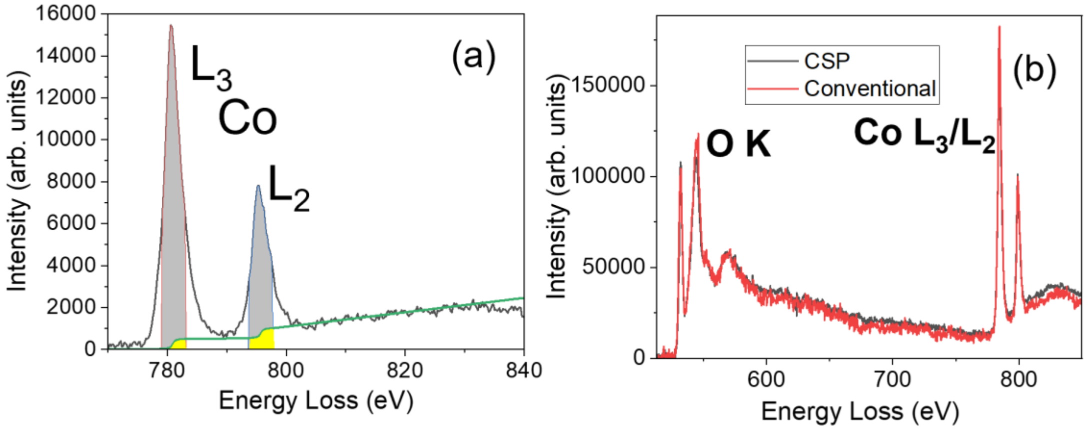

Figure 6.4.8 (a) Illustration of a procedure used to determine the L_3/L_2 white-line intensity ratio for Co. Black-line – experimental spectrum containing Co L_3 and L_2 lines from the cold-sintered NCO after subtracting the power-law background and removing plural scattering. Green line – a double-arctan function fitted to the spectrum with the 2:1 L_2:L_3 step ratio to model the continuum background. Grey-shaded areas under the peaks – integration windows. (b) Comparison of EEL spectra containing O K and Co L_3/L_2 edges between the conventional and cold-sintered NCO (similar thickness of about 100 nm).

6.5 Conclusion

The effect of densification (conventional and cold sintering) techniques and transient solvents on the morphology, phase, magnetic and electrical properties of NCO ceramic revealed different but distinct responses. The X-ray diffraction patterns of the NCO ceramic revealed the advantages of the aqueous cold sintering method over the conventional densification route. The aqueous (H_2O) cold-sintered NCO show a pure single-phase ceramic, and the conventional sintered NCO remains identical to the NCO green powder with impurity peaks of Co_3O_4 at 14.61 and 17.20, 2θ degrees. Cold sintering with organic transient solvents presents additional peaks corresponding to the organic solvent in the NCO ceramic. However, the NCO phase remains $P6_3/mmc$ irrespective of the transient solvents or densification methods. All the NCO cold-sintered SEM micrographs appear consistent with the measured relative density. Aqueous (H_2O and 1M NaOH solution) cold-sintered NCO exhibited the best densities and presented a facile and benign method of achieving almost complete sintering of NCO. Polishing of NCO pellets causes significant issues as artefacts are easily induced during this process. Also, prolonged exposure of the fractured NCO surface rapidly degrades the NCO ceramic at ambient and different transient solvents and salts produce different micrographic properties. Aqueous (H_2O and 1M NaOH solution) cold-sintered NCO samples produced identical results, while organic solvent and salts produced similar results among themselves, which was different from the aqueous cold-sintered NCO samples. The magnetic behaviour of NCO strongly depended on the densification route, with the aqueous (H_2O) cold-sintered sample showing classic paramagnetic behaviour on cooling. The conventionally sintered samples initially followed a paramagnetic response on cooling but deviated at 6 K to become a spin glass. The electron diffraction patterns in TEM reveal a range of different super-structures in both conventional and cold-sintered samples. Statistical analysis of the population of each super-structure type is problematic in electron diffraction as only a small sample size of patterns can be obtained. However, the conventionally sintered samples have a larger number of grains that exhibited the xxx superstructure. In addition, different transient solvents and densification methods produced different electrical responses on the NCO ceramics and the room temperature ionic conductivity ranges between $\sim 10^{-2}$ to 10^{-5} S/cm.

Overall, the results suggested that the aqueous cold-sintering method is beneficial in densifying materials that volatilise at higher temperatures and is potentially a benign, facile method that could be adopted in the fabrication of cathodes in Na-ion solid-state batteries.

6.6 References

[1] Y. Fang, X.-Y. Yu, X.W.D. Lou, A Practical High-Energy Cathode for Sodium-ion Batteries based on uniform P2-$Na_{0.7}CoO_2$ Microspheres, Angewandte Chemie International Edition. 56 (2017) 5801–5805. doi.org/10.1002/anie.201702024.

[2] L. Gao, S. Chen, L. Zhang, X. Yang, Self-supported $Na_{0.7}CoO_2$ nano-sheet arrays as cathodes for high-performance sodium-ion batteries, Journal of Power Sources. 396 (2018) 379–385. doi.org/10.1016/j.jpowsour.2018.06.047.

[3] L. Xue, X. Shi, B. Lin, Q. Guo, Y. Zhao, H. Xia, Self-standing P2/P3 hetero-structured $Na_{0.7}CoO_2$ nano-sheet arrays as 3D cathodes for flexible sodium-ion batteries, 457 (2020) 228059–228059. doi.org/10.1016/j.jpowsour.2020.228059.

[4] M. Medarde, M. Mena, J.L. Gavilano, E. Pomjakushina, J. Sugiyama, K. Kamazawa, V. Pomjakushin, D. Sheptyakov, B. Batlogg, H.R. Ott, M Mansson, F. Jurányi, 1D to 2D Na^+ ion Diffusion inherently linked to structural transitions in $Na_{0.7}CoO_2$, Physical Review Letters. 110 (2013). doi.org/10.1103/physrevlett.110.266401.

[5] C.A. Marianetti, G. Kotliar, Na-induced Correlations in Na_xCoO_2, Physical Review Letters. 98 (2007). doi.org/10.1103/physrevlett.98.176405.

[6] J.L. Gavilano, D. Rau, B. Pedrini, J. Hinderer, H.R. Ott, C.M. Казаков, J. Karpiński, Unconventional charge ordering in $Na_{0.7}CoO_2$ below 300 K, Physical Review B. 69 (2004). doi.org/10.1103/physrevb.69.100404.

[7] J. Y. Son, H. Lee, J.H. Cho, Stress dependence of growth mode change of epitaxial layered cobaltite γ-$Na_{0.7}CoO_2$, Applied Surface Science. 254 (2007) 436–440. doi.org/10.1016/j.apsusc.2007.05.074.

[8] K. Gramm, L. Lundgren, O. Beckman, SQUID Magnetometer for Mangetisation Measurements, Physica Scripta. 13 (1976) 93–95. doi.org/10.1088/0031-8949/13/2/004.

[9] J. Wooldridge, D.M. Paul, G. Balakrishnan, M.R. Lees, Investigation of the spin density wave in Na_xCoO_2, Journal of Physics: Condensed Matter. 17 (2005) 707–718. https://doi.org/10.1088/0953-8984/17/4/013.

[10] D. Prabhakaran, A.T. Boothroyd, R. Coldea, L.M. Helme, D. Alan Tennant, Magnetic Studies of Polycrystalline and Single-Crystal Na_xCoO_2, ArXiv (Cornell University). (2003). https://doi.org/10.48550/arxiv.cond-mat/0312493.

[11] M. Sawicki, W. Stefanowicz, A. Ney, Sensitive SQUID magnetometry for studying nano-magnetism, Semiconductor Science and Technology. 26 (2011) 064006. doi.org/10.1088/0268-1242/26/6/064006.

[12] J. Wooldridge, Paul, G. Balakrishnan, M.R. Lees, The magnetic field and pressure dependence of the magnetic ordering transition in Na_xCoO_2 ($0.6 \leq x \leq 0.72$), Journal of Physics: Condensed Matter. 18 (2006) 4731–4739. doi.org/10.1088/0953-8984/18/19/024.

[13] Y. S. Lee, “Synthetizing and Measuring Superconducting Sodium Cobalt Oxide (Na_xCoO_2) Crystals,” *The Board of Trustees of the Center for Excellence in Education, 23.*, Jul. 2007.

[14] U. Bhattacharya, V.S. Darshane, Spin–glass behaviour of the system $CoFe_{2-x}Ga_xO_4$, Journal of Materials Chemistry. 3 (1993) 299–302. https://doi.org/10.1039/jm9930300299.

[15] Y. Sassa, I. Umegaki, H. Nozaki, O. K. Forslund, C. Delmas, J. C. Orain, A. Amato, D. Andreica, M. Månsson, J. Sugiyama, Investigation of the Magnetic Properties of $Na_{0.7}CoO_2$ Prepared by Electrochemical Reaction, DORA PSI (Paul Scherrer Institute). (2018). https://doi.org/10.7566/jpscp.21.011019.

[16] H. W. Zandbergen, M. L. Foo, Q. Xu, V. Kumar, and R. J. Cava, “Na-ion ordering in Na_xCoO_2: Electron diffraction study,” vol. 70, no. 2, Jul. 2004, https://doi.org/10.1103/physrevb.70.024101.

[17] F. Huang, M.L. Chu, G.J. Shu, H.-S. Sheu, C. Chen, L. Liu, P.A. Lee, F. Chou, X-ray and electron diffraction studies of superlattices and long-range three-dimensional Na ordering inγ-Na_xCoO_2 ($x=0.71$and 0.84), 79 (2009). doi.org/10.1103/physrevb.79.014413.

[18] R. Aso, T. Katsumata, T. Nakamura, Yusuke Watase, Koji Amezawa, and Y. Murakami, “Structural and electronic characterisation of fluorine-doped $La_{0.5}Sr_{0.5}CoO_{3-\delta}$ using electron energy-loss spectroscopy,” May 2023, https://doi.org/10.1093/jmicro/dfad031.

7.0 General Conclusion

As the demand for sustainable energy storage surges, Na-ion compounds have emerged as promising alternatives to conventional Li-ion systems. The exploration of sodium-ion compounds offers numerous advantages, from the abundance and cost-effectiveness of sodium precursors to their comparable electrochemical properties to Li-ion compounds. In this research, three different Na-ion compounds NZSP (known solid electrolyte), NCO (known cathode materials) and NATP (known anode material) were densified using the conventional and cold sintering methods and their properties investigated by XRD, SEM, EDS, FTIR, Raman, dilatometry, SQUID, and impedance spectroscopy to understand their structure-property relations and assess their potential for use as a solid electrolyte in Na-ion solid-state batteries.

Single phase $Na_3Zr_{2-x}Si_2PO_{12-2x}$ (x = 0.6, *m*-ZrO_2 deficient) was prepared using the solid-state reaction method and the results compared with $Na_3Zr_2Si_2PO_{12}$ (stoichiometric) and literature data. X-ray diffraction and Raman spectroscopy study confirmed the formation of single-phase, and a dilatometry study revealed the shrinkage behaviour (volume change) and melt-pool phase of the ceramic. SEM images revealed a dense cuboid grain structure, and impedance spectroscopy $Na_3Zr_{2-x}Si_2PO_{12-2x}$ (x = 0.0 and 0.6) demonstrated the room temperature conductivity was in the range of (10^{-4} S/cm) with bulk and grain boundary conductivity measured at ≤ 293K. The E_a of the $Na_3Zr_{2-x}Si_2PO_{12-2x}$ (x = 0.0 and 0.6) were within the range of 0.27 ± 0.05 eV. Although a single phase was achieved, this was not accompanied by an increase in conductivity, which suggests that the ZrO_2 phase plays little or no direct role in the properties of NZSP. The main function of an excess of ZrO_2 in the formula unit is perhaps to ensure that NZSP remains single-phase monoclinic, which has been reported to have higher conductivity with respect to rhombohedral.

Cold sintering of NZSP could not be achieved without post-annealing at > 400 °C for several hours to obtain a reasonable ρ_r. XRD confirmed no change in phase composition, and the effect of pressing pressure increased the composition of the *m*-ZrO_2 secondary phase. Particle agglomeration rather than clear densification was observed in SEM micrographs, and the ionic conductivity of the cold sintered ceramic was 10x lower than the conventionally sintered NZSP, but E_a (0.35 ± 0.05 eV) was higher, comparable to the literature values. The lack of success with respect to cold sintering was hindered by the complex way NZSP was produced (crushed sintered pellets). Only small quantities of powder could be fabricated and a source of commercial NZSP could not at the time be obtained.

Conventional sintered NATP was compared and contrasted with cold-sintered NATP. The relative density of the conventional sintered NATP was ~ 92.0%, while cold-sintered only achieved close to this value after post-annealing at > 600 °C for several hours. A dilatometer study of the optimum shrinkage temperature was performed, but the results were affected by the formation of the $AlPO_4$ secondary phase, which was absent in the cold-sintered ceramic. Nano-sized grains were revealed by SEM with the ionic conductivity of the conventional sintered sample in the range of 10^{-7} S/cm, with data difficult to obtain for cold-sintered samples due to the low density. The E_a was higher than that of NZSP, and from the data gathered in this study, NATP may not be ideal for solid electrolyte applications in Na-ion solid-state batteries. Overall, this was the least successful section of the work performed in this thesis. Few reliable measurements could be obtained, and further work is required. In retrospect, pre-milling of the commercial powder would perhaps have yielded superior results through better particle compaction and more homogeneous distribution of transient phase and stress during the cold sintering process, although in the case of NCO, this was not necessary.

The NCO showed exciting and intriguing properties for both conventional and cold-sintered methods. Aqueous cold sintered achieved a higher relative density (~ 98.0%) compared to conventional sintering (~ 92.0%). SEM images support the relative density obtained with no second phases observed and $P6_3/mmc$ symmetry describing all peaks, irrespective of the transient solvent used. The effect of transient solvents on the phase, morphology, and electrical properties of the NCO ceramic shows the impact of the transient solvent on the properties of the NCO ceramic. Aqueous cold-sintered NCO had the highest ionic conductivity of ~ 10^{-2} S/cm at room temperature, comparable to the conventional sintered NCO. In contrast, NCO cold-sintered with different transient solvents achieves a lower conductivity. The calculated E_a was in the range of 0.009 - 0.04 eV, and due to the non-linearity of some of the plots, $T^{-1/3}$ and $T^{-1/4}$ were used to understand the mechanisms. The impedance data concluded that NCO may be a suitable cathode material in Na-ion solid-state batteries instead of being a solid electrolyte.

This was a highly successful section of the thesis with NCO cold sintered to > 95% relative density using multiple transient solvents. Densification and phase purity were typically greater for cold than conventional sintering, and overall, the method showed great promise. All solid-state Na ion batteries are currently being researched, and the field is in its infancy, but cold-sintered NCO (or similar compounds) may prove to be a key determinant in the success of this technology through ease of fabrication and the potential mitigation of interfacial reactions.

Due to the high conductivity observed at room temperature (10^{-2} S/cm), the magnetic properties were further investigated using a SQUID magnetometer. Although the results did not reveal NCO to be superconducting, magnetic behaviour was observed to depend on the processing conditions. Paramagnetic behaviour was observed for both methods, but conventionally sintered samples deviated at 6K to a spin glass state.

Spin glasses occur when there is a degree of disorder amongst magnetic dipoles, which then start to act cooperatively on cooling. When the dipolar regions become large enough, they undergo switching in the magnetic field, giving rise to a peak in the susceptibility. The greater magnetic disorder evidenced through spin glass behaviour indicates that there is a small but tangible difference in either the average or the distribution of Co valence states, likely due to greater volatilisation of Na conventionally compared with cold sintered samples.

In summary, this project has established that only the NCO of the Na-ion compounds investigated may be cold-sintered using a benign aqueous transient solvent. This eco-friendly route may be useful in the future development of Na-ion solid-state batteries, facilitating ease of fabrication.

8.0 Future work

Investigation of the three Na-ion compounds (NZSP, NATP and NCO) in this thesis provided valuable information on the densification methods of these compounds. However, further studies are needed to understand the behaviour of these compounds in Na-ion solid-state battery applications.

To gain a complete understanding of the physical, chemical, and electronic properties of the conventionally sintered NZSP ceramic, it is essential to use Inductively Coupled Plasma (ICP) to predict the exact elemental composition and high-resolution X-ray and neutron diffraction to determine the number of atoms of different elements occupying specific sites in the crystal structure (site occupancy). The use of density functional theory (DFT) to determine local structure would provide an understanding of the conduction mechanisms.

Due to time constraints, the stability window, half/full cell charge/discharge curve, the full-cell performance and the coulombic efficiency of the compounds were not investigated. Such work needs to be undertaken, particularly for NZSP and NCO.

For the cold-sintered NZSP, aqueous media were unsuccessful, but exploring different transient solvents may prove beneficial to densification to eliminate post-annealing. An investigation using alternative non-blocking electrodes, such as In-Ga alloy or sputter Au, to eliminate the need for firing at 850 °C is required to understand cold-sintered compounds fully.

For NATP, it is crucial to utilise transmission electron microscopy to determine the crystal structure at the atomic scale. Improving the ceramic's densification is vital to promote this material's conductivity. Additionally, evaluating NATP’s stability window, half/full cell charge/discharge curve, full-cell performance, and coulombic efficiency can help determine its potential as a possible solid electrolyte. For cold-sintered NATP, further investigation is required to predict the best transient solvents to improve the ceramic's densification, microstructure, and electrical properties.

Finally, for NCO ceramics, using Mossbauer spectroscopy to determine the oxidation state and the site occupancy of the cobaltate is essential. Also, the stability window, half/full cell charge/discharge curve, full-cell performance and coulombic efficiency need to be investigated. Given the high density achieved through cold sintering, the fabrication and testing of half cells may be beneficial.

Further work needs to be undertaken to assess the potential of cold sintering in facilitating the formation of ceramic bi/tri layers in the manufacture of Na all-solid-state batteries. Of particular interest would be to determine whether it is useful in mitigating unwanted interfacial reactions.